UNIVERSIDAD COMPLUTENSE DE MADRID
FACULTAD DE CIENCIAS FÍSICAS

TESIS DOCTORAL

Confinamiento en nanoestructuras poliméricas:
preparación propiedades, aplicaciones e implicaciones físicas

MEMORIA PARA OPTAR AL GRADO DE DOCTOR

PRESENTADA POR

Daniel Enrique Martínez-Tong

Directores

Aurora Nogales
Alejandro Sanz

Madrid, 2014

Universidad Complutense de Madrid

Facultad de Ciencias Físicas

Consejo Superior de Investigaciones Científicas

Instituto de Estructura de la Materia

CONFINAMIENTO EN NANOESTRUCTURAS POLIMÉRICAS: PREPARACIÓN, PROPIEDADES, APLICACIONES E IMPLICACIONES FÍSICAS

Daniel Enrique Martínez-Tong

Tesis Doctoral

Directores:

Dr. Aurora Nogales

Dr. Alejandro Sanz

Madrid, 2014

CONFINAMIENTO EN NANOESTRUCTURAS POLIMÉRICAS: PREPARACIÓN, PROPIEDADES, APLICACIONES E IMPLICACIONES FÍSICAS

CONFINEMENT IN POLYMER NANOSTRUCTURES: PREPARATION, PROPERTIES, APPLICATIONS AND PHYSICAL IMPLICATIONS

Daniel Enrique Martínez-Tong

Tesis Doctoral

Directores:

Dr. Aurora Nogales

Dr. Alejandro Sanz

A mi Abuela…la primera científico de la familia

Agradecimientos

Deseo expresar mi agradecimiento:

Al Consejo Superior de Investigaciones Científicas (CSIC) y al Fondo Social Europeo (FSE) por la beca otorgada para la realización de esta tesis doctoral.

A mis supervisores Dra. Aurora Nogales y Dr. Alejandro Sanz por todo el apoyo y la confianza depositada durante los últimos años.

Al grupo SoftMatPol del Instituto de Estructura de la Materia (CSIC): Dr. Tiberio A. Ezquerra, Dra. Mari Cruz García-Gutiérrez, Dra. Amelia Linares, Dr. Daniel R. Rueda, Dr. José Carlos Canalda, Dr. Ignacio Martín-Fabiani, Dr. Jaime Hernánez, Dra. Esperanza Cagiao, Dra. Michelina Soccio, M. Sc. Ávaro Rodriguez-Rodriguez y M. Sc. Jing Cui.

A la Dra. Carolina García en el Instituto de Química Física Rocasolano (CSIC).

Al grupo LANAMAP del Instituto de Química Física Rocasolano (CSIC): Dra. Marta Castillejo, Dra. Esther Rebollar, Dr. Mikel Sanz y Dr. Mohamed Oujja.

Al Dr. Simone Napolitano en la Universite Librè de Bruxelles en Bruselas, Bélgica. Extiendo este agradecimiento a sus estudiantes Caroline Hausmanns y Jean Spiéce. Asimismo, agradezco al Dr. Michael Wübbenhorst y a su estudiante Bram Vanroy por el apoyo en la universidad KU-Leuven, en Leuven, Bélgica.

Al Dr. Carlos León Yebra, en la Universidad Complutense de Madrid, por todo el apoyo que facilitó durante el proceso de matrícula *a distancia* desde Venezuela, y posteriormente durante mi estancia en España.

A los colaboradores en proyectos a lo largo de estos años: Dr. Miguél Ángel López-Manchado y su grupo de trabajo, Dr. Francesc Pérez-Murano, Dra. Nerea Alayo e Ing. Anushka Najar.

Al grupo de física de polímeros en la Universidad Simón Bolívar en Venezuela: Dra. Estrella Abecassis de Laredo, Dr. Alfredo Bello, Dr. Mario Grimau y Dra. Dinorah Newman.

A todo el personal de secretaría y gerencia del Instituto de Estructura de la Materia, quienes se encargaron de procesar gran parte de los trámites legales durante mi período doctoral. Asimismo, al personal de almacén del Rocasolano (CSIC): Consuelo y Eva.

A mi madre Francisca Tong, por tener que soportar esta relación a distancia sin quejarse en momento alguno, sino siempre estar ahí cuando la necesité. A mi familia, en general pero en detalle especial a mi prima Laura Muñoz-Tong y Flia, quienes saben cómo llevar una vida a distancia conmigo desde hace muchísimo rato.

A mi querida Carlita, mi compañera de vida, mi pedacito de Venezuela que viaja conmigo a todas partes.

A mis viejos amigos: Carla Daniela, Carmenelena, Danielito, Érika, Carla Stabile, Cobo, Alfredo, Lucía, *El Catire*, Godoy, Perfetti, Marling, Carlo Guerrero y Flia, Jeanette y Flia, Mariana Molina (+Phil) y a la gorda Lorenzo. Y también a los amigos no tan viejos: Lili Lafont y Paty, Marigel y Nacho, Ana María, Susie Rodrigo, a todos en la Lomo tienda (incluyendo a Pasquale, Max y Yoni…) A los cuban masters': Yanaisis y Redney, Erney, Adianez. A Roberta y Antonio, Santi, Marga, Elisa y Chiara. En el *Roca* gracias a todos los que respondieron los "Buenos días" con una sonrisa todas estas mañanas. A la mejor asesora de estilos Ainhoa Martínez-Parra y como olvidar a mi compañera de piso durante muchísimo tiempo Angela Sciacca.

Y aunque ya están nombradas arriba, gracias a Esther y Michi, por estar ahí siempre que las necesité, fuera y dentro del ámbito científico. Gracias por esas horas de desahogo, por esos cafés, por las ideas *happy*, por ser tan buenas *compañeras de trabajo* (como diría Esther), aunque como me gusta decirlo a mí es: Gracias por ser tan buenas amigas.

Espero no me haya faltado alguien, y si es así, lo siento mucho y gracias a ti también.

dani

Table of contents

List of symbols and abbreviations

$< d >$	Mean diameter of the nanoparticles size distribution
$< \tau >$	mean relaxation time
α	Segmental relaxation
b,c	Shape parameters of the Havriliak-Negami function
C_p	Heat capacity
ΔC_p	Heat capacity increase
$\Delta\varepsilon$	Relaxation strength
ΔT	Temperature change
ΔT_g	Temperature change of the glass transition
E	Electric Field
ε^*	Complex dielectric permittivity
ε'	Real part of ε^*
ε''	Imaginary part of ε^*
E_c	Coercive Field
ξ	Correlation length
F	Laser beam fluence
f	Frequency
h	Thickness
λ	Wavelength
M_n	Number average molecular weight
M_w	Weight average molecular weight
n_c	Number of polymer chains in a nanoparticle
n_{total}	Total number of repeating units in a nanoparticle
ρ	Density
π	= 3.1416
q	quality factor of nanoparticles size distribution
q_y, q_z	Scattering vectors
σ	Conductivity
θ	Angle between incident X-ray beam and the scattering plane
T_B	Boiling temperatura
T_g	Glass transition temperature
T_m	Melting temperature
W	Width of the nanoparticles size distribution
ω	$= 2\pi f$; Angular frequency

2P	2-Propanol
AC	Alternating Current
AFM	Atomic Force Microscopy
BDS	Broadband Dielectric Spectroscopy
CC	Cole-Cole (dielectric function)
CCl4	Carbon Tetrachloride
CHCl3	Chloroform
CRR	Cooperative Rearranging Region

CSIC	Consejo Superior de Investigaciones Científicas, Spain
DC	Direct Current
DMA	N, N-Dimethylacetamide
DSC	Differential Scanning Calorimetry
EG	Ethylene Glycol
GIWAXS	Grazing Incidence Wide Angle X-ray Scattering
H2O	Water
HEP	Heptane
HEX	Hexane
HN	Havriliak-Negami (dielectric function)
IEM-CSIC	Instituto de Estructura de la Materia, Spain
IMB-CSIC	Instituto de Microelectrónica de Barcelona, Spain
IQFR-CSIC	Instituto de Química Física Rocasolano, Spain
KUL	KU-Leuven University, Belgium
NCHV	AFM tapping probes
NIL	Nanoimprint Lithography
P(VDF-TrFE)	Poly(vinyledene fluoride - co - trifluoro ethylene)
P3HT	Poly(3-hexylthiophene)
PBAC	Poly(bisphenol A carbonate)
PBMA	Poly(butyl methacrylate)
PCBM	Phenyl-C61-butyric acid methyl ester
PDLLA	Poly(D,L-lactic acid)
PEMA	Poly(ethyl methacrylate)
PFM	Piezoresponse Force Microscopy
PLA	Poly(lactic acid)
PLAL	Pulsed Laser Ablation in Liquids
PLD	Pulsed Laser Deposition
PLLA	Poly(L-lactic acid)
PPA	Poly(propylene adipate)
PPAz	Poly(propylene azelate)
PPS	Poly(propylene succinate)
PS	Poly(styrene)
SA	ScanAsyst AFM peak force tapping probes
SCM-PIC	Conductive AFM probes
SDS	Sodium Dodecyl Sulfate
THF	Tetrahydrofuran
ULB	Universite Librè de Bruxelles, Belgium
WAXS	Wide Angle X-ray Scattering

Abstract

This Doctoral Thesis presents the results of the preparation, properties and physical implications of polymer systems in confined geometries. The different responses, respect to the bulk material were studied by several techniques such as differential scanning calorimetry, broadband dielectric spectroscopy, x-ray diffraction and atomic force microscopy.

Different preparation methods of polymer confined in 1, 2 and 3 dimensions were tested and applied. In every case, we departed from an amorphous or semicrystalline bulk polymer material that was subsequently processed until a nanostructured was obtained. Advantages and disadvantages of each preparation method are presented. In addition the different preparation methods are carefully highlighted in a step-by-step fashion.

The properties and physical implications of polymers confined in different geometries are studied and presented in different chapter, each one regarding one specific polymer property. We begin by presenting the results on the changes of the glass transition temperature in confined polymers, where we found that the confined structures of polymer nanospheres show a higher glass transition temperature in comparison to their bulk materials. An entropy-based model is presented for discussion of the results. We show that the dependence of the glass transition in confined systems is related to the number of repeating units enclosed in the confined polymer. Afterwards, we present the results of crystallization in restricted geometries. In polymer thin films, we have found that the restriction imposed by the geometry, affects the crystalline morphology and crystallization rate. Also, we show how adsorption between the polymer thin film and supporting substrate becomes important as thickness is reduced to tens of nanometers. Crystallization behavior of polymer nanoparticles is also presented. Finally, the

ferroelectric properties of polymers confined in different nanostructures are studied. Both polymer nanoparticles and polymer thin films are evaluated. In addition to the fundamental studies of ferroelectricity, we propose the possibility of developing physical devices, based on nanostructures, for organic memory systems.

Sumario

En esta tesis doctoral se presentan los resultados en la preparación, propiedades e implicaciones físicas de sistemas poliméricos en geometrías confinadas. Las diferentes respuestas, respecto al material en estado volumétrico, fueron estudiadas a través de diversas técnicas como: calorimetría diferencial de barrido, espectroscopia dieléctrica de banda ancha, difracción de rayos-X y microscopía de fuerzas atómicas.

Varios métodos de preparación de polímeros confinados en 1, 2 y 3 dimensiones fueron probados y aplicados. En cada caso, se inició con un polímero amorfo o semicristalino, el cual se procesó posteriormente hasta obtener una nanoestructura. Se presentan las ventajas y desventajas de cada método de preparación. Además, los diferentes métodos de preparación se resaltan en modo paso-a-paso.

Las propiedades e implicaciones físicas de polímeros confinados en diversas geometrías son estudiadas en diferentes capítulos, cada uno en lo que respecta a una propiedad particular. Iniciamos presentando los resultados en cambios en la temperatura de transición vítrea en polímeros confinados. En este caso encontramos que nanoesferas poliméricas presentan una temperatura de transición vítrea más que el polímero. Para explicar y discutir los resultados, se presenta un modelo basado en la entropía de los sistemas. Se argumenta que la dependencia de la transición vítrea en sistemas confinados está relacionada con el número de unidades de repetición englobadas en la estructura confinada. Luego, presentamos resultados acerca de los procesos de cristalización en geometrías confinadas. En el caso de películas delgadas poliméricas se observó que la restricción impuesta por la geometría afecta a la morfología cristalina y a la tasa de cristalización. Asimismo, se muestra cómo la adsorción entre la película polimérica y el sustrato soporte toma importancia cuando los espesores del polímero se

reducen en torno a las decenas de nanómetros. Finalmente, presentamos las propiedades ferroeléctricas de polímeros confinados en diferentes nanoestructuras. Tanto nanoaprtículas como películas delgadas poliméricas son evaluadas. Más allá de las propiedades ferroeléctricas fundamentales, proponemos la posibilidad de desarrollar dispositivos físicos, basados en nanoestructuras, para sistemas de memoria orgánicas.

CHAPTER 1 – Introduction

School teaches us that matter can be found in three states: solid, liquid and gas. Advanced courses also include plasma as the 4th state of matter. However, considering the *classical* labeling of three states, the distinction between states is made on qualitative differences in properties. For example, solids are able to maintain a fixed volume and shape, while liquids have a constant volume but its shape can adapt to fit its container. Matter in the gaseous state has both variable volume and shape. Nonetheless, it is possible to find materials that cannot be classified according to this labeling, for example, liquid crystals, emulsions, gels, colloids, among others. Soft condensed matter (or ***soft matter*** for brevity) is a convenient term for materials in states of matter that are neither simple liquids nor crystalline solids of the type of other branches of solid state physics[1]. Soft matter materials are sometimes also called *complex fluids*, name which brings in two of the major features of these systems: complexity and flexibility[2, 3]; for example materials that consist of extremely large molecules which also can be easily deformed.

According to Gompper and Schick, dispersion colloids, systems of small amphiphiles and polymers can be classified as "classical" soft matter systems[4]. Specifically, polymers (also known as macromolecules), are built up of a large number of molecular units which are linked together by covalent bonds[5]. Usually, polymers represent organic compounds, containing carbon atoms together with hydrogen, oxygen, nitrogen and halogens. According to the basic IUPAC definition: A polymer is a substance composed of molecules, characterized by the multiple repetition of one or more species of atoms or groups of atoms (constitutional repeating units), linked to each other

in amounts sufficient to provide a set of properties that do not vary markedly with the addition of one or a few of the constitutional repeating units[6]. The fact that polymers are ubiquitous should not blind one to the difficulty of accepting the concept of a giant molecule. It is not now, nor was earlier, an obvious one. It was in 1922 that the German organic chemist, Hermann Staudinger, who coined the term "macromolecule", published a theory claiming that rubber was made of a natural polymer, and that it was the entropic properties of such chains that were the source of the elasticity of the material[4].

When a polymer consists of only one type of constitutional repeating unit (A) is usually called a ***homopolymer*** (…-A-A-A-…). A ***copolymer***, on the other hand, consists of two or more constitutional repeating units (A,B,…)[6]. Several classes of copolymers are possible, such as block copolymers (…-A-A-A-B-B-B-A-A-A-…) or alternating copolymers (…-A-B-A-B-A-B-…). Also, it is possible to find ***random copolymers***, where the constitutional repeating units do not follow any strict pattern. In this case, the probability of finding a given constitutional repeating unit at any site is independent of the nature of the adjacent units at that position[6].

The enormous size of polymer molecules influences their physical properties. In other words, depending on the molecular mass of the polymers, their properties (thermal, mechanical,…) may vary. There is currently no method able to prepare polymers such that all the polymer molecules have the same size. Variations and wide distributions of molar mass among the molar mass is characteristic of all synthetic polymers. This is the reason why the characteristic molar mass of a polymer is given by an average[6]. The most commonly used averages are defined as follows. The ***number average*** (M_n) is given by

$$M_n = \frac{\sum_i N_i M_i}{\sum_i N_i} = \sum_i n_i M_i$$

where N_i is the number of molecules of molar mass M_i, and n_i is the numerical fraction of those molecules. The ***mass*** or ***weight average*** is given by:

$$M_w = \frac{\sum_i N_i M_i^2}{\sum_i N_i M_i} = \frac{\sum_i W_i M_i}{\sum_i W_i} = \sum_i w_i M_i$$

where W_i is the mass of the molecules of molar mass M_i, and w_i is the mass fraction of those molecules. These averages are equal only for a perfectly monodisperse polymer. In all other cases, $M_n < M_w$. The breadth of the molar mass distribution, expressed as its standard deviation (σ), is related to the ratio M_w/M_n (known as the ***polydispersity index***) as follows:

$$\frac{\sigma}{M_n} = \sqrt{\frac{M_w}{M_n} - 1}$$

the standard deviation takes the value zero for $M_w/M_n = 1$. The polydispersity index takes a high value for a sample with broad molar mass distribution, *i. e.* a high σ value[6].

It is useful to divide the polymers into two main classes: the fully amorphous and the semi-crystalline. The fully amorphous polymers show no sharp, Bragg reflections in the X-ray diffractograms taken at any temperature. The reason why these polymers are unable to crystallize is commonly their chain structure. The semi-crystalline polymers show Bragg reflections superimposed on an amorphous background (also known as amorphous halo). Thus, they always consist of two components differing in the degree of

order: a crystalline component composed of thin (around 10 nm) lamella-shaped crystals and an amorphous matrix[6]. But, what characterizes the final structure of a polymer system? Let us consider a polymer which is in its molten state, *i. e.* in a state where the polymer molecules (also known as ***chains*** due to their long macromolecular structure), have as much mobility as possible. The different scenarios that can occur when this polymer is cooled down are shown in figure 1.1. According to this figure, the polymer may either crystallize (route **a**) or cool down to its glassy, amorphous state (route **b**). In this last case, the temperature at which the slope in the specific volume - temperature graph changes, is referred as ***glass transition temperature*** (T_g) or vitrification process. Cooling past the glass transition temperature is accompanied by a dramatic change in the mechanical properties and kinetic processes of the polymers, such as diffusion, viscous flow and molecular reorientations[7].

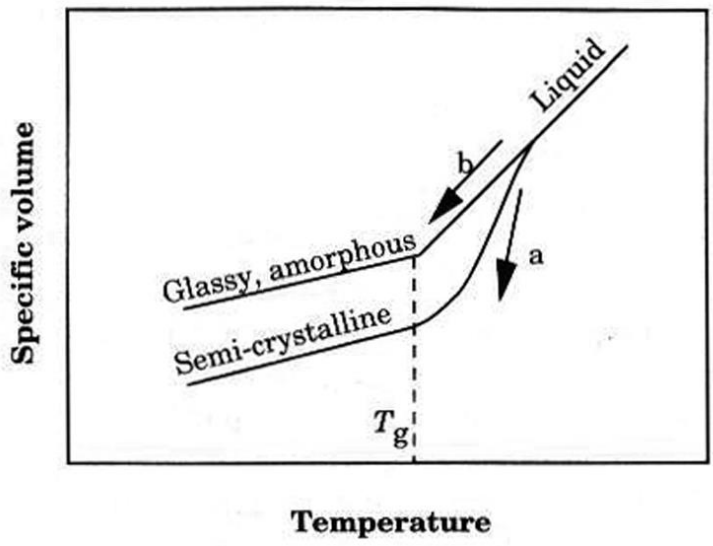

Figure 1.1. Cooling of a liquid following rotes **a** (crystallization) or **b** (glass amorphous structure). Figure taken from reference[6].

The elastic modulus increases by a factor 1000 when the polymeric liquid is cooled below T_g and the modulus of the glass polymers is relatively insensitive to

changes in molar mass and repeating unit structure. In the end, below the glass transition temperature, the macroscopic effects of atomic redistributions can no longer be seen and the polymer looks frozen, just like a disordered solid off thermodynamic equilibrium, namely a ***glass***[8]. Conversely, if the transformation path is reversed, the glass is progressively heated until, at T_g, polymer chains gain enough mobility, just as happens with a crystal is brought up to its melting point.

The actual value of T_g is dependent, on the repeating unit, molecular architecture and the presence of low molar mass species in the polymer. Figure 1.2 shows schematically the effects of the polymer structure and cooling rate on the solidified polymer structure. Going from the molten polymers to the solidified state, results on amorphous or semi-crystalline structures depending on the shape and conformation (ordering of molecules) of the polymer chains and on the thermal history of the system (if the liquid is cooled sufficiently fast, ***quenched***, crystallization can be avoided)[6, 9].

1.1. Theories and models of the glass transition

Thermodynamic and kinetic features are present in the glass transition phenomenon, and these processes are interwoven. For this reason, it is very difficult to put forward a theoretical representation of this transition[8]. The models proposed in the literature, often phenomenological, have put much light on the trend of (kinetic) relaxation phenomena or, respectively, on thermodynamic quantities. Current theories on the glass transition are summarized in the following paragraphs.

The ***free volume*** theory was originally developed for a fluid of hard spheres which simulate the molecules in a liquid. The total volume V_1 of the liquid is divided into one

part that is occupied by the spheres, V_0, and one part of free (void) volume, V_V, where the spheres can carry out diffusive motion. It has been postulated that transport takes place only if the sum of all voids, V_V, is greater than a critical value, $V_{V,c}$. Furthermore, since the free volume consists of variable sized voids, whose distribution is the result of random molecular motion, there are no local concentration variation terms, which would otherwise lead to space rearrangement of the voids. Space concentration of free volume is thus uniform. As the temperature falls, both the occupied volume and the free volume contract. The liquid is different from a glass because in the glass V_V is independent of temperature and is not redistributed, being frozen in the set of positions it occupies at glass formation. Glass transition occurs if $V_V < V_{V,c}$, *i. e.* the glass transition is the temperature at which the glass forming systems (such as polymers) have a certain universal free volume[6, 8].

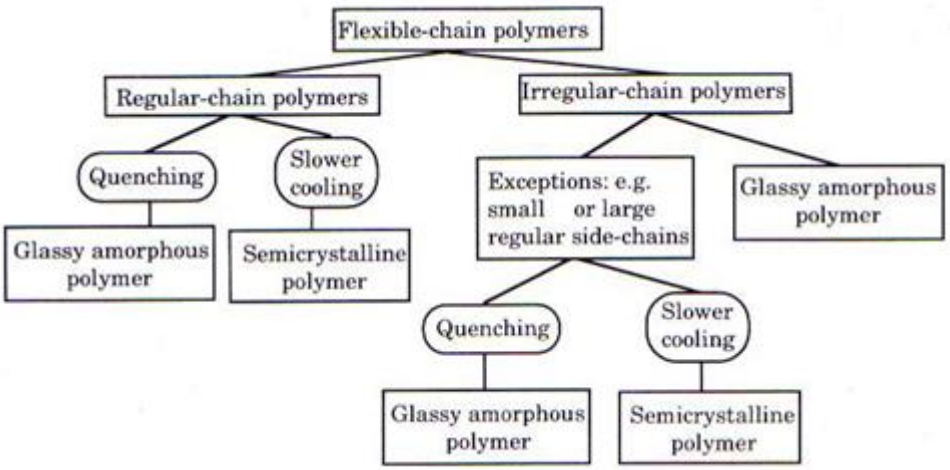

Figure 1.2. The effect of molecular and thermal factors on the structure of the solidified polymer. Scheme taken from reference[6].

The ***kinectic*** theories postulate that there is no true thermodynamic glass transition, but that the glass transition is a purely kinetic phenomenon. Thus, glass trantision takes

place when the response time for the system to reach equilibrium is of the same size as the time-scale of the experiment. Kinetic theories predict that a lowering of the cooling rate will lead to a decrease in the kinetic glass trantision temperature[6].

The ***thermodynamic*** theory was formulated by Gibbs and DiMarzio[10], who argued that, although the observed glass transition is a kinectic phenomenom, the underlying true transition can posses equilibrium properties. This theory aimed to explain the Kauzmann paradox, which can be stated as follows. If the equilibrium properties of a material, entropy (S) and volume (V), are extrapolated through the glass transition, the values of S and V for the glass will be lower than for the corresponding crystals. The equilibrium theory solves the problem by predicting a thermodynamic glass transition reached when the conformational entropy (S_c) takes the value zero. As a glass-forming system is cooled down, the number of possible arrangements (*i. e.* the conformational entropy) of the molecules, decreases gradually with decreasing temperature. This is due to a decrease in the number of vacancies (voids), a decrease in the permutation of the voids and chain segments, and the gradual approach of the chains towards populating the low-energy crystalline state for the crystallizable materials[6].

The firsts attempts to make a theory of the glass transition focused on the question of how it might be possible for an ordinary material, obeying the laws of classical statistical mechanics, to move towards a frozen state, while being increasingly unable to access its true equilibrium structure or respond to some kinds of external forcing on observable time scales[11]. A simple description of this class of phenomena was proposed in 1958 by Adam and Gibbs[12]. Authors proposed a formula providing a suggestive connection between kinetics and thermodynamics:

$$\tau = A\exp\left(\frac{B}{TS_c(T)}\right) \qquad (1.1)$$

where τ is a relaxation time (or, equivalently, the viscosity), *A* and *B* are constants and S_c is the configurational entropy, also understood as the *excess* of entropy per unit volume, measured relative to the crystalline state. Adam and Gibbs interpreted S_c(T) as being inversely proportional to the size of a ***cooperative rearranging region*** (CRR), within which there would be just enough degrees of freedom (*i. e*. entropy) to enable rearrangements[11]. They further assume that the excess energy associated with this region scaled with its volume, so that equation (1.1) could be interpreted as a thermal activation formula[11]. A weakness of this treatment is that the theory does not provide information on the size of the CRRs, and that the fact that CRRs are indistinguishable from each other. However, equation (1.1) describes the relaxation behavior of deepely supercooled liquids remarkably well.

More insight about this subject is given in figure 1.3. Here the temperature dependence of the entropy difference between several supercooled liquids and their stable crystals is presented[9]. We will take the curve for the lactic acid as example. In this case, the entropic surplus is consumed so fast that a modest extrapolation of experimental data predicts its impeding vanishing. In practice, the glass transition intervenes and Δ*S* does not vanish. If the glass transition did not intervene, the liquid entropy would equal the crystal's entropy at a nonzero temperature T_K, known as Kauzmann temperature. Because the entropy of the crystal approaches zero as the temperature of the system tends to zero, the entropy of the liquid would eventually become negative upon cooling, if the extrapoled trend (light blue curve) were to continue. Since entropy is an inherent non-

negative quantity, the state of affairs, to which liquids such as lactic acid are tending when the glass transition intervenes, is an entropy crisis.

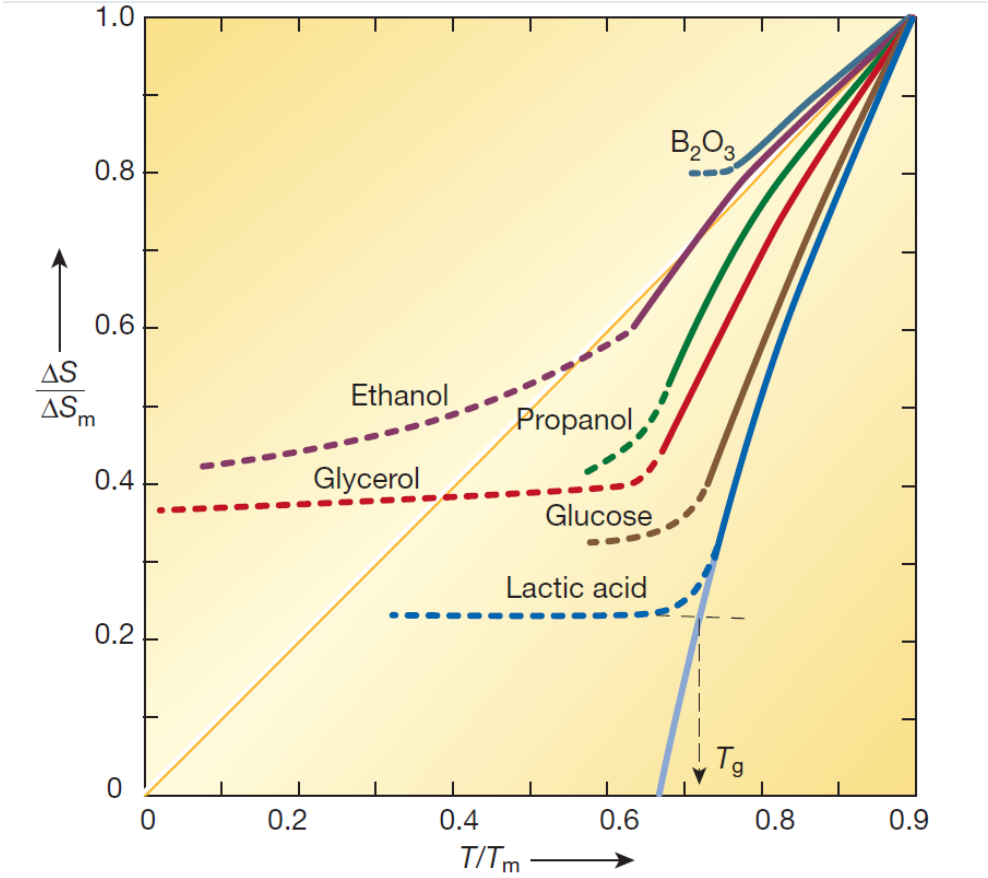

Figure 1.3. Temperature dependence of the entropy difference between several supercooled liquids and their stable crystals at atmospheric pressure. ΔSm is the melting entropy and Tm is the melting temperature[9].

Other models have also been proposed in order to explain the glass transition phenomena. Among them, one can highlight the random first order transition theory (RFOT) and the two order parameter model (TOP). In the RFOT model[13] the supercooled system is envisioned as an aperiodic composite of solid like regions (droplets) of different sizes, inside of which the motion is cooperative during the transition. The TOP model[14] introduces an additional order parameter $\hat{S}$, responsible for locally favored structures that impede crystallization as they are incompatible with long range order. This TOP model,

therefore, also uses dynamics heterogeneity as it predicts the existence of medium range crystalline order regions below the melting point whose size diverges at the glass transition. All the above mentioned model and theories for the glass transition implies the existence of regions with different dynamical characteristics, of a given characteristic length ξ.

1.2. Relaxation phenomena in glass forming systems.

Within the terminology of statistical mechanics, ***relaxation*** means an irreversible process, in contradistinction of time-reversible process of Newtonian mechanics. It is the time-dependent change of a system or a sub-system from one physical or thermodynamic state to another, involving the dissipation of energy[15]. Although the microscopic dynamics of the many-body interacting system is invariant under the reversal of time, nevertheless the system irreversibly moves towards equilibrium[15]. The relaxation process is the time-dependent approach of the system from the initial stationary state to another as a consequence of the change of an external input. The simplest changes include sudden application of the external input at some time to the system initially stationary and kept constant thereafeter or conversely, sudden removal of the external input after it has been applied for a sufficiently enough long time and the system already has become stationary. External inputs can be mechanical stress and strain, electrical stress and dielectric displacement (also their magnetical and chemical equivalents), foreing agents such as humidity, or thermodynamic parameters (temperature, pressure, etc). For example, if the external input is a mechanical stress, then the relaxation is observerd by measuring the strain[15-17].

Nowadays, many experimental techniques have been developed for the study of relaxation, such as mechanical and dielectric methods[18, 19], nuclear magnetic resonance, neutron scattering[20] and light-scattering techniques[21]. These techniques probe not only the dynamics, through different dynamic variables, but also these variables at different length-scales, from the size of atoms and molecules, to macroscopic dimension. The experimental results on dynamics are presented in terms of time/frequency dependence of a quantity in response to the change of another quantity. The time/frequency response becomes independent of the magnitude of the change when the latter is sufficiently small. These are linear responses or linear relaxations, where the time or the frequency does not depende on the size of the perturbation. Experimental results obtained by mechanical and dielectric relaxation techniques are expressed by macroscopic relaxation and compliance functions. On the other hand, the dynamics measured by techniques such as neutron scattering and obtained by molecular dynamics simulations are given at the molecular level [15].

1.3 Slowing down near the glass transition

Another defintion of the T_g is the temperature at which the shear viscosity reaches 10^3 poise. Close to T_g, the viscosity η is extraordinarily sensitive to temperature[9]. For example, for silica, this dependence is reasonable well described by the Arrhenius functionality:

$$\eta = A\exp\left(\frac{E}{k_B T}\right) \tag{1.2}$$

where A and E are temperature-independent parameters and k_B is Boltzmann's constant. Other liquids exhibit an even more pronounced viscous slow-down close to the glass

trantisition. This is reasonably well represented by, over 2-4 orders of magnitude in viscosity, by the Vogel-Fulcher-Tamann (VFT) equation:

$$\eta = A\exp\left(\frac{B}{T - T_0}\right) \tag{1.3}$$

where A and B are temperature-independent constants. Understanding the origin of this extraordinary slow-down of the relaxation processes, near the glass transition, is one of the main challenges in the physics of glasses[9]. Notice that, if a suggested by Kauzmann $S_c(T)$ in equation (1.1) vanishes linearly at $T = T_K$, then, equation (1.1) becomes the VFT equation:

$$\tau_\alpha = \tau_0\exp\left(\frac{T\ D}{T - T_0}\right) \tag{1.4}$$

where $T_0 = T_K$, and D is a parameter sometimes known as the inverse ***fragility***. The fragility is a useful classification of liquids proposed by C. A. Angell[22, 23]. According to this classification, the viscosity and relaxation times of strong liquids follow an Arrhenius behavior, while fragile liquids show marked deviations from the Arrhenius law. Also the concept is closley related to the structural stability of the systems. Figure 1.4 shows a T_g-scaled representation of liquid viscosities. The difference between the strong and fragile behavior is pointed out. The slowing down in the mobility of polymers (increase of viscosity = increase of relaxation time), near the glass transition temperature, is defined as the ***segmental relaxation of polymers*** or ***α-relaxation.*** The adjetive segmental is related to the fact that in this temperature region the relaxation takes place not in single monomers in the polymer structure, but in segments of the polymer chain. This can be understood in terms of the CRRs of the Adam-Gibbs theory of the glass transition.

Viscous liquids close to T_g can exhibit non-exponential relaxation. The temporal behavior of the response function $F(t)$ (for example, the strain resulting from an applied stress, or the polarization in response to an applied electric field) can often be described by the stretched exponential, or Kohlrausch-Williams-Watts (KWW) function:

$$F(t) = \exp\left[-\left(\frac{t}{\tau}\right)^{\beta}\right]; (\beta < 1) \qquad (1.5)$$

where $F(t) = [\sigma(t) - \sigma(\infty)]/[\sigma(0) - \sigma(\infty)]$ and σ is the measured quantity (for example, the instantaneous stress following a step change in deformation). τ in equation (1.5) is a characteristic relaxation time, whose temperature dependence is often non-Arrhenius (fragile behavior). The slowing down of long-time relaxations embodied in equation (1.5), contrasts with the behavior of liquids above the melting point, which are characterized by simple exponential relaxation. Experimental and computational evidence indicates that this slow-down is related to the growth of distinct relaxation domains. Whether each of these spatially heterogeneous domains relaxes exponentially or not is a matter of current interest[9].

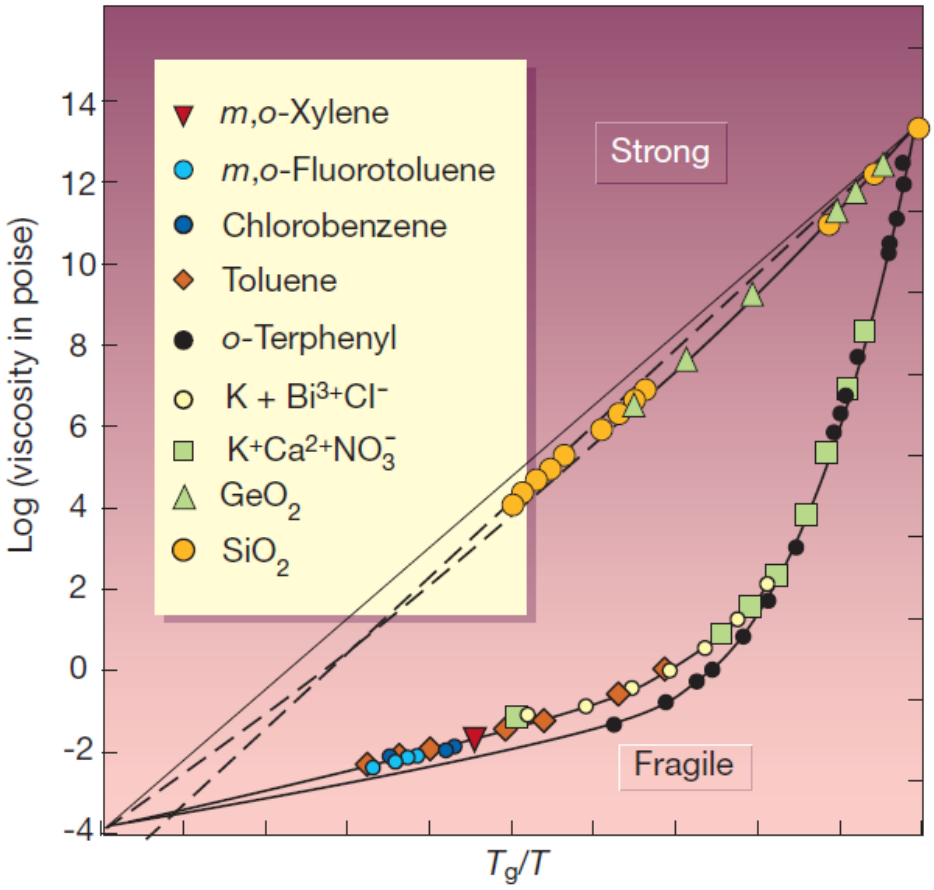

Figure 1.4. Tg-scaled Arrhenius representation of liquid viscosities shows Angell's strong-fragile pattern[9].

1.4. The metastable semi-crystalline state of polymers

At first it may seem questionable that polymers can set up a crystal at all. If one starts from a melt of coiled, mutually interpenetrating macromolecules, it is impossible to attain an ideal crystalline state of extended straight chains with the endgroups assembled in planar interfaces, purely due to kinectic reasons. The requiered complete disentangling would need a too long time, as it is associated with an extremely high entropic activation barrier. Instead, the way in which the polymer systems reacts on these conditions, is that cooling a melt below the equilibrium melting point produces a system which is ***only in part crystalline***[5]. This state is also known as ***semi-crystalline***[24]. One observes layer-like crystallites which are separated by disordered (amorphous) regions, thus setting up a

lamellar two-phase structure. This crystallization process in polymers can be described in the following steps: first, a preciding unmixing takes place in the melt state, whereby sequences which can be extended and incorporated into a growing crystal are separated from chain parts near to entanglements which can only be removed and shifted into the amorphous regions. To be sure, not only entanglements consitute the non-crystallizable chain parts, but endgroups, chemical perturbations like short chain branches, or specific local conformations which oppose a transformation into the helical form, as well. They all become accumulated in the amorphous parts of a partially crytalline system[5].

Semi-crystalline polymers exhibit different characteristic features on different length scales. Figure 1.5 shows a typical semi-crystalline polymer structure in the range of μm – mm, as observed in an optical microscope. It is observed spherical objects, so called ***spherulites,*** which appear as small nuclei somewhere in the view-field and then grow in size. This process is addressed as a crystallization by ***nucleation and growth of spherulites***. The spherulites grow with a constant rate up to the point where they touch each other. Finally, the whole volume is covered by bound spherulites. Their final size depends on the nucleation density and can vary over a large range, from several μm up to some cm[5].

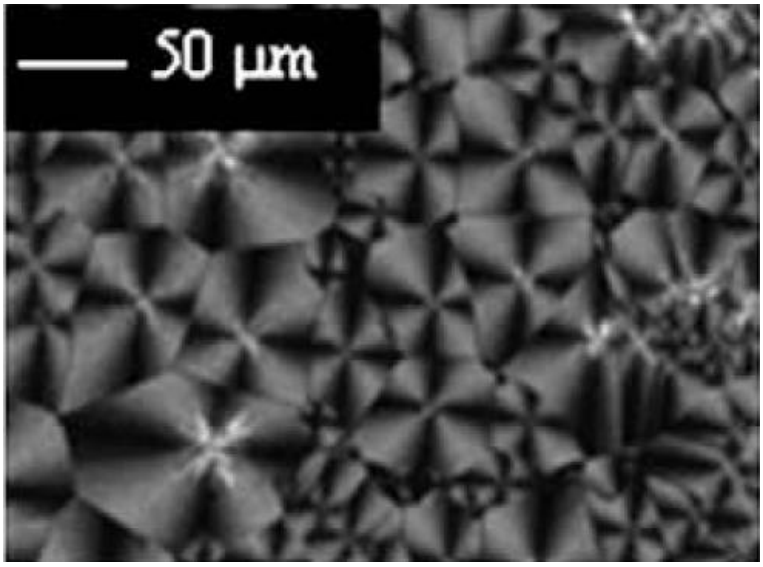

Figure 1.5. Optical micrograph of the spherulitic structure of poly(butylene succinate)[25].

The detailed structure of polymer spherulites can best be studied by atomic force microscopy (AFM)[26-32]. The nondesctructive character of the AFM presents an important advantage in the study of such systems, as they can be destroyed during preparation or observation with classical techniques such as transmission electron microscopy (TEM). Also, AFM studies do not require any special sample preparation such as metal or carbon deposition, or micro-sectioning or staining. Therefore, AFM can provide a great wealth of information on the structure of such systems, without causing any damage to the sample[33]. Figure 1.6 shows an AFM height image of a crystallized sample of poly(D,L-lactic acid). In this image, the spherulitic morphology is also observed with even more detail as in comparison with figure 1.5. Spherulites can be seen to consist of crystals radiating out from a central nucleus. Closer examination of the image shows that crystals are lamellar.

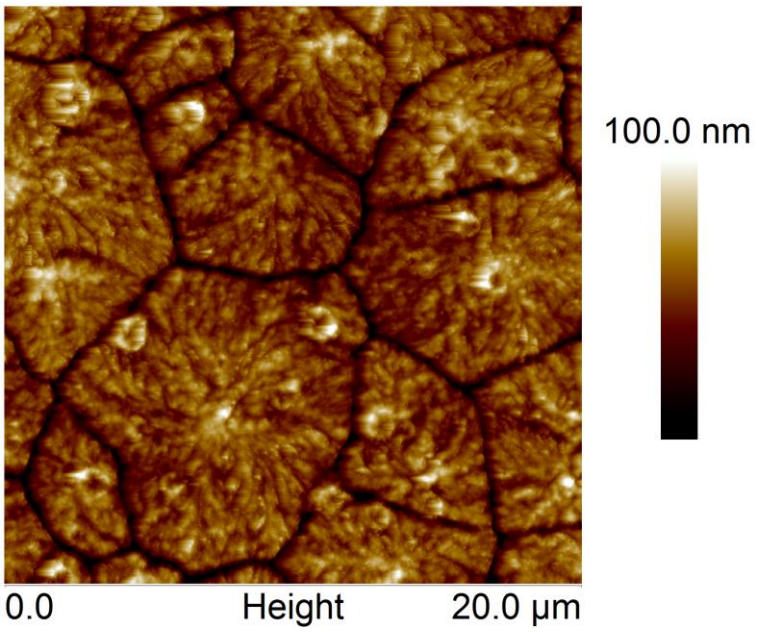

Figure 1.6. Crystalline structure of poly(D,L-lactic acid) observed by AFM (further studied in chapter 6).

As stated in the previous paragraphs, the enormous number of chains entanglements in a polymer melt does not allow a complete crystallization of the system. Thus, it is impossible for the amount of organization required to form a 100% crystalline polymer to take place during crystallization. This allows introducing the concept of ***degree of crystallinity,*** *i. e.* what ratio of the polymer system has transformed from amorphous to crystalline, for a given temperature and time[5, 24].A powerful method of determining the degree of crystallinity is wide-angle X-ray scattering (WAXS). A typical WAXS pattern for a semi-crystalline polymer is shown in figure 1.7, where the scattered intensity is plotted against the diffraction angle 2θ.

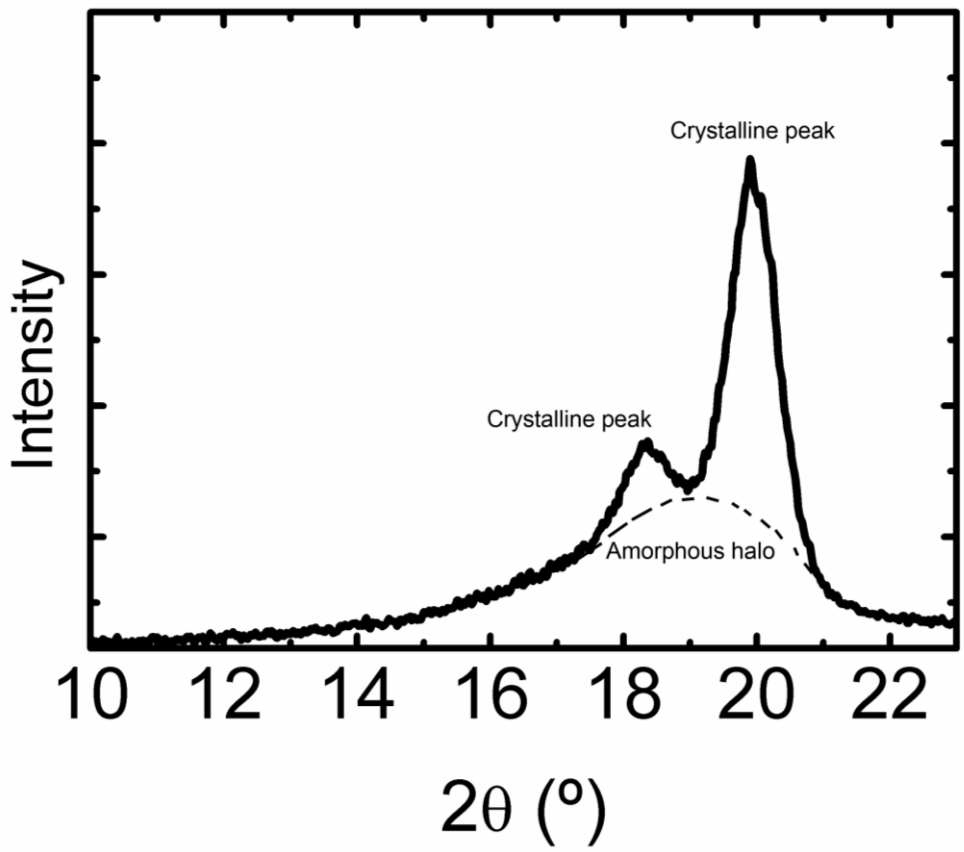

Figure 1.7. WAXS pattern for poly(vinilydene fluoride - trifluoroethylene) (further studied in chapter 7). The intensity of scattering is plotted as a function of 2θ. The amorphous halo is the area below the dashed curve.

The relatively sharp peaks, observed in figure 1.7, are due to scattering from the crystalline regions, while the broad underlying hump is due to scattering from non-crystalline regions. This hump is known as the ***amorphous halo***. In practice is quite difficult to resolve the scattering curve into area due to each phase. The shape of the amorphous halo can be determined from a WAXS curve for a completely amorphous sample, obtained by rapidly cooling from the molten state. However, for certain polymers this can be difficult or even impossible[5]. Nevertheless, an appropriate idea of the crystallinity can be obtained by the simple trapezium construction of numerical

integration. If the areas of the peaks and halo are found, then the mass fraction of crystals (X_c) is given in a first approximation by:

$$X_C = \frac{A_c}{A_c + A_a} \tag{1.6}$$

where A_a is the area of the amorphous halo and A_c is the area remaining under the crystalline peaks. Although WAXS is a widely used method for determining the degree of crystallinity of semi-crystalline polymers, several other methods, based on density determination, electrical resistivity, enthalpy, among other physical parameters can be also used[5].

1.5. Polymer systems under confinement

The rapid development of nano-science and nanotechnology in the 20th and 21st centuries creates a lot of questions about the structure and surface properties of nano-materials[34]. The prefix ***nano***- is used in a broad way to describe systems where one or several physical dimensions have been reduced to length scales between 1 nm and 100 nm, and also to the application of concepts and understanding of properties (physical, chemical, biological, mechanical,…) that derive as a result of the reduced length scale[35, 36]. The possible change in properties, when a material is nanostructured, is understood as ***confinement effects***[37].

Polymers confined in nanometer-sized geometries have been intensively investigated in the last decades, aiming both to achieve a deeper understanding of finite-size effects in soft matter and to improve the performance of nano-devices and hybrid materials[38]. When designing and preparing nanostructures, one or several physical

dimensions can be affected. For example, if a nanostructured polymer system is prepared in a way that two dimensions have macroscopic dimensions, while the remaining is in the nanometer scale, the resulting material is said to be one dimensionally confined (1D-confinement). This is the case of ***polymer thin films***. If two dimensions have nanometer scales, one can talk about two dimensional confinement (2D-confiment), which is the case of ***nanowires*** and nanotubes. Finally, when all three dimensions are in the nanometer length scale, such as in ***nanoparticles***, the polymer is said to be three-dimensionally confined (3D-confinement). Moreover, confined polymer structures can be further processed to obtain *à la carte* nano-features, such as nanostructured surfaces on polymer thin films[39], alignment of polymer nanowires by percolation into nanoporous membranes[40, 41], or even physical responsive polymer nanoparticles[42].

1.5.1. Polymer thin films

Polymer thin films are one of the most studied polymer systems at the nanoscale[43]. From 1986 to 2006, publications in this area increased in more than a factor 10 (according to Elsevier Scopus). Interest in this area has relied in two main factors. First, from a technological point of view, polymer thin films are used as coatings in the electronics industry and in biomedical applications[44]. Due to the miniaturization of devices, thicknesses of the polymer layers have been fairly reduced, which lead us to the second factor of study: physical implications reducing the polymer thickness down to a few nanometers[45].

Polymer thin films have been usually prepared by the spin coating protocol. In this technique, widely discussed in chapter 2, a polymer solution is casted on top of a rotating substrate, generally a silicon wafer. Rapid evaporation of the solvent, due to the spinning,

allows obtaining continuous polymer films in a thickness scale below 100 nm. However, other techniques have been employed to prepared polymer thin films, such as physical vapor deposition (PVD)[46] and matrix assisted pulsed laser evaporation (MAPLE)[47-49].

From the fundamental point of view, the pioneering works by Keddie and collaborators[50, 51], are possibly regarded as the start point that set interest in the physical implications of polymer thin films[52, 53]. In these works, the authors observed, by ellipsometry measurements, that the glass transition temperature of polystyrene thin films decreased as thickness is reduced[50]. Throughout the following years, the mentioned authors have shown that this decrease could be related to the existence of a free-surface layer in the polymer films[53]. The free-surface layer can be understood as a polymer layer, the one closer to the air, which has an enhanced mobility[54]. This model had to be invoked, since the changes in T_g occurred for film thicknesses much higher than the size of the CRR, and thus the T_g reduction could not be related directly to cooperative rearrangement.

Contemporary with Keddie's works, other authors have stated that the modification of the glass transition temperature, $\Delta T_g = T_g(h) - T_g(\text{BULK})$, with h as the thickness, is influenced by the surface nature[54, 55]. It has been reported that the sign of ΔT_g is directly related to the strength of the interfacial polymer-substrate interactions. Namely, $\Delta T_g < 0$ corresponds to weak interactions, whereas $\Delta T_g > 0$ corresponds to strong interactions[37, 38, 56, 57]. It has been also pointed out that changes in T_g correspond to the thickening of the layer of polymer chains ***irreversibly adsorbed*** into the supporting surface (also known as ***residual layer***[58]). This residual layer might act as local free volume, altering the structural dynamics and, thus, T_g. This *increase* in free volume, with

respect to the bulk, caused for example by packing frustration, might result in an acceleration of the segmental dynamics and thus justify reductions of T_g even in the presence of slower dynamics associated to chain adsorption[59].

Confinement of semi-crystalline polymers into thin films can affect both the morphology and the growth of the resultant crystals. Because of the growing interest in nanotechnology, it becomes important to understand crystallization in low dimensional space under confinement[60]. As the desired size of the product material gets increasingly smaller, it is important to determine the variations in crystal morphology, growth and/or kinetics, in comparison to the bulk. There are two common ways to study crystallization in confinement[60]. One is in block copolymers with at least one crystalline component[61, 62]; the other is in thin films[38, 63]. In the latter case, the crystallization process is affected, generally, when the film thickness is less than the average spherulitic dimension. In that case, the semi-crystalline material will crystallize into flattened spherulites or discoids[64]. Thin films of the size of a monolayer can be also prepared. This is achieved when the thickness is in the order of magnitude as the radius of gyration (R_g) of the polymer chain. R_g is defined as the root-mean-square distance of the collection of atoms from their common centre of gravity. These films has been considered as ***ultra-thin films***[38]. In these cases, an external nucleation is always require to spawn a crystallization process[65]. Homogeneous nucleation is highly suppressed and typically a diffusion control growth pattern can be observed, which corresponds to polymer flat on lamellae growing flat on the substrate[66, 67].

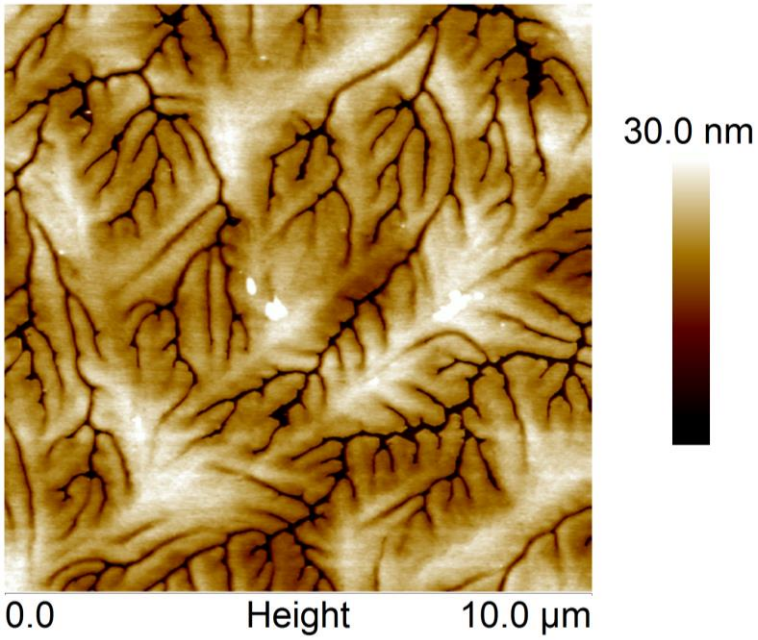

Figure 1.8. AFM height image of a crystallized poly(D,L-lactic acid) ultra-thin film (further studied in chapter 6). The flat on (dendritic) structure can be observed in the whole image.

This type of ***denditric*** patterns are shown in figure 1.8, observed by AFM. Irreversible adsorbed polymer chains, into the supporting substrate can also influence the crystallization behavior of polymer thin films. Recently[63], it has been reported that poly(ethylene terephthalate) (PET) films thinner than 20 nm did not crystallize, even after prolongated annealing in the temperature range where the crystallization rate reaches its maximum value. Authors observed that this threshold correlated with the total thickness of the irreversibly adsorbed layer of polymer into the substrate, thus, as chain adsorption increased, the entropic barrier required for the formation of crystalline structures also increased.

1.5.2. Polymer nanoparticles

Nanoparticles have a surprising long history. Their preparation is neither an exclusive result of modern research nor restricted to man-made materials. Naturally

occurring nanoparticles include organic (proteins, polyssacharides, viruses, among other) as well as inorganic compounds (iron oxyhydroxides, aluminosilicates, metals, …), and are produced by weathering, volcano eruptions, wildfires or microbial processes[68]. ***Polymer nanoparticles*** can be defined as being colloidal systems, which have usually diameters from around 5-10 nm to an upper size limit of 1000 nm, although the general range lies about 100-500 nm[69]. The term "polymer nanoparticles" is a collective term used for any type of nano-sized particles, but specifically for polymer nanospheres and nanocapsules. ***Polymer nanospheres*** are defined as matrix particles, that is, particles whose entire volume is solid; ***polymer nanocapsules*** are vesicular systems, *i. e.* a shell that can serve as container for other systems[69]. Polymer nanoparticles have found use in a number of applications[70] like coating and functionalization of surfaces[71-73], adhesives[74], drug delivery systems[69, 75-78], enhanced polymer blends preparations[79], organic-photovoltaic systems[80-84] and smart/stimuli-responsive materials[85-87]. The applications of polymer nanoparticles are significantly affected by their physical properties as well as surface morphology. Both factors can be controlled by the preparation method used to generate such particles[70].

Methods for preparing nanoparticles can be broadly separated in two classes[82, 88]: in-situ (direct) polymerization in disperse phase systems and ***postpolymerization dispersion*** of separately prepared polymers. In the first case, the preparation method is considered a polymer synthesis, since one departs from a monomer to obtain a nanostructured polymer system. In the second case, also referred as ***secondary dispersion***, a previously synthetized polymer is used in solution and reprocessed to generate the nanostructures. Both methods have their merits and limitations. Postpolymerization nanoparticle generation can rely on commercially available polymers, with given physic-

chemical specifications, and does not require equipment or expertise in organic and polymer synthesis. Direct polymerization, is not restricted to polymers soluble in organic solvents and in principle can afford a broader scope of nanoparticles in terms of size control and particle structure. However, nanoparticles prepared by direct polymerization must be extensively purified in order to avoid contamination by sub products of the synthesis.

As in confinement in thin films, fundamental physical properties of polymers confined in nanoparticles have been widely discussed. Authors have found that glass transition temperature in nanoparticles varies from that of the bulk polymer. For example, Zhang and collaborators[89] found that PS nanoparticles from 600 nm down to 90 nm in diameter showed a strong decrease of T_g in even 60 ºC, as measured by differential scanning calorimetry (DSC). Authors proposed the existence of a free surface layer on the nanoparticle's surface, responsible for the observed changes. In a following investigation[90], these authors observed, by broadband dielectric spectroscopy, that the polymer nanoparticles showed a decoupling between the glass transition phenomena and the segmental relaxation, due to the geometrical confinement. While the segmental relaxation of the polymer chains remained unchanged, the glass transition temperature moved towards lower temperatures as diameter was decreased. However, the decrease in T_g in confined polymer nanoparticles is not an universal feature of these systems. Years ago, Qian et al[91] measured the DSC curve of polymer nanoparticles and observed an increase of T_g, respect to the bulk material. Several other studies throughout the following years, mostly carried out by DSC, have also proposed the possibility of an increase in the glass transition temperature in polymers confined to nanoparticles[92-95]. It has been proposed that the increase in T_g in the polymer nanoparticles is related to changes in the

entropy of the polymer chains in the confined geometry[93]. In other words, the possible conformations that can adopt the polymer chain is restricted by the confinement, leading to a decreases in entropy and finally to the increase in T_g.

1.5.3. Applications of polymers in confinement

Besides the study of the fundamental properties of polymers confined in the nanometric scale, in the past decade it has been explored the possibility of using polymer nanostructures to prepare and develop devices with technological applications[96]. Nanostructured polymers cover a wide spectrum of applications, ranging from stimuli-responsive systems[97] and materials with shape-memory effects[98], up to applications in organic electronics[99] and photoresponsive materials[82]. Among these systems, the ferroelectric behavior of polymer materials in confinement has also been studied[99, 100].

Ferroelectricity enables the switching of electric polarization and has long been an important topic in condensed-matter science. Its application is important as a basic element of devices and memories[101]. In recent years, the piezoelectricity, ferroelectricity, and pyroelectricity of ferroelectric polymers such as poly(vinylidenefluoride) (PVDF) and its copolymers with trifluoroethylene (TrFE) have been widely investigated in both bulk and confined geometries[99-101]. With increasing demand for miniaturization in microelectronics, ferroelectric nanostructures have attracted considerable practical and theoretical interest. P(VDF-TrFE) nanostructures are especially interesting towards the development of memory applications. The ferroelectric behavior of polymers can be studied by DSC, BDS[102] and X-ray scattering[40]. Also, the piezo-response force microscopy (PFM), an AFM-based technique, has been specifically developed to study ferroelectricity at the nanoscale[103-106].

1.6. Main objectives and content of the thesis

The main objective of this Doctoral Thesis was the preparation of polymer systems under several confined geometries, and to study the physical changes that resulted from confinement. In order to fulfill this main objective, this research was focused on two specific aspects. First, the preparation of several polymer nanostructures (nanoparticles, thin films and modified surfaces) using several polymer systems (both amorphous and semi-crystalline). Then, measurements of the physical properties of the prepared polymer nanostructures were performed in order to provide further information about the possible changes induced by confinement. In the case of amorphous polymer nanoparticles, the evolution of the glass transition was followed by means of differential scanning calorimetry. For semi-crystalline polymers, the crystallization behavior was studied by atomic force microscopy, X-ray diffraction and broadband dielectric spectroscopy. This last technique allowed not only observing the physical changes regarding the crystallization kinetics in confinement but also let attaining information about the adsorption mechanisms in polymer/substrate interactions. Finally, the ferroelectric behavior in confined polymer structures was also studied, where possible applications of the polymer nanostructures were evaluated.

In order to develop the presented objectives, this work is divided in the following chapters. In ***Chapter 2***, the materials and the methods used throughout the whole work are presented and described. Specifically, the general physico-chemical properties of polymer and non-polymeric materials as well as those of the solvents and liquid media are given. Results are divided in two broad sections. The first section covers chapters 3 and 4 and it is called ***Part A – Preparation of polymer nanostructures***. In ***Chapter 3***, the preparation

of polymer nanostructures, such as nanoparticles and thin films is presented. Preparation protocols are discussed for a wide variety of polymers. Also, the limitations encountered in each method are shown. The preparation methods are taken to a next level in ***Chapter 4***. In this chapter, preparation of nanoparticles in liquid media, by laser ablation is presented. The extent and content of these results led to a discussion about how the different physico-chemical parameters of the liquid media are related to the formation of nanostructures. Second section of results is called ***Part B - Physical properties and applications of polymer nanostructures*.** In this section, chapters 5, 6 and 7, deal with physical properties of polymers in confinement. In ***Chapter 5***, the variation in the glass transition temperature of polymer nanospheres is presented, along with a thermodynamic model developed to explain how confinement alters the chain arrangement in the nanoparticles. Afterwards, the crystallization behavior of polymers in confinement is evaluated in ***Chapter 6***. In this chapter, both polymer thin films and nanoparticles were used as samples. In ***Chapter 7*** the ferroelectric behavior of polymers in confinement is presented. As in the previous chapter, polymer nanoparticles and polymer thin films were used. In this case, not only the fundamental physical properties are analyzed, but also some applications of the nanostructured materials are presented. ***Chapter 8*** presents a global discussion regarding all the results obtained in this thesis, which led to the ***Conclusions.***

Most of the experimental work presented in this work was developed at facilities of the Instituto de Estructura de la Materia (IEM-CSIC) in Madrid, Spain. However, collaborations with several other institutions were also performed. In ***Chapter 3***, part of the work was performed with the support of Dr. Carolina García at the Instituto de Química Física Rocasolano (IQFR-CSIC) in Madrid, Spain. In ***Chapter 4***, the laser

irradiations were performed at the LANAMAP group of the IQFR-CSIC, with the assistance of Dr. Esther Rebollar. In ***Chapter 6***, the work on capped polymer thin films was developed in Belgium in collaboration with Dr. Simone Napolitano at the Universite Librè de Bruxelles (ULB) in Bruxelles and with Dr. Michael Wübbenhorst at the KU-Leuven (KUL) in Leuven. Finally, the nanoimprint lithography surfaces, presented in ***Chapters 3*** and ***7***, were performed at the Instituto de Microelectrónica de Barcelona (IMB-CSIC) in Barcelona, Spain, with the collaboration of Dr. Fransesc Pérez-Murano.

Even though this Doctoral Thesis has been developed almost completely in Spain, it is written in English in order to facilitate and promote its scientific impact. Nonetheless, an extensive resume in Spanish is attached at the end of the manuscript.

1.7. References

1. Jones, R. A. L., *Soft Condensed Matter*. Oxford University Press: Great Britain, 2002.
2. de Gennes, P. G., Soft Matter. In *Nobel Lecture*, Stockholm, 1991.
3. de Gennes, P. G. *Reviews of Modern Physics* **1992,** 64, (3), 645-648.
4. Gompper, G.; Schick, M., An Introduction to Soft Matter. In *Soft Matter*, Wiley-VCH Verlag GmbH & Co. KGaA: 2007; pp 1-16.
5. Strobl, G., *The Physics of Polymers*. Springer: Germany, 1996.
6. Gedde, U. W., *Polymer Physics*. Chapman & Hall: England, 1995.
7. Ngai, K. L., Glass-Forming Substances and Systems. In *Relaxation and Diffusion in Complex Systems*, Springer New York: 2011; pp 49-638.
8. Ossi, P. M., The Glass Transition. In *Disordered Materials*, Springer Berlin Heidelberg: 2006; pp 55-93.
9. Debenedetti, P. G.; Stillinger, F. H. *Nature* **2001,** 410, (6825), 259-67.
10. Gibbs, J. H.; DiMarzio, E. A. *The Journal of Chemical Physics* **1958,** 28, (3), 373-383.
11. Langer, J. S. *Reports on Progress in Physics* **2014,** 77, (4), 042501.
12. Adam, G.; Gibbs, J. H. *The Journal of Chemical Physics* **1965,** 43, (1), 139-146.
13. Lubchenko, V.; Wolynes, P. G. *Annual Review of Physical Chemistry* **2007,** 58, 235-266.
14. Tanaka, H. *The Journal of Chemical Physics* **1999,** 111, (7), 3163-3174.
15. Ngai, K. L., Introduction to the Problems of Relaxation and Diffusion in Complex Systems. In *Relaxation and Diffusion in Complex Systems*, Springer New York: 2011; pp 1-47.
16. Schönhals, A.; Friedrich, K., Theory of Dielectric Relaxation. In *Broadband Dielectric Spectroscopy*, Friedrich, K.; Schönhals, A., Eds. Springer: Berlin, 2002.
17. McCrum, N. G.; Read, B. E.; Williams, G., *Anelastic and Dielectric Effects in Polymer Solids*. Dover Publications, Inc.: New York, 1967.
18. Martín-Fabiani, I.; Linares, A.; Nogales, A.; Ezquerra, T. A. *Polymer* **2013,** 54, (21), 5892-5898.
19. Soccio, M.; Nogales, A.; Martín-Fabiani, I.; Lotti, N.; Munari, A.; Ezquerra, T. A. *Polymer* **2014,** 55, (6), 1552-1559.
20. Sanz, A.; Ezquerra, T. A.; Garcia-Gutierrez, M. C.; Puente-Orench, I.; Campo, J.; Nogales, A. *European Physical Journal E: Soft Matter and Biological Physics* **2013,** 36, 24.
21. Hernández, R.; Nogales, A.; Sprung, M.; Mijangos, C.; Ezquerra, T. A. *The Journal of Chemical Physics* **2014,** 140, (2), -.
22. Angell, C. A. *Science* **1995,** 267, (5206), 1924-1935.

23. Angell, C. A. *Polymer* **1997,** 38, (26), 6261-6266.
24. Young, R. J., *Introduction to Polymers*. Chapman and Hall Ltd: London, 1983.
25. Soccio, M.; Lotti, N.; Finelli, L.; Munari, A. *European Polymer Journal* **2009,** 45, (1), 171-181.
26. Drake, B.; Prater, C.; Weisenhorn, A.; Gould, S.; Albrecht, T.; Quate, C.; Cannell, D.; Hansma, H.; Hansma, P. *Science* **1989,** 243, (4898), 1586-1589.
27. Magonov, S. N.; Reneker, D. H. *Annual Review of Materials Science* **1997,** 27, (1), 175-222.
28. Li, L.; Chan, C.-M.; Yeung, K. L.; Li, J.-X.; Ng, K.-M.; Lei, Y. *Macromolecules* **2000,** 34, (2), 316-325.
29. Hobbs, J. K.; Humphris, A. D. L.; Miles, M. J. *Macromolecules* **2001,** 34, (16), 5508-5519.
30. Thompson, C.; Champness, N. R.; Khlobystov, A. N.; Roberts, C. J.; SchrÖDer, M.; Tendler, S. J. B.; Wilkinson, M. J. *Journal of Microscopy* **2004,** 214, (3), 261-271.
31. Ivanov, D. A.; Bar, G.; Dosière, M.; Koch, M. H. J. *Macromolecules* **2008,** 41, (23), 9224-9233.
32. Thomas, C.; Seguela, R.; Detrez, F.; Miri, V.; Vanmansart, C. *Polymer* **2009,** 50, (15), 3714-3723.
33. Ivanov, D. A.; Magonov, S. N., Atomic Force Microscopy Studies of Semicrystalline Polymers at Variable Temperature. In *Polymer Crystallization*, Reiter, G.; Sommer, J.-U., Eds. Springer-Verlag Germany, 2003.
34. Svorcik, V.; Slepicka, P.; Siegel, J.; Reznickova, A.; Lyutakov, O.; Kvitek, O.; Hubacek, T.; Slepickova Kasalkova, N.; Kolska, Z., Nanostructuring of Solid Surfaces. In *Nanostructures : Properties, Production Methods and Applications*, Dong, Y., Ed. Nova Science Publishers, Inc.: Hauppauge, NY, USA, 2013.
35. Gates, B. D.; Xu, Q.; Stewart, M.; Ryan, D.; Willson, C. G.; Whitesides, G. M. *Chemical Reviews* **2005,** 105, (4), 1171-1196.
36. Martín Gago, J. A.; Briones Llorente, C.; Casero Junquera, E.; Serena Domingo, P. A., *Nanotecnologia y Nanociencia: Entre la ciencia ficción del presente y la tecnología del futuro*. Fundación Española para la Ciencia y la Tecnología: Madrid, 2008.
37. Alcoutlabi, M.; McKenna, G. B. *Journal of Physics: Condensed Matter* **2005,** 17, (15), R461.
38. Napolitano, S.; Capponi, S.; Vanroy, B. *Eur. Phys. J. E* **2013,** 36, (6), 1-37.
39. Rebollar, E.; Pérez, S.; Hernández, J. J.; Martín-Fabiani, I.; Rueda, D. R.; Ezquerra, T. A.; Castillejo, M. *Langmuir* **2011,** 27, (9), 5596-5606.
40. Garcia-Gutierrez, M.-C.; Linares, A.; Martin-Fabiani, I.; Hernandez, J. J.; Soccio, M.; Rueda, D. R.; Ezquerra, T. A.; Reynolds, M. *Nanoscale* **2013,** 5, (13), 6006-6012.
41. Martin, J.; Campoy-Quiles, M.; Nogales, A.; Garriga, M.; Alonso, M. I.; Goni, A. R.; Martin-Gonzalez, M. *Soft Matter* **2014,** 10, (18), 3335-3346.
42. Deng, R.; Liang, F.; Li, W.; Yang, Z.; Zhu, J. *Macromolecules* **2013,** 46, (17), 7012-7017.
43. Tsui, O. K. C.; Rusell, T. P., *Polymer Thin Films*. World Scientific: 2008.
44. Vendra, V. K.; Wu, L.; Krishnan, S., Polymer Thin Films for Biomedical Applications. In *Nanomaterials for Life Sciences Vol 5: Nanostructured Thin Films and Surfaces*, Kumar, C. S. S. R., Ed. Wiley-VCH Verlag GmbH: 2010.
45. McKenna, G. B. *Eur. Phys. J. Spec. Top.* **2007,** 141, (1), 291-301.
46. Zhao, Y. P.; Fortin, J. B.; Bonvallet, G.; Wang, G. C.; Lu, T. M. *Physical Review Letters* **2000,** 85, (15), 3229-3232.
47. Wu, P. K.; Ringeisen, B. R.; Callahan, J.; Brooks, M.; Bubb, D. M.; Wu, H. D.; Piqué, A.; Spargo, B.; McGill, R. A.; Chrisey, D. B. *Thin Solid Films* **2001,** 398–399, (0), 607-614.
48. Shepard, K. B.; Priestley, R. D. *Macromolecular Chemistry and Physics* **2013,** 214, (8), 862-872.
49. Caricato, A. P., MAPLE and MALDI: Theory and Experiments. In *Lasers in Materials Science*, Castillejo, M.; Ossi, P. M.; Zhigilei, L., Eds. Springer: 2014.
50. Keddie, J. L.; Jones, R. A. L.; Cory, R. A. *EPL (Europhysics Letters)* **1994,** 27, (1), 59.
51. Keddie, J. L.; Jones, R. A. L.; Cory, R. A. *Faraday Discussions* **1994,** 98, (0), 219-230.
52. de Gennes, P. G. *Eur. Phys. J. E* **2000,** 2, (3), 201-205.
53. Forrest, J. A.; Dalnoki-Veress, K. *Advances in Colloid and Interface Science* **2001,** 94, (1–3), 167-195.
54. Forrest, J. A.; Dalnoki-Veress, K.; Stevens, J. R.; Dutcher, J. R. *Physical Review Letters* **1996,** 77, (10), 2002-2005.
55. Wallace, W. E.; van Zanten, J. H.; Wu, W. L. *Physical Review E* **1995,** 52, (4), R3329-R3332.
56. Fryer, D. S.; Peters, R. D.; Kim, E. J.; Tomaszewski, J. E.; de Pablo, J. J.; Nealey, P. F.; White, C. C.; Wu, W.-l. *Macromolecules* **2001,** 34, (16), 5627-5634.
57. Grohens, Y.; Hamon, L.; Reiter, G.; Soldera, A.; Holl, Y. *European Physical Journal E: Soft Matter and Biological Physics* **2002,** 8, 217-224.
58. Fujii, Y.; Yang, Z.; Leach, J.; Atarashi, H.; Tanaka, K.; Tsui, O. K. C. *Macromolecules* **2009,** 42, (19), 7418-7422.
59. Napolitano, S.; Rotella, C.; Wübbenhorst, M. *ACS Macro Letters* **2012,** 1, (10), 1189-1193.
60. Van Horn, R. M.; Cheng, S. Z. D., Crystallization in Polymer Thin Films: Morphology and Growth. In *Polymer Thin Films*, Tsui, O. K. C.; Rusell, T. P., Eds. World Scientific: 2008.
61. Sanz, A.; Nogales, A.; Ezquerra, T. A. *Soft Matter* **2011,** 7, (14), 6477-6483.
62. Soccio, M.; Lotti, N.; Munari, A. *J Therm Anal Calorim* **2013,** 114, (2), 677-688.
63. Vanroy, B.; Wübbenhorst, M.; Napolitano, S. *ACS Macro Letters* **2013,** 2, (2), 168-172.
64. Müller, A. J.; Arnal, M. L.; Lorenzo, A. T., Crystallization in Nano-confined Polymeric Systems. In *Handbook of Polymer Crystallization*, Piorkowska, E.; Rutledge, G. C., Eds. Wiley: USA, 2013.
65. Despotopoulou, M. M.; Frank, C. W.; Miller, R. D.; Rabolt, J. F. *Macromolecules* **1996,** 29, (18), 5797-5804.
66. Sommer, J.-U.; Reiter, G. *Thermochimica Acta* **2005,** 432, (2), 135-147.

67. Reiter, G. *Chemical Society Reviews* **2014,** 43, (7), 2055-2065.
68. Heiligtag, F. J.; Niederberger, M. *Materials Today* **2013,** 16, (7–8), 262-271.
69. Lu, X.-Y.; Wu, D.-C.; Li, Z.-J.; Chen, G.-Q., Chpater 7 - Polymer Nanoparticles. In *Progress in Molecular Biology and Translational Science*, Antonio, V., Ed. Academic Press: 2011; Vol. Volume 104, pp 299-323.
70. Mittal, V., Polymer Latex Technology. In *Advanced Polymer Nanoparticles*, Mittal, V., Ed. CRC Press 2010.
71. Lin, C.-A. J.; Sperling, R. A.; Li, J. K.; Yang, T.-Y.; Li, P.-Y.; Zanella, M.; Chang, W. H.; Parak, W. J. *Small* **2008,** 4, (3), 334-341.
72. Zhang, F.; Lees, E.; Amin, F.; Rivera_Gil, P.; Yang, F.; Mulvaney, P.; Parak, W. J. *Small* **2011,** 7, (22), 3113-3127.
73. Marcelo, G.; Martinho, J. M. G.; Farinha, J. P. S. *The Journal of Physical Chemistry B* **2013,** 117, (12), 3416-3427.
74. Taylor, A. C., Adhesives with Nanoparticles. In *Handbook of Adhesion Technology*, da Silva, L. M.; Öchsner, A.; Adams, R., Eds. Springer Berlin Heidelberg: 2011; pp 1437-1460.
75. Panyam, J.; Labhasetwar, V. *Advanced Drug Delivery Reviews* **2003,** 55, (3), 329-347.
76. Allen, T. M.; Cullis, P. R. *Science* **2004,** 303, (5665), 1818-1822.
77. Tang, B. C.; Dawson, M.; Lai, S. K.; Wang, Y.-Y.; Suk, J. S.; Yang, M.; Zeitlin, P.; Boyle, M. P.; Fu, J.; Hanes, J. *Proceedings of the National Academy of Sciences* **2009,** 106, (46), 19268-19273.
78. Tran, N. T. D.; Truong, N. P.; Gu, W.; Jia, Z.; Cooper, M. A.; Monteiro, M. J. *Biomacromolecules* **2013,** 14, (2), 495-502.
79. Kietzke, T.; Neher, D.; Landfester, K.; Montenegro, R.; Guntner, R.; Scherf, U. *Nat Mater* **2003,** 2, (6), 408-412.
80. Wu, C.; Szymanski, C.; McNeill, J. *Langmuir* **2006,** 22, (7), 2956-2960.
81. Tuncel, D.; Demir, H. V. *Nanoscale* **2010,** 2, (4), 484-494.
82. Pecher, J.; Mecking, S. *Chemical Reviews* **2010,** 110, (10), 6260-6279.
83. Park, E.-J.; Erdem, T.; Ibrahimova, V.; Nizamoglu, S.; Demir, H. V.; Tuncel, D. *ACS Nano* **2011,** 5, (4), 2483-2492.
84. MacNeill, C. M.; Graham, E. G.; Levi-Polyachenko, N. H. *Journal of Polymer Science Part A: Polymer Chemistry* **2014,** 52, (11), 1622-1632.
85. Weaver, J. V. M., ph-Responsive Polymer Nanoparticles. In *Advanced Polymer Nanoparticles*, Mittal, V., Ed. CRC Press, 2010.
86. Soleimani, M.; Haley, J. C.; Majonis, D.; Guerin, G.; Lau, W.; Winnik, M. A. *Journal of the American Chemical Society* **2011,** 133, (29), 11299-11307.
87. Jackson, A. W.; Fulton, D. A. *Polymer Chemistry* **2013,** 4, (1), 31-45.
88. Zhang, C.; Guo, Y.; Priestley, R. D. *Journal of Polymer Science Part B: Polymer Physics* **2013,** 51, (7), 574-586.
89. Zhang, C.; Guo, Y.; Priestley, R. D. *Macromolecules* **2011,** 44, (10), 4001-4006.
90. Zhang, C.; Boucher, V. M.; Cangialosi, D.; Priestley, R. D. *Polymer* **2013,** 54, (1), 230-235.
91. Qian, R.; Wu, L.; Shen, D.; Napper, D. H.; Mann, R. A.; Sangster, D. F. *Macromolecules* **1993,** 26, (11), 2950-2953.
92. Pilcher, S. C.; Ford, W. T. *Macromolecules* **1998,** 31, (11), 3454-3460.
93. Mi, Y.; Xue, G.; Wang, X. *Polymer* **2002,** 43, (25), 6701-6705.
94. Li, L.; Li, B.; Chen, J.; Zhou, D.; Xue, G.; Liu, X. *Polymer* **2004,** 45, (8), 2813-2816.
95. Guo, Y.; Morozov, A.; Schneider, D.; Chung, J. W.; Zhang, C.; Waldmann, M.; Yao, N.; Fytas, G.; Arnold, C. B.; Priestley, R. D. *Nat Mater* **2012,** 11, (4), 337-343.
96. Dai, L., *Intelligent Macromolecules for Smart Devices: From Materials Synthesis to Device Applications*. Springer-Verlag: Londo, 2004.
97. Cabane, E.; Zhang, X.; Langowska, K.; Palivan, C.; Meier, W. *Biointerphases* **2012,** 7, (1-4), 1-27.
98. Wu, T.; Frydrych, M.; O'Kelly, K.; Chen, B. *Biomacromolecules* **2014,** In press.
99. Hu, Z.; Tian, M.; Nysten, B.; Jonas, A. M. *Nature materials* **2009,** 8, 62-7.
100. Xiao, Z.; Dong, Q.; Sharma, P.; Yuan, Y.; Mao, B.; Tian, W.; Gruverman, A.; Huang, J. *Advanced Energy Materials* **2013,** 3, (12), 1581-1588.
101. Horiuchi, S.; Tokura, Y. *Nat Mater* **2008,** 7, (5), 357-366.
102. Serghei, A.; Lutkenhaus, J. L.; Miranda, D. F.; McEnnis, K.; Kremer, F.; Russell, T. P. *Small* **2010,** 6, (16), 1822-1826.
103. Kalinin, S.; Bonnell, D. *Physical Review B* **2002,** 65, 1-11.
104. Bonnell, D. A.; Kalinin, S. V.; Kholkin, A. L.; Gruverman, A. *MRS Bulletin* **2011,** 34, 648-657.
105. Sharma, P.; Reece, T. J.; Ducharme, S.; Gruverman, A. *Nano Lett.* **2011,** 11, (5), 1970-1975.
106. Hong, C.-C.; Huang, S.-Y.; Shieh, J.; Chen, S.-H. *Macromolecules* **2012,** 45, 1580-1586.

CHAPTER 2 – Materials & Methods

2. 1. Materials

2.1.1 Polymers

Polymers used throughout the following chapters are presented alphabetically in the following paragraphs.

Poly(3-hexylthiophene)

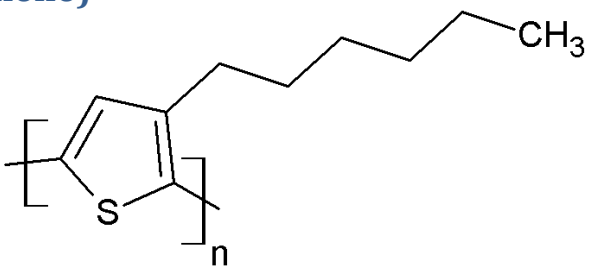

Sketch of the P3HT repeating unit

The poly(3-hexylthiophene-2,5-diyl), from now on abbreviated as P3HT, is a conjugated semi-crystalline polymer, with electrical properties widely used nowadays in the development of organic electronic and opto-electronic materials[1-5]. The term *conjugated* applies to polymeric materials composed of macromolecules with main chains consisting of a sequence of conjugated multiple bonds[6]. A conjugated polymer where the molecules of π-electrons are delocalized along the main chain is referred to as a π-conjugated polymer. The polythiophene based polymers, such as the P3HT, are examples of π-conjugated polymers[6]. In this work, P3HT was purchased from Ossila (Batch M102). The tradename of the polymer is *lisicon*® SP001. The weight average molecular weight (M_w) is 65200 g/mol and its number average molecular weight (M_n) is 29600 g/mol

(M_w/M_n = 2.2). Its regioregularity is 95.7%. P3HT was used in solution for the preparation of nanoparticles (chapter 3).

Poly(bisphenol A carbonate)

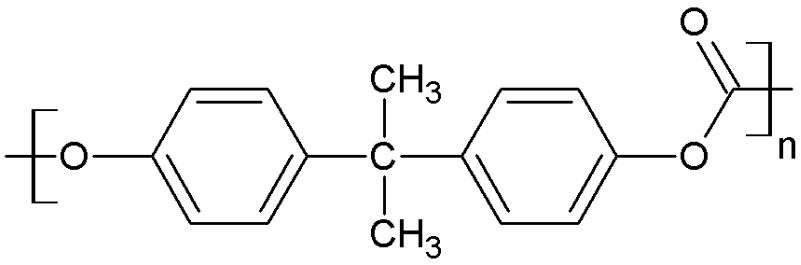

Sketch of the PBAC repeating unit

The poly[oxycarbonyloxy-1,4-phenylene(dimethylmethylene)-1,4-phenylene], also known as poly(bisphenol A carbonate) and abbreviated from now on as PBAC is an amorphous polymer composed of macromolecules containing carbonate linkages (–O–(C=O)–O–) in the backbone[6]. PBAC is a thermoplastic aromatic polyester that has been widely used in the scientific community to model and understand phenomena at nanometric lengthscales[7-10]. PBAC was purchased from Innovative Plastics by the tradename *Lexan*® (ML3021A, SABIC I-P), and have the following properties: M_w = 44400 g/mol, M_n = 23500 g/mol (M_w/M_n = 1.9). PBAC was used for the preparation of nanoparticles (chapter 3) and for experiments of pulsed laser ablation in liquids (chapter 4). In this last case, PBAC targets for ablation were prepared using the following steps. First, the as received PBAC was dried in a vacuum oven for 16 hours at 100 ºC.

Afterwards, PBAC films were prepared in a thermoplastic press as follows: the polymer pellets were annealed at 220 ºC for 2 minutes. Then, a pressure of 20 bar was applied for 3 minutes. The film was cooled down, inside the press, using cold cartridges. The resulting PBAC films had a thickness h = (0.9 ± 0.1) mm.

Poly(ethyl methacrylate)

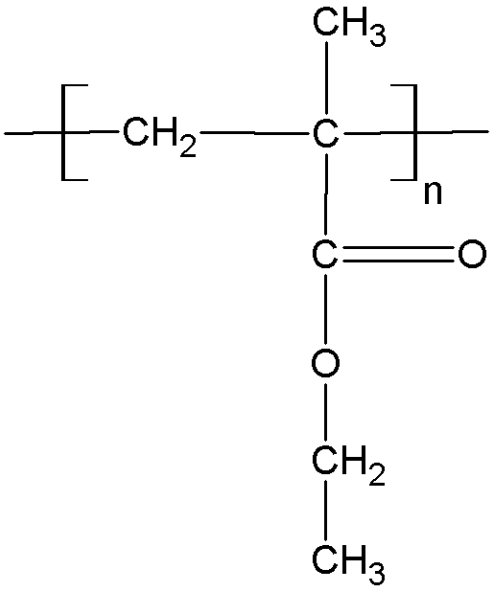

Sketch of the PEMA repeating unit

The poly[1-(ethoxycarbonyl)-1-methylethylene], also known as poly(ethyl methacrylate) and abbreviated from now on as PEMA, is an amorphous acrylic thermoplastic polymer formed from methacrylic acid and related monomers[6]. Poly(n-alkyl methacrylates) (PnMAs) such as PEMA, have been previously studied to relate the structural and dynamical properties of polymers, since these polymer series display a complex molecular structure coupled with a variety of relaxational processes[11]. The PnMAs are generally classified by their side chain. In this context, PEMA is located in an intermediate stage between poly(methyl methacrylate) (PMMA) and higher order PnMAs. Also, PEMA has been used to study dynamics of diblock copolymers[12], preparation of

polymer blends[13], and organic electronic applications[14]. PEMA was purchased from Polysciences (#0.197), and have the following properties: M_w = 50000 g/mol (M_w/M_n = 1.11). PEMA was used in solution for the preparation of nanoparticles (chapter 3)

Poly(lactic acid)

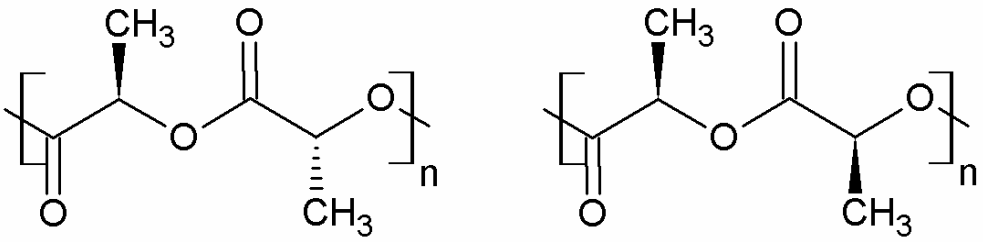

(Left) Sketch of a PLLA repeating unit. (Right) Sketch of a D,L- dimer

The poly(lactic acid), from now on abbreviated as PLA, is an aliphatic thermoplastic polymer, commonly made from α-hydroxy acids which are considered biodegradable, biocompatible and compostable[15, 16]. Although the term *acid* is generally included in its name, PLA is a polyester instead of a poly*acid*[15]. Nowadays, PLA resins have mostly been used for biomedical applications such as drug delivery systems[17-20] and bone implants[21, 22]. Thanks to the mechanical properties, comparable to those of polystyrene, PLA could reasonably substitute conventional polymers in domains such as packaging[23].

Generally, PLA grades are copolymers of poly(L-lactic acid) (PLLA) and poly(D,L-lactic acid) (PDLLA), which are produced from L-lactides and D,L-lactides, respectively[23]. The letters D, and L are related to Dextrorotation (D) and Levorotation (L), and refer to the polymer property of rotating plane polarized light. If the light rotates clockwise as it approaches an observer, this is known as dextrorotation, light with a

rotation to the right. If the light rotates counter-clockwise as it approaches the observer, then the light exhibits levorotation, rotation to the left. The ratio of L- to D,L-enantiomers is known to affect the properties of PLA, such as the melting temperature and the degree of crystallinity[23]. In this work, PLLA and PDLLA copolymers have been used. PLLA was purchased from Sigma-Aldrich (Aldrich 94829-1G-F), with the following properties: M_w = 67000 g/mol (M_w/M_n = 1.4). PDLLA (NatureWorks, PLA 2002D) was kindly provided by M.A. López-Manchado. It has a D-content of 4.25% and ρ = 1.24 g/cm^3. PLLA was used in solution for preparation of thin films (chapter 3). PDLLA was used in solution for preparation of nanoparticles (chapter 3).

Poly(styrene)

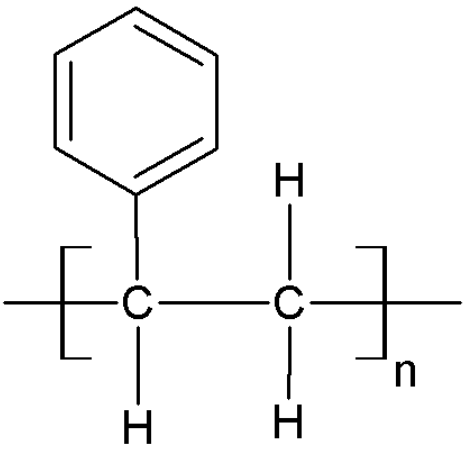

Sketch of the PS repeating unit

The poly(1-phenylethylene), also known as poly(styrene) and abbreviated from now on as PS, is a synthetic aromatic polymer made from the monomer phenylethylene[6]. PS is considered a vinyl polymer since its monomer derives from the vinyl group (-CH=CH$_2$). Also, PS is perhaps the most used polymer to study confinement effects in the past two decades[24-31]. In this work, PS was purchased from Polymer Source Inc (Sample #

P8647-S), having the following properties: M_w = 55500 g/mol (M_w/M_n = 1.07). PS was used in solution for preparation of nanoparticles (chapter 3).

Poly(vinylidene fluoride-*co*-trifluoro ethylene)

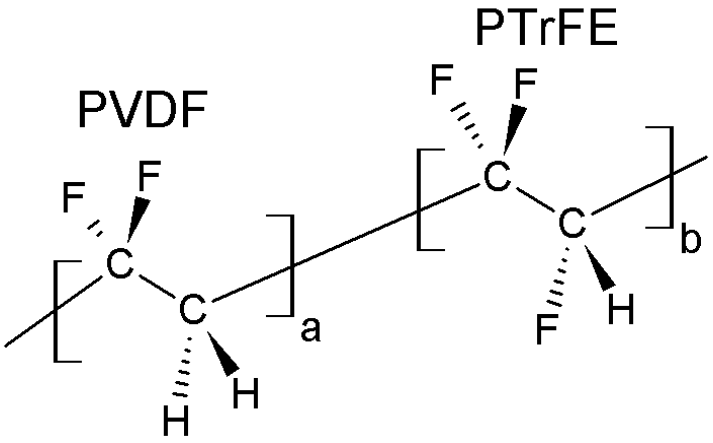

Sketch of the P(VDF-TrFE) copolymer repeating units

The poly(vinylidene fluoride-co-trifluoro ethylene), abbreviated from now on as P(VDF-TrFE) is a semi-crystalline fluoro-copolymer. The term fluoro polymer can be generally regarded as a structure-based name indicating the presence of C-F bonds in the constitutional repeating units. The P(VDF-TrFE) copolymer is formed by the poly(1,1-difluoroethene), also known as poly(vinylidene fluoride) (PVDF) and poly(trifluoro ethene) (PTrFE). The P(VDF-TrFE) copolymer has been widely studied due to its ferroelectric and piezoelectric properties[32-39]. In this work the P(VDF-TrFE) random copolymers were purchased from Piezotech S.A.S. Two molar concentrations of 76:24 and 56:44 (VDF:TrFE ratio), as revealed by Nuclear Magnetic Resonance (NMR), were used. P(VDF-TrFE) was used in solution for preparation of nanoparticles (chapter 3). Also thin films of P(VDF-TrFE) were used for preparing nanoimprint lithography structured surfaces (chapter 3).

2.1.2 Non-polymeric materials

Besides polymers, other solid-state materials were used throughout the development of this work, and are presented in the following lines.

Phenyl-C71-butyric acid methyl ester

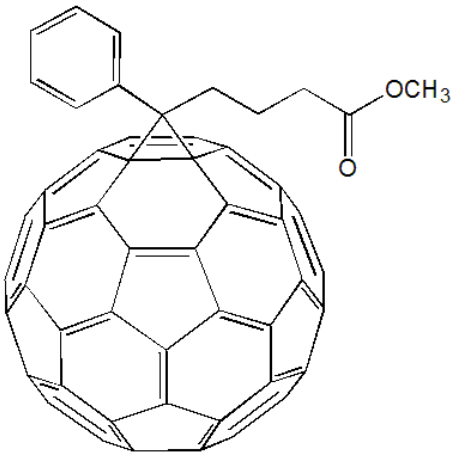

Sketch of the PCBM molecule

The methyl 5-(3'*H*-cyclopropa[1,9](C_{71}-I_h)[5,6]fullerenyl-5-phenylpentanoate, also known as phenyl-C_{71}-butyric acid methyl ester and abbreviated from now on as PCBM, is a functionalized molecule of the C_{70} fullerene with the addition of diazoalkanes[40]. It is mainly used as component in the developments of organic photoresponsive materials when blended with other polymers such as P3HT[41-45]. PCBM was purchased from Ossila (PCBM70-990-640mg) and has a molecular mass of 910.88 g/mol. PCBM was used in solution for the preparation of nanoparticles (chapter 3).

Sodium dodecyl sulphate

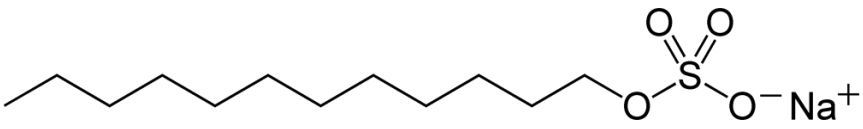

Sketch of the SDS molecule

Sodium lauryl sulphate, also known as sodium dodecyl sulphate and abbreviated from now on as SDS, is an anionic surfactant used extensively in a number of applications, such as cleaning agents, removal of oil stains and residues, engine degreases, among others[46]. It is a salt consisting of a 12-carbon tail attached to a sulphate group, giving the material the amphiphilic properties required of a detergent. SDS was purchased from Sigma-Aldrich (436143-100G) and has a molecular mass of 288.37 g/mol. SDS was used in an aqueous solution as stabilizing agent for the preparation of nanoparticles (chapter 3).

2.1.3 Solvents

The variety of polymers and techniques used throughout this work has led to the requirement of several solvents. Table 2.1 shows the different solvents used, with the most important properties required in the following chapters.

Other liquid media were used in this work. Acetone (IUPAC name: Propanone) and 2-Propanol were used for cleaning glass equipment. Distilled water was used for preparation of nanoparticles (chapter 3).

Table 2.1. Solvents used throughout this work

Solvent	Abbreviation	Boiling Point (ºC)	Water miscibility	Polymers dissolved
Trichloromethane (Chloroform)	$CHCl_3$	62	No	PBAC PEMA PS PLLA PDLLA
Oxolane (Tetrahydrofuran)	THF	66	Yes	PEMA PDLLA
N,N-dimethylacetamide	DMA	165	Yes	P(VDF-TrFE)

2.1.4 Wafers for microscopy measurements.

Microscopy measurements at the nanoscale require surfaces with nanometric rugosity in order to perform high quality measurements. During this work we have used silicon (Si) wafers as microscopy substrates. Two different types of wafers were employed, depending on the measurement to be performed: *Regular* (semi-conductive) Si wafers and *Doped* (conductive) Si wafers. Table 2.2. shows the physical properties of the different Si wafers.

Table 2.2. Silicon wafers characteristics

Wafer	Orientation	Thickness (μm)	Resistivity (Ω cm)
Regular	100	100 ± 5	1 -20
Doped	100	550 ± 50	0.001-0.005

Due to the contact with air, Si wafers (both regular and doped) form a silicon oxide layer on their surface. This layer has been estimated to have around 2 nm in thickness, as revealed by ellipsometry measurements at ULB-BXL. The SiO_2 layer has generally no impact for the preparation of polymer thin films and for the measurement of physical properties via scanning probe microscopy. However, when the polymer is dispersed in a liquid media (as for the case of nanoparticles in chapter 3), the oxide layer acts as a hydrophobic surface, and the deposition of sample tends to be quite difficult. In order to overcome this issue, Si wafers can be treated in a so called *piranha* solution. This solution is a mixture of sulphuric acid (H_2SO_4) and oxygen peroxide (H_2O_2) in a 3:2 proportion. Usually, 100 mL of solution are prepared, so 60 mL of sulphuric acid are added on 40 mL of oxygen peroxide. Immediately, the Si wafers are submerged into the solution and left for 30 minutes. The chemical reaction between solution and wafers acts as a *cleaning* procedure, substituting the O_2 layer for an OH one. Thus, the final Si wafer surface has a hydrophilic character. Afterwards, treated Si wafers are rinsed in distilled water and dried under a nitrogen flow. The deposition procedure is performed immediately to avoid the oxidation of the layer.

2. 2. Methods

In the following paragraphs, the different experimental methods and techniques used during this work will be described.

2.2.1. Methods related to the preparation of polymer nanoparticles

Dialysis

The dialysis procedure consists in the exchange of material through a semi-permeable membrane, due to different rates of diffusion[47]. The dialysis protocol has been

explored in chapter 3 during several preparation methods of polymer nanoparticles. Through dialysis it has been possible to purify polymer nanoparticles and to separate polymer solvents, such as DMA, from an emulsion. In this work, dialysis was performed using a Visking membrane (Visking DTV by Medicell Int Ltd.). The cutoff range of the membrane was 10-12 kg/mol, meaning that all particles with a molecular weight below the threshold can escape from the membrane. The as received membrane was prepared following the methods available in the literature[48]. Afterwards, the membrane was rinsed in distilled water and one end was tied with a knot. Polymer solution/emulsion was poured into the membrane and the other end was also tied. Afterwards, the filled membrane was submerged in a beaker with distilled water (2 L). Several water changes were performed, depending on each preparation method.

Lyophilization

The lyophilization protocol consists in the removal of the liquid media from a solution/emulsion. During the dehydration process the sample is frozen while centrifuged and the pressure is reduced to allow the frozen liquid to sublimate. At the end, a solid liquid-free powder is obtained. Throughout this work the lyophilisation protocol was performed at IQFR-CSIC. A custom made machine was employed and the polymer nanoparticle emulsion was distributed in 1 mL samples using centrifuge tubes. The resulting *solid powder of nanoparticles* has been used in the development of this work, as presented in chapters 4, 5 and 6.

Filtering

For several preparation methods, polymer solutions were filtered prior to use. We have used Teflon syringe filters with 0.2 μm pore diameter. The procedure goes as follows. Once the solution was dissolved, by eye inspection, it was removed from its container using a glass syringe. For each polymer/solvent combination a different syringe was used. Afterwards, the syringe needle was substituted for the filter and the solution was poured into a new glass bottle. The remaining solution inside the filter was discarded.

2.2.2. Methods for evaluation of physical properties

Differential scanning calorimetry

The differential scanning calorimetry (DSC) measures the change of the difference in temperature between a sample and a corresponding reference while they are subjected to a controlled temperature program[49]. The heat flow difference is related to the temperature changes of the sample. These might indicate both physical phase transitions and/or chemical reactions[49]. Calorimetry measurements were performed using a Perkin Elmer DSC8500 instrument equipped with an *Intracooler 2* sub ambient device and calibrated with high purity indium standards. In order to measure the thermal transition of the samples, the external block temperature was set at -100 ºC. This allows measurements between -70 ºC up to 250 ºC. Samples (bulk and/or lyophilized nanoparticle powder) were encapsulated in aluminium pans, provided by Pelkin Elmer. The weights of the samples were measured in a Sartorious analytical balance (ME235S, accuracy 0.05 mg). Different heating rates have been used depending on the measurements to be performed, as stated in each chapter.

Wide Angle X-Ray Scattering

Wide Angle X-Ray Scattering (WAXS) is generally used for determine the crystalline structure of a sample. The term *wide* relates to the distribution of angles that can be measured, generally between 2θ = 5º and $2\theta >$ 30º, where 2θ is related to the spacing of diffracting planes by[50]:

$$n\lambda = 2d \sin\theta \qquad (2.1)$$

where n is an integer, λ is the wavelength of the X-ray beam, d is the spacing for a given set of diffracting planes and 2θ is the angle between the incident and diffracted X-ray beam. Equation (2.1) is referred as Bragg's Law[50]. WAXS investigations were carried out in transmission geometry using a Bruker AXS Nanostar X-ray scattering instrument. The instrument uses Cu Kα radiation (wavelength λ=0.154 nm) produced by a sealed tube. The sample chamber is under vacuum and at controlled temperature. For WAXS experiments in temperature, bulk and/or lyophilized nanoparticles were packed in aluminum sheets. The scattered X-rays are detected on a two-dimensional multiwire area detector (Bruker Hi-Star) and converted to one-dimensional scattering intensity as a fuction of 2θ by azimuth integration. The sample-to-detector distance was 10 cm.

Grazing Incidence Wide Angle X-ray Scattering

Grazing Incidence X-ray Scattering at Wide Angles (GIWAXS) experiments were carried out using the facilities of the BW4 beamline at HASYLAB (DESY, Hamburg, Germany). The experimental set-up for grazing incidence scattering at the BW4 beamline has been previously discussed in the literature[51-53]. A conceptual scheme of the experimental set-up is shown in figure 2.1. In the GIWAXS geometry samples are

positioned horizontally. In the case of nanostructures with linear geometries, samples are aligned with the lines parallel to the X-ray beam[54]. The incoming X-ray beam reaches the sample with a certain incidence angle α_i. The incidence and reflected beams define the vertical scattering plane. Both the scattering plane and the sample plane intersect the detector along the meridian and the horizon lines respectively which are the reference to measure the angles ω and α. The scattering can be interpreted on the basis of the two orthogonal scattering vectors $q_z = (2\pi/\lambda)\ (\sin\alpha_i + \sin\alpha)$ and $q_y = (2\pi/\lambda)\ \sin\omega\ \cos\alpha$, being λ the wavelength of the X-ray beam. The scattering vectors provide information about structural correlations perpendicular and parallel to the film plane respectively. In our case an X-ray wavelength λ= 0.138 nm, with a beam size of 40x20 μm^2 was used. Scattered intensity was recorded by a Mar CCD detector of 2048x2048 pixels with a resolution of 79.1 μm per pixel, and a sample-to-detector distance of about 0.11 m. An incidence angle of α_i = 0.4° was typically selected in our case. Acquisition times were optimized in order to get maximum number of counts avoiding saturation of the detector.

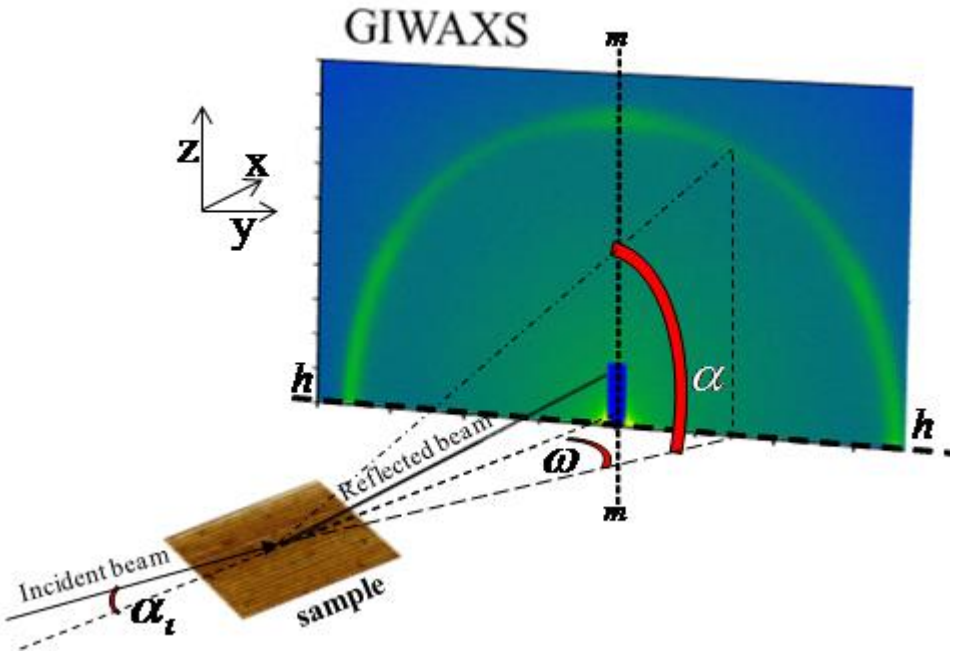

Figure. 2.1. Conceptual scheme of a GIWAXS experiment. The scattering plane, containing both the direct and the specular beams intersects the 2D detector along the meridian, m-m line. The horizon, h-h line, is the intersection between the sample plane and the plane of the 2D detector that are perpendicular to each other. Each point on the pattern can be characterized by the exit angle, α, and the out of scattering plane angle ω. Longer sample-to-detector distance is required for a GISAXS experiment than for a GIWAXS one.

Broadband Dielectric Spectroscopy

Broadband dielectric spectroscopy (BDS) measures the complex dielectric permittivity $\varepsilon^*(\omega) = \varepsilon'(\omega) - i\varepsilon''(\omega)$ as a function of frequency, where ε' and ε'' are referred to as dielectric constant and dielectric loss respectively[55]. The complex dielectric permittivity can be measured in an extraordinary frequency (F) range from 10^{-6} Hz up to 10^{11} Hz. To span this dynamic range, a variety of experimental setups, based on different measurement principles have to be combined. From 10^{-6} Hz to 10^{7} Hz, lumped circuit methods are used in which the sample is treated as a parallel or serial circuit of an ideal capacitor and an ohmnic resistor. For a capacitor C^* filled with a material under study, the complex dielectric permittivity is defined as:

$$\varepsilon^*(\omega) = \varepsilon'(\omega) - i\varepsilon''(\omega) = \frac{C^*}{C_0} \tag{2.2}$$

where C_0 is the vacuum capacitance of the arrangement and ω is the angular frequency (ω=2πF). Using a sinusoidal electric field: $E^*(w) = E_0 \exp(i\omega t)$, at field strengths within linear response (for most materials $E_0 \leq 10^6$ V cm^{-1}) the dielectric function can be derived by measuring the complex impedance $Z^*(\omega)$ of the sample:

$$\varepsilon^*(\omega) = \frac{J^*(\omega)}{i\omega\varepsilon_0 E^*(\omega)} = \frac{1}{i\omega Z^*(\omega) C_0} \tag{2.3}$$

In this work, BDS measurements were carried out in a Novocontrol broadband dielectric spectrometer. In the frequency range $10^{-1} < F$ (Hz) $< 10^7$, measurements were carried out using an ALPHA impedance analyzer. The schematics of this impedance bridge are shown in figure 2.2, and consists of a sample impedance $Z^*_S(\omega)$ and an adjustable compensation impedance $Z^*_C(\omega)$. On the left hand of figure 2.2, the generator drives the sample with fixed and known A.C. voltage $U^*_S(\omega)$ which causes the current $I^*_S(\omega)$ to flow into P_I. On the right hand side of the bridge, the variable amplitude-phase generator feeds the current $I^*_C(\omega)$ through the compensation impedance $Z^*_C(\omega)$ into P_I. The bridge will be balanced if $I^*_S(\omega)$ equals $-I^*_C(\omega)$ which corresponds to $I_0 = 0$. Any deviation is detected by the zero voltage detector which changes the amplitude and phase of the variable amplitude phase generator, as long as $I_0 \neq 0$. In the balanced state, the sample impedance is calculated as:

$$Z_S^*(\omega) = \frac{U_S^*(\omega)}{I_S^*(\omega)} = -\frac{U_S^*(\omega)}{U_C^*(\omega)} Z_C^*(\omega) \tag{2.4}$$

With increasing frequency, the geometrical dimensions of the sample capacitor become more and more important, limiting this approach to about 10 MHz. In addition, parasitic impedances caused by the cables, connectors, etc. become important at frequencies > 100 kHz. Using distributed circuit methods, in the frequency range $10^6 < F$ (Hz) $< 10^{11}$, the complex dielectric function is deduced by measuring the complex propagation factor (in reflection or transmission). In this case, waveguides as well as cavity techniques can be applied. In this research, for $10^6 < F$ (Hz) $< 10^9$ a waveguide technique was employed, using a HP42 analyzer. Independently of the frequency range, the temperature was controlled by a nitrogen jet (QUATRO from Novocontrol) with a temperature error during every single frequency sweep of ±0.1 ºC.

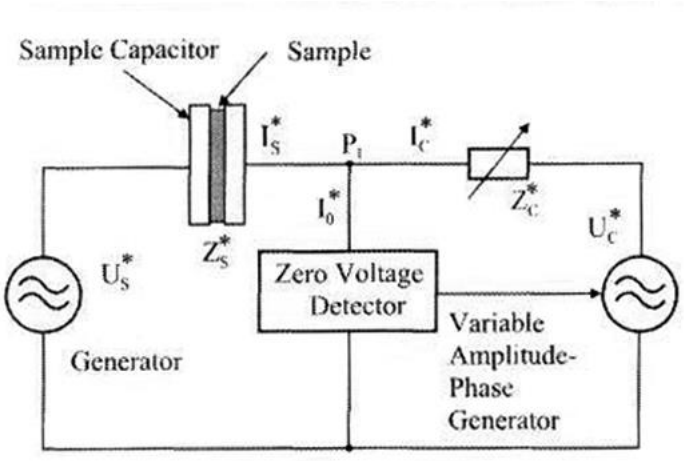

Figure 2.2. Scheme of an impedance bridge[55]

Relaxational processes observed by BDS are characterized by a resolved maxima in ε''(ω) and inflection points in ε'(ω). These feature in ε*(ω) can be analyzed in terms of the Havriliak-Negami (HN) model function[56]. This empirical equation describes the complex permittivity as [55]:

$$\varepsilon^*_{\mathrm{HN}}(\omega) = \varepsilon_\infty + \frac{\Delta\varepsilon}{(1 + (i\omega\tau_{\mathrm{HN}})^b)^c} \qquad \textbf{(2.5)}$$

where ω is the angular frequency ($\omega = 2\pi F$), $\Delta\varepsilon$ is the dielectric relaxation strength. The shape parameters b and c describe the symmetric and asymmetric broadening of the complex dielectric function respectively, and it holds that $0 < b, c \leq 1$. The central relaxation time τ_{HN} is related to the mean relaxation time $<\tau>$ of the relaxation time distribution function by:

$$<\tau>= \tau_{HN}\left[\sin\frac{b\pi}{2+2c}\right]^{-1/b}\left[\sin\frac{bc\pi}{2+2c}\right]^{1/b} \qquad \textbf{(2.6)}$$

The mean relaxation time $<\tau>$ can be obtained experimentally also through the frequency of the maximum loss, F_{max}, by $<\tau> = 1/(2\pi F_{max})$. The HN model function was applied to the dielectric data in chapter 6; however, from equation (2.5) one can arrive at other dielectric model functions. Specifically, if $c = 1$ in equation (2.5), one gets:

$$\varepsilon^*_{CC}(\omega) = \varepsilon_\infty + \frac{\Delta\varepsilon}{1+(i\omega\tau_{CC})^b} \qquad \textbf{(2.7)}$$

which is known as the Cole-Cole (CC) model function[55]. In this case, the relaxation curve only shows a symmetric broadening, characterized via the parameter b. Also, for these symmetric relaxation processes $\tau_{CC} = <\tau>$. The Cole-Cole model function was applied to the dielectric data in chapter 5.

Atomic Force Microscopy

The Atomic Force Microscopy is a scanning probe technique capable of measuring nanometric surface features. It was developed by Binnig, Quale and Geber around 1986[57], who took the design of the Scanning Tunneling Microscope (STM) and adapted it for measuring non-conductive samples. In general, the AFM works by

measuring the veritcal motion of a cantilever beam with ultra small mass as it scans a surface. The cantilever has a nanometric tip attached to its end, that is responsible for detecting the topographic morphology. The force requiered to move this beam through measurable distances (10^{-4} Å) can be as small as 10^{-18} N. This level of sensitivity is around the regime of interatomic forces. Although the AFM was originally design for measuring topographic images, nowadays it is possible to get information about physical processes at the nanoscale[58]. For example, AFM physical techniques allow measurement of mechanical properties[59], dielectric spectroscopy[60], ferroelectric response[61], semi-conductor properties[62], among others. Here, AFM measurements were mainly focused on evaluating topographic features at the nanoscale. We have used a Multimode 8 microscope (Bruker), equipped with a Nanoscope V controller (Bruker). For topograpy measurements, different scanning modes have been used throughout the following chapters, and will be described in the following paragprahs.

Contact Mode[58]. In contact mode (CM), the cantilever is scanned through the surface at a fixed deflection setpoint, *i. e.* at a constant force between tip and sample. As topographic features are found, the system generates a feedback that maintains the deflection constant, thus causing a vertical deflection on the tip. This deflection is measured by a photodetector and the topographic profile can be generated in a raster pattern. In this thesis, contact mode measurements were carried out at a deflection set point of 0.3 V, using SCM-PIC probes by Bruker (table 2.3).

Amplitude Modulation (Tapping)[58]. In the amplitude modulation AFM mode (TAP), the cantilever is scanned through the surface as it is being vibrated at a certain frequency (generally around 10^5 Hz). The system feedback controls the vibration of the

tip at a certain amplitude setpoint, imposing that the amplitude of the periodic movement must be kept constant as topographic features are found, thus causing a vertical deflection on the cantilever beam. This AFM mode is also known as *Tapping Mode.* In our work, tapping mode experiments were carried out at an amplitude setpoint between 0.3 and 0.4 V, using several probes detailed in table 2.3.

Peak Force Tapping[63]. The Peak Force Tapping (PF) mode, is an specific scanning mode developed by Bruker. In this scanning mode, the cantilever remains at rest while the piezo-scanner is modulated at a fixed frequency of 2 kHz and at a constant setpoint. During the modulation, there is a sample-tip interaction that generates a nanoidentation of the sample's surface in the elastic regime (without permanent deformation). The level of identation is controlled by the feedback system and it is maintained constant at the selected setpoint. As topography features are found the deflection of the cantilever is measured. In this work, PF images were taken at a constant setpoint between 0.1 and 0.5 V and using ScanAsyst (SA) probes (table 2.3).

Table 2.3. AFM probes used throughout the following chapters.

Probe	Manufacturer	Elastic constant (N/m)	Tip Radius (nm)	Conductive covering	Technique
SCM-PIC	Bruker	0.2	20	YES	Contact Mode Piezo-response Force Microscopy
NCHV	Bruker	40	10	NO	Tapping

NSG30	NT-MDT	40	8	YES	Tapping
SA	Bruker	0.4	2	YES	Peak Force Tapping

Piezoresponse Force Microscopy

The piezoresponse force microscopy (PFM) is a contact mode AFM technique that allows measuring the topographic features of a ferroelectric sample while determining its ferroelectric domains, simultaneously[64]. The basic idea of PFM is to affect locally the piezoelectric sample surface by the electric field and to analyse resulting displacements of the sample surface[65]. The PFM technique is based on the converse piezoelectric effect, which is a linear coupling between the electrical and mechanical properties of a material. Since all ferroelectrics exhibit piezoelectricity, an electric field applied to a ferroelectric sample results in changes of its dimensions. To detect the polarization orientation the AFM tip is used as a top electrode, which is moved over the sample surface while a bias is being applied. The electric field generated in the sample causes the domains with the polarization parallel to the field to extend and the domains with opposite polarization to contract. If the polarization vector is perpendicular to the electric field, there is no piezoelectric deformation along the field direction, but a shear strain appears in the ferroelectric, leading to displacements of the sample surface parallel to itself, along the polarization direction. The AFM probe tip moving according to the surface displacement causes normal or torsion (because of friction) deflections to the cantilever. Direction of the deflection depends on the mutual orientations of the electric field and domain polarization.

PFM measurements were carried out by means of a Nanoscope V AFM (Bruker), in the piezoresponse mode. The topography and the ferroelectric signals were acquired simultaneously. The microscope was used in contact mode, with a low deflection set-point (0.3 V) in order to avoid damaging the samples. The selected probes were the SCM-PIC (Bruker), which have a low spring constant (0.2 N/m) and a conductive PtIr layer. Through the PFM technique, hysteresis cycles were recorded applying a tip bias ramp from -12 V to 12 V at a frequency of 0.1 Hz and collection of 1024 samples. Local poling was carried out using the tip as the top electrode. In every case, a DC bias (± 12 V) was applied for 5 minutes. The control of points and lines drawn in the ferroelectric phase was made by means of the Point and Shoot protocol, available in the Nanoscope 8.15 software. The PFM out-of-plane signal was taken applying an AC voltage of 2 V at a frequency of 60 kHz between sample and tip. The PFM in-plane response was characterized modulating the photodetector signal through a lock-in amplifier and measuring the changes in the first harmonic. Measured amplitudes are related to the local electromechanical response of the sample surface during application of an AC voltage.

2.3. References

1. Sirringhaus, H.; Brown, P. J.; Friend, R. H.; Nielsen, M. M.; Bechgaard, K.; Langeveld-Voss, B. M. W.; Spiering, A. J. H.; Janssen, R. A. J.; Meijer, E. W.; Herwig, P.; De Leeuw, D. M. *Nature* **1999,** 401, (6754), 685-688.
2. Padinger, F.; Rittberger, R. S.; Sariciftci, N. S. *Advanced Functional Materials* **2003,** 13, (1), 85-88.
3. Kim, Y.; Cook, S.; Tuladhar, S. M.; Choulis, S. A.; Nelson, J.; Durrant, J. R.; Bradley, D. D. C.; Giles, M.; McCulloch, I.; Ha, C. S.; Ree, M. *Nature Materials* **2006,** 5, (3), 197-203.
4. Yang, X.; Loos, J.; Veenstra, S. C.; Verhees, W. J. H.; Wienk, M. M.; Kroon, J. M.; Michels, M. A. J.; Janssen, R. A. J. *Nano Letters* **2005,** 5, (4), 579-583.
5. Martin, J.; Campoy-Quiles, M.; Nogales, A.; Garriga, M.; Alonso, M. I.; Goni, A. R.; Martin-Gonzalez, M. *Soft Matter* **2014,** 10, (18), 3335-3346.
6. Barón, M.; Hellwich, K. H.; Hess, M.; Horie, K.; Jenkins, A. D.; Jones, R. G.; Kahovec, J.; Kratochvíl, P.; Metanomski, W. V.; Mormann, W.; Stepto, R. F. T.; Vohlídal, J.; Wilks, E. S. *Pure and Applied Chemistry* **2009,** 81, (6), 1131-1186.
7. Wang, H. L.; Toppare, L.; Fernandez, J. E. *Macromolecules* **1990,** 23, (4), 1053-1059.
8. Cepak, V. M.; Martin, C. R. *Chemistry of Materials* **1999,** 11, (5), 1363-1367.
9. Rebollar, E.; Vázquez de Aldana, J. R.; Pérez-Hernández, J. A.; Ezquerra, T. A.; Moreno, P.; Castillejo, M. *Applied Physics Letters* **2012,** 100, (4), -.
10. Yin, H.; Napolitano, S.; Schönhals, A. *Macromolecules* **2012,** 45, (3), 1652-1662.
11. Genix, A. C.; Arbe, A.; Colmenero, J.; Wuttke, J.; Richter, D. *Macromolecules* **2012,** 45, (5), 2522-2536.
12. Sanz, A.; Nogales, A.; Ezquerra, T. A. *Soft Matter* **2011,** 7, (14), 6477-6483.
13. Voulgaris, D.; Petridis, D. *Polymer* **2002,** 43, (8), 2213-2218.
14. Li, J.; Tan, S.; Ding, S.; Li, H.; Yang, L.; Zhang, Z. *Journal of Materials Chemistry* **2012,** 22, (44), 23468-23476.

15. Garlotta, D. *Journal of Polymers and the Environment* **2001,** 9, (2), 63-84.
16. Anderson, J. M.; Shive, M. S. *Advanced Drug Delivery Reviews* **2012,** 64, Supplement, (0), 72-82.
17. Kumari, A.; Yadav, S. K.; Yadav, S. C. *Colloids and Surfaces B: Biointerfaces* **2010,** 75, (1), 1-18.
18. Kataoka, K.; Harada, A.; Nagasaki, Y. *Advanced Drug Delivery Reviews* **2012,** 64, Supplement, (0), 37-48.
19. Rösler, A.; Vandermeulen, G. W. M.; Klok, H.-A. *Advanced Drug Delivery Reviews* **2012,** 64, Supplement, (0), 270-279.
20. Zhang, Y.; Chan, H. F.; Leong, K. W. *Advanced Drug Delivery Reviews* **2013,** 65, (1), 104-120.
21. Castellani, C.; Lindtner, R. A.; Hausbrandt, P.; Tschegg, E.; Stanzl-Tschegg, S. E.; Zanoni, G.; Beck, S.; Weinberg, A.-M. *Acta Biomaterialia* **2011,** 7, (1), 432-440.
22. Bose, S.; Roy, M.; Bandyopadhyay, A. *Trends in Biotechnology* **2012,** 30, (10), 546-554.
23. Martin, O.; Avérous, L. *Polymer* **2001,** 42, (14), 6209-6219.
24. Keddie, J. L.; Jones, R. A. L.; Cory, R. A. *EPL (Europhysics Letters)* **1994,** 27, (1), 59.
25. Forrest, J. A.; Dalnoki-Veress, K.; Stevens, J. R.; Dutcher, J. R. *Physical Review Letters* **1996,** 77, (10), 2002-2005.
26. Meli, L.; Pham, J. Q.; Johnston, K. P.; Green, P. F. *Physical Review E* **2004,** 69, (5), 051601.
27. Stafford, C. M.; Harrison, C.; Beers, K. L.; Karim, A.; Amis, E. J.; VanLandingham, M. R.; Kim, H.-C.; Volksen, W.; Miller, R. D.; Simonyi, E. E. *Nat Mater* **2004,** 3, (8), 545-550.
28. Lunov, O.; Syrovets, T.; Loos, C.; Beil, J.; Delacher, M.; Tron, K.; Nienhaus, G. U.; Musyanovych, A.; Mailänder, V.; Landfester, K.; Simmet, T. *ACS Nano* **2011,** 5, (3), 1657-1669.
29. Yang, Z.; Fujii, Y.; Lee, F. K.; Lam, C.-H.; Tsui, O. K. C. *Science* **2010,** 328, (5986), 1676-1679.
30. Paeng, K.; Swallen, S. F.; Ediger, M. D. *Journal of the American Chemical Society* **2011,** 133, (22), 8444-8447.
31. Kao, J.; Jeong, S.-J.; Jiang, Z.; Lee, D. H.; Aissou, K.; Ross, C. A.; Russell, T. P.; Xu, T. *Advanced Materials* **2014**, n/a-n/a.
32. Davis, G. T.; Furukawa, T.; Lovinger, A. J.; Broadhurst, M. G. *Macromolecules* **1982,** 15, (2), 329-333.
33. Lovinger, A. J. *Science* **1983,** 220, (4602), 1115-1121.
34. Baltá_Calleja, F. J.; Arche, A. G.; Ezquerra, T. A.; Cruz, C. S.; Batallan, F.; Frick, B.; López-Cabarcos, E. *Advances in Polymer Science* **1993,** 108, 1-48.
35. Ezquerra, T. A.; Kremer, F.; Baltá-Calleja, F. J.; Lopez Cabarcos, E. *Journal of Polymer Science Part B: Polymer Physics* **1994,** 32, (8), 1449-1455.
36. Kang, S. J.; Bae, I.; Shin, Y. J.; Park, Y. J.; Huh, J.; Park, S.-M.; Kim, H.-C.; Park, C. *Nano Letters* **2011,** 11, (1), 138-144.
37. Hong, C.-C.; Huang, S.-Y.; Shieh, J.; Chen, S.-H. *Macromolecules* **2012,** 45, (3), 1580-1586.
38. Zhu, L.; Wang, Q. *Macromolecules* **2012,** 45, (7), 2937-2954.
39. Guo, D.; Setter, N. *Macromolecules* **2013,** 46, (5), 1883-1889.
40. Hummelen, J. C.; Knight, B. W.; LePeq, F.; Wudl, F.; Yao, J.; Wilkins, C. L. *The Journal of Organic Chemistry* **1995,** 60, (3), 532-538.
41. Gorenflot, J.; Heiber, M. C.; Baumann, A.; Lorrmann, J.; Gunz, M.; Kämpgen, A.; Dyakonov, V.; Deibel, C. *Journal of Applied Physics* **2014,** 115, (14), -.
42. Dissanayake, D. M. N. M.; Ashraf, A.; Pang, Y.; Eisaman, M. D. *Advanced Energy Materials* **2014,** 4, (2), n/a-n/a.
43. Hauch, J. A.; Schilinsky, P.; Choulis, S. A.; Childers, R.; Biele, M.; Brabec, C. J. *Solar Energy Materials and Solar Cells* **2008,** 92, (7), 727-731.
44. Dang, M. T.; Hirsch, L.; Wantz, G. *Advanced Materials* **2011,** 23, (31), 3597-3602.
45. Kniepert, J.; Lange, I.; van der Kaap, N. J.; Koster, L. J. A.; Neher, D. *Advanced Energy Materials* **2014**, n/a-n/a.
46. *Polymer-Surfactant Systems*. Marcel Dekkar: 1998.
47. Reed, R.; Holmes, D.; Weyers, J.; Jones, A., *Practical Skills in Biomolecular Sciences*. 3rd ed.; Pearson Education Limited: England, 2007.
48. Bollag, D. M.; Rozycki, M. D.; Edelstein, S. J., *Protein Methods*. Wiley-Liss Inc: 1996.
49. Höhne, G. W. H.; Hemminger, W. F.; Flammersheim, H.-J., *Differential Scanning Calorimetry*. Springer-Verlag: 2003.
50. Kittel, C., *Introduction to Solid State Physics*. 8th ed.; John Wiley & Sons Inc: 2005.
51. Perlich, J.; Rubeck, J.; Botta, S.; Gehrke, R.; Roth, S. V.; Ruderer, M. A.; Prams, S. M.; Rawolle, M.; Zhong, Q.; Körstgens, V.; Müller-Buschbaum, P. *Review of Scientific Instruments* **2010,** 81, (10), -.
52. Roth, S. V.; Döhrmann, R.; Dommach, M.; Kuhlmann, M.; Kröger, I.; Gehrke, R.; Walter, H.; Schroer, C.; Lengeler, B.; Müller-Buschbaum, P. *Review of Scientific Instruments* **2006,** 77, (8), -.
53. Timmann, A.; Döhrmann, R.; Schubert, T.; Schulte-Schrepping, H.; Hahn, U.; Kuhlmann, M.; Gehrke, R.; Roth, S. V.; Schropp, A.; Schroer, C.; Lengeler, B. *Review of Scientific Instruments* **2009,** 80, (4), -.
54. Hernández, J. J.; Rueda, D. R.; García-Gutiérrez, M. C.; Nogales, A.; Ezquerra, T. A.; Soccio, M.; Lotti, N.; Munari, A. *Langmuir* **2010,** 26, (13), 10731-10737.
55. Kremer, F.; Schönhals, A., *Broadband Dielectric Spectroscopy*. Springer: 2003.
56. Havriliak, S.; Negami, S. *Polymer* **1967,** 8, (0), 161.
57. Binnig, G.; Quate, C. F.; Gerber, C. *Physical Review Letters* **1986,** 56, (9), 930-933.
58. Schönherr, H.; Vancso, G. J., *Scanning Force Microscopy of Polymers*. Springer: 2010.
59. Dokukin, M.; Sokolov, I. *Langmuir* **2012,** 28, (46), 16060-71.

60. Schwartz, G. A.; Riedel, C.; Arinero, R.; Tordjeman, P.; Alegría, A.; Colmenero, J. *Ultramicroscopy* **2011,** 111, (8), 1366-1369.
61. Hu, Z.; Tian, M.; Nysten, B.; Jonas, A. M. *Nat Mater* **2009,** 8, (1), 62-67.
62. Karagiannidis, P. G.; Kassavetis, S.; Pitsalidis, C.; Logothetidis, S. *Thin Solid Films* **2011,** 519, (12), 4105-4109.
63. Kaemmer, S. B., Aplication Note #133. Introduction to Bruker's ScanAsyst and PeakForce Tapping AFM technology. Bruker, Ed. 2011.
64. Wu, S., Piezoresponse Force Microscopy. Application Note. Technologies, A., Ed. 2007.
65. Alexe, M.; Gruverman, A., *Nanoscale Characterization of Ferroelectric Materials*. Springer: 2004.

Results

Part A – Preparation of polymer nanostructures

CHAPTER 3 – On the preparation of confined polymer structures.

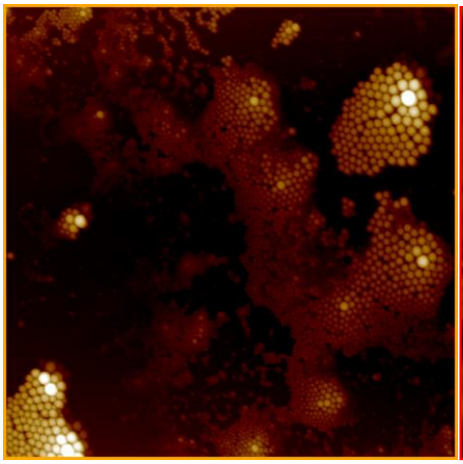

Poly(ethyl methacrylate) nanoparticles
(3x3) μm^2

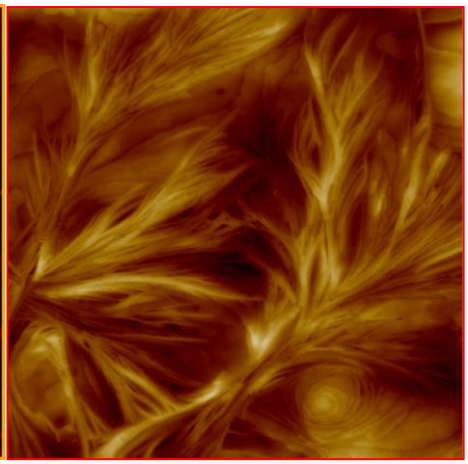

Poly(Lactic Acid) semi-crystalline thin film
(5x5) μm^2

Confined polymer nanostructures have been prepared following different techniques. In a first section, the preparation of three dimensionally confined polymer nanostructures is discussed. Four different techniques are presented, allowing a wide range of amorphous and semi-crystalline polymers to be nanostructured. Afterwards, in a second section, confined structures in thin film geometries are presented. In this case, two different techniques are discussed. In general, for every preparation method the protocol followed is presented in separated "boxes". Finally, for every case the limitations of each technique are discussed.

Three dimensionally confined polymer structures

3.1. The miniemulsion technique

The miniemulsion technique is an oil-in-water post-polymerization dispersion protocol to prepare polymer nanoparticles, which has been widely discussed by K. Landfester in the last decade[1-3]. A custom protocol based on this technique was implemented at the facilities of IEM-CSIC, and it is presented in box 1 and scheme 3.1. In the miniemulsion technique, a polymeric solution is dispersed into a non-solvent containing a surfactant system. In the present case, all polymers were dissolved in chloroform ($CHCl_3$). The polymer solution was added to an aqueous surfactant solution of SDS. Please note that polymer solvent must be immiscible with water. Pre-emulsification is obtained by stirring at room temperature and afterwards, ultrasonication of the stirred mixture allows obtaining a miniemulsion. Evaporation of the organic solvent under stirring yields a dispersion of polymeric nanospheres in a non-solvent medium. To eliminate the excess of SDS, suspensions were dialyzed against distilled water. The size of the obtained nanospheres is governed principally by the concentration of the polymeric solution and by the concentration of the surfactant.

Following this recipe, nanoparticles of several amorphous polymers, such as poly(ethyl methacrylate) (PEMA), poly(styrene) (PS) and poly(bisphenol A carbonate) (PBAC), were prepared. Also, this same protocol allowed preparing nanoparticles of semi-crystalline polymers as poly(D,L-lactic acid) (PDLLA), poly(3-hexylthiophene) (P3HT) and of the low molecular weight compound PCBM. Since in the miniemulsion technique, the precursor material is the bulk polymer of known molecular weight, only one parameter, that is nanoparticle diameter, needs to be adjusted during the process. Also, no residuals or contaminants are present in the final product, since no catalysts are needed,

in comparison to other nanoparticle preparation processes such as the in situ polymerization method[4].

BOX 1 – THE MINIEMULSION PROTOCOL

1. A polymer solution in $CHCl_3$ is prepared in a 15 mL disposable glass bottle.
2. An aqueous solution of surfactant is prepared in a separated 15 mL disposable glass bottle.

   -- Both solutions are stirred independently until complete dissolution, by eye inspection –
3. 3.5 mL of polymer solution is poured into 10 mL of the aqueous surfactant solution and the emulsion is **stirred at room temperature at 1250 rpm for 1 hour**. The glass bottle is sealed with *parafilm* in order to avoid evaporation of the components.
4. After stirring, the emulsion is **ultrasonicated in an ultrasonic bath.** During this time it is ensured that the temperature of the water bath is kept constant around 20 ºC.
5. Afterwards, lid is removed from the glass bottle and it is **heated up to 66 ºC and stirred at 1080 rpm to let chloroform evaporation**. To allow a homogeneous heating, the bottle was covered in aluminum foil.

   -- A stable dispersion of polymeric nanospheres in a non-solvent media is obtained --
6. To eliminate the excess of surfactant, the nanoparticle suspension is dialyzed against distilled water using a dialysis membrane. Several water changes are performed during a total dialysis time of 72 hours.

   Specific details of concentrations and times are presented throughout the chapter.

3.1.1. Preparation of amorphous polymer nanoparticles via the miniemulsion technique

The miniemulsion technique was used to prepare particles of amorphous polymers. In a first glance, we followed the protocol described in box 1 in order to prepare surfactant aided particles of PEMA, PS and PBAC. This allowed a wide study and understanding of the technique. General details of concentrations and ultrasonication times are given in table 3.1. Following this protocol, samples labeled as PEMA1 and PEMA3 were prepared, in order to obtain two different size distributions by playing with

solutions concentrations and ultrasonication times. On the other hand, PS and PBAC samples were labeled PS-NANO and PBAC-NANO.

Furthermore, we modified the miniemulsion technique in order to prepare a precipitate of nanospheres without surfactant. By this method, a stable precipitation of PEMA micro- to nanospheres in water is obtained. The proposed method is nearly similar to the one presented above, with the only difference being the absence of surfactant. In order to obtain different distribution sizes, two different approaches were applied. The same procedure as the one reported in box 1, without the aid of surfactant, yields to a precipitate in the form of spheres with mean diameters around 230 nm. In table 3.1, PEMA4 is prepared in this way. To obtain smaller spheres without surfactant, steps 1, 2 & 3 in box 1 were followed, but the ultrasonication of the emulsion was performed in an open flask, and it was extended until complete evaporation of $CHCl_3$. In this way PEMA2 was prepared (table 3.1). To avoid contamination from possible bulk precipitate in these two preparation methods, once the respective protocols are complete, the samples were filtered with a filter paper.

Table 3.1. Preparation conditions for the different studied samples of PEMA, PS and PBAC particles by the miniemulsion technique.

Sample	Polymeric Solution Concentration (wt %)	Surfactant Solution Concentration (wt %)	Ultrasonication time (min)	Evaporation time (min)
PEMA1	0.2	1	5	210 (66 ºC)
PEMA2	2	---	210	---
PEMA3	5	0.3	1/3	210 (66 ºC)
PEMA4	2	---	5	210 (66 ºC)
PS-NANO	0.2	1	5	210 (66 ºC)
PBAC-NANO	0.2	1	5	210 (66 ºC)

Scheme 3.1 The miniemulsion protocol

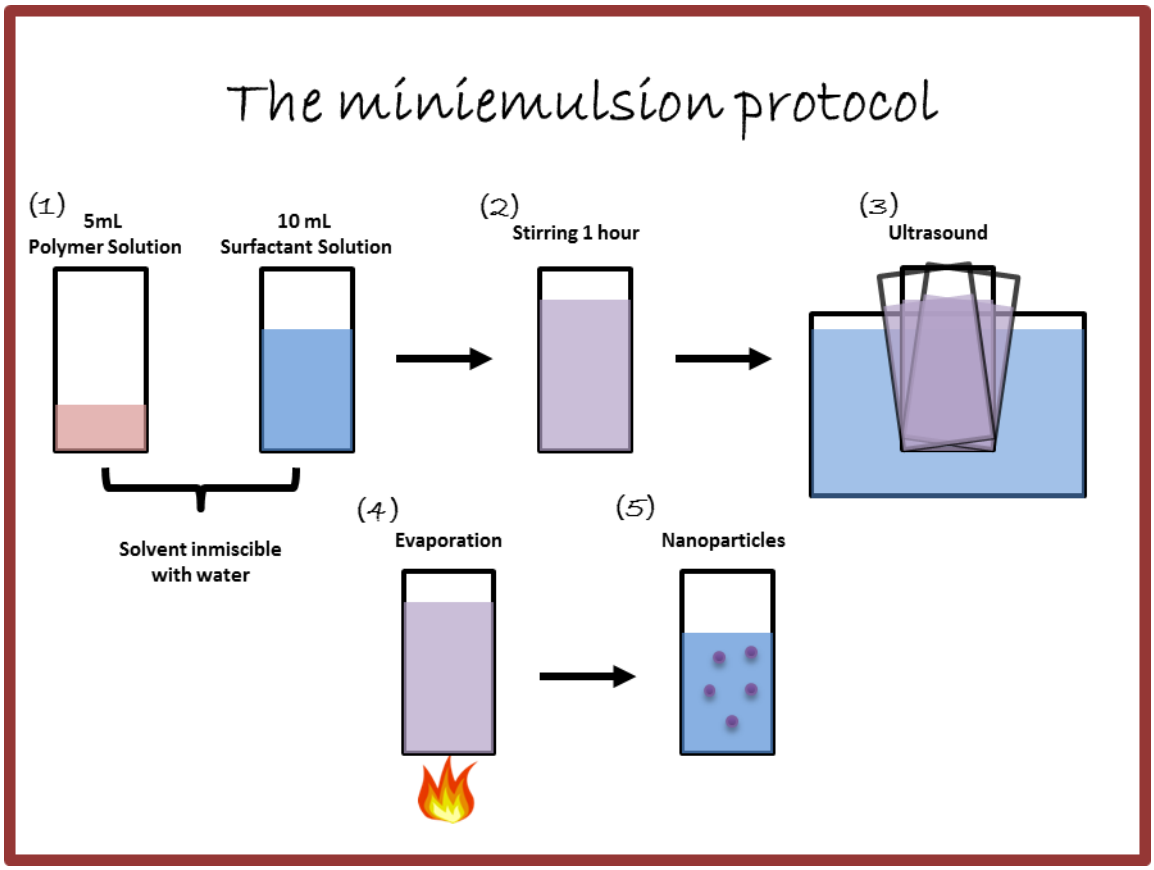

The size distribution and shape of the obtained nanoparticles were characterized by Atomic Force Microscopy (AFM). Images were collected using the Peak Force Tapping mode, with SA probes. The samples for AFM analysis were spin coated on regular silicon wafers, previously treated with a piranha solution. AFM measurements confirmed that the particles prepared are spheres with submicron diameters: no other geometrical structures were found. Figure 3.1 presents (3x3)μm AFM height images of selected samples prepared with and without surfactant, namely PEMA1, PEMA3 and PEMA2, PEMA4, respectively, together with their respective size distributions. Quantitative analysis of the size distribution was performed in several regions of spun coated silicon wafers (Figure 3.1 e and f) and details are given in table 3.2. In this table and during the rest of this chapter, the mean diameter refers to the most probable size diameter that can be encountered, while the width refers to the half width at half

maximum of the Gaussian distribution. The AFM experiments revealed that preparations with and without surfactant lead to morphologically similar nanoparticles. No pronounced ripening effects in the absence of surfactant for this specific polymer are observed. The final diameter distribution is governed principally by the concentration of the polymer solution and by the interplay between the ultrasonication and the evaporation of chloroform times. In both preparation methods (with and without surfactant) the conditions were chosen to obtain particles with diameter in the submicron range, referred from now on as submicron particles. Spheres with diameter below 100 nm are referred hereafter as nanometer size particles. For formulations with SDS, the results are comparable with those available in the literature for other types of polymers[2, 5, 6]. From the particle size distributions, it is possible defining a *quality factor* of the resulting nanospheres as follows:

$$Q = \frac{W}{< d >} \tag{3.1}$$

where W is the width of the distribution (nm) and $<d>$ is the mean diameter (nm). The closer the factor Q is to zero, the better is the resulting preparation in terms of size monodispersity. Results of the Q values obtained for PEMA nanoparticles are summarized in table 3.2. It is found that smaller particles show a Q value around 0.55, while in bigger particles it reduces down to 0.4. However, the error shows that it is possible arguing that Q remain almost constant, without any changes independently of particle size.

Table 3. 2. Characteristics of the size distribution of amorphous polymer nanoparticles prepared by the miniemulsion technique.

Sample	Size Distribution (nm)	Width of the distribution (nm)	Mean Diameter (nm)	*Q*
PEMA1	< 20 – 100	(20 ± 2)	(35 ± 1)	0.57±0.07
PEMA2	<20 – 120	(22 ± 2)	(42 ± 1)	0.52±0.06
PEMA3	100 – >600	(100 ± 30)	(220 ± 20)	0.4±0.2
PEMA4	100 – >600	(100 ± 30)	(230 ± 30)	0.4±0.2
PS-NANO	< 20 – 100	(24 ± 3)	(35 ± 1)	0.7±0.1
PBAC-NANO	<20 – 120	(22 ± 5)	(52 ± 2)	0.4±0.1

Figure 3.2 shows (3x3)μm AFM height images of PS nanoparticles (left column) and PBAC nanoparticles (right column), taken with the same conditions as in the surfactant aided PEMA case. These AFM images reveal that both PS and PBAC show a distribution of nanoparticles with spherical shape without ripening or coalescence effects. As for PEMA, an analysis of the size distribution of the particles was performed, which results are summarized in table 3.2. It can be seen that for PS nanoparticles, a mean diameter of 35 nm with a size distribution of about 20 nm was found. These results equal the one of PEMA1. On the other hand, PBAC nanoparticles present a slightly bigger mean diameter of about 50 nm in comparison to the other polymers. This difference can be understood in terms of the lower flexibility of PBAC in relation to PS and PEMA. Also it is interesting to remark the fact that for any polymer, following the same protocol of nanoparticle preparation, size distribution remained almost constant and around 20 nm, however, quality factor seems to be a little bit better for PBAC in comparison to PS.

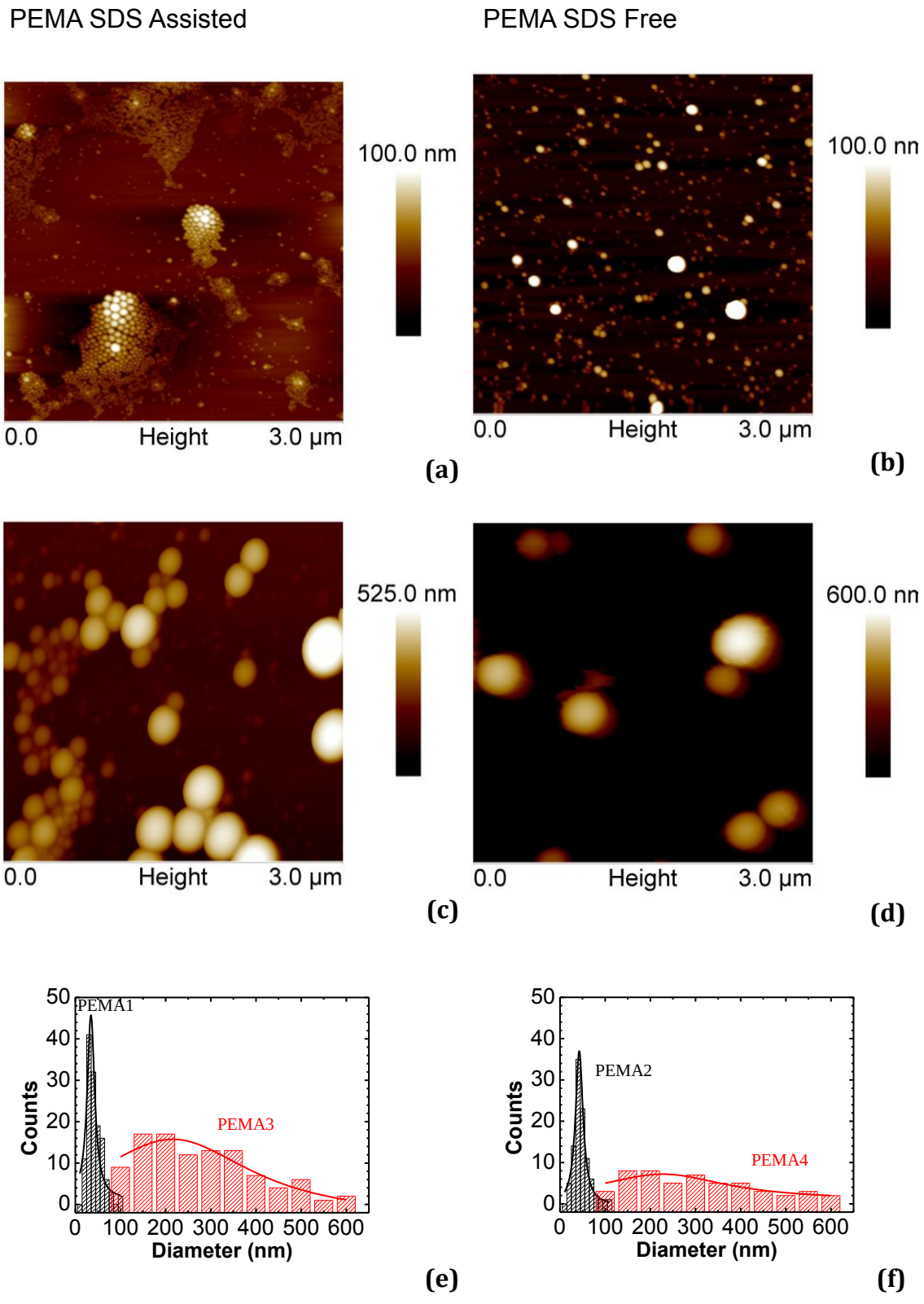

Figure 3. 1. AFM images and histograms for PEMA nanoparticles. Left. SDS assisted PEMA particles (a and c), with 0.2 wt% and 5 wt% concentration respectively, (PEMA1 and PEMA3 from table 1) and their corresponding diameter distributions (e). Right. SDS free PEMA particles (b and d), with 2 wt% concentration in each case (PEMA2 and PEMA4 from table 1), and its corresponding size distribution (f).

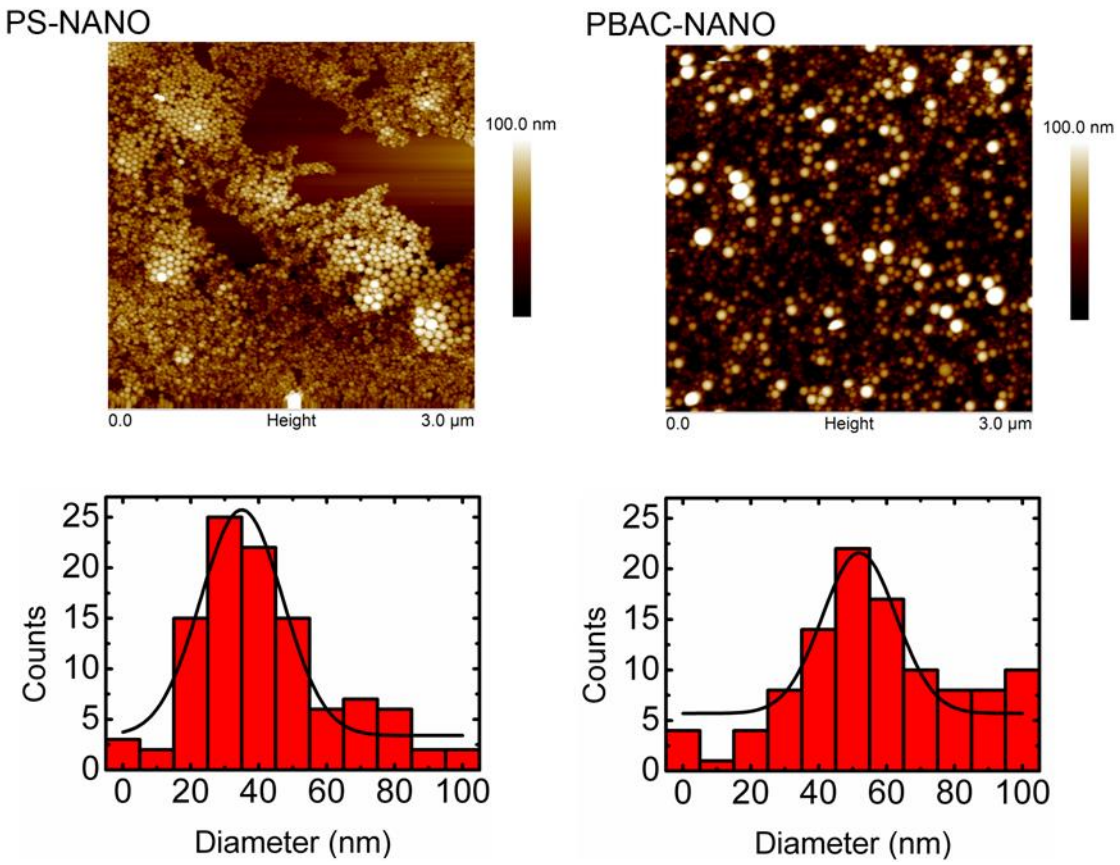

Figure 3. 2. AFM images and histograms for PS and PBAC nanoparticles. Left. SDS assisted PS particles with 0.2 wt% concentration and its corresponding diameter distribution. Right. SDS assisted PBAC particles with 0.2 wt% concentration and its corresponding size distribution.

3.1.2. Preparation of semi-crystalline polymer nanoparticles via the miniemulsion technique.

Previously, several groups have reported the possibility of preparing semi-crystalline polymer nanoparticles using the miniemulsion technique[6-11]. Following their work, we designed a protocol to prepare surfactant aided nanoparticles of the semi-crystalline polymers PDLLA and P3HT. Also the low molecular weight material PCBM was prepared. The protocol followed the same steps presented in box 1, with the conditions shown in table 3.3.

Table 3.3. Nanoparticles preparation conditions for the semi-crystalline samples PLA, P3HT and PCBM by the miniemulsion technique.

Sample	Polymeric Solution (wt %)	Surfactant Solution (wt %)	Ultrasonication time (min)	Evaporation time (min)
PLA-NANO	0.2	1	15	210 (66 ºC)
P3HT-NANO				
PCBM-NANO				

First row of figure 3.3a shows (3x3)μm AFM height images of PDLLA nanoparticles (left) and PCBM nanoparticles (right). AFM images were taken with the same conditions as in the previous cases. For both images it is seen that the prepared nanoparticles, present a spherical shape without ripening and/or coalescence. As for the previous cases, an analysis of the size distribution of the particles was performed, which results are shown in the second row of figure 3.3 Results of the distributions are summarized in table 3.4.

Table 3. 4. Characteristics of the size distribution of semi-crystalline polymer nanoparticles.

Sample	Size Distribution (nm)	Width of the distribution (nm)	Mean Diameter (nm)	*Q*
PLA-NANO	< 20 – 100	(26 ± 2)	(46 ± 1)	0.57±0.06
PCBM-NANO	30 – 120	(29 ± 5)	(73 ± 2)	0.40±0.08

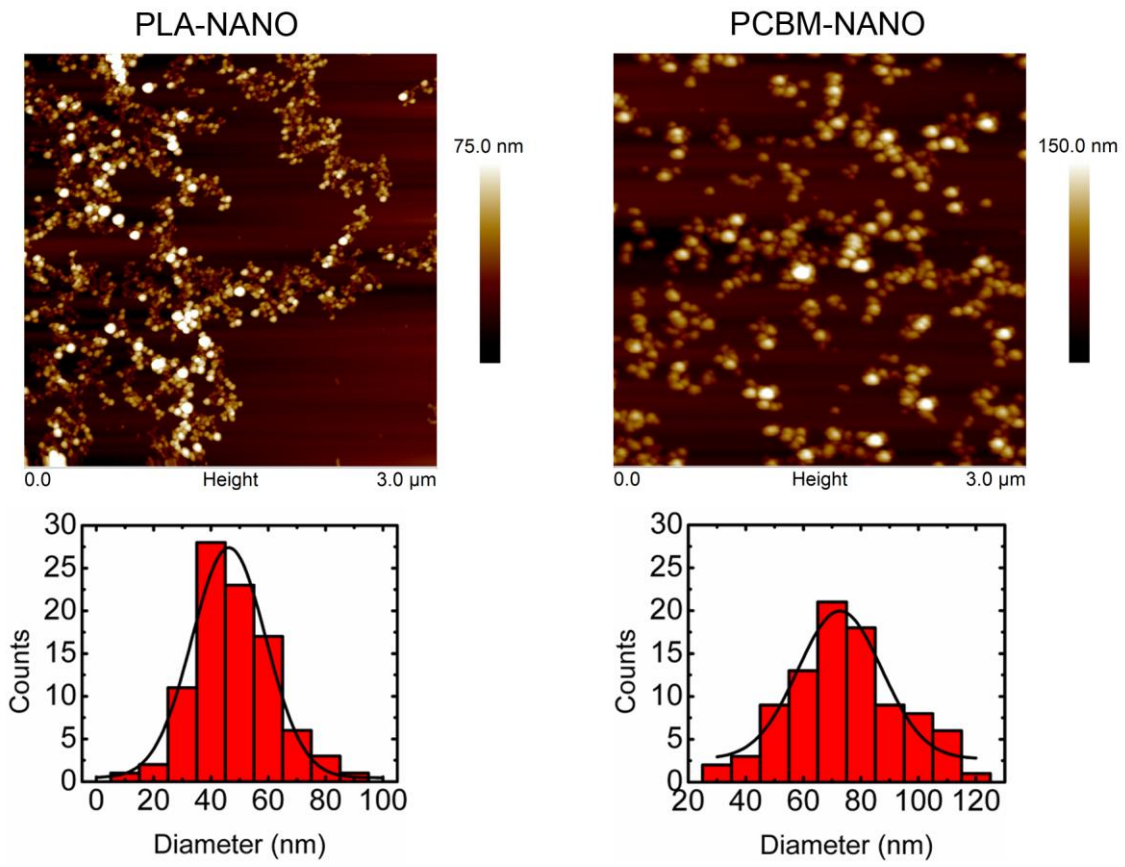

Figure 3. 3a. AFM images and histograms for PDLLA (left) and PCBM (right) nanoparticles prepared at 0.2 wt%. Histograms represent the diameter distributions of the nanoparticles.

Specifically, PDLLA nanoparticles showed a size distribution between 20 and 100 nm in diameter, quite similar to the evidenced for the amorphous polymer particles in the past section, with a mean diameter of 46 nm. The nanoparticles of PCBM present a bigger mean diameter (73 nm) in comparison with the PLA nanoparticles and the amorphous polymers in the past section, with a size distribution width quite similar. The possibility of preparing nanoparticles of this compound, with absence of ripening is related to its crystalline behaviour and high melting temperature (about 250 ºC[12]). Although the molecular weight of the compound is much lower in comparison to the rest of the polymers so far presented, its much bigger mean diameter (almost double in comparison with the polymers) can be related to its non-polymeric nature. The absence of folding capabilities in the PCBM might be responsible for this result. The crystalline nature of

PCBM might be one of the reasons for the particles to be stable.

Figure 3.3b shows a (5x5)μm^2 AFM height image of the prepared P3HT nanoparticles by the miniemulsion method. This polymer is of great interest towards the development or organic photoresponsive materials and devices. In the image is observed that the preparation method lead to nanospheres of diameters around 50 nm. No coalescence or ripening is observed.

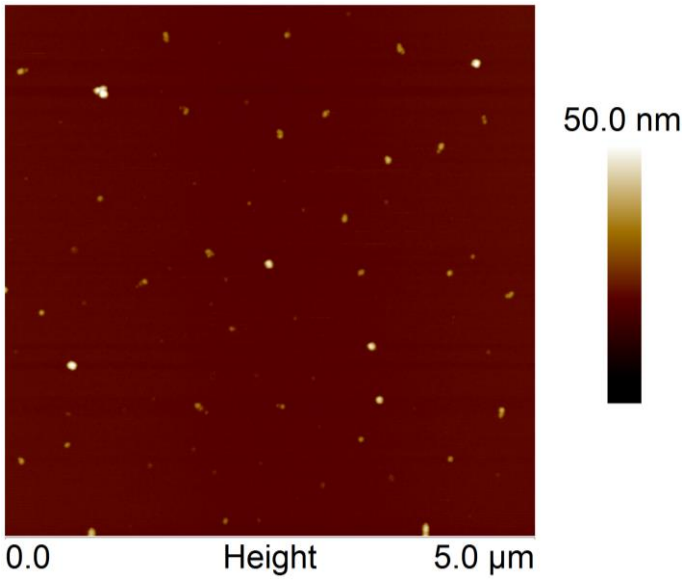

Figure 3.3b. AFM height image of P3HT nanoparticles prepared by the miniemulsion method.

3.1.3. Limitations of the miniemulsion technique

As for any preparation technique, the miniemulsion protocol has its limitations. First, it must be ensured that there is no compatibility between the polymer solvent and water; even a slight miscibility can be critical. Second, the polymer must be well dissolved in the solvent when mixing with the aqueous solution. In any other case, the polymer will macro-precipitate. However, even polymers that follow the specifications above mentioned cannot be prepared via this technique.

Perhaps the most critical factor to take into account when thinking if a polymer is suitable for preparation is the glass transition temperature (T_g), when considering amorphous materials, or kinetics of crystallization and the melting temperature (T_m) when dealing with semi-crystalline polymers. For every case, the T_g or T_m must have a higher value than the evaporation temperature of the solvent. For example, if working with $CHCl_3$, as in our case, any of these temperatures must be above 62 ºC (Table 2.1). However if the polymer system has fast crystallization kinetics, it can remain stable even if its T_g is well below the evaporation temperature. We have found this inconvenient when trying to prepare nanoparticles of poly(butyl methacrylate) (PBMA), which glass transition temperature is 40 ± 1 ºC, as revealed by differential scanning calorimetry at our facilities. In a first attempt, the protocol presented in box 1 was followed but after evaporation of the chloroform, a macro-precipitate of the polymer was found inside the bottle. This result was interpreted since above T_g the polymer chains present high mobility and the system behaves liquid-like, thus it cannot be contained inside the nanodroplets of solvent in water. On a second attempt, we tried to evaporate the $CHCl_3$ at room temperature, under stirring for several hours, but the result remained the same. This result also happened when trying to prepare nanospheres of the aliphatic polyesters poly(propylene succinate) (PPS) and poly(propylene adipate) (PPA), These semi-crystalline polymers have glass transition temperatures between -40 ºC to -20 ºC and melting temperatures between 40 ºC to 46 ºC[13]. The evaporation of the solvent at room temperature lead to macro-precipitation. As a final test, we tried to prepare nanoparticles of poly(propylene azelate) (PPAz). This linear aliphatic polyester belongs to the same family as PPS and PPA, with a T_g of -56ºC and melting temperature of 49 ºC[14]; however, its kinetics of crystallization is much faster in comparison to PPS and PPA[14]. Following the miniemulsion protocol so far discussed, and letting chloroform evaporation through

12 hours, at room temperature, under stirring, the final dispersion did not macro-precipitate. The resulting PPAz was analysed by AFM and the results are shown in figure 3.4. PPAz particles did not present the same spherical form discussed for amorphous and semi-crystalline polymers, but a more complex structure. In diameter, these particles show a size distribution between 150 nm and 600 nm; however, height distribution goes between 20 and 60 nm. Also, the particles surface is not as smooth as in the previous cases. For PPAz, a sort of rugosity is evidenced all around the particles. Literature suggests that the morphology evidenced by AFM, might resemble the flat-on lamellae observed in PPAz thin films[14]. This fact, along with the absence of macroscopical precipitation of the polymer, allows concluding that as the chloroform evaporated from the emulsion, PPAz particles were able to crystallize inside the droplets in order to avoid coalescence. Once all solvent was gone, the polymer rested in its semi-crystalline state and thus no agglomeration and precipitation could take place.

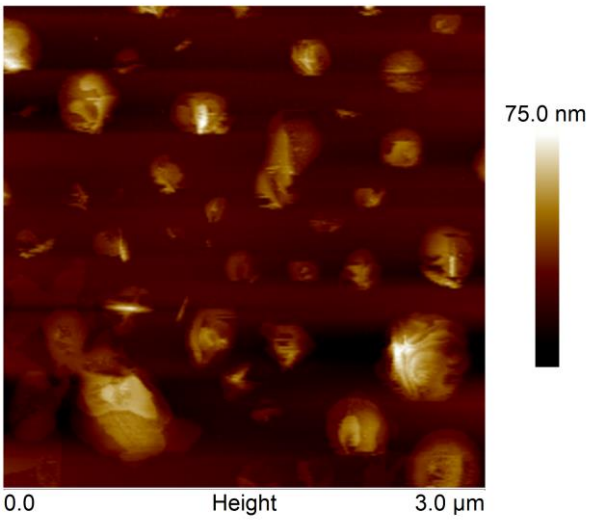

Figure 3. 4. (3x3)µm AFM height image of a PPAz nanoparticle preparation.

Finally, another question that might arise when analysing the miniemulsion technique can be related to the possibility of changing the water medium for other liquids

such as alcohols or hydrocarbons. There are several reasons why one might replace water, such as the miscibility of the desired polymer solvent (for example, THF, DMA, acetone, etc) or the possibility of performing physical and/or chemical analysis after preparation, in which water might act as source of unwanted signals, for example broadband dielectric spectroscopy. These limitations raised when preparing nanoparticles of the ferroelectric copolymer poly(vinilydene fluoride – co – trifluoro ethylene) P(VDF-TrFE), which dissolves in DMA. In that case several problems came to consideration. First, water must be replaced not only because its miscibility with DMA, but also because its boiling point (T_B) is lower in comparison to the one of the solvent (T_B = 165 ºC for DMA). We managed to replace water with n-decane (T_B = 210 ºC for n-decane); nonetheless, under this combintacion (DMA / n-decane), SDS proved to be not useful for preparation of nanoparticles, since no stabilization of the emulsion was attained. Literature suggests that for this type of water-in-oil like emulsion, another surfactants might be used, such as sodium bis(2-ethylexyl) sulfosuccinate (AOT)[15]. Due to all the limitations and changes that must be applied to the miniemulsion protocol when replacing water, other protocol was tested when dealing with this ferroelectric polymer. This new protocol is now presented in the following section.

3.2. Solvent-displacement techniques

As stated in the previous section, one of the main limitations of the miniemulsion protocol is related to the possibility of using a polymer solvent miscible with water. In order to overcome this issue, we have studied other nanoparticle preparation methods, based on the so called solvent-displacement technique. These are postpolymerization dispersion methods that rely on crashing out hydrophobic polymer chains in solution by displacing a solvent with a non-solvent, generally water. Both polymer solvent and non-

solvent must be miscible among them. As in the miniemulsion technique, due to the inherent nature of using bulk polymer chains of known molecular weight as the precursor material for nanoprecipitation, only the nanoparticle diameter needs to be adjusted during the process, and there are no sources of residual contaminants that can affect the cores of the generated nanoparticles. In this section we present two methods based on the solvent-displacement technique, specifically, the dialysis nanoprecipitation and the reprecipitation techniques. Recently, nanoprecipitation methods, based on the solvent-displacement premise, have been reported for the preparation of nanoparticles based on several polymers, such as PLA[16, 17], poly(ε-caprolactone)[18], PS[19] and poly(methyl methacrylate)[20]. Also, nanoparticles of P3HT[21] as well as of the P3HT/PCBM blend[22, 23] have been prepared following this type of protocols.

3.2.1. Dialysis nanoprecipitation

This method has been recently discussed by C. Zhang and co-workers[24] for the preparation of PS nanospheres. A custom protocol based on this technique was implemented at the facilities of the IEM-CSIC and it is presented in box 2 and scheme 3.2.

For implementing this technique we have chosen the ferroelectric copolymer P(VDF-TrFE), at two molar concentrations, namely 76:24 and 56:44 (VDF:TrFE). Polymer solutions were prepared at a fixed concentration of 5 mg/mL, using DMA as solvent. 5 mL of solution was poured into a dialysis membrane and dialyzed against distilled water. The different relative concentration of DMA inside and outside the membrane submerged in water leads to a chemical difference. In order to establish equilibrium DMA, molecules escape from the membrane, as water molecules go inside.

Both liquids have a molecular weight well below the cutoff range of the membrane so the interchange is plausible. Since polymer chains do not dissolve in water, a controlled precipitation takes place inside the membrane. Once chemical equilibrium is reached, water must be changed in order to promote the continuous exchange of DMA and water, until all the polymer solvent is gone from the membrane and a stable emulsion of polymer nanoparticles in water is obtained. The whole experiment is conducted at room temperature.

BOX 2 – THE DIALYSIS NANOPRECIPITATION PROTOCOL

1. A polymer solution in DMA (T_B = 165 ºC. M_w = 87.12 Da) is prepared in a 15 mL disposable glass bottle. DMA is miscible with water.

2. A dialysis membrane is gently washed in DMA, both outside and inside faces, and let it soaking in solvent for 30 minutes.

3. 5 mL of the polymer solution are gently poured into the dialysis membrane. The membrane is closed at both side using simple knots. Care must be taken to no let any air space in the membrane.

4. Afterwards the membrane is submerged in a 2 L container of distilled water. The dialysis process takes places due to the chemical difference inside and outside the membrane.

5. To overcome the chemical equilibrium, several water changes are performed during the nanoprecipitation process. The first 2 hours, 4 water changes are performed each 30 minutes. Then, 4 more water changes are performed each hour. Throughout this time, the original clear polymer solution starts becoming cloudy, sign of the polymer nanoprecipitation inside the membrane. Finally, the membrane is left stirring in distilled water overnight.

6. At the end, a polymer nanoprecipitate is found inside the membrane.

Polymer nanospheres were spun coated in silicon wafers, previously treated with a piranha solution. The resulting material was analyzed by AFM in the Tapping protocol, using NCHV probes. Figure 3.5 shows (3x3)μm height images.

Scheme 3.2 The dialysis nanoprecipitation protocol

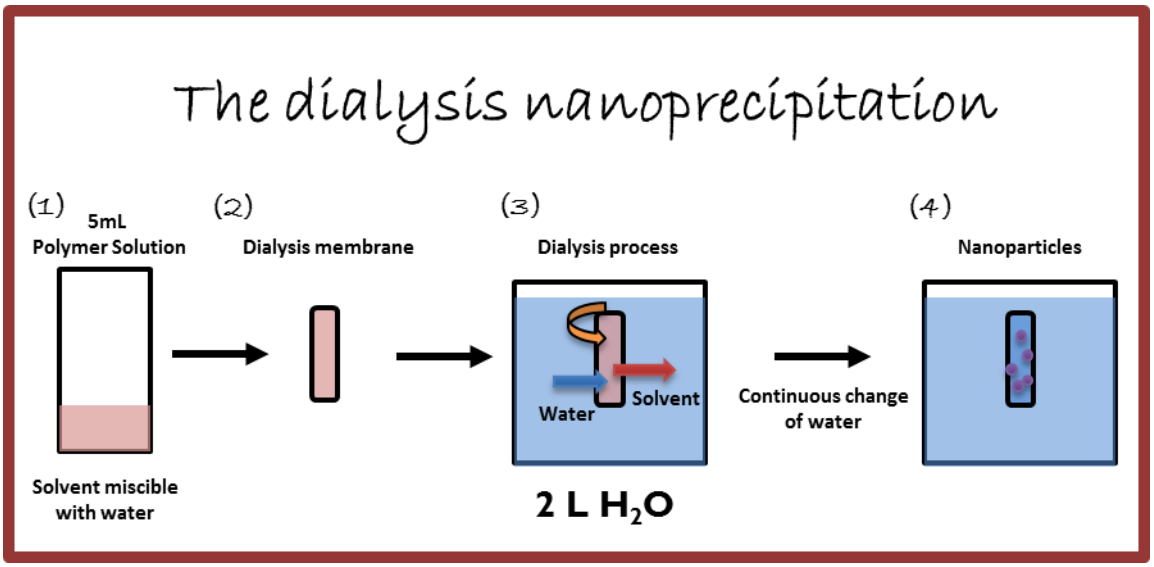

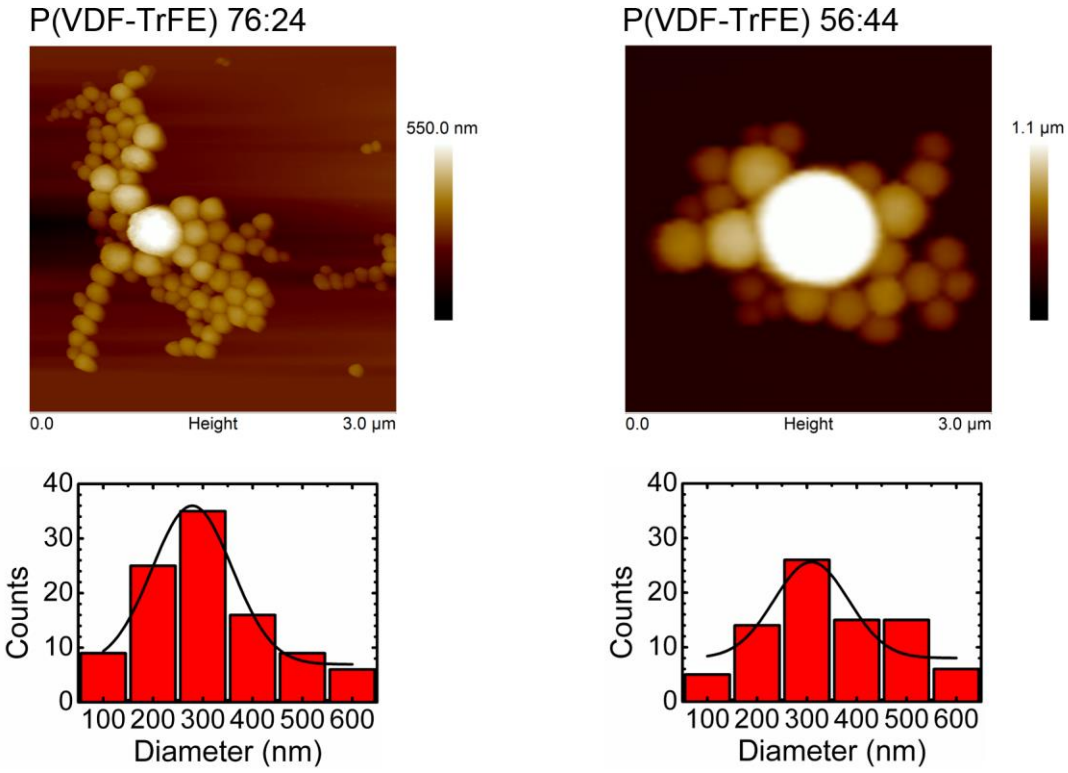

Figure 3. 5. AFM images and histograms for P(VDF-TrFE) nanoparticles. Molar concentration 76:24 (left), and 56:44 (right). Histograms represent the diameter distributions of the nanoparticles.

AFM images show that it is possible to prepare nanoparticles of this ferroelectric copolymer, for both molar concentrations. All particles present a spherical geometry and

no signs of coalescence or ripening are seen. However, in comparison to the miniemulsion method, the size distribution of the nanospheres is quite different. From the histograms shown in figure 3.5, which results are summarized in table 3.6, nanospheres show diameters in the range of the hundreds of nanometers. This is an increase in size in almost a factor 10 in comparison to the previous technique. Both molar concentrations of the P(VDF-TrFE) show similar values for the size distribution, with a mean diameter around 300 nm and a width of the distribution of about 160 nm, although nanoparticles of the 56:44 concentration seems to have a slightly bigger mean diameter. Nonetheless, our results are comparable to the ones presented by Zhang et al[24]. In their experiment, for PS nanoparticles prepared by the same method, using the same polymer/solvent concentration, and the same solvent (DMA), the mean diameter was found to be around 170 nm. In the case of the ferroelectric copolymer here presented, the increase of the mean diameter might be related to the semi-crystalline nature of the material.

Table 3.6. Characteristics of the size distribution of the semi-crystalline copolymer P(VDF-TrFE) nanoparticles, prepared by the dialysis nanoprecipitation.

Sample	Molar concentration	Size Distribution (nm)	Width of the distribution (nm)	Mean Diameter (nm)	*Q*
Ferro76	76:24	100 – > 600	(160 ± 10)	(280 ± 5)	0.57±0.05
Ferro56	56:44		(150 ± 60)	(310 ± 30)	0.5±0.2

3.2.2. Limits of the dialysis nanoprecipitation

In order to further test the applicability of this method, nanoparticles of other polymers were tried to prepare under the protocol presented in box 2. Polymers

unsuccessfully tested by the miniemulsion technique, such as PBMA, PPS and PPA were tried to be prepared under this approach. DMA and THF were used as solvents (independently), but for every case a macro-precipitate was found. As before, this might be related to the high mobility of the polymer chains in the solvent and the kinetics of crystallization, at room temperature, that do not allow the formation of a stable dispersion. Another problem is the possibility of obtaining nanoparticles with mean diameters below 100 nm. Although there is a dependence on the final diameter with the polymer/solvent concentration[24] there are not great changes in the nominal size. For example, as presented by Zhang, the change of diameter when going from a 5 mg/mL solution to a 1 mg/mL one is only of about 20 nm. If lower concentrations are used, it is expected that the 100 nm barrier could be overcome; however, this would be a low throughput method.

3.2.3. The Reprecipitation method

In order to reduce the mean diameters of the dialysis nanoprecipitation technique, we implemented another solvent-displacement method, called the reprecipitation method. Following the works by Okabe[21] and Gesquiere[22], a custom protocol was implemented at the facilities of IEM-CSIC and it is presented in box 3 and scheme 3.3.

The reprecipitation method goes as follows. First, a polymer solution is prepared, with the condition that the solvent mixes seamlessly with water. After complete dissolution, the polymer solution is filtered with a syringe filter (pore diameter about 0.2 μm) to avoid presence of macroscopic polymer aggregates that might lead to macro-precipitation of the solution. Afterwards, 5 mL of the filtered polymer solution is rapidly injected into 10 mL of distilled water. Solvent-water miscibility leads to a separation of

the polymer from the solvent, which leads to a precipitation into water. Since during the injection nanometric bubbles are formed, the final polymer precipitation takes place in a nanometric length scale. To allow solvent evaporation, the solution is heated at 66 ºC, during continuous stirring, for 2 hours. Finally, a stable dispersion of surfactant free polymer nanoparticles in water is obtained.

BOX 3 – THE REPRECIPITATION PROTOCOL

1. A polymer solution in THF is prepared in a 15 mL disposable glass bottle.
2. After complete dissolution, by eye inspection, the polymer solution is filtered through a syringe filter (Roth, 0.2 μm) into a new glass bottle.
3. 5 mL of the filtered solution are taken with a new syringe and rapidly injected in 10 mL of distilled water. For the water, a 50 mL glass is used.
4. The resulting emulsion is stirred for 30 minutes at room temperature and then stirred and heated at 66 ºC for 2 hours to allow complete evaporation of the solvent. The glass is covered in aluminum foil to allow homogeneous heating.
5. An emulsion of polymer nanospheres in water is obtained.

Scheme 3.3. The reprecipitation method

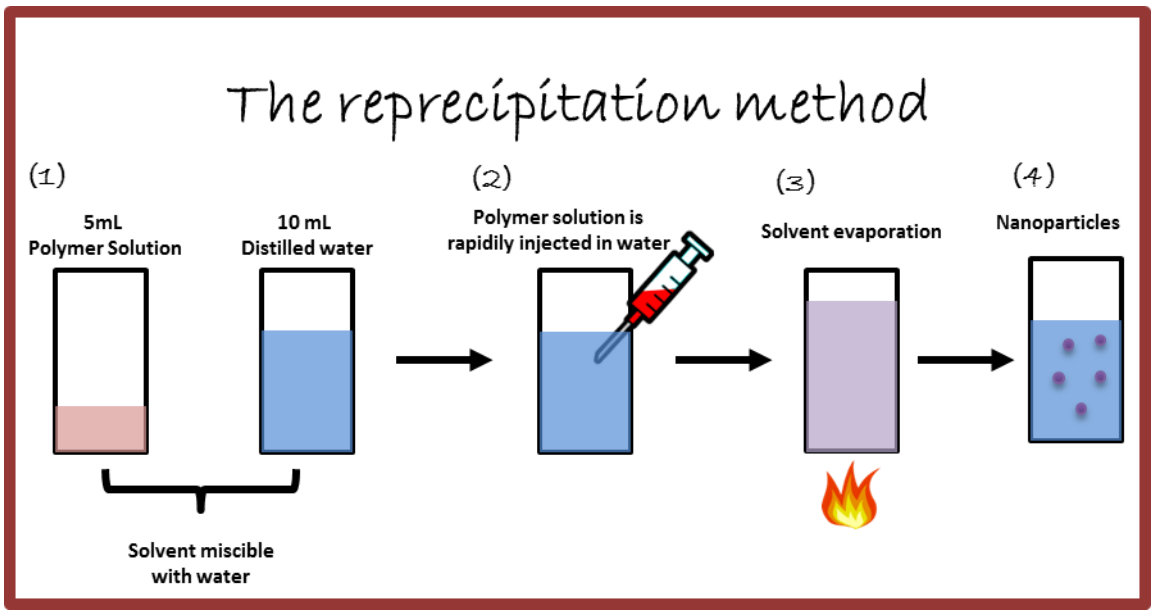

In order test the possibilities of this technique, PEMA nanospheres were prepared using THF as solvent. Two different concentrations of PEMA in THF were used independently: 10 mg/mL and 2 mg/mL. These samples are labeled as PEMA-R1 and PEMA-R2, respectively. (3x3)μm AFM height images of the resulting nanoparticles are shown in figure 3.6. Images were taken on tapping mode, using NCHV probes.

For both polymer solutions, stable dispersions of PEMA nanoparticles are obtained. In every case, particles show a spherical geometry without signs of ripening and/or coalescence. However, a dependence of mean particle diameter with solution concentration can be evidenced. From the size distribution histograms, is it seen that the higher concentration sample shows a mean diameter around 300 nm, which decreases as polymer/solvent concentration decreases. Going from 10 mg/mL down to 2 mg/mL generates a decrease of a factor 3 in the mean diameter. However, from the *Q* values calculated, the size distribution does not suffer important changes.

Table 3. 7. Characteristics of the size distribution of PEMA nanoparticles, prepared by the reprecipitation method.

Sample	Solution concentration	Size Distribution (nm)	Width of the distribution (nm)	Mean Diameter (nm)	*Q*
PEMA-R1	10 mg/mL	100 - > 600	(200 ± 40)	(300 ± 10)	0.7±0.2
PEMA-R2	2 mg/mL	60 – 150	(50 ± 30)	(100 ± 3)	0.5±0.3

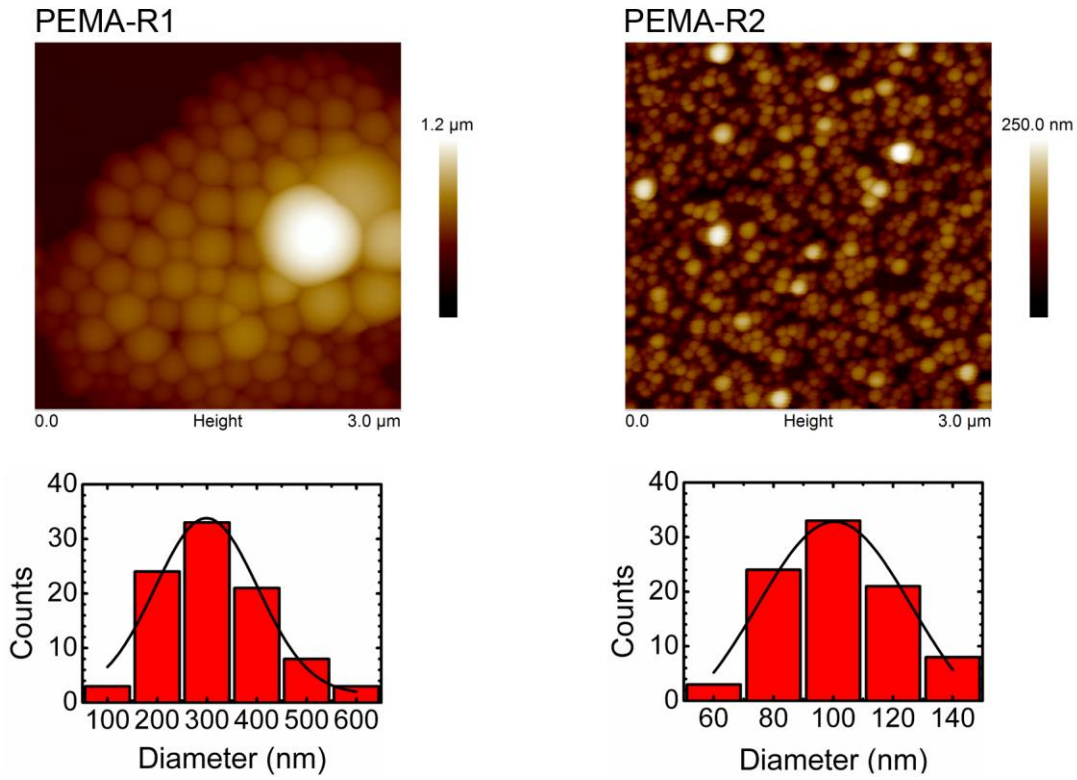

Figure 3. 6. AFM images and histograms for PEMA nanoparticles prepared by the reprecipitation method. PEMA/THF concentrations 10 mg/mL (left), and 2 mg/mL (right). Histograms represent the diameter distributions of the nanoparticles.

Once the method was proven successful, it was used to prepare nanoparticles of PDLLA. Once again, THF was used as the solvent in which three different polymer/solvent concentrations were prepared: 6 mg/mL, 3 mg/mL and 1 mg/mL. Following the nomenclature used for the PEMA nanoparticles, PDLLA samples are labeled as PLA-R1, PLA-R2 and PLA-R3, in order of decreasing concentration. Same protocol as the presented in box 3 was implemented. (3x3)µm AFM height images of spun coated Si wafers with the resulting emulsions are shown in figure 3.7. Images were taken on tapping mode using NCHV probes.

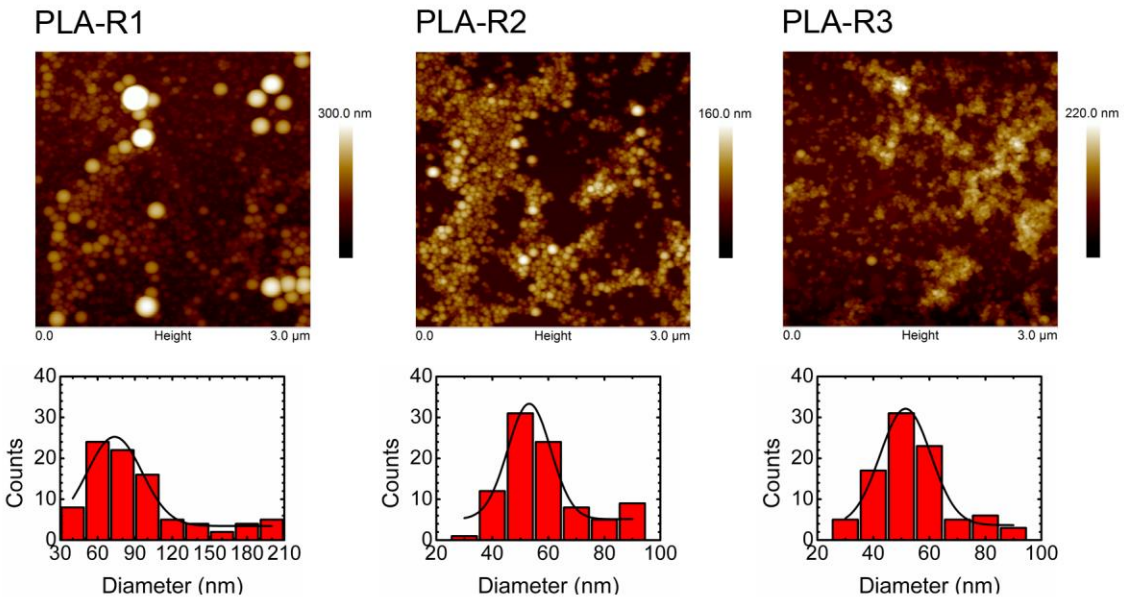

Figure 3. 7. AFM images and histograms for PLA nanoparticles by the reprecipitation method. PLA/THF concentrations 6 mg/mL (left), 3 mg/mL (center) and 1 mg/mL (right). Histograms represent the diameter distributions of the nanoparticles.

For all preparations, nanoparticles of spherical shape are found. As in the PEMA case, the nanoparticles size suffers changes as polymer/solvent concentration varies, as summarized in table 3.8. Size distribution for PLA-R1 show that the mean particle diameter is located around 74 nm with a high distribution width that goes from 30 up to 200 nm. As the concentration is reduced, not only the mean particle size is decreased but also the size distribution gets narrower, as evidenced by the changes in the *Q* values. This is the case for PLA-R2 where the concentration is reduced to half of the PLA-R1. In this case, the mean size decreased from 74 nm down to 53 nm and size distribution shortens its limits. As concentration is further decreased, as in PLA-R3 (1 mg/mL), no significant changes in size can be found. While the particles retain its spherical shape, mean diameter and distribution keep almost the same as in the PLA-R2 case.

Table 3. 8. Characteristics of the size distribution of PLA nanoparticles, prepared by the reprecipitation method.

Sample	Solution concentration	Size Distribution (nm)	Width of the distribution (nm)	Mean Diameter (nm)	*Q*
PLA-R1	6 mg/mL	30 – 200	(44 ± 6)	(74 ± 2)	0.6±0.1
PLA-R2	3 mg/mL	20 – 100	(15 ± 3)	(53 ± 3)	0.28±0.07
PLA-R3	1 mg/mL	20 – 100	(18 ± 2)	(51 ± 1)	0.35±0.04
PLA-R4 spheres	0.5 mg/mL	40 – 100	(26 ± 2)	(65 ± 1)	0.40±0.04
PLA-R4 capsules	0.5 mg/mL	40 – 150	(18 ± 2)	(83 ± 1)	0.22±0.03

Although mean diameter seems to reach a sort of plateau as concentration decreases, a more diluted concentration was also tested. In this case, 0.5 mg/mL of PLA in THF were dissolved and sample was prepared as presented in box 3. Following the nomenclature, this diluted sample was named PLA-R4. Figure 3.8 shows AFM images of the resulting nanoparticles. Figure 3.8(A) shows a (3x3)μm AFM height image of the resulting nanoparticles. This image was taken on Tapping mode, using NCHV probes. Two different geometrical shapes can be identified. First, spherical nanospheres of mean diameter about 65 nm are observed (figure 3.8(C)); however, a new geometrical structure is also present. In order to get more detail, AFM images at (1x1)μm size were taken using ultrasharp probes. As seen in figure 3.8 (B), sorts of nanocapsules can also be found. Their structure can be distinguished by height profiles, as the one presented in figure 3.8 (D). The proportion between nanospheres and nanocapsules can be calculated and it was found to be around 70/30 (spheres/capsules). Size distributions were quantified and results are shown in figure 3.8 (C), and summarized in table 3.8. From the histograms it is

seen that nanospheres present a slight lower diameter and distribution width in comparison to the nanocapsules. Moreover, comparing with the other concentrations (PLA-R1 to R3), nanospheres show a mean diameter closer to the preparation of highest concentration (PLA-R1), which allows concluding that preparation at diluted concentrations do not allow reducing size diameter but generates new structures.

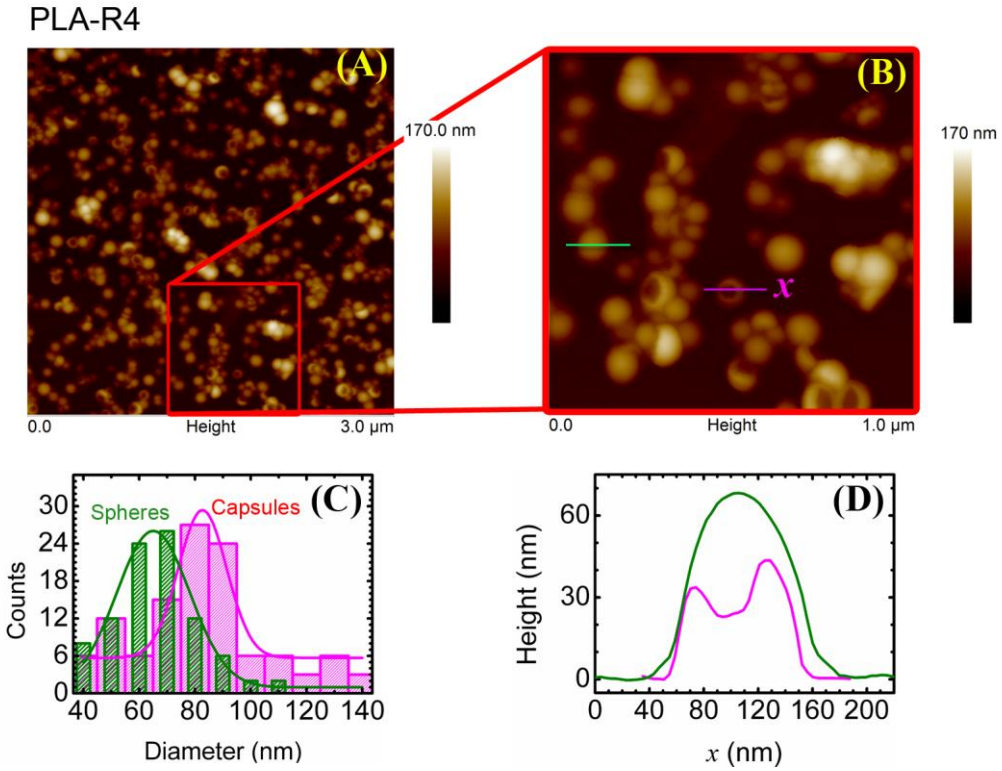

Figure 3. 8. AFM images and histograms for PLA-R4 nanoparticles by the reprecipitation method. (A) 3x3 mm AFM height image. (B) AFM zoom image (1x1 mm) of the highlighted zone presented in figure (A). (C) Size distribution histograms for nanospheres (green) and nanocapsules (magenta). (D) Section profile of the nanosphere and a nanocapsule highlighted in figure (B).

3.2.4. Beyond the reprecipitation method

As stated initially, literature has shown that the reprecipitation method is a successful technique for nanoparticle preparation of several polymers. However, in most cases the solvent used has a boiling temperature below that of the water, in order to ensure the possibility of evaporation without elimination of the dispersing medium. However, some polymers of high technological interest nowadays cannot be dissolved in

this kind of solvents. This is the case of the ferroelectric copolymer P(VDF-TrFE). In section 3.2.1, the dialysis nanoprecipitation protocol was implemented and nanospheres of this system were prepared. However, mean size above 100 nm was found, which can be limited towards proposing them as candidates for organic electronic technologies.

BOX 4 – THE REPRECIPITATION PROTOCOL. PART 2

This box describes the protocol to follow when using the reprecipitation method with a solvent which must be miscible with water, but which boiling temperature is above.

1. A polymer solution in DMA is prepared in a 15 mL disposable glass bottle.
2. After complete dissolution, by eye inspection, the polymer solution is filtered through a syringe filter (Roth, 0.2 μm) into a new glass bottle.
3. 5 mL of the filtered solution are taken with a new syringe and rapidly injected in 10 mL of distilled water. For the water, a 50 mL glass is used.
4. The resulting emulsion is immediately poured into a dialysis membrane, previously washed and rinsed with distilled water. The membrane is closed at both side using simple knots. Care must be taken to no let any air space in the membrane.
5. Afterwards the membrane is submerged in a 2 L container of distilled water. The dialysis process takes places due to the chemical difference inside and outside the membrane.
6. To overcome the chemical equilibrium, several water changes are performed during the process. The first 2 hours, 4 water changes are performed each 30 minutes. Then, 4 more water changes are performed each hour. Throughout this time, the original clear polymer solution starts becoming cloudy, sign of the polymer nanoprecipitation inside the membrane. Finally, the membrane is left stirring in distilled water overnight.

In order to obtain smaller particle sizes, we have applied the reprecipitation method. However, since P(VDF-TrFE) dissolves in DMA, which boiling point is above the one of the water, the protocol previously proposed needed to be adjusted. In general, steps 1 to 5, presented in box 3 were followed as before. In order to eliminate the solvent, without increasing the temperature up to its boiling point, immediately after injecting the polymer solution into water, the resulting polymer emulsion (water + DMA + polymer) was poured into a dialysis membrane, and submerged in water reservoir. In this case, the

solvent is eliminated by the equilibrium of the chemical potential inside and outside the dialysis membrane. After several water changes, a polymer emulsion in water was obtained. The details of the protocol are highlighted in box 4 and scheme 3.4.

Scheme 3.4. The reprecipitation method part 2

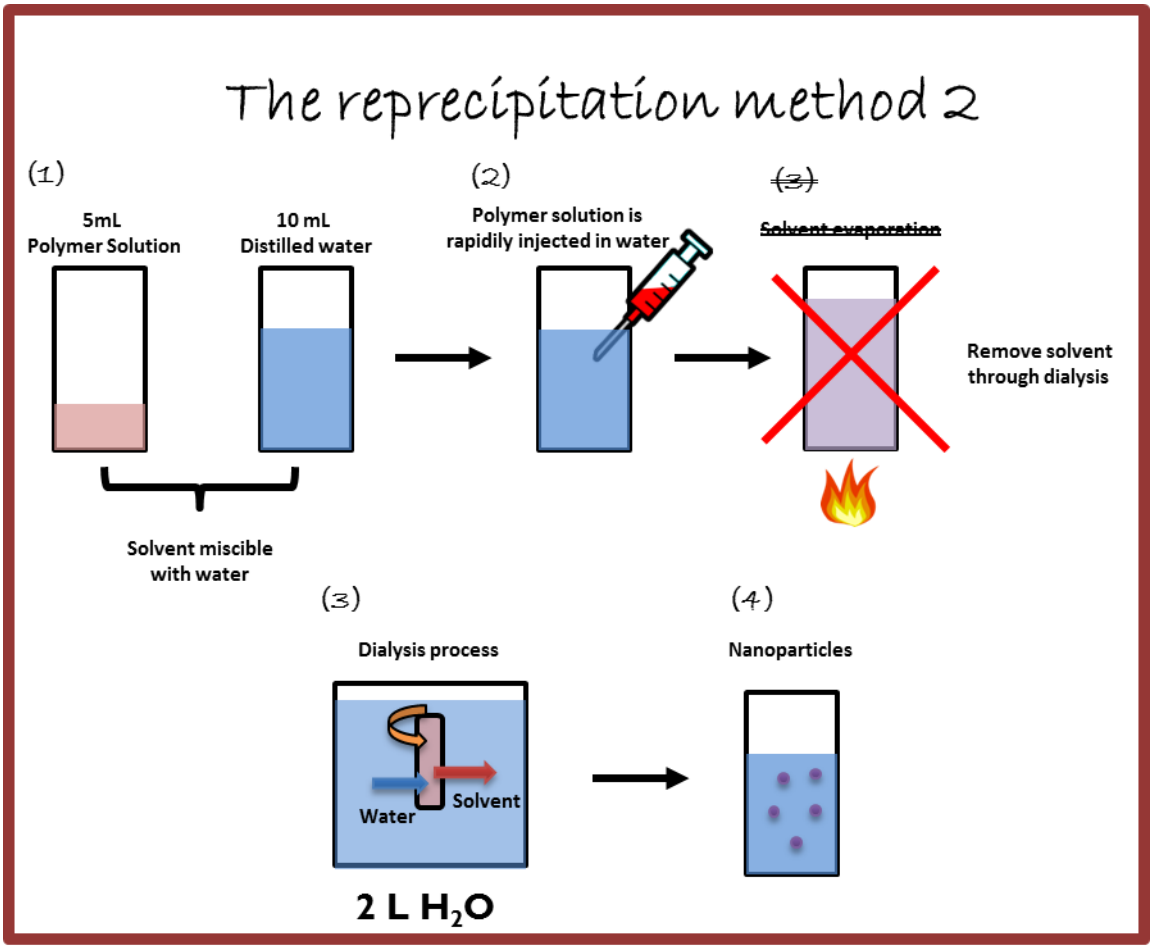

P(VDF-TrFE) at a molar concentration of 76:24 (VDF:TrFE) was used in this case. A polymer solution in DMA was prepared at a concentration of 1 mg/mL. A (3x3)µm AFM height image (tapping, NCHV) of the resulting emulsion is presented in figure 3.9. A stable dispersion of polymer particles can be found via the AFM image. The dispersion consists of nanoparticles of spherical shape. No ripening or coalescence effects seem to be present. Size distribution histogram shows that nanoparticles present a mean

diameter of (88 ± 1) nm, with a distribution width of (30 ± 10) nm (Q = 0.3±0.1). Comparing with the results of the nanoprecipitation method (section 3.2.1) a reduction of the mean diameter of the particles of a factor 3 and an improvement in the quality factor was achieved.

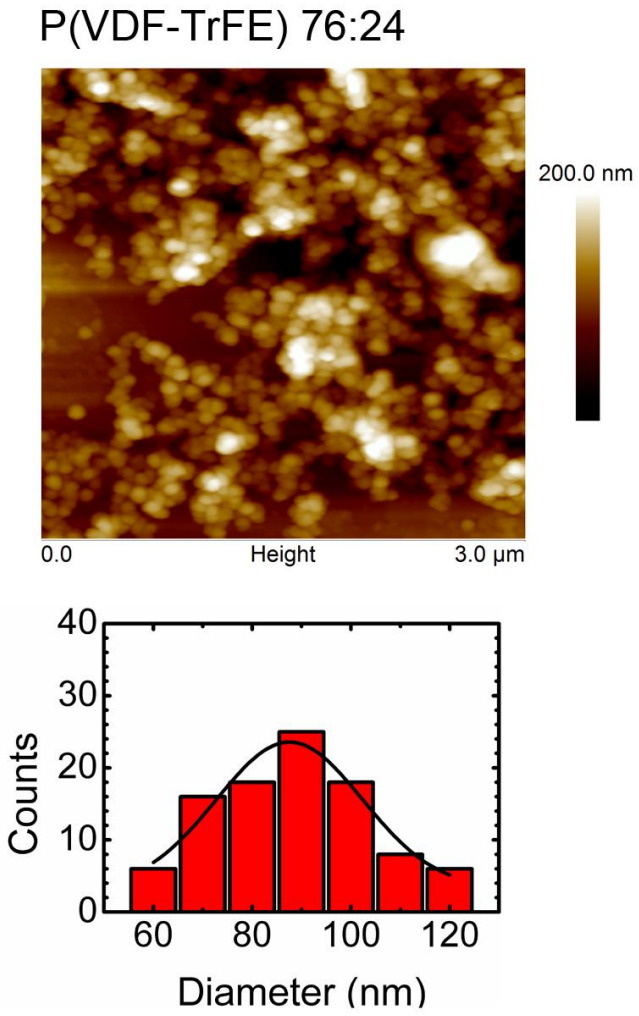

Figure 3. 9. (Up) AFM image and (down) histogram for P(VDF-TrFE) nanoparticles by the reprecipitation method part 2. AFM image size is 3x3 µm.

Results gathered for the reprecipitation method, for all polymers shown, have been summarized in figure 3.10. This figure shows a plot of the mean diameter obtained, as a function of the initial polymer/solvent concentration. Error bars are related to the width of

the size distribution. First, as evidenced for all polymer preparations, as the solvent/polymer concentration increases, the resulting mean diameter increases. At low concentrations, the mean diameter of the polymer particles does not change much, reaching a sort of plateau.

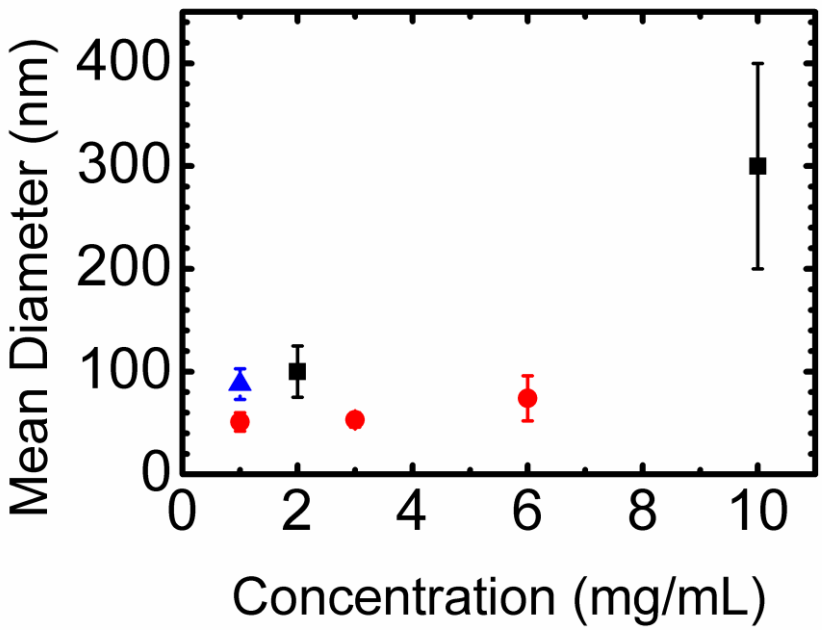

Figure 3. 10. Mean diameter size of nanoparticles prepared by the reprecipitation method, as a function of the original polymer/solvent concentration, for PEMA (■), PDLLA (●) and P(VDF-TrFE) (▲).

3.2.5. Limitations of the reprecipitation method

The main factor to be considered when preparing nanoparticles via this method is the miscibility between solvent and water. Good miscibility must be expected. Tests performed with immiscible solvent/water mixtures (for example chloroform/water) showed a macroscopically precipitation of the polymer. Also, it must be taken into consideration the solubility of the polymer in the solvent/water mixture. If the solvent dissolves well the polymer, there might be a chance that although diluted with water it could still possibly interact with the polymer chains. This conclusion was achieved when

trying to prepare PBAC nanoparticles via the reprecipitation method (following box 3). We found that following the protocol that worked well for PEMA and PDLLA, PBAC always resulted in a macroscopically precipitate. In order to further understand the issue, solubility tests were performed on all these amorphous polymers. A 1:2 proportion of solvent:water was prepared and pellets of the bulk polymers were tried to dissolve, following a 1 mg/mL of polymer/solvent concentration. Although PEMA and PDLLA did not dissolved, as expected from the previous results of nanoparticle preparation, it was possible to dissolve the PBAC. Lower solvent:water proportions were tested (1:3 and 1:5) and still the PBAC was dissolved.

The readily protocol available for preparing nanoparticles via the reprecipitation method, allowed testing its limits by using an immiscible blend of PPS and PPA, previously discussed in the miniemulsion method. A 50-50 blend (wt%) was dissolved in THF at a 1 mg/mL concentration and rapidly injected in water, following the 1-5 steps in box 3. However, evaporation of the THF was performed at room temperature during continuous stirring for several hours. The main idea was to keep temperature as low as possible so the polymer blend remained below its melting temperature and thus coalescence and ripening effects could be avoided. After solvent was gone, a fraction of the polymer was macroscopically precipitated and removed with tweezers from the water. However, the resulting liquid showed the grayish color, usually found when nanoparticles are present. In order to evaluate the resulting emulsion, Si wafers were spun coated and (3x3)μm AFM height images were taken and shown in figure 3.11.

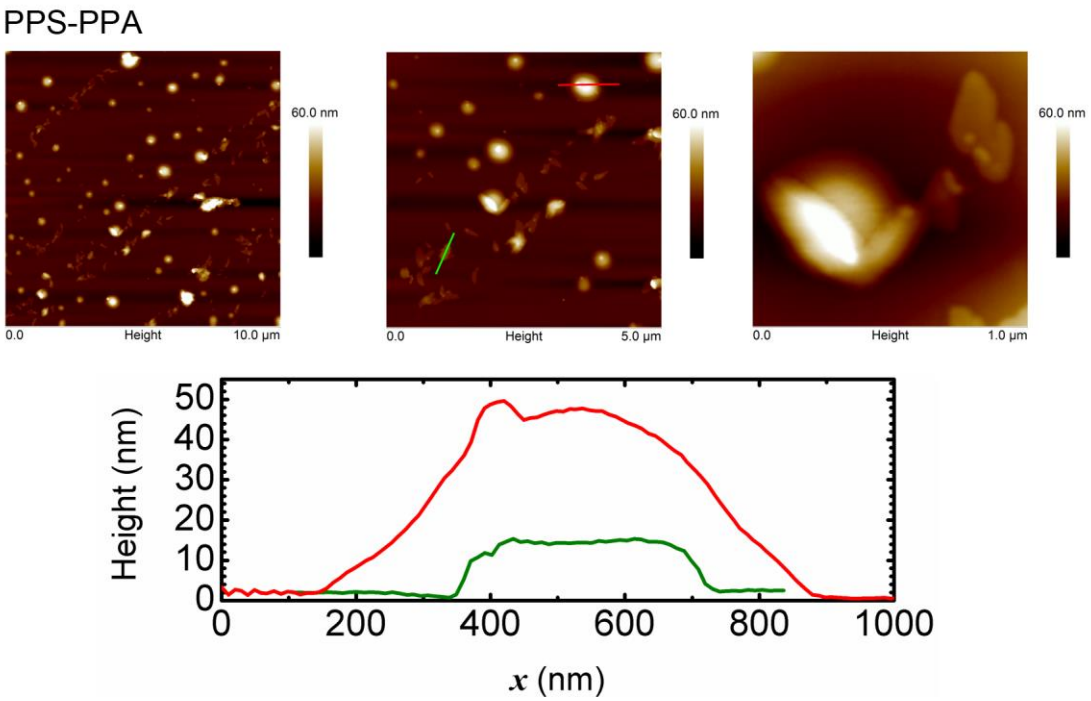

Figure 3. 11. (Up) AFM images of PPS-PPA nanoparticles prepared via the reprecipitation method. Images sizes, from left to right 10x10 µm, 5x5 µm, 1x1 µm. (Down) Height profile of a round shaped nanoparticle (red) and an anisotropic particle (green).

Two families of particles are found as a result of the preparation method. First, round shaped particles can be distinguished from the AFM images. These particles are not spherical since there are big differences between their diameters (d) and heights (h), such that the distributions follow: d = 100 – 600 nm, and h = 6 – 60 nm. An example of a height profile of one of these particles is shown in figure 3.11 (down, red line). Also, round shape particles show that in several cases, different structures are found inside them. As seen in the 1x1 µm AFM image in figure 3.11, the particle shows two sorts of walls coming out of one of its edges. These walls resemble the edge-on type of crystalline structures, previously reported for thin films of these systems in the literature[25]. On the other hand, anisotropic particles with lengths = 100 – 500 nm, and heights = 6 – 20 nm are also found in the AFM images. Their section profile (figure 3.11, green line) shows that these particles are almost flat at their tops, resembling flat-on crystals observed in thin films[14]. The possibility of existence of *nano*-crystalline structures in these particles

can be understood in the following way. Although PPS and PPA have glass transition temperatures well below room temperature, is their crystalline structure what allows them to remain in a mechanical stable state up to 45 ºC. As solvent was slowly evaporated from the emulsion, polymer chains had enough time and mobility to partially organize, allowing the structures to remain stable, avoiding coalescence. Although the final particles are not completely spherical, the formation of possible *nano*-crystals, could be of interest towards understanding the organization of polymer chains under confinement.

Polymer structures confined in thin films

3.4 Polymer thin films

Polymer thin films are bi-dimensional structures that consist of stable films in a thickness range that goes from 100 nm down to a few nanometers. Several techniques have been proposed to prepare these structures, such as Physical Vapor Deposition[26, 27], Laser Ablation[28], Pulsed Laser Deposition[29], Matrix Assisted Pulsed Laser Evaporation[30, 31] and Spin Casting. This last technique is the one used through the development of this work and will be further discussed. In spin casting, also known as spin coating, a polymer solution is poured on top of a substrate, which can be a Si wafer, an ITO substrate, a glass slide, etc, until a meniscus that covers the entire area is formed. Afterwards, the substrate is spun at a certain speed for a couple of minutes. During the spinning, the polymer solvent quickly evaporates, and thin polymer films are obtained. The physical process of rapid solvent evaporation by spin coating and its consequences on the organization of the polymer chains have been widely discussed by de Gennes[32, 33]. Final thickness depends on two factors, speed of rotation and polymer concentration. Fixing the speed of rotation, it is possible to play with polymer concentration to obtain a variety of thicknesses. Also,

an advantage of this technique is that one departs from a bulk polymer of known molecular weight and chemical structure that does not suffer any changes in those parameters during the coating process.

During this work, polymer thin films have been prepared at the facilities of the IEM-CSIC, as well as in ULB and at KUL. However, in every place the same protocol was followed and it is highlighted in box 5 and scheme 3.5. Figure 3.12 shows (3x3)μm AFM images of polymer thin films prepared by the protocol just described. AFM images were taken under a tapping protocol using NCHV probes. Three different polymers have been chosen as examples to be presented in this section. Discussion about the physical implications of these materials confined in thin films will be discussed in chapter6. Figure 3.12 left, shows an AFM height image of a PBAC thin film (thickness $h \approx 300$ nm, as revealed by AFM). Almost no topographic features can be seen in the AFM image, which is the typical result when dealing with films of amorphous polymers. On the other hand, center and right panels of figure 3.12, show the results obtained for the semi-crystalline polymers P(VDF-TrFE) ($h \approx 100$ nm, as revealed by AFM) and PDLLA ($h \approx 300$ nm, as revealed by AFM), respectively. In these two cases, several topographic features can be elucidated. These types of materials are called **supported polymer films**. These are polymer films with thicknesses around and below 10^2 nm, in which one side is physically attached to a surface while the top surface remains free

BOX 5 – SPIN COATING OF POLYMER THIN FILMS

1. A polymer solution is prepared in a 15 mL disposable glass bottle.

2. After complete dissolution, by eye inspection, the polymer solution is filtered through a syringe filter into a new glass bottle.

3. Substrates, on which the polymers will be deposited, are cleaned in acetone and afterwards in isopropanol. Finally substrates are dried under nitrogen flow.

4. A piece of the substrate is fixed on top of the coating machine. A further cleaning procedure is performed, in which a drop of the polymer solvent is spin coated into the substrate, to avoid possible presence of contaminants.

5. A drop of polymer solution is poured on top of the substrate. Size of the drop depends on the size of the substrate; however, the important factor is that the drop covers completely the substrate.

6. Immediately after pouring the drop, rotation must start. In this work we have used a rotation speed of 3000 rpm, for 2 minutes. It is important noticing that if one does not starts the rotation immediately after pouring the drop, solvent evaporation will take place and undesirable effects might appear.

7. Once the time has finished, the machine is stopped and the coated substrate is removed. A polymer thin film supported on a substrate is obtained.

Scheme 3.5. Spin Coating

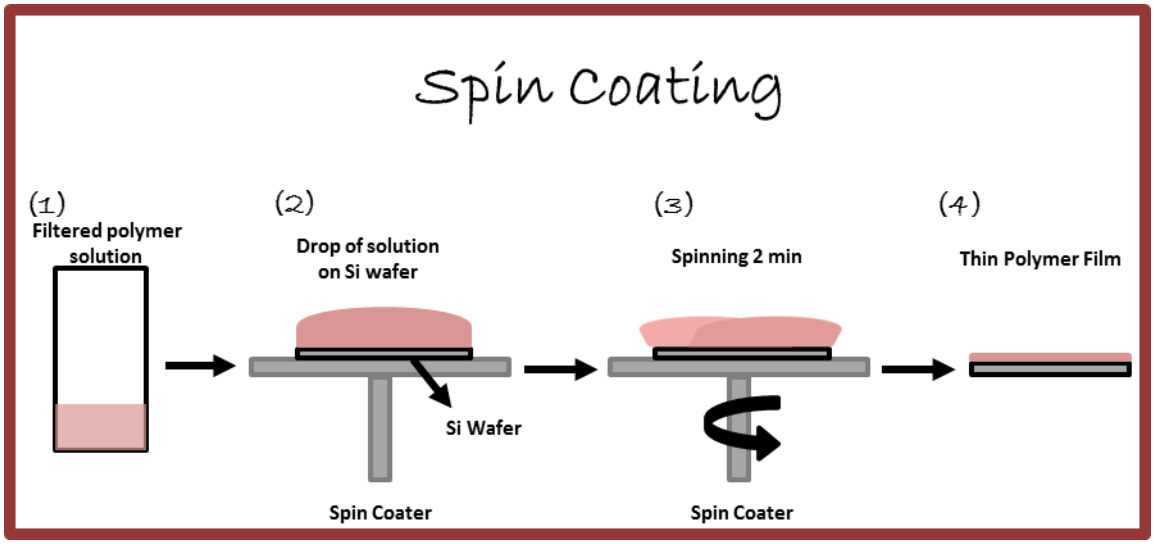

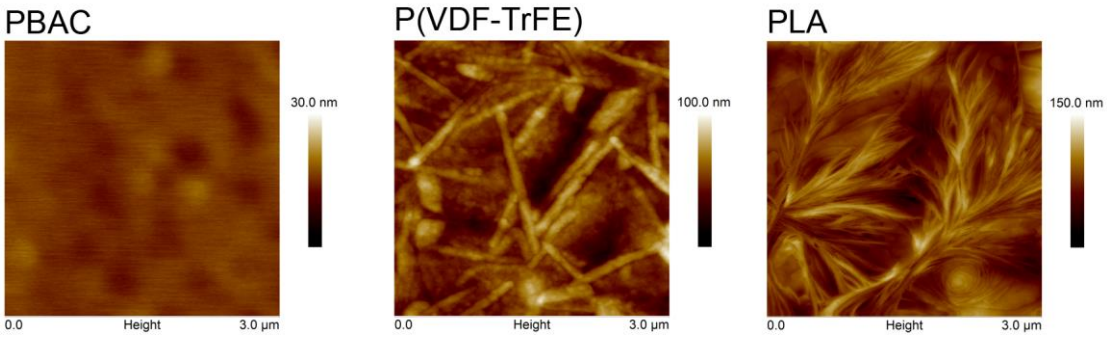

Figure 3. 12. AFM height images of PBAC (left), P(VDF-TrFE) (center) and PLA (right).

Another possibility can be the preparation of **capped polymer films**. In capped thin films the polymer is stacked between to adsorbing walls, as in a *sandwich* structure. Capping polymer films between conductive layers, allows measurement of the current flow generated upon application of an AC electric field, perpendicular to the surface, allowing the study of polymer dynamics via broadband dielectric spectroscopy (BDS). The preparation of capped films for BDS is described in the following lines. First, square glass substrates of about (4x4) cm^2 and thickness around 0.3 cm are cleaned in a solution of water and detergent. Afterwards glass substrates are rinsed in acetone and 2-propanol and dried with a nitrogen flow. An aluminum layer (1.5x4) cm^2 is evaporated on top of the glass substrates. The thickness of this layer is about 60 nm (controlled via a quartz microbalance) and it serves as the bottom electrode for dielectric measurements. After evaporation, the samples are taken out of the evaporator in order to deposit the polymer thin films by spin coating on top of the whole substrate. Thickness of the films was controlled by the polymer-solvent concentration. Since the spin coating procedure covers the entire glass substrate, the non-aluminized zones were carefully cleaned using the same solvent. Once spin coating was completed, samples were annealed at the boiling temperature of the solvent for 30 minutes, to allow possible solvent residues to evaporate. Finally, another layer of aluminum was evaporated on top of the polymer film. In this case, 5 aluminum strips were evaporated such that a part of the strip lied on top of the

polymer while the rest on top of the glass. This allowed preparing 5 top electrodes for measurements. Scheme 3.6 shows the process.

Scheme 3.6. Capped Polymer Films

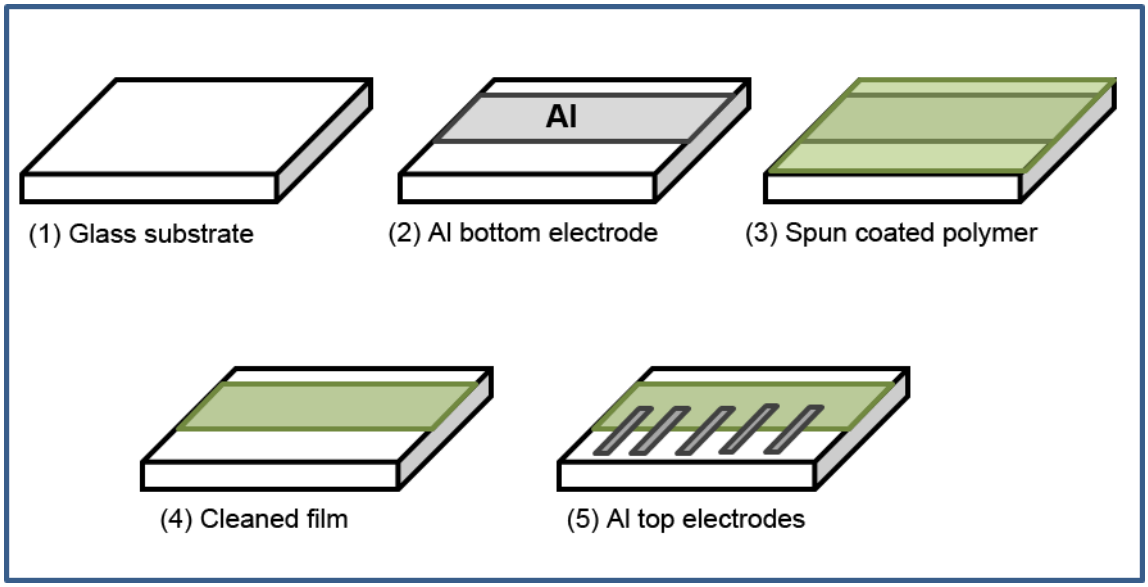

3.5 Nanoimprint Lithography

Nanoimprint lithography (NIL) is an emerging nanopatterning method, combining nanometer-scale resolution and high throughput. In a top-down approach, a rigid stamp with a surface relief, generally fabricated by electron beam lithography is pressed into a thin film of soft material, for example a polymer. The film is hardened before the stamp is retrieved, and the surface relief is copied into the thin film[34-36]. A pattern with nano- to micrometer scale features can be replicated in a parallel process, and the stamp may be reused many times. This makes nanoimprint lithography a promising technique for volume manufacturing of nanostructured components. At present, structures with feature sizes down to 5 nm have been prepared, and the resolution is limited by the ability to manufacture the stamp relief[34, 37]. For historical reasons, the term nanoimprint lithography refers to a hot embossing process, where a thin film of thermoplastic material is softened

by heating it, and the embossed film is hardened again when it is cooled down.

In a collaboration with IMB-CSIC, we have prepared nanogratings on thin films of P(VDF-TrFE), by nanoimprint lithography. A sketch of the process is presented in scheme 3.7 and described in the following parragraph. The selected molar concentration of the copolymer was 76:24. In order to prepare nanostructures via NIL, one must start from a polymer thin film, which was prepared following a similar protocol as the highlighted in box 5, previous section. P(VDF-TrFE) was dissolved in DMA at a concentration of 40 g/L. A fixed amount of 0.1 ml of polymer solution was deposited by a syringe on a rectangular (2 x 2 cm^2) silicon substrate. An initial acceleration was applied for 4 s in order to reach a rotational speed of 4800 rpm. This final speed was kept for 2 min. Polymer films of thickness about (100 ± 5) nm, as measured by AFM, are typically obtained under these conditions. We performed NIL at a constant molding temperature and pressure using a thermal nanoimprint machine (by Obducat). Silicon stamps were prepared by electron beam lithography, metal deposition lift-off, and reactive ion etching. The nanostructured array on the stamp covers an area of (1.5 x 1.5 mm^2). The resulting height of the lines was (135 ± 5 nm), as determined by AFM (Tapping mode, NCHV probes).

The arrays of lines and trenches were fabricated on mesa-type silicon stamps to facilitate the imprinting process[36]. The area of the mesa is 2 x 2 mm^2 and about 400 nm of height and it was defined by means of optical lithography and wet silicon etching. To facilitate stamp separation after embossing, stamps were coated with a monolayer of perfluorodecyltrichlorosilane deposited from the gas phase. During the imprint process, first, the silicon stamp and the polymer coating were heated up to 180 ºC without

applying pressure until reaching a steady temperature. Subsequently, the polymer film was nanostructured by applying a pressure of 4053 kPa extruding the softened polymer material to fill the nanocavities in the stamp. Temperature and pressure were kept fixed for 5 min. After this step, the system was cooled down to 50 ºC, keeping the applied pressure. After removing the pressure, the system was allowed to gradually cool down to room temperature and then the polymer nanostructures were self-detached from the silicon master stamp.

Scheme 3.7. Nanoimprint Lithography

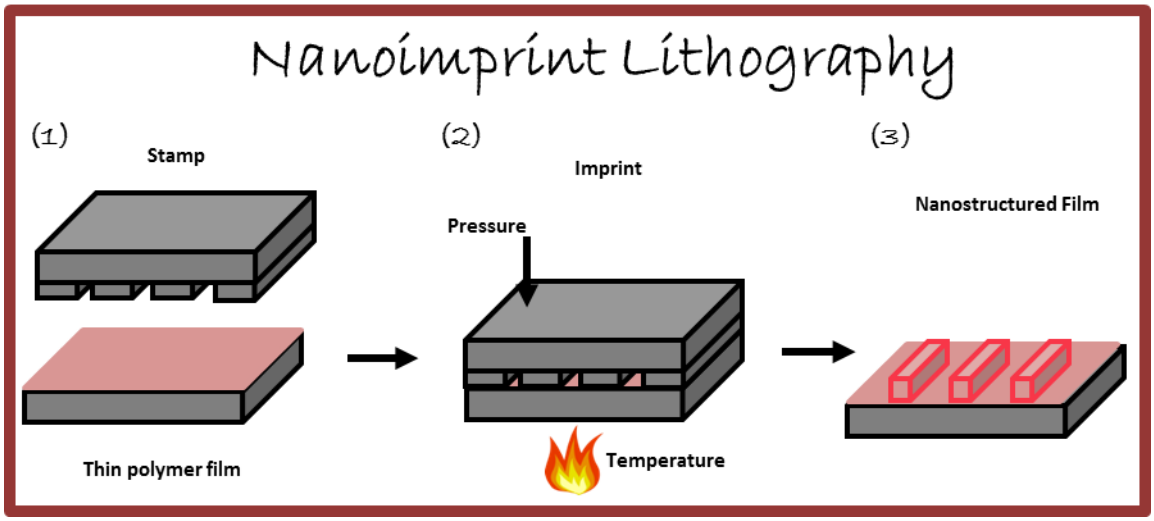

Figure 3.13 shows a (3x3)μm AFM height image of the nanoimprinted structures. A height profile in a direction perpendicular to that of the imprinted lines is also shown. The topography of the polymer film, before NIL, is the one found in figure 3.12 center. AFM height image of the nanoimprinted film shows a series of nanogratings. Almost no defects, such as discontinuous lines, can be seen. The final imprinted structures have a height of about (130 ± 10) nm, quite similar to the original stamp and a pitch (line-to-line of about (210 ± 10) nm, as seen in the profile image. Comparing the original thin film (figure 3.12 center) with the nanoimprinted one (3.13 left) it is possible to see that the needle-like crystals are no longer seen in after the NIL process. As previously proposed in

the literature, confinement imposed by nanoimprint lithography might be able to alter the molecular structures of the original thin films[38, 39]. These details as well as the limitations of the NIL protocol will be further discussed in chapter 7.

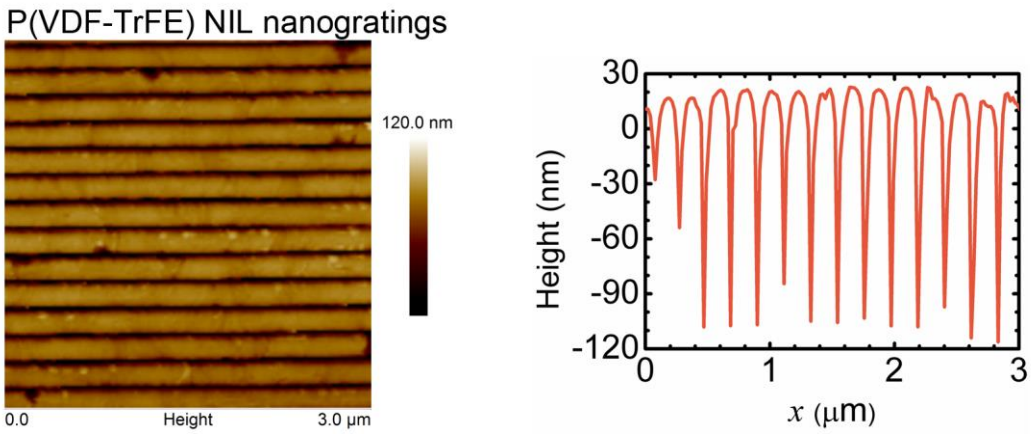

Figure 3. 13. (Left) AFM height image of nanogratings obtained by NIL on a P(VDF-TrFE) thin film. (Right) Height profile of the nanogratings in a direction perpendicular to the lines.

3.6. Summary

Throughout this chapter, we have presented the protocols to prepare confined polymer nanostructures. In the first section, 3D confined polymer nanoparticles were prepared following a variety of methods. We have optimized the protocols to obtain sub-100nm particles. This size threshold is of great interest towards the study of polymer physics under confinement and technological applications, as will be shown in the following chapters. On the other hand, second part of the chapter showed the possibilities of preparing confined polymer structures into thin film geometries. The spin casting technique was discussed and some examples were presented that will be further used in the following chapters. Finally, nanoimprint lithography is presented as a technique for nanostructuring polymer thin films. Wide technological applications of NIL structured samples are found nowadays and will be discussed in chapter 7.

3.6. References

1. Landfester, K. *Advanced Materials* **2001,** 13, (10), 765-768.
2. Kietzke, T.; Neher, D.; Kumke, M.; Ghazy, O.; Ziener, U.; Landfester, K. *Small* **2007,** 3, (6), 1041-1048.
3. Landfester, K. *Angewandte Chemie International Edition* **2009,** 48, (25), 4488-4507.
4. Zhang, C.; Guo, Y.; Priestley, R. D. *Macromolecules* **2011,** 44, (10), 4001-4006.
5. Staff, R. H.; Rupper, P.; Lieberwirth, I.; Landfester, K.; Crespy, D. *Soft Matter* **2011,** 7, (21), 10219-10226.
6. Staff, R. H.; Lieberwirth, I.; Landfester, K.; Crespy, D. *Macromolecular Chemistry and Physics* **2012,** 213, (3), 351-358.
7. Ulum, S.; Holmes, N.; Darwis, D.; Burke, K.; David Kilcoyne, A. L.; Zhou, X.; Belcher, W.; Dastoor, P. *Solar Energy Materials and Solar Cells* **2013,** 110, (0), 43-48.
8. Landfester, K.; Montenegro, R.; Scherf, U.; Güntner, R.; Asawapirom, U.; Patil, S.; Neher, D.; Kietzke, T. *Advanced Materials* **2002,** 14, (9), 651-655.
9. Nagarjuna, G.; Baghgar, M.; Labastide, J. A.; Algaier, D. D.; Barnes, M. D.; Venkataraman, D. *ACS Nano* **2012,** 6, (12), 10750-10758.
10. Bag, M.; Gehan, T. S.; Algaier, D. D.; Liu, F.; Nagarjuna, G.; Lahti, P. M.; Russell, T. P.; Venkataraman, D. *Advanced Materials* **2013,** 25, (44), 6411-6415.
11. Lee, Y.-b.; Lee, S. H.; Kim, K.; Lee, J. W.; Han, K.-Y.; Kim, J.; Joo, J. *Journal of Materials Chemistry* **2012,** 22, (6), 2485-2490.
12. Mens, R.; Chambon, S.; Bertho, S.; Reggers, G.; Ruttens, B.; D'Haen, J.; Manca, J.; Carleer, R.; Vanderzande, D.; Adriaensens, P. *Magnetic Resonance in Chemistry* **2011,** 49, (5), 242-247.
13. Soccio, M.; Lotti, N.; Finelli, L.; Gazzano, M.; Munari, A. *European Polymer Journal* **2009,** 45, (11), 3236-3248.
14. Rueda, D. R.; Hernández, J. J.; García-Gutiérrez, M. C.; Ezquerra, T. A.; Soccio, M.; Lotti, N.; Munari, A.; Perlich, J.; Serna, R. *Langmuir* **2010,** 26, (22), 17540-17545.
15. Wipf, R.; Jaksch, S.; Stühn, B. *Colloid Polym Sci* **2010,** 288, (5), 589-601.
16. Leo, E.; Brina, B.; Forni, F.; Vandelli, M. A. *International Journal of Pharmaceutics* **2004,** 278, (1), 133-141.
17. Legrand, P.; Lesieur, S.; Bochot, A.; Gref, R.; Raatjes, W.; Barratt, G.; Vauthier, C. *International Journal of Pharmaceutics* **2007,** 344, (1–2), 33-43.
18. Lince, F.; Marchisio, D. L.; Barresi, A. A. *Journal of Colloid and Interface Science* **2008,** 322, (2), 505-515.
19. Hornig, S.; Heinze, T.; Becer, C. R.; Schubert, U. S. *Journal of Materials Chemistry* **2009,** 19, (23), 3838-3840.
20. Aubry, J.; Ganachaud, F.; Cohen Addad, J.-P.; Cabane, B. *Langmuir* **2009,** 25, (4), 1970-1979.
21. Shimizu, H.; Yamada, M.; Wada, R.; Okabe, M. *Polym. J* **2007,** 40, (1), 33-36.
22. Hu, Z.; Gesquiere, A. J. *Chemical Physics Letters* **2009,** 476, (1–3), 51-55.
23. Clafton, S. N.; Huang, D. M.; Massey, W. R.; Kee, T. W. *The Journal of Physical Chemistry B* **2013,** 117, (16), 4626-4633.
24. Zhang, C.; Chung, J. W.; Priestley, R. D. *Macromolecular Rapid Communications* **2012,** 33, (20), 1798-1803.
25. Hernández, J. J.; Rueda, D. R.; García-Gutiérrez, M. C.; Nogales, A.; Ezquerra, T. A.; Soccio, M.; Lotti, N.; Munari, A. *Langmuir* **2010,** 26, (13), 10731-10737.
26. Usui, H. In *Formation of polymer thin films and interface control by physical vapor deposition*, 2009; 2009.
27. Usui, H., Preparation of Polymer Thin Films by Physical Vapor Deposition. In *Functional Polymer Films*, Wiley-VCH Verlag GmbH & Co. KGaA: 2011; pp 287-318.
28. Blanchet, G. B.; Fincher, C. R.; Jackson, C. L.; Shah, S. I.; Gardner, K. H. *Science* **1993,** 262, (5134), 719-721.
29. Rebollar, E.; Mm, V.; Gaspard, S.; Oujja, M.; Corrales, T.; Georgiou, S.; Domingo, C.; Bosch, P.; Castillejo, M. *Journal of Physics: Conference Series* **2007,** 59, (1), 305.
30. Caricato, A. P.; Luches, A.; Leggieri, G.; Martino, M.; Rella, R. *Vacuum* **2012,** 86, (6), 661-666.
31. Shepard, K. B.; Priestley, R. D. *Macromolecular Chemistry and Physics* **2013,** 214, (8), 862-872.
32. Reiter, G.; de Gennes, P. G. *European Physical Journal E* **2001,** 6, 25-28.
33. de Gennes, P. G. *European Physical Journal E* **2002,** 7, 31-34.
34. Schift, H., Nanoimprint Lithography. In *Springer Handbook of Nanotechnology*, Bhushan, B., Ed. Springer Berlin Heildelberg: 2007.
35. Guo, L. J. *Advanced Materials* **2007,** 19, (4), 495-513.
36. Rueda, D. R.; Martin-Fabiani, I.; Soccio, M.; Alayo, N.; Perez-Murano, F.; Rebollar, E.; Garcia-Gutierrez, M. C.; Castillejo, M.; Ezquerra, T. A. *Journal of Applied Crystallography* **2012,** 45, (5), 1038-1045.
37. Schift, H. *Journal of Vacuum Science & Technology B* **2008,** 26, (2), 458-480.
38. Hu, Z.; Tian, M.; Nysten, B.; Jonas, A. M. *Nat Mater* **2009,** 8, (1), 62-67.
39. Kassa, H. G.; Cai, R.; Marrani, A.; Nysten, B.; Hu, Z.; Jonas, A. M. *Macromolecules* **2013,** 46, (21), 8569-8579.

CHAPTER 4 – On the preparation of nanoparticles by laser ablation.

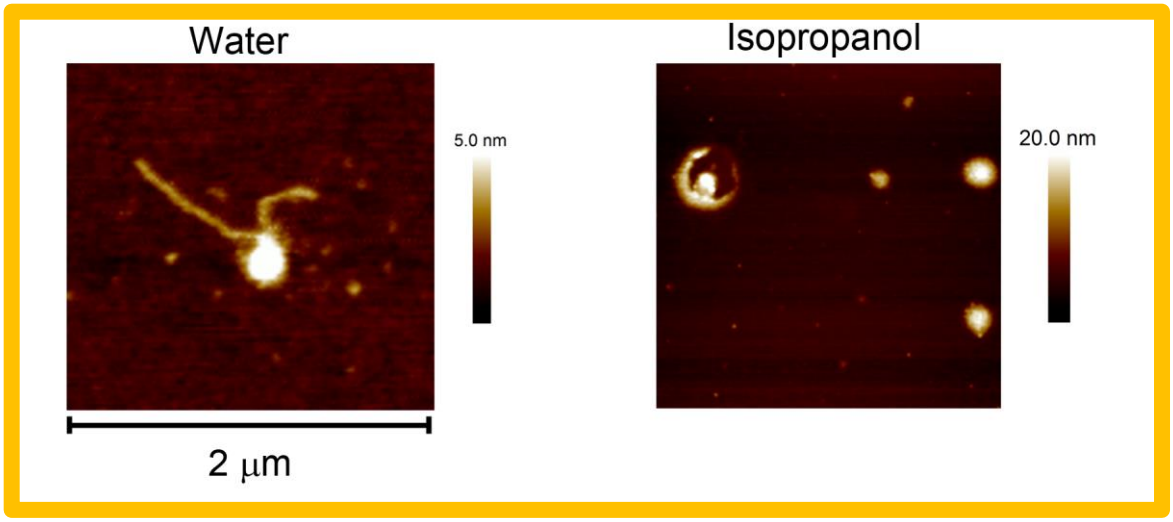

(2x2)μm^2 AFM topography images of nanostructures prepared by laser ablation in liquids.

Pulsed Laser Ablation in Liquids (PLAL) was used to prepare nanoparticles. A poly(bisphenol A carbonate) polymer sample was used as target. Using water as liquid, a transition between nanospheres and nanoparticle/strands is evidenced as a function of fluence. For other five liquids, the procedure was repeated. It was seen that the morphology of the nanostructures was dependent on the liquid medium. Details on the future work to be performed is also presented at the end of the chapter.

4. 1. Introduction

The last few years have witnessed the emergence of a new family of nanofabrication techniques with specific capabilities based in the use of lasers[1]. Laser irradiation techniques, such as laser induced periodic surface structuring (LIPSS)[2, 3], laser induced forward transfer (LIFT)[4], matrix-assisted pulsed laser evaporation (MAPLE)[5], among several others, are widely used for nanopatterning and/or nanofabrication of soft matter. An interesting point of research is the way polymer chains arrange after the interaction with the laser beam. For example, it has been shown that during a MAPLE deposition of poly(methyl methacrylate), the resulting surface consisted in an agglomeration of *nanoglobules*. These nanostructures showed an increased T_g in comparison to a bulk sample, that was explained by arguing a change in the density of the system.

Also, laser techniques have been used for the preparation of nanoparticles. For example, platinum nanoparticles have been prepared by laser ablation in aqueous solutions[6]. This technique is called pulsed laser ablation of solids in liquid environments (PLAL). Nanoparticles of polymer materials have been also prepared by this technique, as reported by Lazare and collaborators. These authors have prepared organic nanoparticles of several polymer such as poly(ethylene terephthalate) (PET), poly(carbonate) (PBAC), poly(imide) (PI) and poly(styrene) (PS)[7-9] by PLAL in water. Throughout their research, authors have shown that after ablation, a suspension of nanoparticles in water can be obtained with mean diameters well below 50 nm. However, several analyses show that the nanoparticles are rich in carboxylic groups and carbon. This result can be expected since depending on the fluence of the laser beam, preparation of polymer nanostructures via laser interactions can damage the final state of the material. Previously it has been

also observed that polymer films prepared by pulsed laser deposition (PLD) have shown a decrease in their molecular weights[10, 11].

In this chapter, we present the preparation of nanoparticles by PLAL. Several conditions, such as laser fluence and influence of liquid mediums have been explored. The work here described was performed through collaboration between our research group at IEM-CSIC and the LANAMAP group at the IQFR-CSIC.

4.2. Materials and techniques

Materials

Experiments of PLAL were carried out in poly(bisphenol A carbonate). PBAC targets for ablation were prepared as explained in chapter 2. Several liquid mediums were used during the PLAL experiments. The most important physicochemical characteristics of the liquids are summarized in table 4.1. Another important parameter, not listed in table 4.1, is the absorbance of the liquids at the laser wavelength (λ = 266 nm) used in the PLAL experiments. Since the laser beam has to go through the liquid mediums to reach the sample, it is desirable to know whether energy is lost in the path. Figure 4.1 shows the ultraviolet (UV) absorbance spectra of the liquids. Data were acquired by a double-beam spectrophotometer (Shimadzu UV-3600) using a 10 mm optical path quartz cuvette.

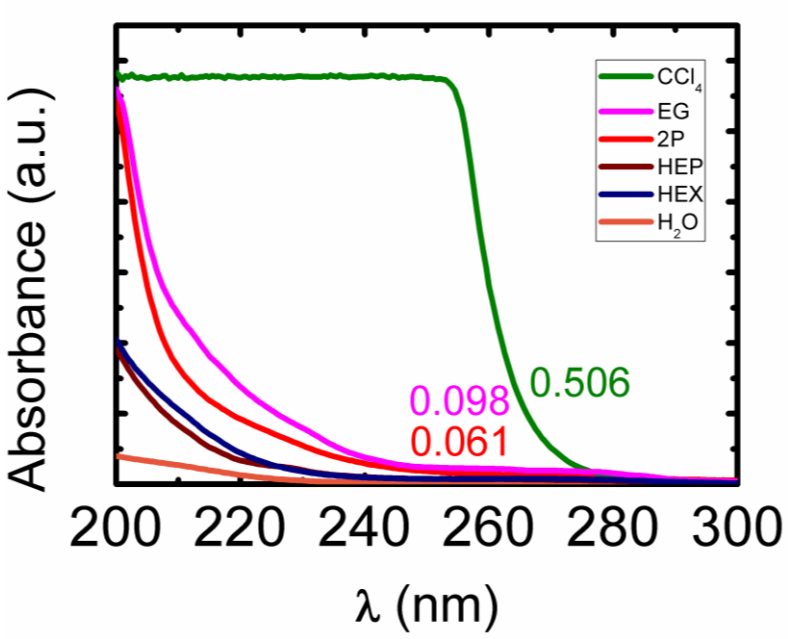

Figure 4.1. Optical absorption spectra of the different liquid mediums used in the PLAL experiments.

At λ = 266 nm, H_2O, HEP and HEX shows no absorbance, while the 2P and EG signal slightly deviates from zero. The only case where UV absorption could be important is in the CCl_4. Care must be taken into consideration when analysing the results for this medium.

The obtained suspensions were analysed by AFM (tapping mode, NCHV probes). For any case, 20 μL of the resulting suspension was drop-casted on a regular Si wafer. Deposition was left drying for 20 hours at ambient conditions, except for the case of ethylene glycol. For this specific liquid, the casted Si wafer was dried under vacuum, at 30 ºC.

Table 4.1. Liquid mediums used for the PLAL experiments. Density, thermal conductivity and viscosity are the measured values at room temperature.

Liquid	Density[12] (g/cm^3)	Boiling Point[12] (°C)	Thermal conductivity[13] (W/m K)	Viscosity[14] (g/m s)	PBAC Solubility
Distilled Water (H_2O)	1	100	0.606	0.8909	Non-Soluble
2-Propanol (2P)	0.79	82	0.141	2.0436	Non-Soluble
n-Heptane (HEP)	0.68	98	0.123	0.3967	Non-Soluble
n-Hexane (HEX)	0.66	68	0.120	0.2942	Non-Soluble
Carbon Tetrachloride (CCl_4)	1.6	77	0.103	0.9004	Swelling
Ethylene Glycol (EG)	1.1	197	0.254	13.8	Non-Soluble

Pulsed Laser Ablation in Liquids

In the Pulsed Laser Ablation of solid materials in Liquids (PLAL), a solid target is immersed in a liquid environment and irradiated with a laser beam, at a fluence above its ablation threshold. The laser-polymer interaction generates a plasma plume (also known as ablation plume), that carries the material from the solid target into the liquid

environment. As material is removed from the target due to the laser interaction, the liquid phase has the capability to provide efficient thermal quenching of the ablation products and to retain them into new suspensions which can be subsequently analysed and used[7]. An important fact to consider is that in PLAL the liquids confine the movement of the plasma plume. Therefore, a series of processes including generation, transformation and condensation of the plasma plume resulting from laser ablation of solids in liquid environments takes place under the conditions of the liquid confinement[15].

The experimental setup used for the PLAL experiments is based on a previous work by Cueto et al[6]. The PBAC target was immersed in a certain liquid (table 4.1) and ablated with the fourth harmonic of a Q-switched Nd:YAG laser (Quantel Brilliant B) operating at a repetition rate of 10 Hz. The fourth harmonic of this laser is centred at a wavelength λ = 266 nm (ultraviolet region). This wavelength was chosen since PBAC absorbs light efficiently in this region of the electromagnetic spectrum[8] Absorption coefficient for this PBAC sample has been previously measured and has a value of 18000 cm^{-1} [16]. The pulse duration was τ = 4 ns, measured as half width at half maximum. The PBAC target was placed at the bottom of a glass vessel filled with a 10 mm column of any of the liquids. The laser beam was focused by a 12.5 cm focal length lens situated approximately at 10 cm from the target, to achieve a spot diameter of about 1 mm diameter. The diameter of the spot was measured from the trace left by a laser pulse on an uncoated PVC plate. Placing the laser focus after the PBAC target has the advantage of reducing the potential interaction of the laser pulses with the ablation plume, as well as to avoid the breakdown of the water. The vessel was rotated at about 10 rpm during ablation to avoid target cratering. Several laser fluences (ranging from 1.0 down to 0.1 J cm^{-2}) were employed. Laser fluence is defined as the energy of the laser beam, divided by the

area of the beam's spot. These different fluences were achieved by reducing the laser energy using attenuator plates. Irradiation energies were measured just after the focusing lens, using a Joulemeter. The nanoparticle dispersions were produced by irradiating the sample for 1 hour (36000 pulses).

The experimental setup is presented in scheme 4.1. First, the laser beam hits a dichroic mirror at 45 º that leads it to an attenuator plate. Afterwards, a second dichroic mirror (laser beam incident at 45 º) guides the beam to a Pellin-Broca prism, where the possible remaining of the first and second harmonic of the laser beam can be eliminated. Next, a third dichroic mirror (laser beam incident at 45º) leads the beam to the focusing lens and finally, to the sample.

4.3. Preparation of nanoparticles by PLAL

4.3.1. Study as a function of the fluence

In order to understand the PLAL process in PBAC, first the preparation of nanoparticles in H_2O, using several laser fluences (F) was tested. Figure 4.2 shows (5x5)μm^2 AFM topography images of the deposited suspensions, after irradiation at 1 Jcm^{-2} (left) and 0.4 Jcm^{-2} (right). The diameter distributions are also included, in which the continuous curves represent lognormal distributions.

AFM images show that the deposited material after irradiation is made-up of nanoparticles. For both fluences, these nanoparticles show a spherical geometry, with mean diameters of 54 ± 10 nm at 1 Jcm^{-2} and 48 ± 10 at 0.4 Jcm^{-2}. In this last case, the AFM image shows sort of islands in the topography of the deposited material. These

islands can be related to possible agglomeration of material as it reaches the surface, as previously reported[7]. These aggregates had not been taken into consideration for the statistical size distribution analysis

Scheme 4.1. PLAL setup

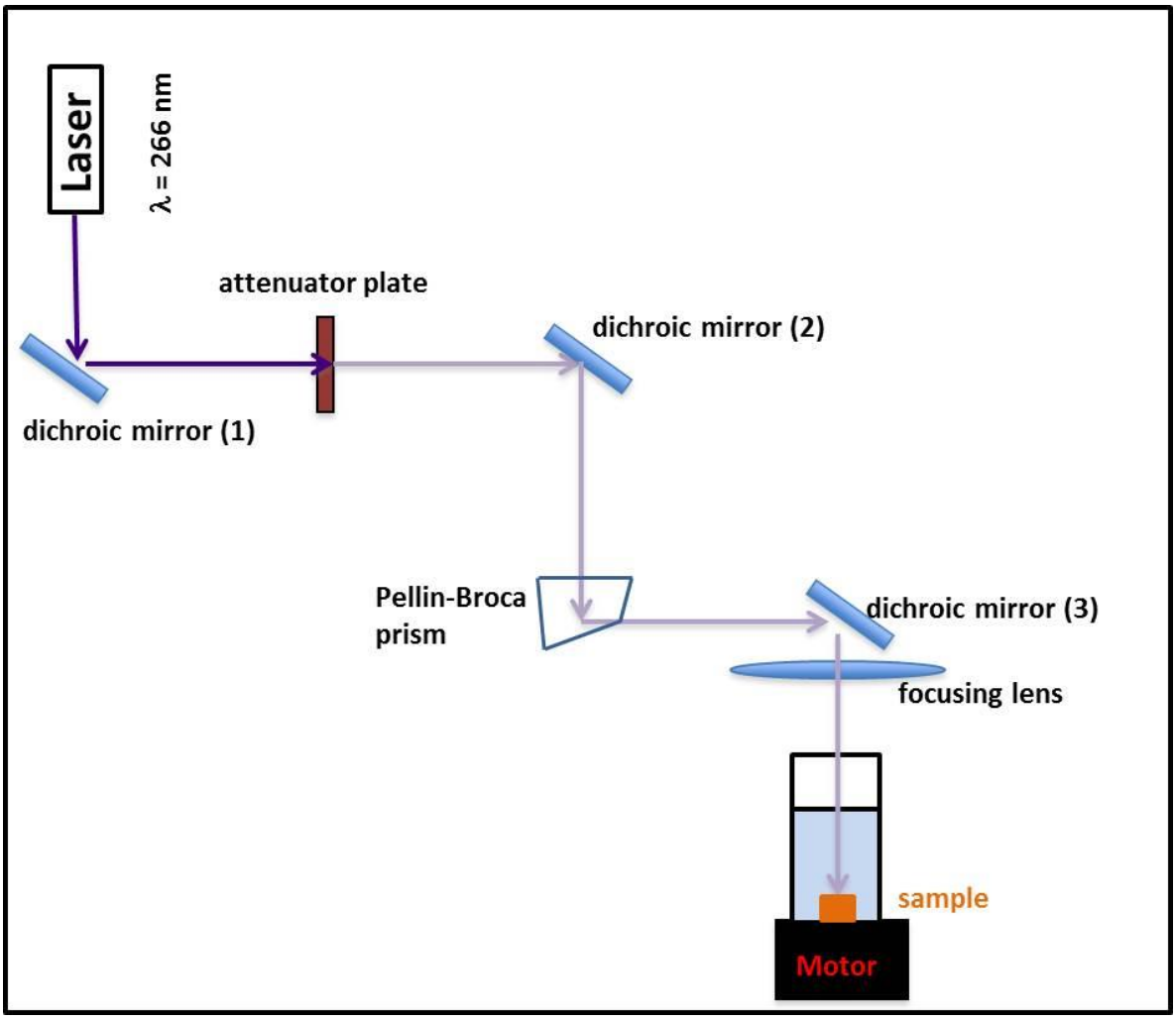

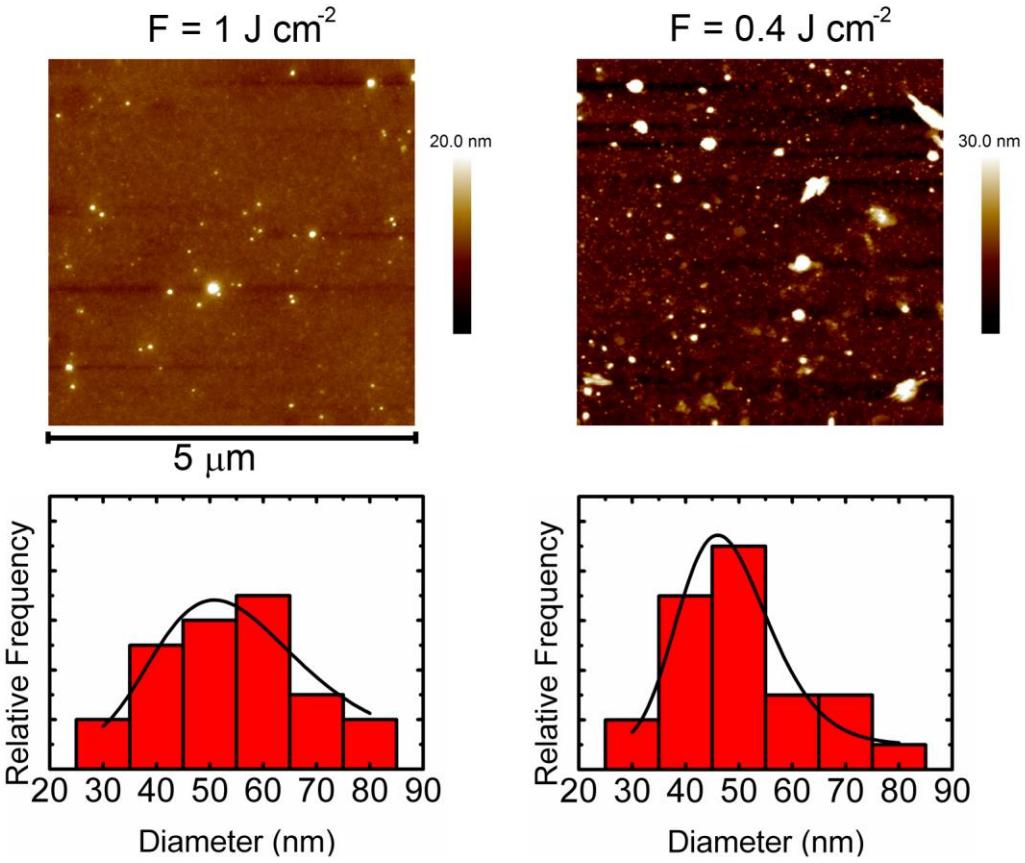

Figure 4.2. AFM topography images and size distributions of the resulting nanoparticles after irradiation a PBAC target at F = 1 Jcm^{-2} and 0.4 Jcm^{-2}.

Heights of the nanoparticles do not agree with their diameter distribution, being the nanoparticles much more wide that high. However, a detailed analysis of the AFM images, for both fluences, showed that nanoparticles are not standing on the surface of the Si wafers, but it seems that there is a continuum of ablated material on the surface, from which the nanoparticles arise. Roughness analysis showed that the *continuum* phase in the AFM images of deposited nanoparticles has a rugosity of about 1 nm, while a cleaned Si wafer had a rugosity below 0.1 nm. Whether the continuum in the nanoparticle images is made of even smaller particles or it is ablated material without any specific geometry or by solvents residues, cannot be distinguished. Regarding the impact of laser energy on the chemical structure of the polymer, previous studies of laser deposition of PBAC, at fluences around 1 Jcm^{-2}, have shown chemical changes in the deposited material[17] (in

comparison to the target), and even the possibility of obtaining amorphous carbon structures[18, 19]. In a previous work by Lazare[7], PLAL experiments were carried out using PBAC targets in H_2O. In this work a similar setup as the one presented in scheme 4.1 was used (λ = 248 nm, τ = 25 ns, KrF pulsed excimer laser). At F = 0.5 Jcm^{-2}, these authors observed that the prepared suspensions in water consisted of nanoparticles of similar size as the observed in figure 4.2. However, chemical analysis showed that some particles had a chemical structure similar to that of the PBAC monomer while others, of smaller size, were carbon-rich graphite-like particles. Also, in Lazare's work, sample was not rotated while performing the PLAL experiments. As the laser beam struck always in the same place, generation of carbon-like material could be more susceptible. It is important to state that not only there can be chemical changes in the monomeric structure of a polymer after laser irradiation, but also its molecular weight can be affected, generally showing a decrease in comparison to the target. The molecular weight decrease of the polymer structures can be attributed to the partial repolymerization of the thermally unzipped monomers during the ablation process[20-23]. Hansen and Robitaille have shown that for PLD experiments on PBAC, no chemical modifications in the deposits are found when the laser fluence lies between 50 $mJcm^{-2}$ – 130 $mJcm^{-2}$, but a molecular weight decrease from 40000 g/mol to 1200 g/mol was found[20, 21].

Based on these results, we have reduced the fluence of the laser beam even further. Figure 4.3 shows (2x2)μm^2 AFM topography images of deposited suspensions prepared at 200 $mJcm^{-2}$ (left) and 100 $mJcm^{-2}$ (right). For both fluences the resulting morphology follows a similar behavior. First, spherical nanoparticles can be observed. Bottom of figure 4.3 shows the diameter distributions of these nanostructures, where the mean diameter is 20 ± 5 nm for irradiations at 200 $mJcm^{-2}$, and 18 ± 5 nm for irradiations at 100

mJcm^{-2}. This indicates that diameter has decreased in more than half in comparison to the high fluences results (Figure 4.2).

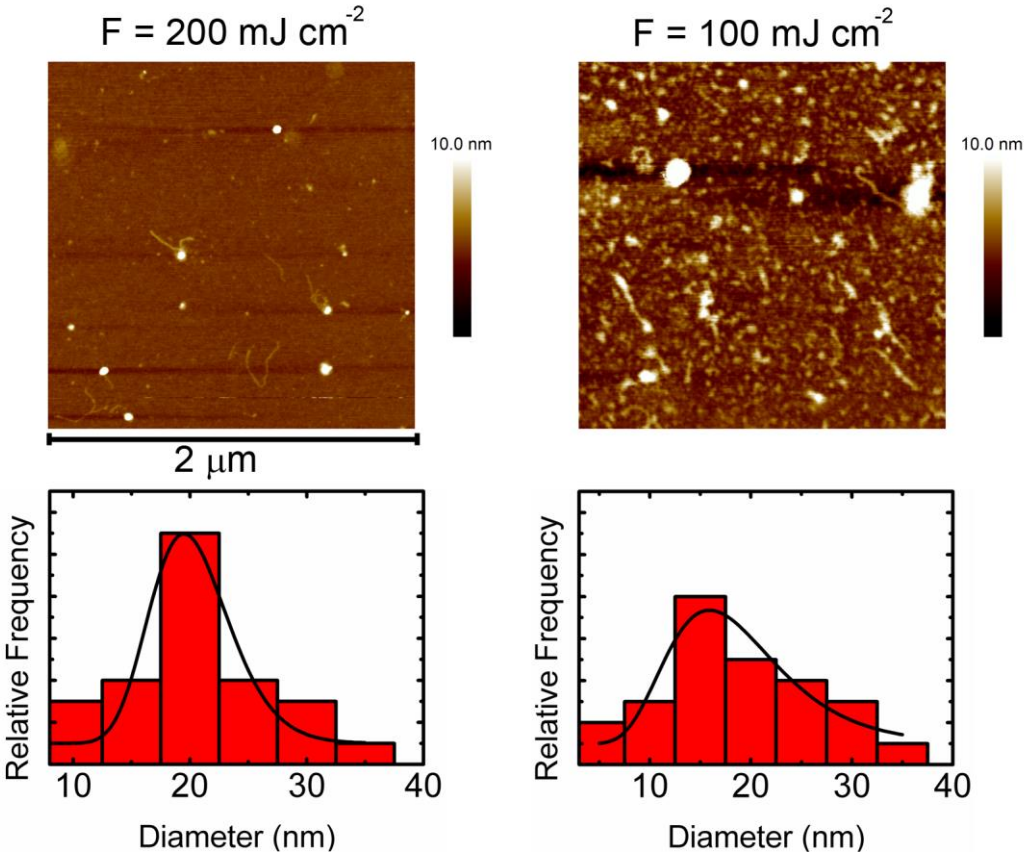

Figure 4.3. AFM topography images of nanostructures formed by PLAL of PBAC at 200 mJcm^{-2} (left) and 100 mJcm^{-2} (right) and size distributions for spherical shaped nanoparticles.

Figure 4.4 shows the variation of the mean diameter as a function of fluence for spherical nanoparticles. It is observed that nanoparticle mean size decreases as fluence decreases. Also, it seems that this variation follows a step-like trend, indicating that there might be a fluence at which the change in size occurs all of the sudden. Moreover, from the data in figure 4.4, one might argue that at both extremes, the size will reach a sort of plateau, *i. e.* independently of the increase/decrease of the fluence, nanoparticle size could reach a limit size.

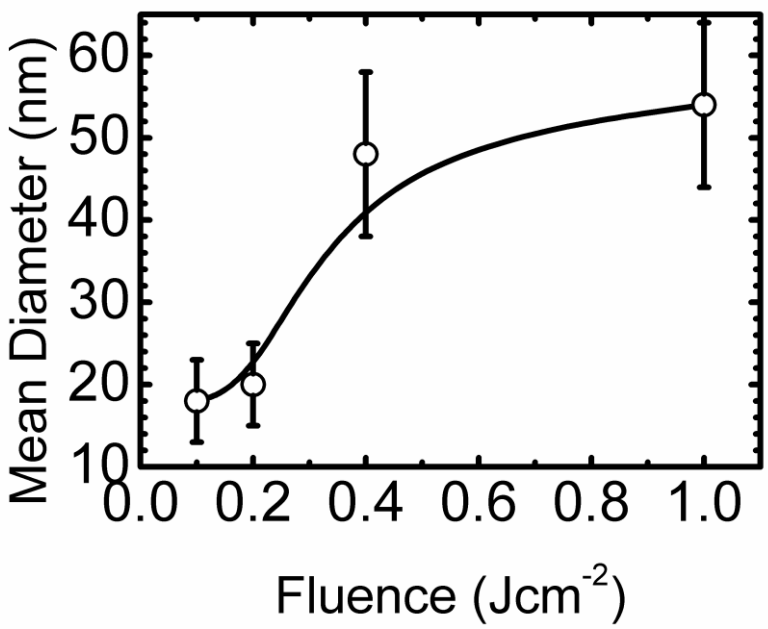

Figure 4.4. Mean diameter of spherical nanoparticles, as a function of fluence, for PLAL irradiations in water.

In figure 4.3, new geometrical structures are also observed, specifically, strand-like structures and particle structures with strand *attachments*. The PLAL experiments at these low fluences were performed several times and the morphology of the nanostructures was reproducible. Figure 4.5 shows detailed AFM topography images of these new nanostructures. The nanoparticle + strand attachments (left and right images) seem to have the same morphology at both fluences. It is observed a continuous circular core, from which the strands emerge. The height of these strands lies between 1 – 3 nm, and lengths around 100 – 300 nm. On the other hand cores are much higher, around 10 – 15 nm and have diameters between 50 -150 nm. AFM resolution does not allow distinguishing whether the core has features in its top. Figure 4.5 (center) shows an AFM topography image of a single strand, observed at the 200 $mJcm^{-2}$ fluence. It has a height of about 1 nm and total length of 450 nm.

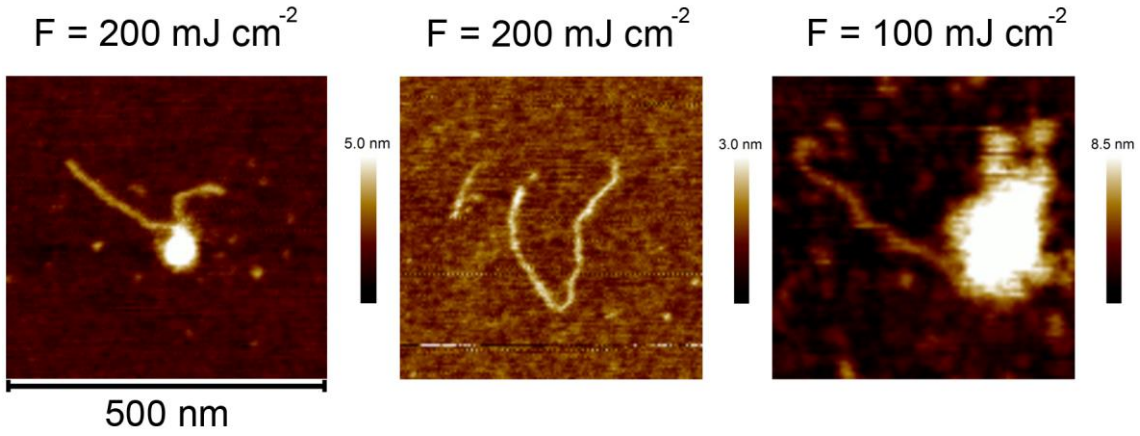

Figure 4.5. AFM topography images showing in detailed the nanostructures formed by PLAL of PBAC at 200 $mJcm^{-2}$ (left and center) and 100 $mJcm^{-2}$ (right).

Several factors during the PLAL process can be related to the appearance of strand-like nanostructures at these fluences. It can be argued that the formation of these nanostructures could be related to the mechanisms of molecular ejection. The different size distributions and structures can be related to the penetration of the laser beam into the PBAC target. At high fluences, ablation can occur at deeper layers of the target than at lower fluences, indicating that material ejected from deeper layers has more mass and thus a higher diameter. As fluence is reduced, not only size is reduced due to the different penetration of the laser beam, but also the appearances of new geometrical sturctures might indicate that the ablated particles have more interaction with the liquid surroundings. In the PLAL setup, as the laser beam heats the PBAC target the liquid environment is also affected. Previously, Leveugle and Zhigilei[24] have shown, via molecular dynamics simulations, that during the ablation process by MAPLE, the original randomly oriented molecules in the target have a tendency to extend along the flow in the ablation plume and to thread through the liquid regions. In their simulations, the polymer + liquid environment lead to the formation of complex polymer elongated structures in the direction of the ablation plume expansion[24]. Also, these authors have shown a dependency of this process with the fluence of the laser beam. For low fluences,

elongated polymer structures appear, while as fluence is increased, the material was ejected as clusters[24, 25]. These facts can be compared to the results collected so far for the PLAL nanostructures in this work. Also, at high fluences, there are higher amounts of ejected material, as revealed by the AFM images. The ejected material at high fluences has more kinetic energy in comparison to the ones at low fluences. This might induce more collisions in the ablation plume that ultimately lead to coalescence of material and thus higher diameters of the resulting nanoparticles.

4.3.2. Study as a function of the liquid environment

As stated previously, in PLAL experiments the liquid environment confines the movement of the plasma plume. Thus, the physicochemical properties of a particular liquid might have different interactions with the plume. In order to address this point, we have performed PLAL experiments in different liquid mediums (table 4.1). The experiments were carried out at F = 100 $mJcm^{-2}$ for 1 hour. This fluence was chosen following the low chemical modifications previously observed in the literature for PBAC PLD experiments[20] and in order to compare the results with the appearance of the stranded nanostructures in H_2O. Figure 4.6 shows (2x2)μm^2 AFM topography images of the deposited samples. For all liquids, the formation of nanoparticles with individual geometries is observed. An image of the irradiation in water is also included for comparison, in which the elongated nanostructures, described in figures 4.3 and 4.5, are also observed. These sorts of structures are also seen in CCl_4 and HEX. Specifically, in CCl_4 isolated spherical and elongated nanoparticles as well as particles + strands nanostructures are seen in the AFM image. Although these results qualitatively resemble the results of water, the sizes of the nanostructures are different. In CCl_4, the strands

emerging from the spherical particles have heights between 10 – 20 nm and lengths between 100 – 200 nm.

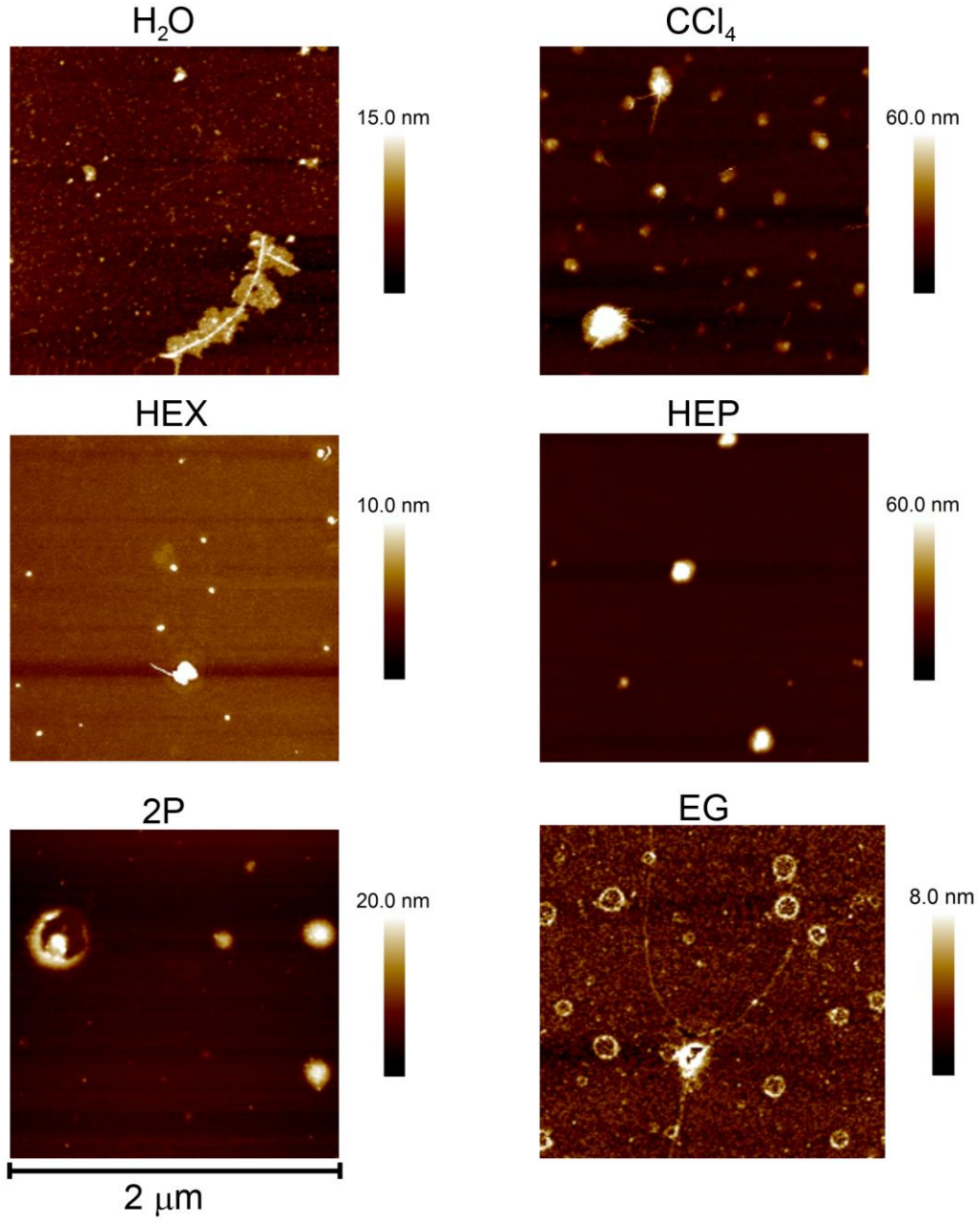

Figure 4.6. AFM topography images showing in detailed the nanostructures formed by PLAL of PBAC in several liquids at 100 mJcm^{-2}. The abbreviation of the liquids can be found in table 4.1.

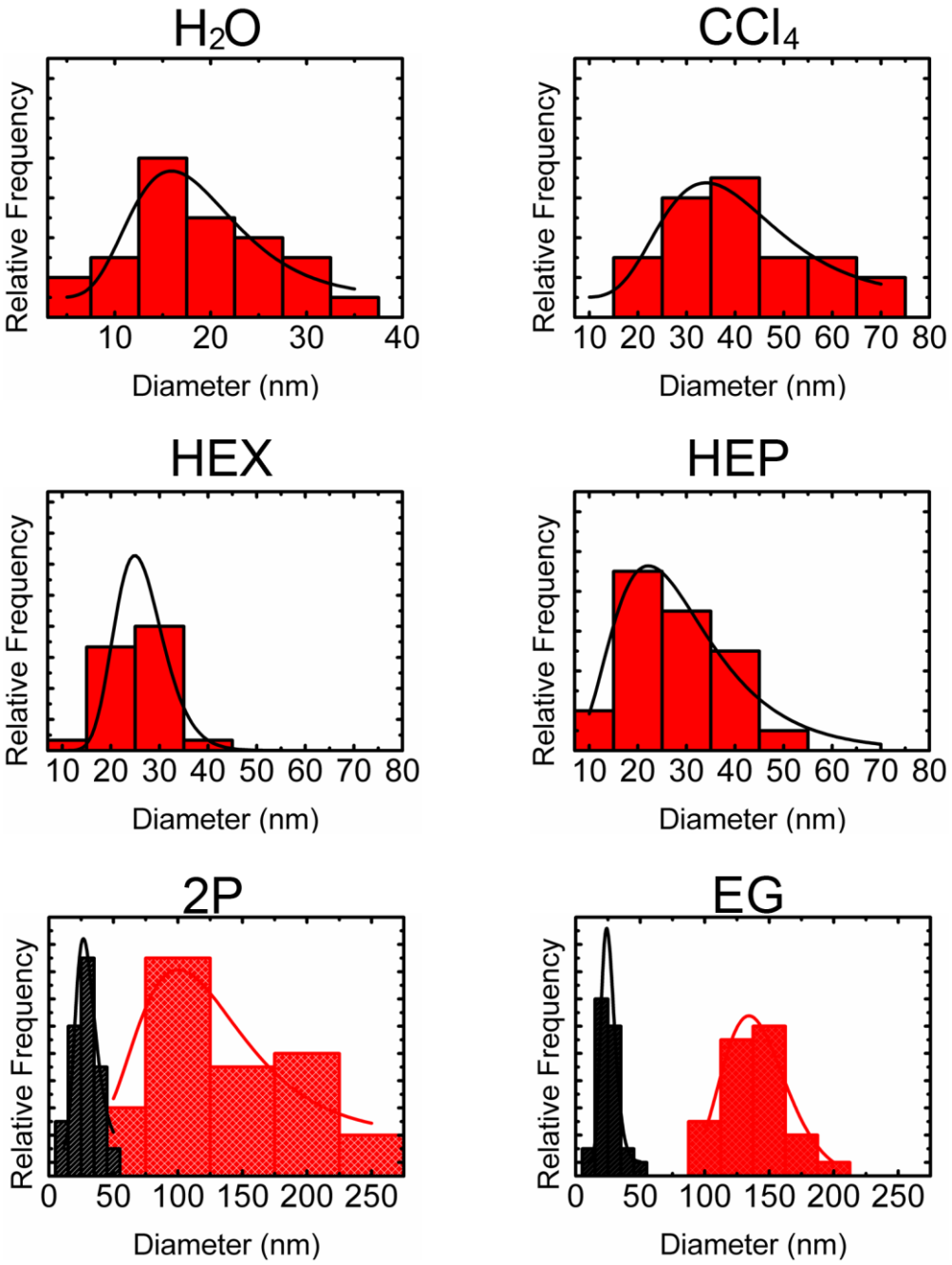

Figure 4.7. Size distribution histograms of nanostructures prepared by PLAL in different liquids. In 2P, black distribution corresponds to small size nanospheres while red distribution corresponds to big size nanospheres. In EG, black distribution correspond to nanospheres and red distribution to toroids.

Figure 4.7 shows the diameter size distributions of spherical particles for each solvent. For CCl_4, the spherical particles that serve as cores for the strands cover a wide spectrum of diameters from 20 – 80 nm, having a mean size of 40 nm. However it must be taken into consideration that CCl_4 is the liquid that absorbs more light and also the one in which the PBAC is more susceptible to be soluble. In a macroscopic solubility

experiment, 24 mg of PBAC were immersed in 2 mL of CCl_4. For times comparable to the experimental time of the PLAL protocol, sample did not show any changes by eye inspection. However, after a few days swelling and whitening of the PBAC was observed. Although it can be argued that the deposited sample after PLAL in this liquid might not be contaminated by solubility of the PBAC target, if a reduction of the molecular weight took place, CCl_4 could be interacting with the ejected material.

PLAL experiments in HEX show nanoparticles with a mean diameter of 26 nm. The strands have diameters and lengths in the same range as the observed in CCl_4. However, there are much more nanoparticles than strands in the AFM images. For the rest of the liquids, the nanoparticles+strands geometry is not observed anymore. In the case of HEP, only spherical particles are observed throughout the AFM images. These particles have mean diameters about 27 nm, and heights between 5 and 20 nm. Roughness tests show that particles lie on top of the Si substrate and thus cannot be considered as nanospheres but *nanodiscs* or nanocylinders. AFM image of the particles prepared in 2P shows that there are three types of structures. First, two families of nanoparticles can be observed, which diameters are presented in the corresponding histogram of figure 4.7. Small particles, having a mean diameter of 29 nm, are fairly similar to those observed in HEP. On the other hand, bigger particles, with mean diameters of about 120 nm are also observed. Furthermore, a new geometrical structure is also found.

As seen in figure 4.6, in the bottom-left corner one may observe a sort of toroid structure surrounding a particle. The particle seems to be physically attached to the toroid through one of its sides. The toroids in 2P are not fully closed and have thicknesses around 10 nm and diameters around 350 nm. These sorts of structures have been

reproducible and are observed in several zones of the deposited samples. The nature of the toroidal particles can be discussed heavily. One might argue that these particles are formed during the ablation process in the liquid, while on the other hand it is also possible to think that the particular shape can be formed during the deposition/drying process. Nevertheless, in both cases we propose that this structure is formed by an original nanosphere that collapses due to the influence of its surroundings. The question why these toroid/particle systems are only found in the irradiation in 2P remains open.

Finally, results of PLAL experiments in EG are presented. In this case, a continuum of nanoparticles, without an specific geometry, is observed throughout the entire AFM image. The roughness of this phase is about 1 nm, which is much higher in comparison to the one of Si. Some spherical particles can be also observed in the continuum, having mean diameters of 25 nm; however, the most important features are toroids, as in 2P, but with the difference that in EG there are no particles in their centers. The EG toroids seem to emerge from the continuum, having thicknesses between 1 – 5 nm and mean diameters of about 140 nm. These geometrical factors remain fairly constant among all the analyzed structures. Also, the toroids EG present a fully closed loop, contrary to the observed in 2P. Strands are also present in the PLAL experiments using EG. As the toroids, the strands emerge from the continuum of material that covers the Si wafer, having thicknesses around 1 nm and lengths in the order of 1 micron.

Gathering results, there is a dependence of the nanoparticle formation with the liquid environment. Several structures, such as nanospheres, strands, cylinders and toroids can be formed by only changing the liquid medium. This could be explained by the

different mechanisms of molecular ejection from the target, as well as from the different physic-chemical characteristics of each liquid. One could argue that as the PBAC target is being ablated, the high temperatures at the target surface could lead to the formation of bubbles due to the evaporation of the solvent. These bubbles could be related to the formation of the different nanoparticle structures. According to Lazare[26], the temperature at the surface of the target suffers an increase (ΔT) as the laser ablates the material, such that:

$$\Delta T = \frac{\alpha F}{\rho C_p} \tag{4.1}$$

where F is the laser fluence (= 0.1 Jcm^{-2}), while α (= 18000 cm^{-1}), ρ (=1200 kg cm^{-3}) and C_p (= 1207 J kg^{-1} K^{-1}) are the absorption coefficient, density and heat capacity of PBAC[16], respectively. Equation (4.1) shows that the PBAC surface, under the irradiation conditions in this work, suffers an increase in temperature ΔT = 1240 K. This increase is much higher in comparison to the different boiling points of the liquids used in this work, *i. e*. the formation of bubbles due to local evaporation of the solvent should be similar for all the mediums. Thus, the different sizes and morphologies cannot be accounted to this factor.

Another factor that can be considered to affect the nanostructuring in PLAL experiments is the density of the liquids. Since we worked at a fixed volume (1 mL), density is proportional to the mass of the liquid in the vessel. Thus, in this work, a higher density implies a higher mass of liquid in the vessel. This fact could affect the ablation plume and thus the formation of nanostructures. Table 4.2 shows the mean diameter of nanoparticles in different liquid mediums, as a function of increasing density of the liquids. In the case of 2P and EG, only the mean size of nanoparticles with spherical-like

shape and small diameter is taken into consideration. For the first three liquids in table 4.2, as density increases so does the mean diameter of the nanoparticles. However, this consideration does not remain true for the rest of the mediums, and thus can be discarded.

Table 4.2. Mean diameter of nanoparticles as a function of liquid density.

Liquid	Density[12] (g/cm^3)	Size (nm)
n-Hexane (HEX)	0.66	26 ± 3
n-Heptane (HEP)	0.68	27 ± 3
2-Propanol (2P)	0.79	29 ± 3
Distilled Water (H_2O)	1	18 ± 2
Ethylene Glycol (EG)	1.1	25 ± 3
Carbon Tetrachloride (CCl_4)	1.6	40 ± 5

Recently, Russo et al[27] have prepared nanoparticles of copper, by laser ablation, in different gas mediums such as argon (Ar) and helium (He). Authors have found that particle size was dependent on the surrounding gas, being the mean diameters smaller for irradiations in He than in Ar. Experiment and simulations led to concluded that the different size distributions were a consequence of the much higher thermal conductivity of helium (ten times greater than argon). Consequently, the vapor plume cools faster for ablation in helium. The faster cooling rate induces a higher supersaturation ratio and a shorter condensation duration, which result in smaller particles from condensation. Also, De Bonis and collaborators[28] have performed PLAL experiments in different liquids, namely: water and acetone, using Palladium (Pd) as target. It was found that the mean diameter of the nanoparticles obtained in acetone was slightly higher than those obtained in water under the same conditions. According to the authors, these results could be

related to the thermal properties of the liquids, which could affect the cooling times of the plume. Since thermal conductivity of water is larger than that of acetone, a faster cooling of the plume would result in smaller particle size.

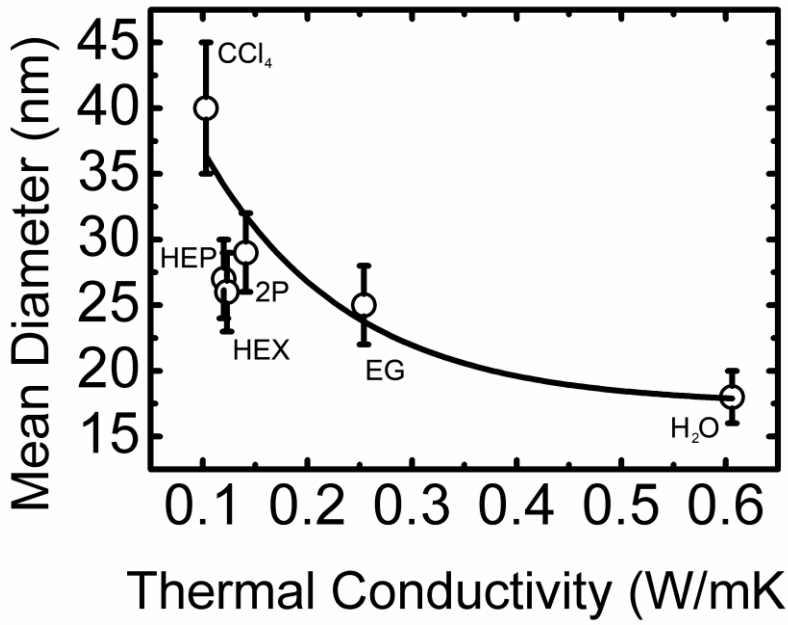

Figure 4.8. Mean diameter of nanoparticles as a function of the thermal conductivity of the different liquids. Line is a guide for the eye.

Based on these works, figure 4.8 shows the mean diameter of nanoparticles as a function of the thermal conductivity of the liquids used in this work. As for table 4.2, only spherical-like particles are taken into consideration. Continuous line in figure 4.8 is a guide for the eye. The distribution of mean diameters as a function of the thermal conductivity shows a trend indicating that as the thermal conductivity of the liquid increases, the nanoparticle diameter decreases. This result is in line with the proposals of Russo[27] and De Bonis[28], where a faster cooling rate, induced by the liquid, leads to smaller nanoparticles, just like in quenching procedure. Regarding the different shapes of the nanostructures, thermal conductivity does not provide further information. Since all the liquids present different properties, multiple factors should be taken into consideration.

If one classifies the liquids used in this work, as a function of increasing viscosity, as shown in table 4.3, shape of the different nanostructures can be explained.

Table 4.3. Nanostructure shapes as a function of liquid viscosity.

Liquid	Viscosity[14] (g/m s)	Nanoparticle shape
n-Hexane (HEX)	0.2942	Spherical nanoparticles. Some strands
n-Heptane (HEP)	0.3967	Spherical nanoparticles
Distilled Water (H_2O)	0.8909	Spherical nanoparticles with and without strands
Carbon Tetrachloride (CCl_4)	0.9004	Spherical nanoparticles. Increasing of strands in comparison to H_2O
2-Propanol (2P)	2.0436	Two distributions of spherical nanoparticles. Some toroids (not completely closed) start appearing
Ethylene Glycol (EG)	13.8	Continuous surface and small nanoparticles. Toroids proportion increases significatively

First, HEX and HEP are the two liquids with the lower viscosity values. In both cases, the distribution of sizes and shape of the nanoparticles are quite similar, with the slight variation of some strands in the HEX AFM image. As viscosity increases, the appearance of nanoparticles+strands morphologies becomes more significant (H_2O and CCl_4). As viscosity further increases, new structures appear, such as the bimodal distribution of spherical nanoparticles in 2P and the toroids in EG. These results can be understood since the expansion of the ablation plume finds an opposing force by the

liquids depending on the viscosity. This could affect the homogeneity of the ablation plume and thus, the different shapes of the nanoparticles cannot reorganize into spherical systems.

4.4. Ongoing and future research

PLAL experiments using PBAC as target have shown the possibility of preparation of several nanostructures, depending on the laser fluence and on the liquid mediums used. However, several problems must be approached in order to get a better understanding of the results. First, it must be studied the chemical composition of the nanostructures in order to determine the possible chemical changes suffered by the PBAC during the ablation process. In this case, X-ray Photoelectron Spectroscopy (XPS) measurements can be performed. For these experiments, a square sample area of about 1x1 cm is required, which can have a thickness as small as only a few nanometers. To prepare this sample, the liquid containing the ablated material was lyophilized. Afterwards, $CHCl_3$ was added and the solution was spin coated in a Si wafer. AFM measurements revealed that a film was formed. Nowadays, XPS experiments are being carried out. Another problem to face is the possible change of the molecular weights in the nanoparticles. In this case, Gel Permeation Chromatography (GPC) experiments can be performed. For GPC, a solid sample of about 5 mg is required. The throughput of PLAL experiments is quite low, around 0.1 mg per hour of irradiation and mL of liquid; however, not only throughput/time are the important factors to consider. Also the concentration of mass in volume of liquid will be an important factor since the possible 5 mg of material will be dispersed in 50 mL of liquid. Nowadays we are working of protocols to concentrate sample (centrifugation, precipitation,…) in order to recover the desire amount of sample.

4.5. Summary

PLAL experiments were carried out in water, as well as in several other liquids. First, by changing the fluence, a decrease in the mean diameter of the nanoparticles was found. Also, reduction of fluence was found to lead to transition from nanospheres to nanoparticles/strands, in water ablations. This transition was explained as the different liquid-solid interactions that take place during the ablation process. Afterwards, the liquid mediums dependence was studied. By varying the liquids, different nanostructures, such as spheres, strands and toroids, were obtained. Several physico-chemical parameters of the different solvents were used to explain the results obtained. The different size distributions were related to the thermal conductivity of the systems, as previously reported in the literature. On the other hand, viscosity of the liquids seems to be responsible for the development of the different nanostructures. However, several other parameters remain as possible candidates to be taken into consideration, such as solubility, and dipolar moment, among others. Finally, the chemical characterization of the nanostructures is still under research. The different techniques that we desire to use and the ideal protocol to be followed were presented and explained.

4.6. References

1. Castillejo, M.; Ezquerra, T. A.; Oujja, M.; Rebollar, E., Laser Nanofabrication of Soft Matter. In *Lasers in Materials Science*, Castillejo, M.; Ossi, P. M.; Zhigilei, L., Eds. Springer: 2014.
2. Castillejo, M.; Ezquerra, T. A.; Martín, M.; Oujja, M.; Pérez, S.; Rebollar, E. *AIP Conference Proceedings* **2012,** 1464, (1), 372-380.
3. Rebollar, E.; Vazquez de Aldana, J. R.; Martin-Fabiani, I.; Hernandez, M.; Rueda, D. R.; Ezquerra, T. A.; Domingo, C.; Moreno, P.; Castillejo, M. *Physical Chemistry Chemical Physics* **2013,** 15, (27), 11287-11298.
4. Brown, M. S.; Kattamis, N. T.; Arnold, C. B. *Journal of Applied Physics* **2010,** 107, (8), -.
5. Shepard, K. B.; Priestley, R. D. *Macromolecular Chemistry and Physics* **2013,** 214, (8), 862-872.
6. Cueto, M.; Sanz, M.; Oujja, M.; Gámez, F.; Martínez−Haya, B.; Castillejo, M. *The Journal of Physical Chemistry C* **2011,** 115, (45), 22217-22224.
7. Elaboudi, I.; Lazare, S.; Belin, C.; Bruneel, J. L.; Servant, L. *Applied Surface Science* **2007,** 253, (19), 7835-7839.
8. Elaboudi, I.; Lazare, S.; Belin, C.; Talaga, D.; Labrugère, C. *Appl. Phys. A* **2008,** 92, (4), 743-748.
9. Elaboudi, I.; Lazare, S.; Belin, C.; Talaga, D.; Labrugère, C. *Appl. Phys. A* **2008,** 93, (4), 827-831.
10. Blanchet, G. B. *Macromolecules* **1995,** 28, (13), 4603-4607.
11. Caricato, A. P., MAPLE and MALDI: Theory and Experiments. In *Lasers in Materials Science*, Castillejo, M.; Ossi, P. M.; Zhigilei, L., Eds. Springer: 2014.
12. According to the decription of the bottle.
13. *CRC Handbook of Chemistry and Physics*. 85th ed.; CRC Press: 2003.

14. Kruusing, A., Chapter Eight - Liquids and Their Properties. In *Handbook of Liquids-Assisted Laser Processing*, Kruusing, A., Ed. Elsevier: Amsterdam, 2008; pp 315-385.
15. Yang, G. W. *Progress in Materials Science* **2007,** 52, (4), 648-698.
16. Rebollar, E.; Pérez, S.; Hernández, J. J.; Martín-Fabiani, I.; Rueda, D. R.; Ezquerra, T. A.; Castillejo, M. *Langmuir* **2011,** 27, (9), 5596-5606.
17. Tsuboi, Y.; Adachi, H.; Yamamoto, E.; Itaya, A. *Japanese Journal of Applied Physics* **2002,** 41, (2R), 885.
18. Voevodin, A. A.; Laube, S. J. P.; Walck, S. D.; Solomon, J. S.; Donley, M. S.; Zabinski, J. S. *Journal of Applied Physics* **1995,** 78, (6), 4123-4130.
19. Voevodin, A. A.; Donley, M. S.; Zabinski, J. S.; Bultman, J. E. *Surface and Coatings Technology* **1995,** 76–77, Part 2, 534-539.
20. Hansen, S. G.; Robitaille, T. E. *Applied Physics Letters* **1988,** 52, (1), 81-83.
21. Hansen, S. G.; Robitaille, T. E. *Journal of Applied Physics* **1988,** 64, (4), 2122-2129.
22. Blanchet, G. B.; Shah, S. I. *Applied Physics Letters* **1993,** 62, (9), 1026-1028.
23. Chrisey, D. B.; Piqué, A.; McGill, R. A.; Horwitz, J. S.; Ringeisen, B. R.; Bubb, D. M.; Wu, P. K. *Chemical Reviews* **2003,** 103, (2), 553-576.
24. Leveugle, E.; Zhigilei, L. V. *Journal of Applied Physics* **2007,** 102, (7), -.
25. Leveugle, E.; Zhigilei, L. V.; Sellinger, A.; Fitz-Gerald, J. M. *Applied Surface Science* **2007,** 253, (15), 6456-6460.
26. Lazare, S.; Tokarev, V.; Sionkowska, A.; Wiśniewski, M. *Appl. Phys. A* **2005,** 81, (3), 465-470.
27. Wen, S.-B.; Mao, X.; Greif, R.; Russo, R. E. *Journal of Applied Physics* **2007,** 101, (12), -.
28. Bonis, A.; Sansone, M.; Galasso, A.; Santagata, A.; Teghil, R. *Appl. Phys. A* **2014**, 1-6.

Results

Part B – Physical properties and applications of polymer nanostructures

CHAPTER 5 – On the Glass Transition Temperature variations of 3D confined polymer nanoparticles

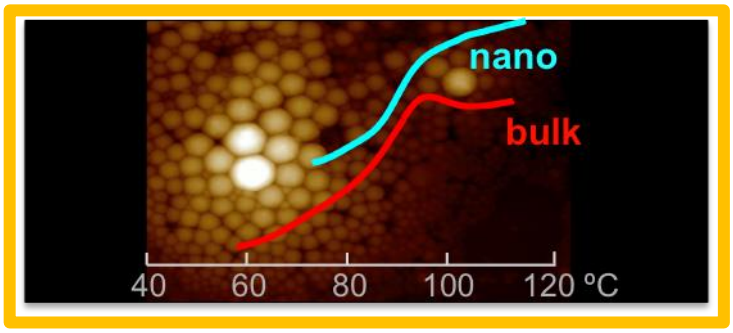

DSC Tg variation of confined polymer nanoparticles in comparison to the bulk. Back image: AFM topography image of PEMA nanoparticles. Image has 2 microns on its wider edge.

Polymer nanospheres with different size distributions were prepared by the miniemulsion technique described in chapter 3. The calorimetric trace of these spheres showed an increase of the glass transition temperature, with respect to its bulk value, that has been evaluated by means of a model based on entropic considerations. The 3D-confinement, imposed by the nanospheres, leads to a limiting number of repeating polymer units in the sphere and thus to a reduction of the possible configuration states of the polymer chains, which is ultimately related to variations of the glass transition temperature. Our model has been evaluated against the data available in the literature. Good agreement between data and model is found for many cases, proving that confinement is related to reductions in entropy for these systems.

*Part of the work described in this chapter has been published in *Macromolecules* 2013, **46**(11), 4698-4705

5.1. Introduction

For several years, modification of the physical properties due to size effects when approaching nanometer lengths in glass forming systems in general, and in polymers in particular, has been strongly debated. Among the different properties, variations of the glass transition of confined polymers have motivated a good number of experimental works[1-4]. Confinement experiments have been considered a very elegant way of probing the existence of a correlation length (ξ) of cooperative motions that produces the observed slowing down of the dynamics upon cooling, as the temperature approaches the supercooled liquid to glass transition temperature[2]. As the confining length approaches the order of the correlation length, modification of the properties is expected. However, in real experiments, besides pure finite size effects, other factors like the enhanced role of interfaces appear[5, 6]. Moreover, very recently it has been pointed out that, finite size and interfacial effects are not the only ones to be considered in confinement experiments to univocally determine the deviation from bulk behavior. In thin films, recent models and experiments evidenced, that other parameters, like the interfacial free volume[7], should also be taken into account. Another fact to consider that particularly applies to the case of polymer films is the changes in polymer chain conformations when subjected to confinement. In this respect, different confinement geometries would imply different conformations. In thin films (1 dimension is confined)[6] and nanowires (2 dimensions are restricted)[8] the motions of the polymer molecules are modified in at least one of the directions of the space. Therefore, the observed effect will be anisotropic. Recently, ultrastable glasses of poly(methyl methacrylate) (PMMA) have been reported[9], with a glass transition temperature in some cases up to 40 °C higher than that of the bulk polymer. Those ultrastable glasses are formed by the assembly of nearly spherical polymer nanoglobules. In this geometry, the globular nature of individual polymer chains

is preserved while confinement is imposed by the size of the globules. Few experiments on the glass transition and the dynamical properties of polymer nanospheres have been recently published, but again, there seems to be some controversy about the impact of the confinement on the observed physical properties. In this chapter we show how spherical polymer particles that contain less than a threshold number of repeating units exhibit an increase of the glass transition temperature. We propose a model to establish the key parameter that controls the shift of the glass transition temperature in globular 3D-confinement. All the work described in this chapter was performed at the facilities of IEM-CSIC and IQFR-CSIC.

5.2. Samples and techniques

Polymer nanoparticles of PEMA, PS and PBAC were prepared following the miniemulsion method, previously detailed in chapter 3 (section 3.1.1.). In order to evaluate the changes in their glass transition temperature, differential scanning calorimetry (DSC) measurements were performed. Calorimetry has been shown to be an effective analytical tool to characterize the glass transition and phase transformations under confinement[10]. For performing DSC measurements, we lyophilized the nanoparticles emulsions. The details of the lyophilisation protocol are widely described in chapter 2 (section 2.2.1.). In order to measure the glass transition of the samples, the external block temperature of the DSC was set at -100 ºC. The lyophilized nanoparticle powder was encapsulated in aluminium pans and heated from 0 ºC up to well above the expected glass transition temperature (T_g) at a rate of 60 ºC·min^{-1}. This rate was selected so a good calorimetric response could be obtained even when the amount of sample was in the detection limit (~ 3 mg). The glass-transition temperature was taken as the midpoint

of the heat capacity increment ΔC_p associated with the glass-to-rubber transition which gave the same value as the one taken from the maximum peak of the heat flow derivative.

5. 3. Glass transition of amorphous polymers

Throughout this section, the influence of three dimensional confinement on the glass transition temperature of several polymer nanoparticles will be presented and discussed. First we begin by showing the results for nanometric particles. Afterwards, the results on sub-micrometric particles will be presented. Finally, a model discussing the effects on both types of particles is proposed.

5.3.1 Nanometric particles

Glass transition temperature variations of the amorphous polymer nanoparticles are presented in figures 5.1, 5.2 and 5.3. The heat capacity derivative (dC_p/dT), in which the T_g appears as a peak, is also presented. This is an alternative and much more sensitive method to analyze changes in the heat flow since allows observing weak C_p jumps or broadened transitions. If present, the broadening can be related to a distribution of glass transition temperatures along the sample, for example, due to size effects in the system. In every case, the bulk calorimetric trace, obtained under the same conditions, is also presented for comparison.

As a general trend, the three studied nanostructured polymers show features indicating a glass transition temperature higher than that of the bulk, but with particular details depending on the polymer. The heat flow derivatives (dH/dT) show pronounced wider peaks in comparison to the bulk. The fact that in confinement, the calorimetric peak

related to the T_g gets wider, can be interpreted as the existence of a relative broad distribution of glass transition temperatures.

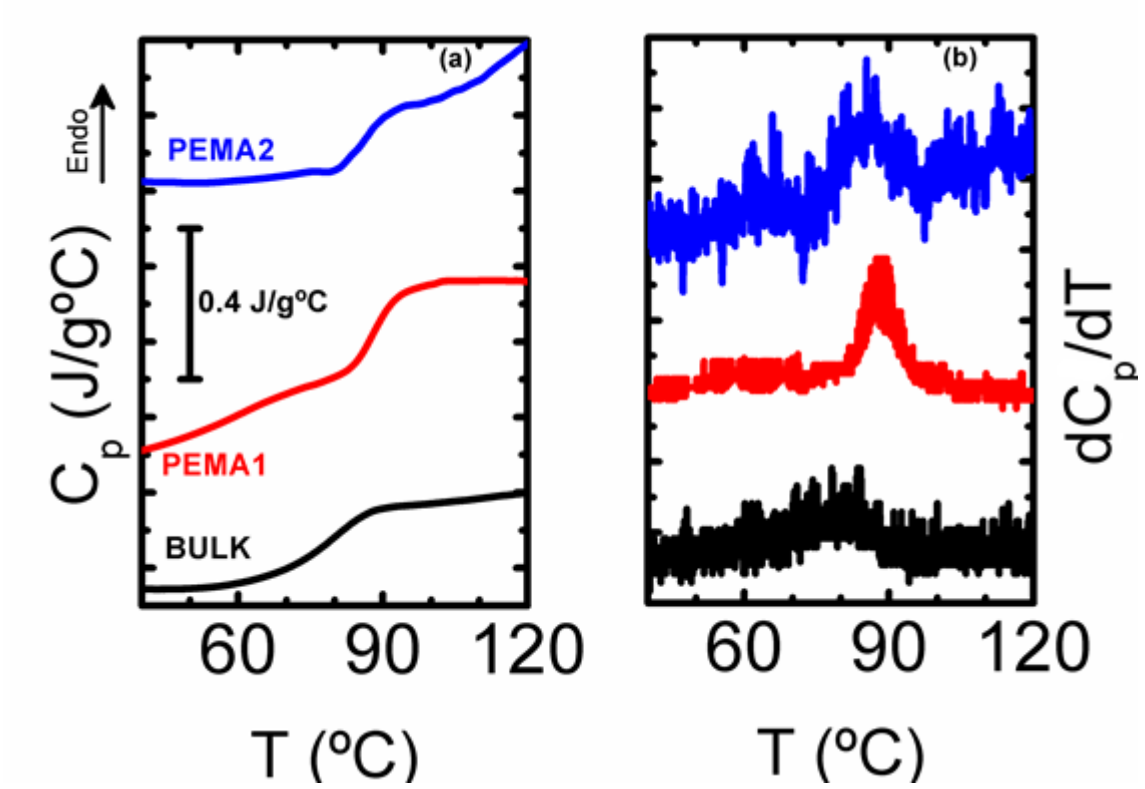

Figure 5.1. (a) DSC normalized traces of bulk PEMA (black) and PEMA nanometric spheres. Red line corresponds to surfactant aided spheres, whereas the blue curve corresponds to surfactant free spheres. **(b)** Derivative of the heat flow with respect to T of the heat flow shown in **(a).**

Specifically, PEMA nanoparticles (figure 5.1.) show an increase in T_g with respect to the bulk (T_{gBULK}) in both surfactant free and surfactant aided nanoparticles. This indicates that SDS seems to not play a role in the thermodynamical changes suffered by the confined particles. PS nanoparticles (figure 5.2) show a glass transition calorimetric trace at temperatures higher than T_{gBULK}, with a shape that resembles a physical aging process. To take this fact into consideration, in this sample the fictive temperature was also calculated and coincides with the T_g determined by the increase at half ΔC_p. In the PBAC nanoparticles (figure 5.3) the calorimetric trace is more complex. Heat flow curve shows two transitions. First, at 160 ºC a peak-like transition is observed. Heat flow

derivative shows that this peak coincides with the position of the bulk T_g of the PBAC. Moreover, at around 185 ºC another transition can be observed from the heat flow curve, as well as from the *dH/dT* plot. This may indicate that there is a population of spheres of enough size to exhibit a bulk like behavior (peak at low temperatures) and other population of spheres that exhibit a confined like response (high temperature). DSC quantitative results are summarized in table 5.1.

Table 5.1. Calorimetry results of confined polymer nanospheres

Sample	T_g (ºC)	ΔCp (J/gºC)
PEMA1	(88 ± 1)	(0.22 ± 0.01)
PEMA2	(86 ± 1)	(0.20 ± 0.02)
PEMA3	(82 ± 1) (88 ± 1)	(0.22 ± 0.01)
PEMA4	(80 ± 1) (88 ± 1)	(0.22 ± 0.01)
PEMA BULK	(80 ± 1)	(0.21 ± 0.01)
PS-NANO	(120 ± 1)	(0.31 ± 0.02)
PS BULK	(110 ± 1)	(0.31 ± 0.01)
PBAC-NANO	(185 ± 1)	(0.45 ± 0.01)
PBAC BULK	(162 ± 2)	(0.30 ± 0.01)

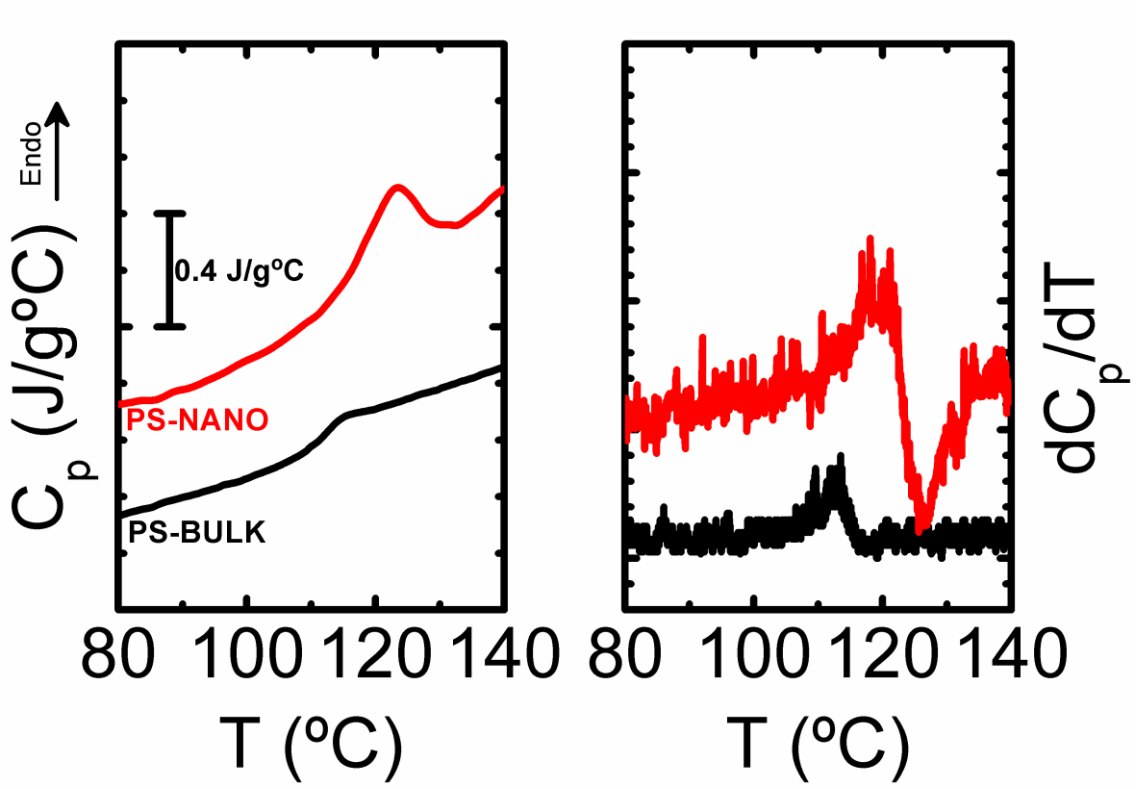

Figure 5.2. DSC trace and heat flow derivative of PS surfactant aided nanoparticles.

In order to rule out that any of the observed features in the DSC traces of the nanostructured polymers arise from the presence of SDS, calorimetric experiments on pure SDS were performed under the same conditions. Figure 5.4 shows the DSC trace of pure SDS. Two peaks are seen in the calorimetric response, with maxima around 27 ºC and 127 ºC. None of these peaks are seen in the DSC trace of the surfactant aided nanoparticles, indicating that the dialysis protocol reduced the amounts of surfactant values non detectable by the equipment. Since both surfactant free and surfactant aided particles show behavior comparable between on another, and no traces of surfactant are detected in the DSC of the nanoparticles, changes in T_g cannot be related to the presence of the surfactant but to variations in the molecular arrangements due to confinement.

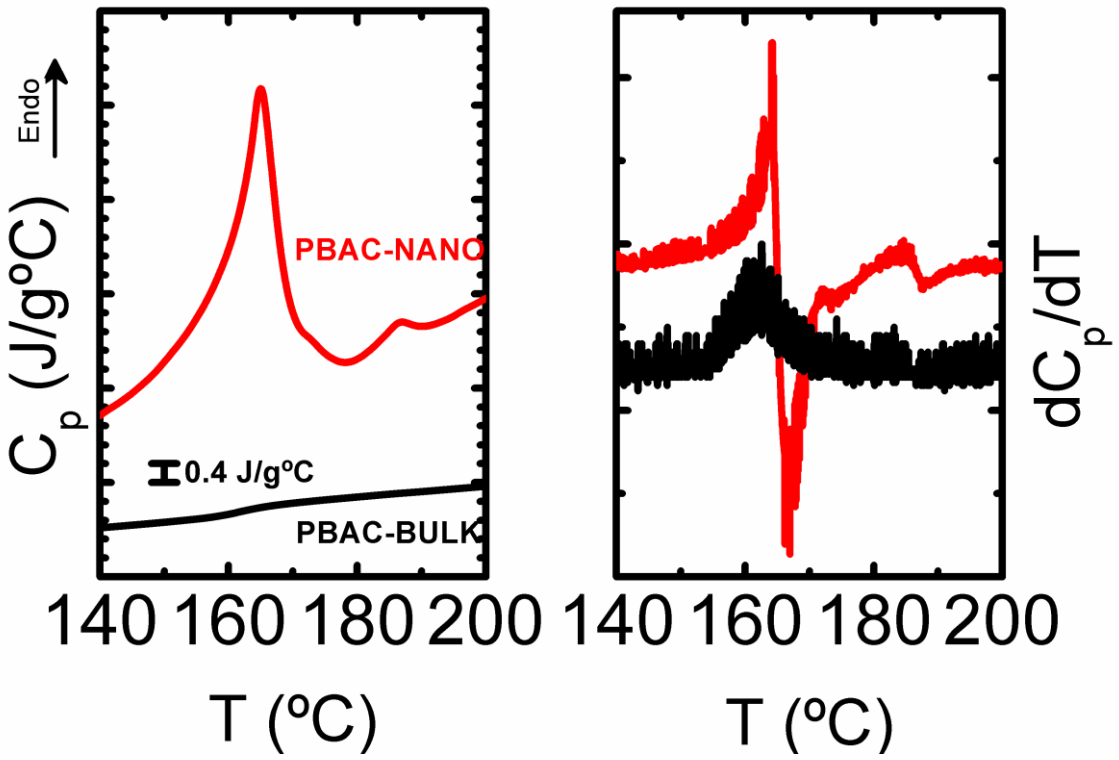

Figure 5.3. DSC trace and heat flow derivative of PBAC surfactant aided nanoparticles.

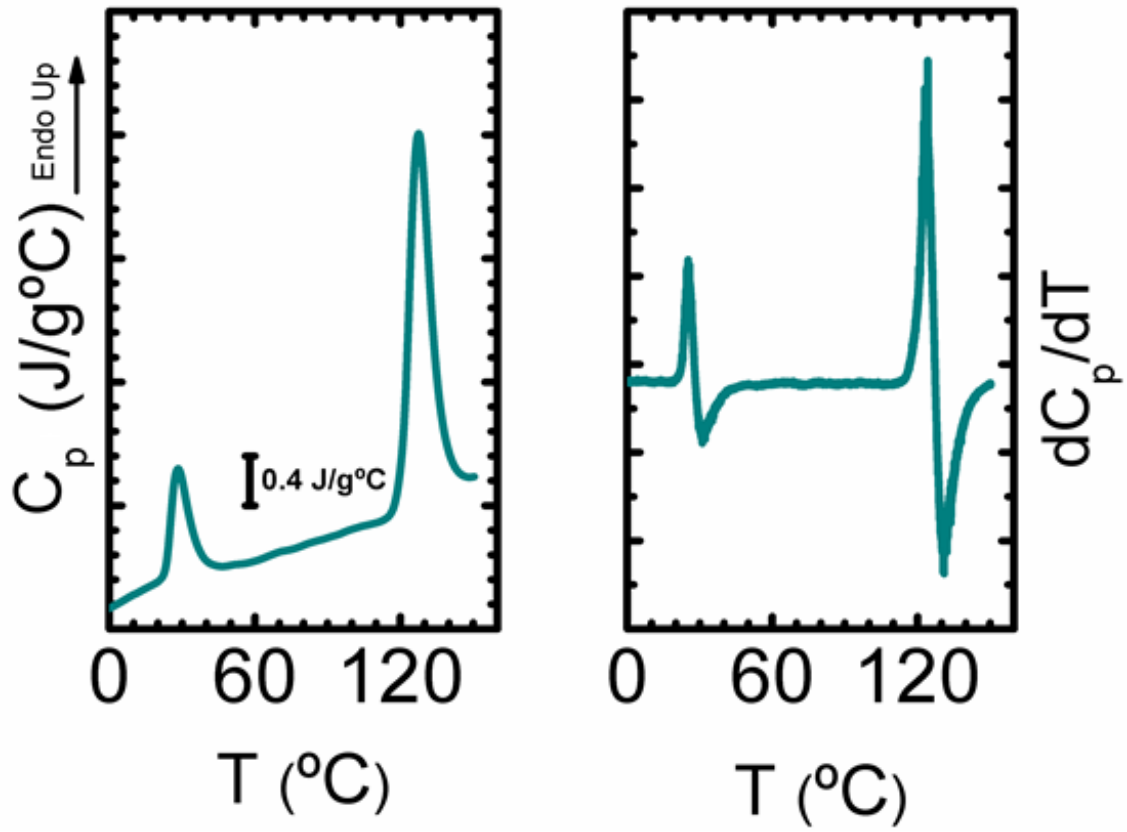

Figure 5.4. DSC trace of pure SDS (left). Heat flow derivative (right)

The general trend found in these results indicates that T_g increases when polymers are subjected to 3D-geometrical confinement. However, it is interesting that for different polymers, the way the confined T_g appears seems to change. This leads to asking the question whether how polymer nature is influenced by confinement arises. In table 5.1 it can be seen that for a variety of polymers the same T_g trend is maintained but not necessarily the magnitude of the T_g increase should be the same. Figure 5.5 shows the change of T_g ($\Delta T_g = T_{gNANO} - T_{gBULK}$) as a function of the bulk T_g of the polymers prepared by surfactant aided miniemulsion in this work. It is seen that ΔT_g increases with the bulk T_g of the polymer, indicating that polymer nature affects to the restrictions imposed. In section 5.3.4., this result is further discussed.

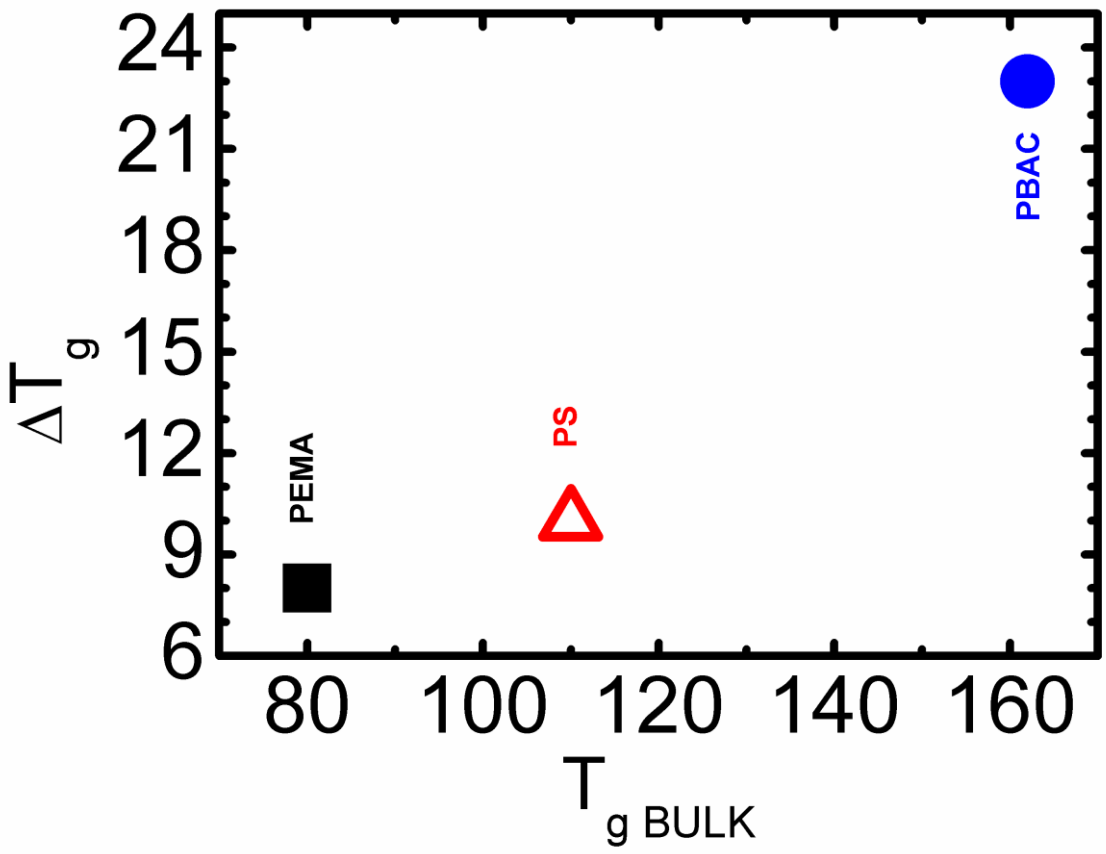

Figure 5.5. Change of T_g ($\Delta T_g = T_{gNANO} - T_{gBULK}$) as a function of the bulk T_g for the polymers prepared by surfactant aided miniemulsion.

5.3.2 Sub-micrometric particles

Influence of confinement on T_g was evaluated for PEMA sub-micrometer particles. DSC traces from these particles are presented in figure 5.6. The bulk calorimetric trace is also presented for comparison. The DSC results for these particles are summarized in table 5.1. In a first glance, the temperature position of the T_g is less affected by the volume restriction imposed by the micrometer confinement. In the case of surfactant aided particles (red line), the T_g appears in *dH/dT* with its maximum slightly displaced toward higher temperatures. As in the nanoparticles, a broader distribution of glass transition temperatures is observed. This is in agreement with the distribution of particles sizes that have been observed in the AFM images, where besides the larger particles, a non-negligible population of small spheres is observed. In the submicron spheres prepared by the non-surfactant method (PEMA4), the calorimetric trace in the T_g region appears to be very similar to that of the bulk. This can be related to the diameter distribution of the spheres. However, *dH/dT* for this submicron sample shows a small peak at high temperatures, indicated with an * in figure 5.6, that can be correlated to the response of small sized spheres that are seen in the AFM image. This small peak was verified in several DSC scans of samples with similar size distribution corroborating that this was not an artifact. In comparison with the sub-micrometer spheres, nanometric particles show a higher increase on the values of the T_g and the dH/dT peak gets narrower. These results point towards an increase of the glass transition temperature with decreasing particle size (table 5.1).

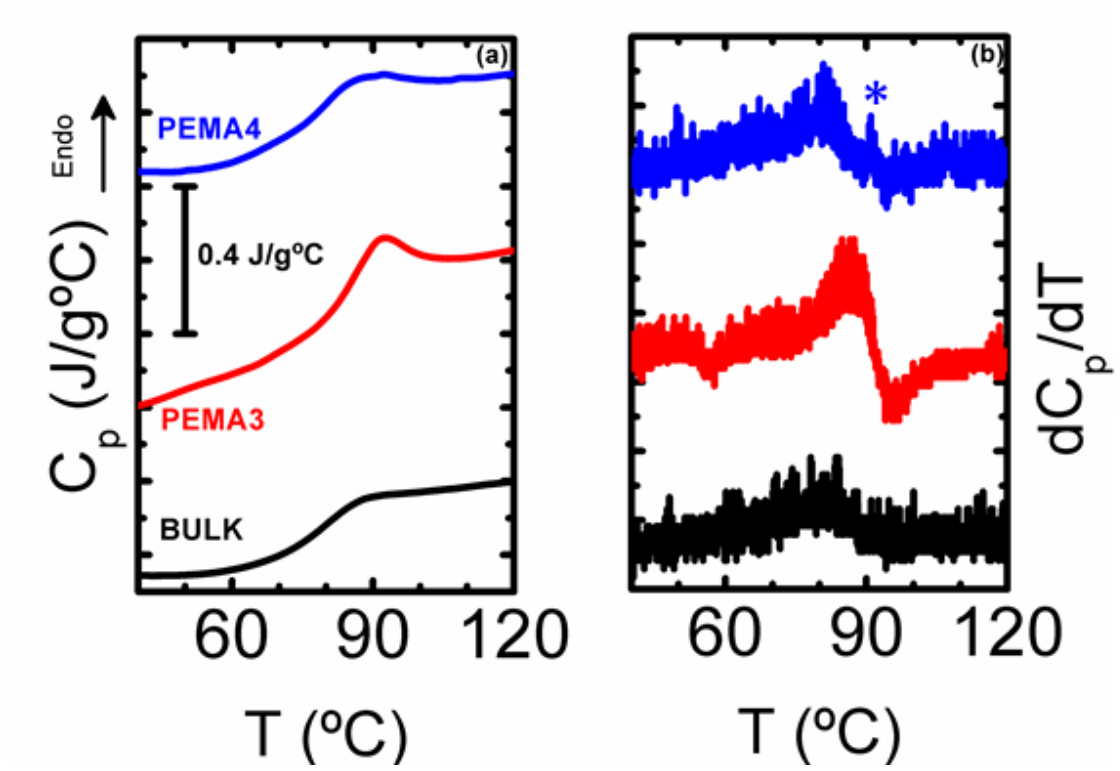

Figure 5.6. (a) DSC normalized traces of bulk PEMA (black) and PEMA sub-micrometer spheres. Red line corresponds to surfactant aided spheres, whereas the blue curve corresponds to surfactant free spheres. **(b)** Derivative of the heat flow with respect to T of the heat flow shown in **(a).**

5.4. Geometrical confinement above Tg

An interesting fact to be analyzed is whether nanospheres retained their shape even after heated above T_g. Nanoparticles of PEMA, deposited on Si were selected as sample. A first AFM topography scan was conducted (tapping, NCHV probe) and showed a nanoparticles array similar to the presented in chapter 3 for PEMA1. This result is shown in figure 5.7(a). Then, the sample was heated outside the microscope, following the same protocol as in the DSC experiment. Afterwards, another AFM topography scan was conducted, which results are shown in figure 5.7(b). In this figure, no nanoparticles can be found, but agglomerated *islands* are seen, which resemble the original dispersion of particles. This result can be evaluated also from the DSC trace. Subsequent DSC runs show that in all the nanostructured samples, the T_g returned to its bulk value after the first scan (Figure 5.7(c) and Figure 5.7(d) as an example). This effect can be understood by

considering the possible coalescence of different spheres once the system has enough mobility to allow interdifussion of chains from different spheres. These results are reproducible for PS and PBAC nanoparticles.

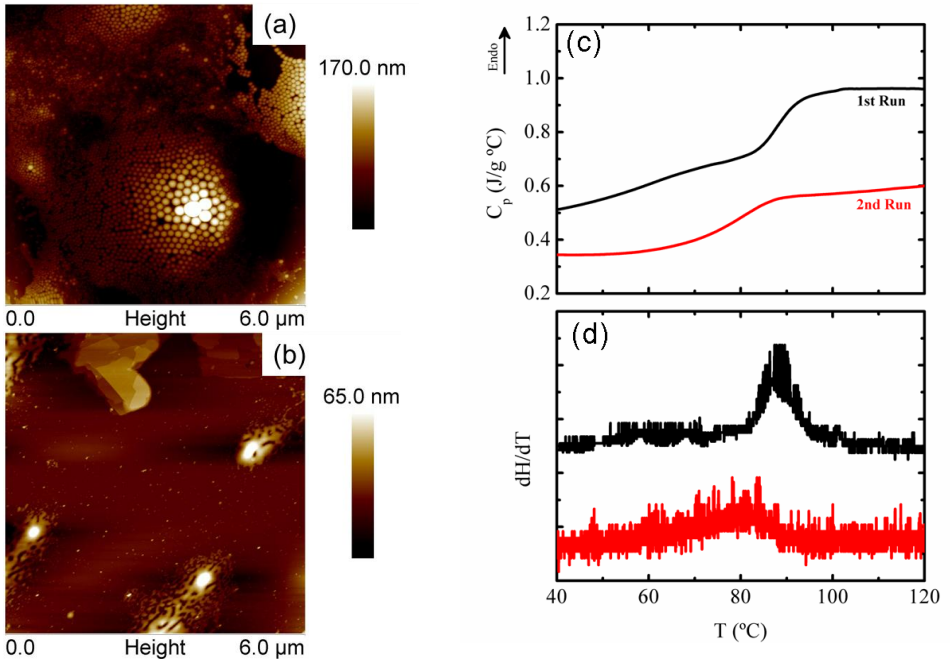

Figure 5.7. AFM scans (a) before and (b) after a DSC scan of PEMA nanoparticles (PEMA1). (c) DSC normalized traces of the 1st and 2nd scans, and (d) corresponding derivative of the heat flow. Similar results are obtained for SDS free PEMA nanoparticles.

5.5. Molecular arrangement in confiment

All of our results indicate that the three dimensional structuring of amorphous polymers in nanometer size spheres leads to an increase of the glass transition temperature with respect to that of the bulk. In this line, it has been reported very recently, an increase of 40ºC with respect to the bulk T_g of poly(methyl methacrylate) (PMMA) spherical nanoglobules with sizes ranging between 20 and 500 nm[9]. Li and coworkers [11], also showed that for nano-particle aggregates of atactic PMMA confined to nanospheres of 20-40 nm in diameter, there is an increase of 20 ºC in the T_g. The authors suggest the existence of a hard amorphous region, where the cooperative motion of the

repeating units was restricted. The increase of the T_g, due to the geometrical confinement, is not restricted to methacrylates. For example, similar increase in T_g has been reported for polystyrene nanoparticles [12, 13]. This behaviour was attributed to the hypothesis that when the polymer chains are in spheroid form, the chains are more compressed than on the bulk state. [12]. However, the literature on the subject shows the same controversy in the shift of T_g in confined polymer systems into nanospheres or nanodroplets, as well as in polymer thin films[4, 14-16]. The nanospheres assemblies prepared in this work provide an ideal system to study these effects, since interaction with any substrate has been minimized by the fact that most of the existent interphases are polymer/air and polymer/polymer, and, on the other hand, the imposed confinement is 3-dimensional, that allows to avoid possible chain stretching effects that appears in thin films, and that for sure have an impact on the glass transition temperature of the systems, besides size confinement.

There are several reviews available in the literature that discuss the issue of confinement entropy and its impact on T_g [4, 17]. First, based on the configurational entropy theory of the glass transition, developed by Gibbs and Di Marzio [18, 19] and extended by Adam and Gibbs [20] (equation 1.1, chapter 1), taking into account simply size effects, T_g should increase in confined polymers. Several years ago, Mi et al presented a thermodynamic model for accounting the increase of T_g in nano-sized single chain polymeric particles [21, 22] made of polymers with high molecular weight. The T_g behaviour related to single chain particles (SCP) has been studied extensively in the past decades, and the results for different systems have shown an increase in the glass transition temperature[13, 23-25]. According to the proposed model [21], the increase of the T_g in SCP is related to a decrease of the entropy in the system, due to a different arrangement of the

polymeric chains, imposed by the geometrical confinement. In fact, the model proposes that the behaviour of the T_g in the single chain particles (T_{gs}) is related to the bulk T_g (T_{gb}) by the following equation:

$$\ln \frac{T_{gs}}{T_{gb}} \cong \frac{kN}{\Delta C_p}\left(N^{-x/3} + N^{-2}\ln 2\right) \tag{5.1}$$

where k is the Boltzmann's constant, N the degree of polymerization, ΔC_p the specific heat change of the bulk material and x a constant that equates 5/3 for a self-avoid chain and 2 for a random-walk chain. Note that since the right side of the equation is always positive, the glass transition temperature of the single-chain polymer is always higher than the bulk. It is important to notice that to obtain the single chain polymers, all of the cited authors have worked with systems with high molecular weight (~ 10^6) that resulted in nanoglobules of similar size in comparison to this work. However, it is clear that in our case, as well as in other works [9], the final nanoparticle system is not a single chain polymer, although the behaviour seems to be related. In order to generalize this entropic model for SCP to a confined multiple chain particle system (MCP), the first consideration is how the number of conformations (C) of the polymer chain in the nanosphere is affected by the confinement. The number of conformations of a chain molecule can be calculated following the relation [26]:

$$C \approx \mu^{n_{u-SCP}} \tag{5.2}$$

where $\mu \approx$ 2-6 is the number of rotational isomers, determined by the type of monomer, and $n_{u\text{-}SCP}$ is the number of repeating units in a single chain, that is equal to the parameter N in equation (1). Therefore the main factor controlling the number of conformations of a SCP is the total number of repeating units. To generalize this relation to multiple polymer chains the number of possible conformations can be obtained by means of simple

combinatory mathematics as:

$$C \approx \mu^{n_u \cdot n_c} \tag{5.3}$$

where n_u is the number of repeating units in each chain and n_c is the number of chains per particle. The relation for SCP (equation 5.2) is recovered if $n_c = 1$. From equation (5.3), it follows that the number of conformations of the system is controlled by the product $n_u \cdot n_c$, which is just the total number of repeating units in the particle. According to the results in the literature, the advantage of having a SCP system is that there are less possible states for the organization of the chain (highly ordered system[27]) since $n_{u\text{-}SCP}$ is low, and thus there is a reduced entropy.

Similarly, for MCP the total number of repeating units in the system is the key parameter that controls the possible conformational states, and thus the entropy. Nanospheres offer a framework for obtaining MCP systems with a reduced number of repeating units, regardless the molecular weight of the polymer. Provided that the product $(n_u \cdot n_c) \approx n_{u\text{-}SCP}$, the MCP system should have the same conformational possibilities as the SCP, which leads to a similar entropy behaviour. Possible interaction among different chains should not be different from the interactions of a chain with itself since the entanglement of the polymeric systems, do not allow a chain to distinguish its own repeating units from the rest. Also, in our hypothesis, the influence of the end-groups is not taken into account since its proportion with respect to the total repeating-units is negligible (about 0.5% in the worst case scenario). With these ideas in mind we may postulate that, if a polymer system is confined to a volume where the number of repeating units $(n_u \cdot n_c)$ is below a certain value, the available conformational states are reduced and consequently the arrangement of the chains must be different from that of the bulk. Thus

the entropy of the system is reduced, leading to an increase of T_g. Above this number of repeating units threshold, the system behaves in the same manner as in the bulk state.

In order to probe this postulate, we have analyzed the results available in the literature together with results shown in section 5.3. The number of chains in a polymeric nanoparticle can be calculated following the discussion presented by Pilcher and Ford [24], and using the formula:

$$n_c = \frac{V\rho N_A}{M_W} \tag{5.4}$$

where V is the volume of the nanoparticle, ρ its bulk density, N_A the Avogradro's number and M_W the molecular weight of the polymer. The degree of polymerization (N) can be calculated as:

$$N = n_u = \frac{M_W}{M_O} \tag{5.5}$$

where M_O is the molecular weight of the monomeric unit. Notice that the degree of polymerization (N) is just the number of monomers per polymeric chain, and thus equal to n_u. Finally, the total number of repeating units in a nanoparticle system follows the relation:

$$n_{total} = n_c \cdot n_u = \frac{V\rho N_A}{M_O} \tag{5.6}$$

We have applied this set of equations to the data available in the literature, for amorphous polymers subjected to 3D-confinement. The results are summarized in table 5.2, and arranged with increasing n_{total}.

A trend for the onset of induced confinement effects in polymeric nanospheres is

observed in table 5.2. There are two marked regions, determined by a threshold value of n_{total} around 10^5, where the confinement effects are clearly distinct. For $n_{total} < 10^5$, all the gathered evidence points towards an increase of T_g, that is based on the decrease of entropy in the nanospheres due to less possible conformational states. Notice that this behaviour depends only on the total number of repeating units per particle instead of the number of chains. This observation supports the idea that the value of n_{total} is a key parameter when analyzing the possible conformational states for any polymeric system.

Table 5.2. Changes in T_g in this work and in the literature and their corresponding number of repeating units per particle in each case.

Reference	Polymer	Nanosphere Diameter	Change in Tg	n_c	n_{total}
Li et al. [11]	a-PMMA	20 nm	↑	1.42	**3 x 10^4**
Guo et al. [9]	PMMA	20 nm	↑	198	**3 x 10^4**
Pilcher and Ford. [24]	s-PMMA	20 nm	↑	1.19	**3 x 10^4**
Ming et al. [13]	PS	22 nm	↑	3.73	**4 x 10^4**
Mi et al. [21]	PAL	20 nm	↑	1.00	**4 x 10^4**
Paik and Kar. [12]	PS	25 nm	↑	5.37	**5 x 10^4**
Qian et al. [23]	PS	26 nm	↑	1.51	**6 x 10^4**
Present work[28]	PEMA	35 nm	↑	190	**8 x 10^4**
	PS	35 nm	↑	170	**8x10^4**
	PBAC	52 nm	↑	730	**9x10^4**
Ding et al. [29]	PS	> 40 nm	↓	82.4	**2 x 10^5**
Sasaki et al. [30]	PS	> 42 nm	---	93.6	**2 x 10^5**
Present work	**PEMA**	**> 100 nm**	**---**	**> 5.6 x 10^4**	**> 2 x 10^7**

On the other hand, when n_{total} is increased over 10^5, there seems to be no change in T_g, only contradicted in one particular case. According to the equations previously presented, the larger the values of n_{total}, the higher the entropy of the system since there are more available conformational states of the polymeric repeating units. When this value is

greater than some threshold (~ 10^5), although the system is in nanoscale geometry, the sample behaves just like in the bulk. There are some exceptions to the trend presented here, like the case of polystyrene presented by Ding and coworkers [29]. However, this work and several others have been recently reviewed by Zheng and Simon [31], who managed to prove that problems during the preparation steps lead to a plasticizer effect that ultimately generates the decrease in the T_g. There are other works, as reviewed by Mi et al [22], where the authors evidenced an increase of the entropy in single chain polymeric particles. However, in those works, some key parameters, such as the size of the particles were not presented, so it was impossible to quantify the value of n_{total}. Also, in the case of the work by Sasaki et al [30], although no change in the T_g position could be measured, a clear decrease in the $\Delta \boldsymbol{C}_p$ of the polymer nanospheres, with decreasing diameter of the nanospheres, could be found. Changes in $\Delta \boldsymbol{C}_p$ can be related to changes in entropy of the system, thus agreeing with our model. Anyhow, as reviewed by Koh[20], the change in the T_g position does not always relates to a specific $\Delta \boldsymbol{C}_p$ trend, making the use of this parameter really difficult as a fundamental quantity for describing the changes due to confinement.

In order to further explain the details regarding the increase of T_g in nanoparticles, one should consider the polydispersity on the size of the prepared nanoparticles. From the size distribution histograms, it is possible to obtain a histogram of the number of repeating units per particle studied in this work (section 5.3.1.), and it is presented in Figure 5.8. As observed in this figure, there is a large portion of particles with less repeating units than the provided threshold, and therefore, those nanospheres exhibit a higher T_g than the bulk. In any case, the calculations presented in this figure are estimations, since effects such as polydispersity of the molecular weight has not been

taken into account. These effects and the fact that the mode of the distribution of number of monomers per particle in the case of PBAC is clearly above the established threshold may be the cause of the bimodal T_g observed in PBAC nanospheres (figure 5.3).

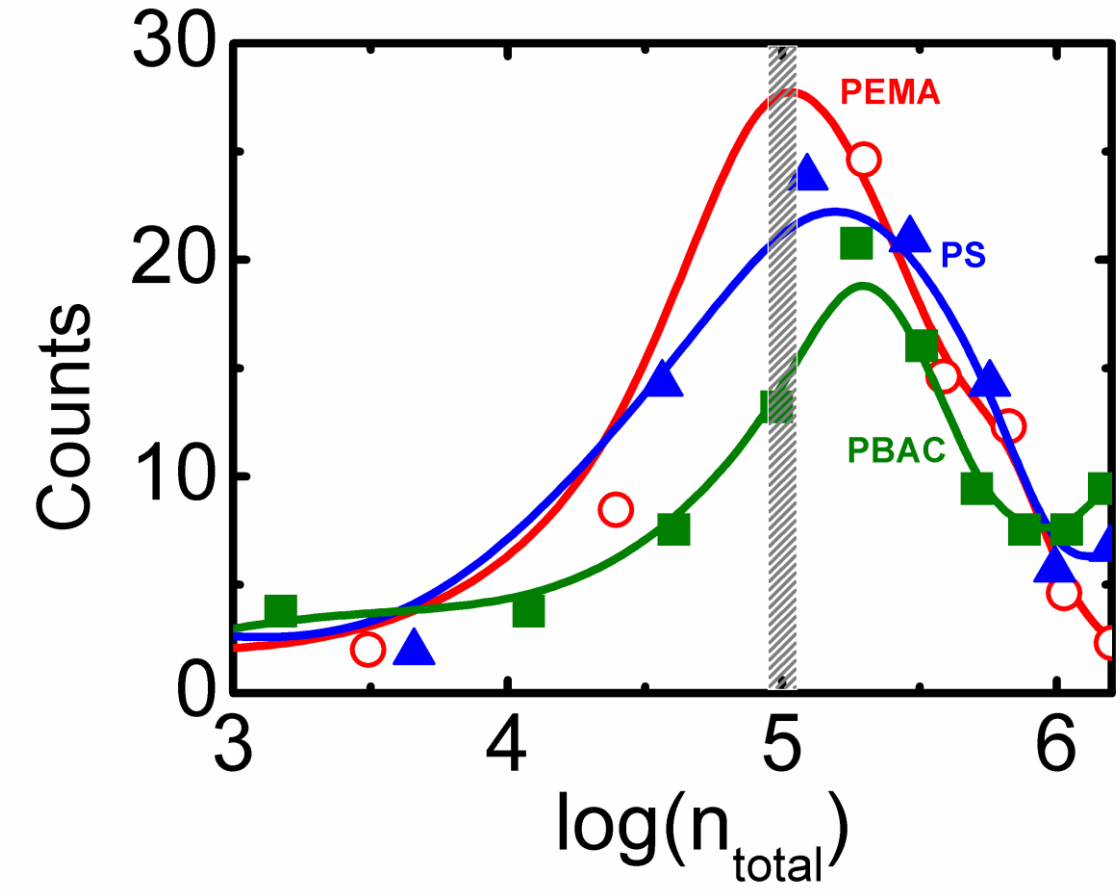

Figure 5.8. Distribution of number of monomers per particle, calculated from the size distributions presented in figures 3.1 and 3.2. (■) PBAC, (▲) PS and (○) PEMA

The experimental results presented here shows that 3D confinement imposed to the polymer chain always results in an increase of glass transition or it does not affect it at all. We have not observed any decrease of T_g with 3D confinement. These evidences can be explained by our proposed model of entropic decrease. However, we are aware that along the literature some authors have found decreases in T_g when polymers are confined into nanospheres. Recent works by Zhang[32] and Feng[33], analyzed the T_g behaviour in PS nanoparticles suspended in water, under several confinement conditions. Both groups found that for surfactant free PS nanoparticles, with diameter from 700 nm to 20 nm, a

decrease in T_g was measured by different DSC approaches. The results were explained using a free surface model by comparing the free nanoparticles with capped PS nanoparticles, with inorganic[32] and surfactant[33] shells, where no thermodynamic change took place. The existence of a free surface layer deals primarily with the interaction between the polymer system and the surrounding media (water in these specific cases) instead of with the arrangement of the polymer within the nanoparticles, as in our model. Also, in these works several approaches have been proposed regarding how to measure the physical properties of nanoparticles in confinement. In both works, a drop of the nanoparticle emulsion was poured into an aluminium pan (specifically designed for liquids), and the calorimetric trace was recorded. To avoid reaching the boiling temperature of water, scans are performed at 6 atm. However, none of the authors discuss the influence of pressure regarding the changes in T_g and/or possible changes in the geometry of the nanostructures. Another method that has been used to measure physical properties of nanoparticles consists in drop casting the emulsion into the sample holder to be used. An accumulation of drops leads to the formation of a *"film of particles"*. Afterwards, the drop casted sample holder is put into vacuum to remove possible excess of water[34]. Although this method allows removing water from the emulsion, handling of the samples is not simple and takes several days if one wish to accumulate enough weight to perform the measurement.

It is worth mentioning new studies conducted by Boucher[35] and Zhang[34] where a decoupling between cooperative segmental mobility and the glass transition temperature, in thin polymer films and organic nanospheres, is suggested. The authors propose that molecular mobility could not be one-to-one related to the calorimetric T_g due to the presence of surface effects in nanoconfined systems and serve as a platform to

contextualize results available in the literature where a T_g decrease is reported. Recent works in thin films geometries point towards the extra free volume induced at the interfaces in these geometries as responsible for perturbation in the glassy dynamics, in particular, modifications in monomer density at the interface[6]. In that framework, our results and analysis suggest that in the PEMA, PS and PBAC nanoparticles with diameters well below 100 nm, the chains are packed in such a way that free volume is considerably reduced compared to the bulk. In this sense, the present system of polymer nanospheres could serve as a platform to test proximity effects for recently proposed models like the lattice model of dynamic heterogeneity and kinetic arrest in glass forming liquids[7].

Although the model here proposed aims to explain the increase of T_g in 3D confined polymers, the question whether how polymer nature is influenced by confinement arises. The polymers studied here have different chain rigidity, and this affects its bulk T_g. To understand the role of rigidity on the observed shift on T_g, going back to figure 5.5, the change of T_g ($\Delta T_g = T_{gNANO} - T_{gBULK}$) as a function of the bulk T_g of the polymers was shown. It is seen that the observed shift in T_g is stronger the higher is the T_g of the bulk polymer. In order to understand this result, we may invoke the Adam and Gibbs[36] theory that predicts the existence of rearranging regions in which several basic structural units may only relax in cooperative way. These regions are named as cooperatively rearranging regions, CRR, and their characteristic size ξ, increases with decreasing temperature. In the Adam-Gibbs theory of the glass transition, the growth of the cooperative length scale as temperature decreases is due to the decrease of the configurational entropy (S_c) which is inversely proportional to the number of *'units'* involved in the relaxation. If one assumes that the number of monomers involved in a

CRR is proportional to its volume, then:

$$\frac{\xi}{2} \approx S_c^{-1/3} \tag{5.7}$$

Therefore, a decrease in the configurational entropy implies an increase in the characteristic size of the CRR. In this sense, the dependence of the shift in T_g with the glass transition may indicate a stronger hindrance of the available configurations when the polymer is more rigid. This serves as evidenced that polymer nature affects the way confinement takes place and thus the restrictions imposed affect the way a polymer forms the cooperative rearranging regions at the glass transition temperature.

5.6. Summary

An increase of the glass transition temperature (T_g) was found for PEMA, PS and PBAC nanoparticles, in a dimension range well below 100 nm. By a systematic preparation and discrimination of the different variables that may affect the glass transition of the droplets of few polymer chains we have demonstrated that the main contributing factor that affects the shift or no shift of the T_g is the number of possible conformations, which is given by the number of monomers in the droplet. In this work we propose that, the 3D-confinement imposed to the polymer chains can be rationalized taking into account thermodynamical considerations and that it should be independent on the polymer system. Precisely, it has been proposed that a decrease of entropy, due to the less possibilities of arrangement of the polymer chains imposed by geometrical confinement, is responsible for the observed positive shift in the glass transition temperature of the nanospheres. These results were explained by invoking a reduction of entropy in the system, due to the decrease of the possible conformational states, which

ultimately lead to a better arrangement of the polymeric chains in the nanosystem. Our model correlates well with a significant amount of results available in the literature for the past two decades, dealing with different polymers and preparation methods.

5.7. References

1. Priestley, R. D.; Ellison, C. J.; Broadbelt, L. J.; Torkelson, J. M. Science **2005,** 309, (5733), 456-459.
2. Richert, R. Annual Review of Physical Chemistry **2011,** 62, (1), 65-84.
3. McKenna, G. B. Eur. Phys. J. Spec. Top. **2007,** 141, (1), 291-301.
4. Alcoutlabi, M.; McKenna, G. B. Journal of Physics: Condensed Matter **2005,** 17, (15), R461.
5. Martín, J.; Mijangos, C.; Sanz, A.; Ezquerra, T. A.; Nogales, A. Macromolecules **2009,** 42, (14), 5395-5401.
6. Napolitano, S.; Rotella, C.; Wubbenhorst, M. Acs Macro Letters **2012,** 1, (10), 1189-1193.
7. Tito, N. B.; Lipson, J. E. G.; Milner, S. T. Soft Matter **2013,** 9, (11), 3173-3180.
8. Uemura, T.; Yanai, N.; Watanabe, S.; Tanaka, H.; Numaguchi, R.; Miyahara, M. T.; Ohta, Y.; Nagaoka, M.; Kitagawa, S. Nat Commun **2010,** 1, 83.
9. Guo, Y.; Morozov, A.; Schneider, D.; Chung, J. W.; Zhang, C.; Waldmann, M.; Yao, N.; Fytas, G.; Arnold, C. B.; Priestley, R. D. Nat Mater **2012,** 11, (4), 337-343.
10. Schick, C. Eur. Phys. J. Spec. Top. **2010,** 189, (1), 3-36.
11. Li, L.; Li, B.; Chen, J.; Zhou, D.; Xue, G.; Liu, X. Polymer **2004,** 45, (8), 2813-2816.
12. Paik, P.; Kar, K. NSTI-Nanotech **2006,** 1, 483-486.
13. Ming, W.; Zhao, J.; Lu, X.; Wang, C.; Fu, S. Macromolecules **1996,** 29, (24), 7678-7682.
14. Forrest, J. A.; Dalnoki-Veress, K. Advances in Colloid and Interface Science **2001,** 94, (1–3), 167-195.
15. Bäumchen, O.; McGraw, J. D.; Forrest, J. A.; Dalnoki-Veress, K. Physical Review Letters **2012,** 109, (5), 055701.
16. Tsui, O. K. C., Anomalous Dynamics of Polymer Films. In Polymer Thin Films, Tsui, O. K. C.; Russell, T. P., Eds. World Scientific: 2008; p 312.
17. Huck, W. T. S. Chemical Communications **2005,** 0, (33), 4143-4148.
18. DiMarzio, E. A.; Gibbs, J. H. The Journal of Chemical Physics **1958,** 28, (5), 807-813.
19. Gibbs, J. H.; DiMarzio, E. A. The Journal of Chemical Physics **1958,** 28, (3), 373-383.
20. Koh, Y. P.; McKenna, G. B.; Simon, S. L. Journal of Polymer Science Part B: Polymer Physics **2006,** 44, (24), 3518-3527.
21. Mi, Y.; Xue, G.; Wang, X. Polymer **2002,** 43, (25), 6701-6705.
22. Mackay, M. E.; Dao, T. T.; Tuteja, A.; Ho, D. L.; Van Horn, B.; Kim, H.-C.; Hawker, C. J. Nat Mater **2003,** 2, (11), 762-766.
23. Qian, R.; Wu, L.; Shen, D.; Napper, D. H.; Mann, R. A.; Sangster, D. F. Macromolecules **1993,** 26, (11), 2950-2953.
24. Pilcher, S. C.; Ford, W. T. Macromolecules **1998,** 31, (11), 3454-3460.
25. Lu, X.; Xue, G.; Mi, Y. Journal of Applied Polymer Science **2011,** 119, (4), 2310-2317.
26. Chan, H. S.; Dill, K. A. Physics Today **1993,** 46, (2), 24-32.
27. Barbara, P. F.; Gesquiere, A. J.; Park, S.-J.; Lee, Y. J. Accounts of Chemical Research **2005,** 38, (7), 602-610.
28. Martínez-Tong, D. E.; Soccio, M.; Sanz, A.; García, C.; Ezquerra, T. A.; Nogales, A. Macromolecules **2013,** 46, (11), 4698-4705.
29. Ding, J.; Xue, G.; Dai, Q.; Cheng, R. Polymer **1993,** 34, (15), 3325-3327.
30. Sasaki, T.; Shimizu, A.; Mourey, T. H.; Thurau, C. T.; Ediger, M. D. The Journal of Chemical Physics **2003,** 119, (16), 8730-8735.
31. Zheng, W.; Simon, S. L. Polymer **2006,** 47, (10), 3520-3527.
32. Zhang, C.; Guo, Y.; Priestley, R. D. Macromolecules **2011,** 44, (10), 4001-4006.
33. Feng, S.; Li, Z.; Liu, R.; Mai, B.; Wu, Q.; Liang, G.; Gao, H.; Zhu, F. Soft Matter **2013,** 9, (18), 4614-4620.
34. Zhang, C.; Boucher, V. M.; Cangialosi, D.; Priestley, R. D. Polymer **2013,** 54, (1), 230-235.
35. Boucher, V. M.; Cangialosi, D.; Yin, H.; Schonhals, A.; Alegria, A.; Colmenero, J. Soft Matter **2012,** 8, (19), 5119-5122.
36. Adam, G.; Gibbs, J. H. The Journal of Chemical Physics **1965,** 43, (1), 139-146.

CHAPTER 6 – On the crystallization behavior under confinement

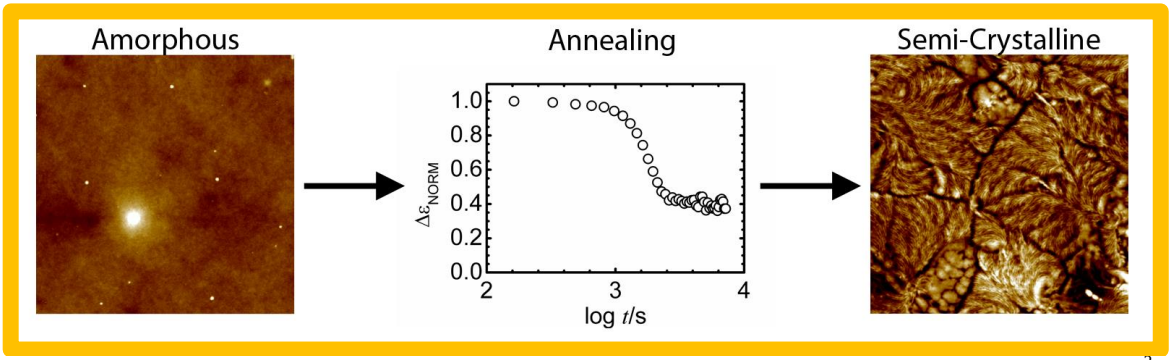

Amorphous to semi-crystalline transition in PLLA. At the corners of the picture, AFM images (5x5)mm^2. In the center, variation of the dielectric strength as a function of time, indicating the crystallization of the polymer chains.

Crystallization of polymers under confinement is presented in this chapter. Two different confined geometries have been explored: polymer thin films and polymer nanoparticles. Poly(lactic acid) based polymers are used a samples, due to their biodegradability/biocompatibility from the applications point of view, and also since these polymers present interesting crystallization morphologies and a crystallization rate that allows following real time organization of the molecules in the experimental time scale. Under the thin film geometry, crystallization is studied first by atomic force microscopy for uncapped films (those with a free polymer layer in contact with air), and afterwards by dielectric spectroscopy in capped films (*sandwich*-like structures). In a second section, crystallization of polymer nanoparticles is studied by x-ray scattering. The impact of preparation methods in the final crystallization of the nanoparticles is discussed. Also, the possibility of preparing nanocrystals from polymer nanoparticles is shown.

*Part of the work described in this chapter has been published in *Macromolecules* 2014, **47**(7), 2354-2360

6. 1. Introduction

Under particular circumstances, some polymers may crystallize. However, it is known that in an assembly of polymer chains that are coiled and mutually interpenetrated, it is nearly impossible to reach a complete crystallization state. Like for smaller molecules[1], crystallization becomes even more sluggish when the chains are confined at the nanoscale level[2, 3]. Confinement is able to induced different morphologies[4, 5], reduced crystallization rates by several orders of magnitude[6, 7], and in some cases, inhibition of crystallization within the experimental time scale[8]. In thin film geometry, the sample thickness becomes a crucial parameter controlling crystallization[2], while surface effects mostly lead to a competition between adsorption to the solid surface and nucleation of polymer crystals [2, 4, 9-11].

Among the most studied confining geometries are thin films, probably due to their presence in a large number of technological applications, and also because it provides an easy control of the level of confinement and tunability of interfacial interactions between polymers and substrates[12]. Also, polymer thin films represent highly metastable forms of matter, presenting unexpected properties [13] which have been widely discussed by the scientific community in the past years [14-21]. In this geometry, it is also possible to attain information of the role of interfacial interactions by intercalating a polymer thin film in between two adsorbing layers[19], although the introduction of burying interfaces limits the possible experimental protocols; for example, metallization of both polymer faces does not permit an optical access to the polymer surface. On the other hand, using confined polymers into droplets and nanoparticles might serve as starting point in order to prepare *nanocrystals* and also to better understand the mechanisms involved during nucleation and crystallization in confined geometries[22, 23].

In this chapter we present the crystallization behavior of polymers in confined geometries. First, polymer thin films are discussed and later on crystallization in polymer nanoparticles is presented. Also, by means of dielectric spectroscopy, the relation between inhibition of crystallization and absorption is investigated.

6.2. Crystallization in polymer thin films

The study of the crystallization of polymer confined to thin films, was carried out at IEM-CSIC, as well as at ULB and at KUL. Poly(L-lactic acid) (PLLA) was used as the case study.

6.2.1. Samples and techniques

Capped thin films, and supported thin films of PLLA were prepared following the protocols described in chapter 3 (section 3.4). For both cases, chloroform was used as solvent. Capped polymer films were prepared to perform broadband dielectric spectroscopy (BDS) measurements. Thickness of the films was controlled by the polymer-solvent concentration. Once spin coating was completed, samples were annealed at 64 ºC for 30 minutes, to allow chloroform residues to evaporate. BDS measurements were conducted isothermally at 70 ºC. Details of the equipment are found in chapter 2 (section 2.2.2). Before BDS measurements, the prepared capped films were melt-quenched outside the spectrometer by placing them on a hot plate at 453 K (180 ºC) for 30 s and then onto the cool surface of a metallic box filled with liquid nitrogen ($T<<T_g$). By this procedure crystallization prior to the measurements is avoided. The dielectric spectra were evaluated within the framework of the phenomenological Havriliak-Negami function (equations 2.5 and 2.6).

In the case of supported thin films, a master solution at 2 wt% was prepared and continuously diluted, in order to obtain several thicknesses. After spin coating, the samples were melt-quenched in a hot plate. This process is carried out by heating the silicon wafers at 180 ºC for 30 s and inmedialty removed and cooled down using a the cool surface of a metallic box filled with liquid nitrogen. This last step was performed to ensure a completely amorphous sample. Thicknesses of the prepared films and crystallization were analyzed by AFM. Topography measurements were condcuted in tapping mode, using NSG30 probes.

6.2.2. Crystallization behavior of capped thin films

BDS is an effective tool to measure the dynamics of polymer materials. Specifically, it has been of great interest towards measuring the segmental (α) relaxation in polymers, previously discussed in chapter 1. Near the glass transition temperature, the α-relaxation can be observed by BDS as a peak in the imaginary part of the dielectric permittivity (ε''). The area under the peak is related to the amount of possible *relaxing units* in the polymer, *i. e.* the polymer units that can freely orient towards the applied electric field. In the case of an amorphous polymer, in principle, all polar units can orient towards the applied field. As the polymer crystallizes, the α-relaxation peak may suffer two possible changes. When polymer chains incorporate into the growing crystal, the fraction of mobile entities is reduced by the hindrance imposed by the crystalline structure, thus leading towards a decrease in the relaxation's peak area (decrease in $\Delta\varepsilon$). Also, this decrease in mobility is evidenced by a change in the position of the maximum of the relaxation peak (τ_α), towards lower frequencies, due to the hindrance of segmental

motions imposed by the crystalline structure. Thereby, the changes in these two parameters serve as signals to monitor the crystallization of polymers.

Following the steps provided in section 6.2.1. PLLA capped films were prepared in a thickness range from 300 nm down to 8 nm (Table 6.1). Results of the BDS isothermal experiments are presented and discussed in three sections. Section (A) presents a description of the effect of nanometric confinement on the α–relaxation of amorphous thin films of PLLA. In Section (B) we discuss the impact of crystallization on the structural peak as a function of the film thicknesses. Finally, in section (C), we analyze the interplay between crystallization kinetics and irreversible chain adsorption on the substrate.

(A) Shape of the relaxation for amorphous thin films

Figure 6.1 shows the dielectric loss data as a function of frequency for two PLLA thin films of thicknesses h = 150 nm and 8 nm, respectively representative of a bulk-like and an interfacial behavior. The top panels show the first dielectric sweep (t = 0 s), where the polymers are in the amorphous state. Dielectric loss curves have been fitted to equation 2.5. In both cases a strong maximum in $\varepsilon''(\omega)$, attributed to the structural (α–) relaxation [24], is centered around 100 Hz. Besides the structural relaxation process, the 150 nm (figure 6.1a) film shows also a conductivity tail (σ) at low frequencies, and an excess of dielectric loss at high frequencies. The latter tail can be related to a local relaxation process, as previously reported for bulk PLLA [24]. Within the experimentally accessible frequency window, the 8 nm thick-film (figure 6.1c) does not shows the conductivity tail, while the local process is covered by a strong process, θ, related to the resistivity of the electrode [19]. This process has been described with a Debye function,

imposing $b = c = 1$ in equation (2.5). When compared with the thicker films, the α–relaxation of the thinner film is broader, less intense and it is shifted towards lower frequencies.

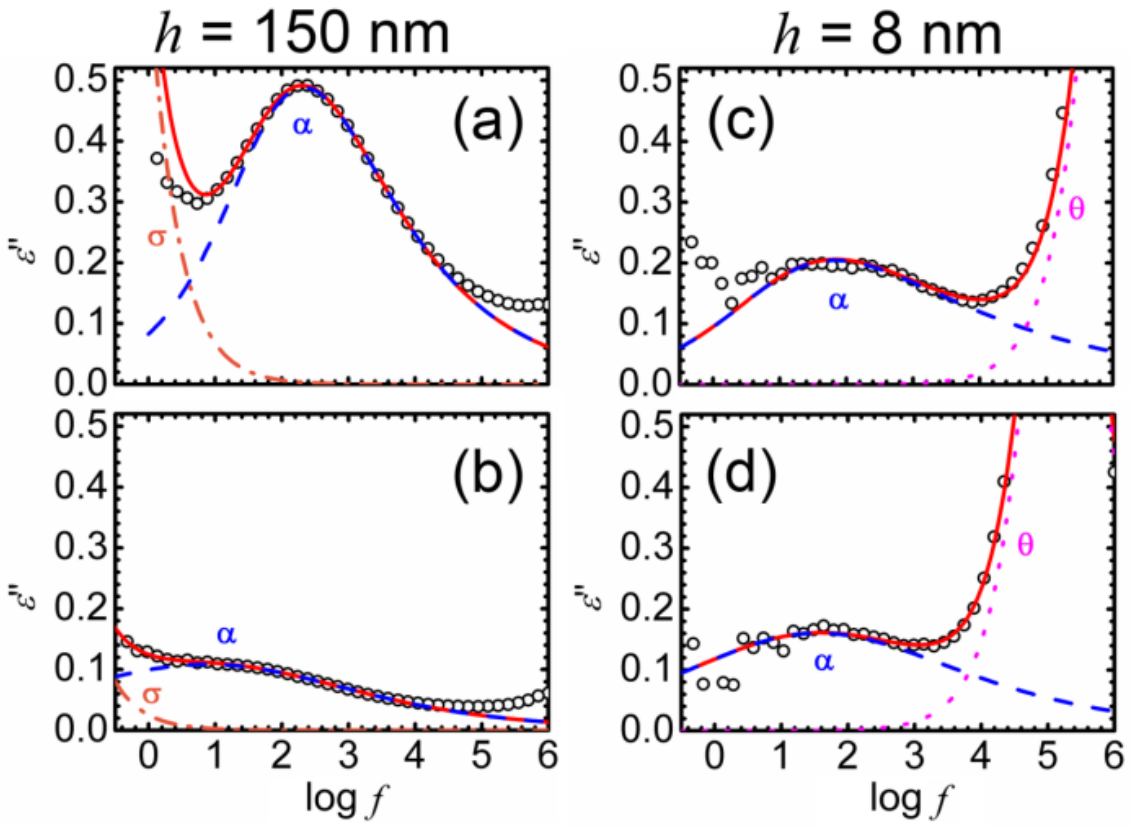

Figure 6.1. BDS spectra for two PLLA thin films. (a) and (b) correspond to a film of thickness = 150 nm, amorphous and semicrystalline (t = 25 min) respectively. (c) and (d) correspond to a film of thickness = 8nm, amorphous first sweep and amorphous last sweep (t =1600 min) respectively.

Figure 6.2 shows the HN parameters of the relaxation curve, for the amorphous films as a function of thickness (h). Figure 6.2(A), shows the α- mean relaxation time $\langle\tau\rangle$, calculated via equation (2.6). $\langle\tau\rangle$ is constant for the thicker films and, below a given thickness threshold (≈ 50nm), it increases with decreasing h. An increase of the mean relaxation time can be related to a hindrance in the motion of the molecular entities involved in the segmental relaxation process [25]. Under the experimental geometry chosen for our experiment (capped electrodes), the slowing of the α-relaxation process with decreasing thickness cannot be related univocally to a single phenomenon, since there is a

competition between the finite size effects and the adsorption of the polymer to the metallic electrodes (polymer-substrate interaction). In the following sections, we present a deeper insight about these effects.

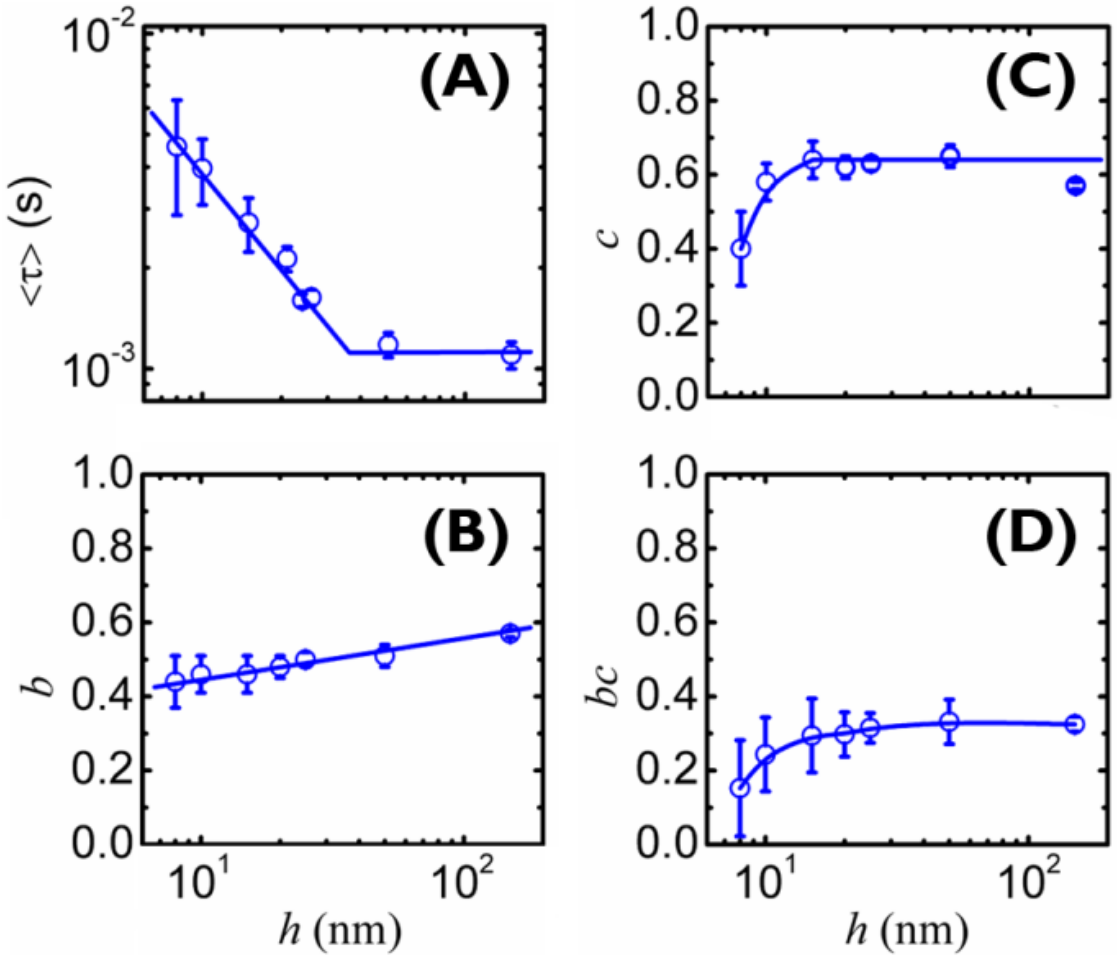

Figure 6.2. Variation of Havriliak-Negami parameters with thickness (*h*) for amorphous PLLA films.

With respect to the shape parameters of the relaxation (figures 6.2(B – D)), for all thicknesses, the values of *b* and *c* indicate that the dielectric function is broad and asymmetric, as for bulk amorphous polymers [25]. However these parameters also show thickness dependence. In particular, the symmetric width *b* of the relaxation function shows a continuous decrease with decreasing film thickness. According to the formalism proposed by Schönhals and Schlösser [26, 27], shape parameters of the HN function, describing the structural relaxation process, can be related to molecular interactions.

Following this model, the thickness dependence of the *b* parameter indicates that in the thinner film, geometrical confinement leads to stronger intermolecular interactions. On the other hand, according to this model, the changes suffered by the local chain dynamics can be evaluated by the asymmetric broadening *c* and the product *bc*. In both cases, these parameters show a plateau for all samples above 20 nm thickness. Below this value, *c* and *bc* exhibit a pronounced decrease with decreasing thickness which can be related to the hindrance in the local chain dynamics due to chain adsorption at the metallic interface. Thus, it is evidenced that the different trends for the *b* and *c* HN parameters might serve as indicators for discerning between confinement and adsorption processes.

(B) Effect of crystallization on the shape of the α relaxation for different thicknesses

The behavior of the α relaxation during crystallization, in the case of the thicker films, is very similar to what has been reported previously for bulk PLLA [24]. Figure 6.1b shows the α relaxation of a 150 nm film after 25 minutes at 343 K. Compared to the data for the amorphous film (figure 6.1a), the maximum of the α-relaxation has shifted toward lower frequencies and its area has decreased. However, the behavior is very different for the thinner films. Figures 6.1c and 6.1d show that, for the 8 nm film no relevant changes in its dielectric spectra are observed, even after t = 1600 min (figure 6.1d). The time evolution of the HN parameters for these films is presented in figure 6.3. The α–relaxation time $<\tau>$ for h = 150 nm, shows a sigmoidal increase with crystallization time similar to what observed in bulk [28].

As the crystallization takes place, there is a reduction of the amount of polymer segments involved in the α relaxations and there is an overall slow-down of the relaxation.

The 8 nm film shows a different behavior, characterized by slight increase of the mean relaxation time with time. Δε for the 150 nm film follows a step-like decrease with increasing time. This sigmoidal decrease of Δε with crystallization time has been interpreted, in the case of crystallizing bulk polymers, as the incorporation of chains into the growing crystals and the consequent inhibition of segmental relaxation [28]. According to that, the sudden decrease in Δε relates to the onset of crystallization as shown for the 150 nm film in figure 6.3.

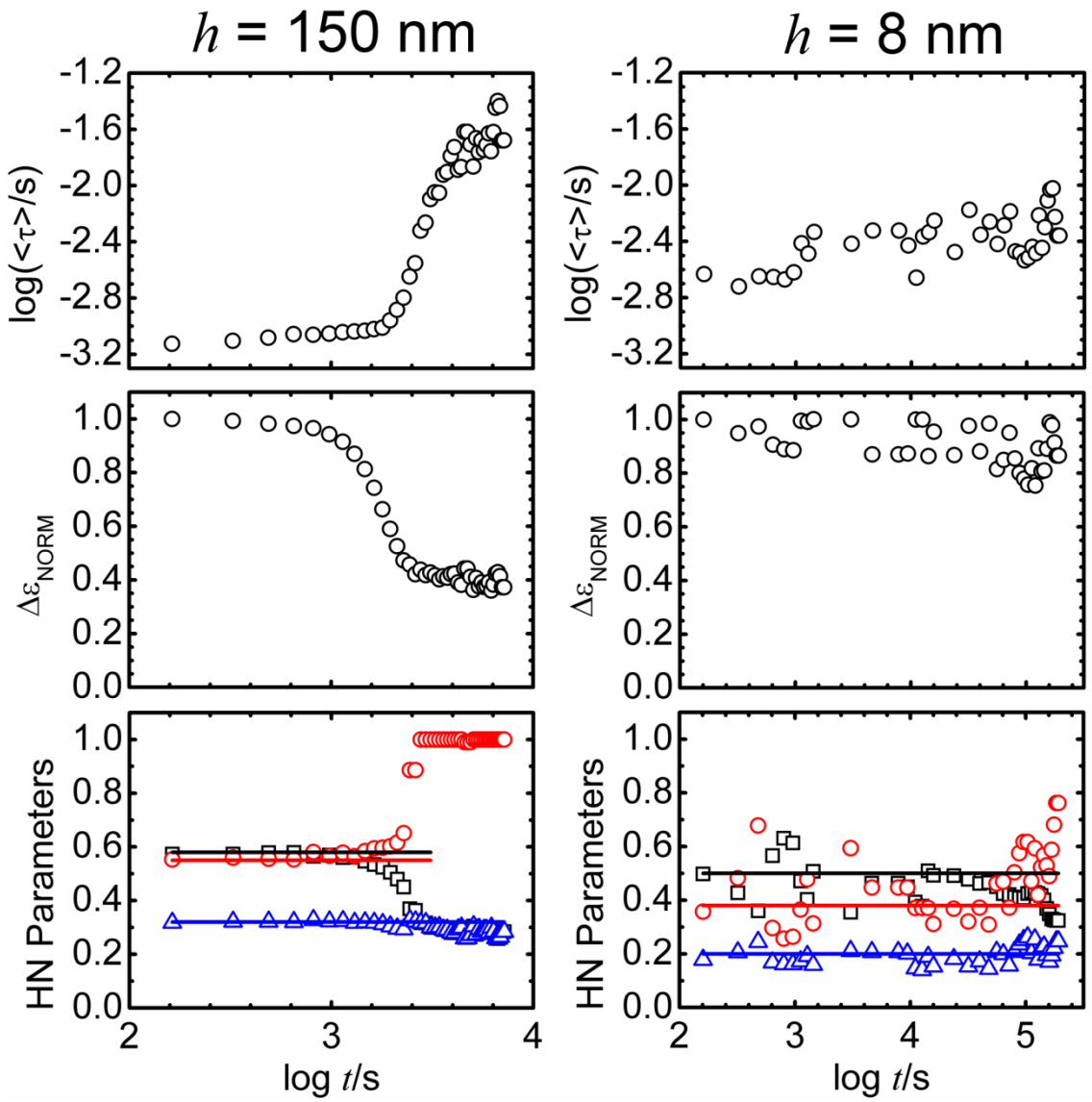

Figure 6.3. (left) 150 nm film. (right) 8 nm film. In HN parameters: □ = *b*, ○= *c*, △= *bc*

The 8 nm film does not show this sigmoidal reduction although Δε slightly decreases linearly with time. Regarding the shape parameters, for the 150 nm *b* tends to decrease after a given crystallization time and *c* increases at the same time, indicating that the relaxation becomes more symmetric and broader as crystallization develops. For the *h* = 8 nm film almost no change in the shape parameters is observed with time. The qualitative difference in the results obtained at 150 and 8 nm hints at a perturbation in the time scale of cold crystallization in the two samples. In particular, the results collected till now imply a severe slowing-down in the crystallization kinetics upon reduction of the thickness. We propose a quantitative analysis of this phenomenon in the next section.

(C) Crystallization kinetics and irreversible chain adsorption

Recent literature demonstrated the possibility to monitor the crystallization kinetics of thin polymer films following the evolution of the dielectric strength, Δε, during the isothermal annealing [2]. Figure 6.4 (left) shows the evolution of Δε as a function of time for every studied sample. In the thickness range between 150 nm – 20 nm, Δε decreases with time in two clear regimes. Initially, a linear decrease of Δε with the logarithm of the crystallization time is observed, with stronger slope for the thinner samples. In the second regime a step like decrease of Δε(*t*) is observed. The onset of this second regime, considered as the time where Δε exhibits a sudden and strong decrease, increases as the thickness is decreased, e.g. for 300 nm thick films 15 min are sufficient to observe a significant drop in Δε, while such a condition is achieved after almost 14 h for the thinner films. Previous works proposed that this logarithmic dependence observed in the initial regime is related to physisorption of the polymer onto the metallic layer [2, 29, 30]. This process, having a similar time evolution as physical aging and secondary

crystallization, reflects the densification of the layer adsorbed onto the metallic substrate. As the polymer film thickness decreases, the volume fraction occupied by adsorbed chains becomes more relevant, which explains the larger deviations from the zero-slope in the thinner films.

As introduced in the previous section and also proposed in the literature [31-35], this sigmoidal decrease in Δε with time observed in the second regime can be related to the crystallization process of the PLLA, which followed by BDS is interpreted as follows. For short times, polymer films are in their amorphous state where all chains contribute to the relaxation process, giving a maximum possible value of Δε. As time increases, chains lose segmental mobility as they incorporate into the growing crystals and thus the relaxation strength decreases in a trend resembling the Avrami equation [2, 24, 28]. Since polymers do not completely crystallize, the result of the crystallization process is a semi-crystalline material, where both amorphous and crystalline phases are present. The remaining amorphous phase contributes to the reminiscent final Δε value.

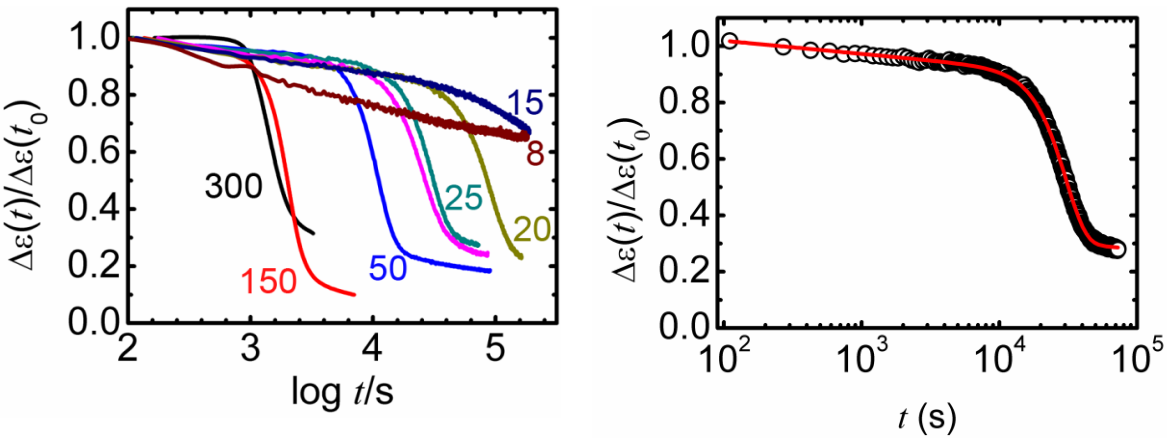

Figure 6.4. (Left) Time evolution of Δε for films of different thickness. Label next to each curve represents the film thickness in nanometers. (Right) Experimental data of a thin film of thickness = 25 nm and fit of equation 6.1 (continuous red line).

Taking into account both primary crystallization and densification upon adsorption, the time dependence of Δε(t) can be described as [2]:

$$\frac{\Delta\varepsilon(t)}{\Delta\varepsilon(t_0)} = 1 - \Gamma \exp\left[-\left(\frac{t}{t_c}\right)^{\beta}\right] - \delta \log(t/t_0) \qquad \textbf{(6.1)}$$

where Γ describes the drop in Δε (proportional to the final crystalline content of the sample), t_c is the crystallization time (taken as the value of *t* when Δε reaches the middle of the step), β relates to the dimensionality of the process and δ is a parameter proportional to the fraction of chains immobilized upon adsorption. Results from fitting equation (6.1.) to our data are shown in table 6.1. An example of the experimental data and fit of equation 6.1 to a thin film of thickness *h* = 25 nm is shown in figure 6.4 (right).

Table 6.1. Avrami parameters for PLLA capped films

***h* (nm)**	**Γ**	**t_c (s)**	**β**	**$\delta/10^{-3}$**
300 ± 20	0.686 ± 0.007	(1.5 ± 0.1)x10^3	3.2 ± 0.1	0
150 ± 10	0.767 ± 0.006	(2.1 ± 0.1)x10^3	3.7 ± 0.1	8 ± 1
50 ± 5	0.673 ± 0.009	(1.10 ± 0.01)x10^4	3.20 ± 0.02	6.3 ± 0.7
25 ± 2	0.593 ± 0.004	(3.06 ± 0.03)x10^4	3.02 ± 0.01	11.4 ± 0.4
24 ± 2	0.542 ± 0.004	(2.64 ± 0.04)x10^4	2.69 ± 0.02	11.3 ± 0.4
20 ± 2	0.532 ± 0.003	(9.21 ± 0.07)x10^4	2.742 ± 0.008	12.7 ± 0.2
15 ± 1	0.25 ± 0.03	(2.2 ± 0.2)x10^5	1.19 ± 0.05	12.7 ± 0.5

Upon confinement, β slightly decreases, the value of Γ decreases and that of δ increases. The correlated trend between the reduction in the quantity of amorphous chains that can crystallize and the increase in the volume fraction of adsorbed chain reveals a competition between the two immobilization processes. Figure 6.5 shows the fraction of chains immobilized upon adsorption (δ) as a function of the final crystalline content of the film (Γ). A clear film thickness dependence is observed: the 300 nm film shows a bulk like behavior without immobilization of chains due to chain adsorption (δ=0); however, as film thickness decreases so does the final crystalline content and the fraction of immobilized chains increases. This confirms the idea that adsorbed chains cannot longer crystallize. Crystallization of chains in the irreversibly adsorbed layer is, in fact, highly hindered. Formation of crystals provides a remarkable enthalpy gain, but ordering via chain folding requires an initial entropic loss that cannot be compensated by the adsorbed chains [2]. The entropic barrier of stem formation increases due to the restriction in conformational degrees of freedom upon chain immobilization, which leads to a neat reduction in crystal growth rate.

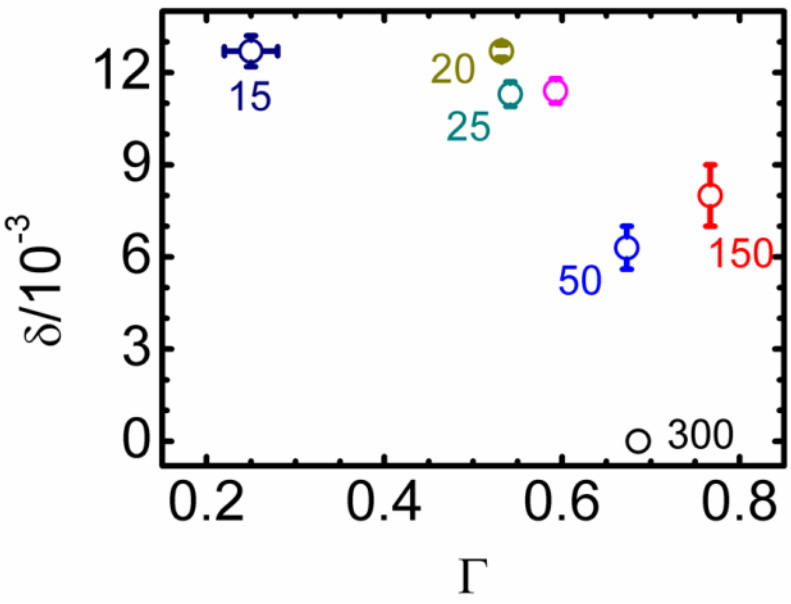

Fig 6.5. Relation between the fraction of immobilized chains as a function of final crystalline content of the polymer films.

The thickness dependence of the crystallization time t_c in a double logarithmic fashion is shown in Figure 6.6. Two different linear regimes of log(t_c) versus log(h) are found. For films in the range between 300-25 nm the slope is about -1, that is, $t_c \sim h^{-1}$. This trend can be rationalized considering the effects of finite size on a process occurring at constant nuclei density. In fact, assuming a constant number of nucleation events occurring per unit of time in the unit of volume, one would expect that, upon confinement, the reduction of the nucleation rate would scale with the sample volume. This hypothesis was validated in the case of homogenous nucleation in nanodroplets of poly(ethylene oxide), where the product of the nucleation rate and the droplet volume was constant [22, 36]. Extending this scenario to the case of thin films, we deduce that in case of a nucleation limited confinement effect, the crystallization time should increase with the inverse of the film thickness [2]. Below 20-25 nm, the value of $\partial\log(t_c)/\partial\log(h)$ significantly increases. In this thickness range, the reduction in crystallization rate is no longer imputable to the mere effect of finite size effects. Moreover, as evidenced in figure 6.2, the HN parameters *c* and *bc* showed as strong decrease around the same threshold thickness. These observations can be correlated to the influence of the interfacial interactions on the confined polymer film, since as stated before, the reduction in *bc* can be related to an increase of hindrance in the local chain dynamics [25, 26]. Finally, the agreement of the changes in both t_c and *bc*, can be related to the range of the polymer/metal interaction. It is remarkable that these conclusions can relate to the change in the crystalline morphology evidenced in the thinner supported films (figures 6.10 and 6.11) shown in the following section. Thus, it is possible questioning about the role of adsorption on the final morphology evidenced in the PLLA supported thin films. However, since at the two thinner supported films dewetting has already started, it is not possible to distinguish between the influence of one effect or the other.

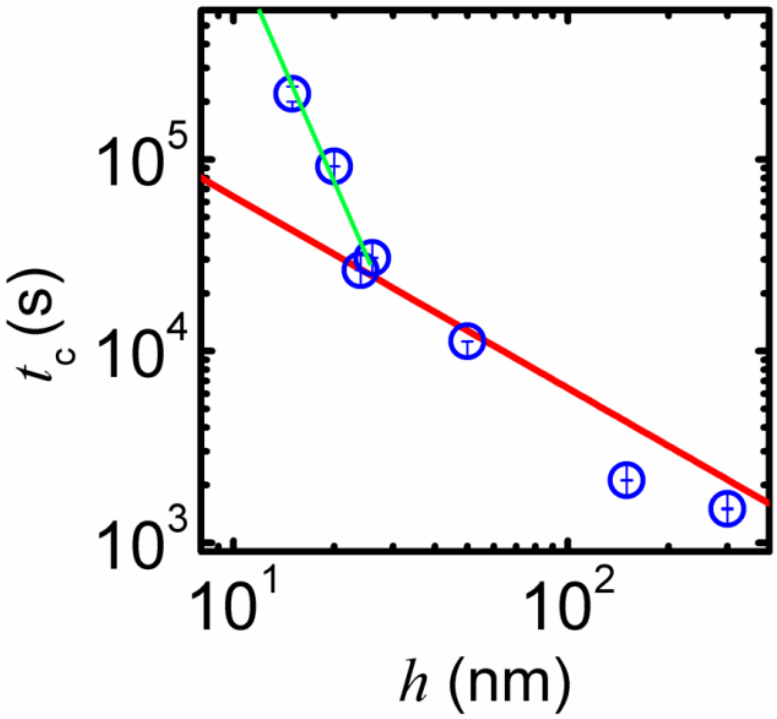

Fig 6.6. Thickness dependence of the crystallization time.

To further study the influence of adsorption, we have calculated the molecular mobility profile of our system in its amorphous state (t = 0 s), via the thickness dependence of the dielectric strength, following the work by Rotella *et al.* [12]. Figure 6.7 shows, the dielectric strength, $\Delta\varepsilon$ as a function of the inverse of thickness, for the amorphous samples. As a general feature of the α–relaxation under confinement, the dielectric strength decreases in the thinnest films. The reduction in $\Delta\varepsilon$ is related to the reduction of the number density of fluctuating dipoles in proximity of the interface, due to chain adsorption, as proven before for single layer [37] and multilayer experiments [38]. In the case of reductions of $\Delta\varepsilon$ scaling as h^{-1}, the profile in mobility is well described by a Heaviside function, representing a sharp transition between an immobilized layer and the bulk-like core of the film. The nonlinear drop of the dielectric strength *vs.* h^{-1} found here

for PLLA and for other systems [12, 39], suggests, on the contrary, the presence of a smooth gradient of molecular mobility penetrating from the metallic interfaces into the film.

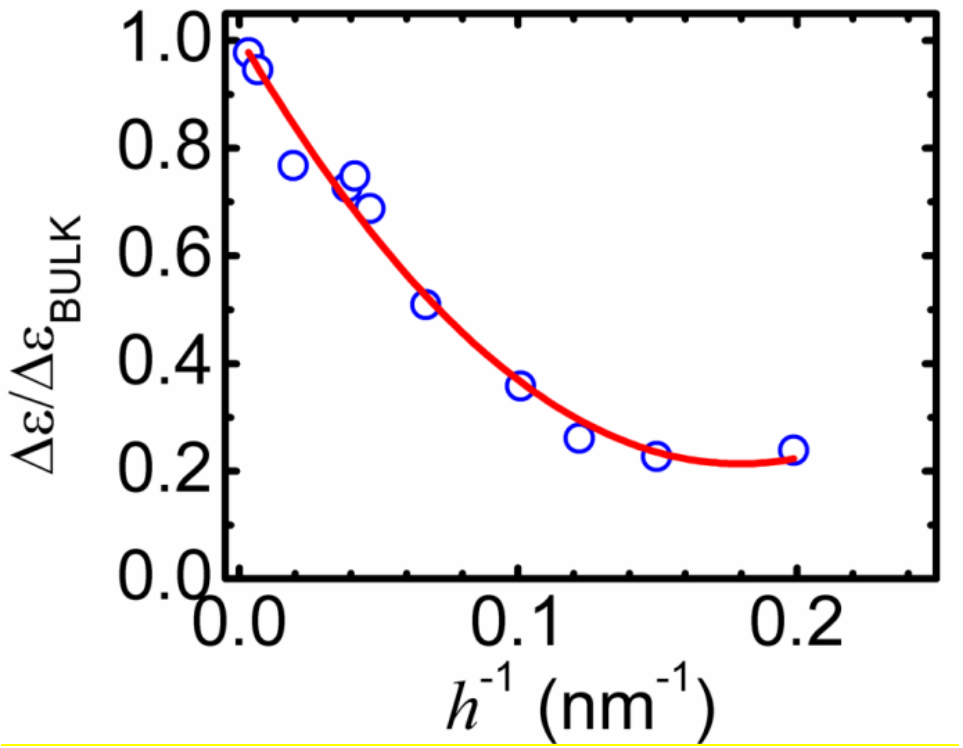

Fig 6.7. Evolution of Δε as a function of inverse film thickness. Line is a guide for the eye.

This gradient is related to chain immobilization due to adsorption into the metallic substrate, from the interface into the core of the film [12, 19, 30] and can be quantitatively described by the following relation [12]:

$$\frac{\Delta\varepsilon(x)}{\Delta\varepsilon_{bulk}} = \left[\tanh^2\left(3\frac{x}{\varphi} + \rho\right) + \tanh^2\left(3\frac{x-h}{\varphi} - \rho\right)\right] - c \qquad \textbf{(6.2.)}$$

where x is the distance from an interface and h is the film thickness. The parameter φ is related to the penetration depth of the reduction of the dielectric strength [12], while ρ is correlated to the interfacial value of Δε, as $\tanh^2(\rho) = \Delta\varepsilon_{interface} / \Delta\varepsilon_{bulk}$. Bulk value in the

core of films thicker than 2φ is ensured subtracting the constant $c = \tanh^2(3h/\varphi + \rho)$. The procedure to calculate the total dielectric response of a film of thickness h, was accomplished via a layer resolved approach, extensively described in [37]. Using the input experimental data presented in figure 6.7, we obtained the best fitting parameters of equation (6.2) upon minimization of the squared deviations, in comparison to the experimental data: φ = (7 ± 2) nm, ρ = (0.44 ± 0.05). Figure 6.8 shows the computed profile of Δε, normalized respect to its bulk value, as a function of the distance from the metallic wall. This figure indicates the mobility profile of the system and serves as a graphical interpretation of the parameters φ and ρ.

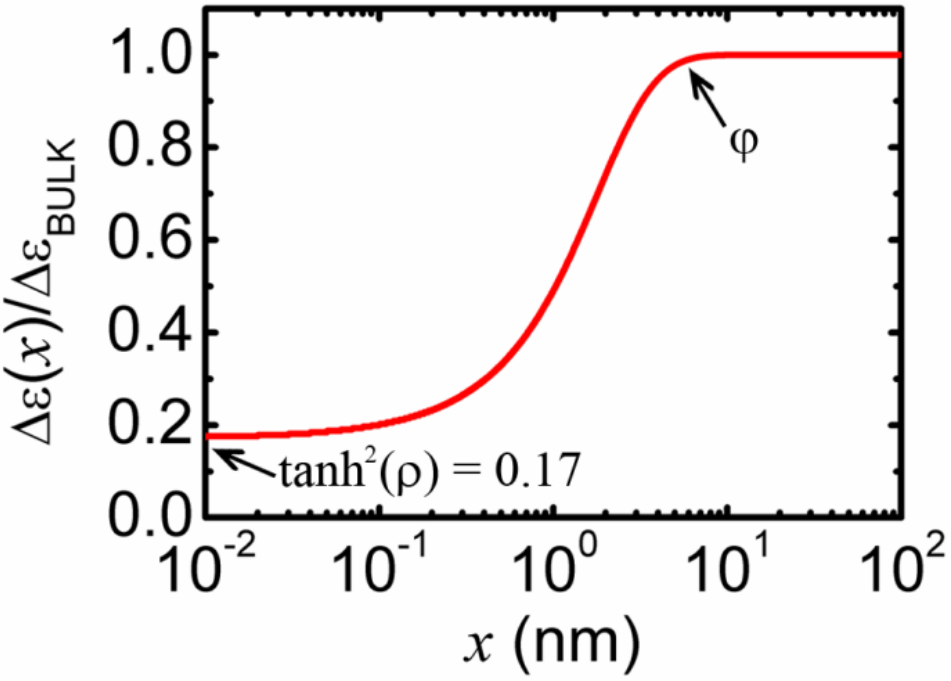

Fig 6.8. Profile of mobility at one interface for PLLA, calculated from equation (6.2) for a very thick film (h >> 2φ).

In figure 6.8, the mobility profile shows a step-like reduction from higher to lower values of x, that is, the further the polymer is away from the interface the more its behavior becomes more bulk-like. In the specific case for PLLA, above $x \approx 10$ nm, the dielectric strength of the system presents a bulk-like response. Nevertheless, for 10 >

x(nm) >1 $\Delta\varepsilon$ decreases approaching the solid wall down to a final plateau where the dielectric strength is reduced to 17% of its bulk value. Therefore, the interfacial region for x < 10 nm can be considered as an indication for the length scale where the adsorption of the polymer into one interface occurs. Finally the fact that $\Delta\varepsilon/\Delta\varepsilon_{bulk}$ extrapolates to a finite value at x = 0 is the manifestation of a residual dielectric activity in the interfacial volume in high interaction with the metals [12]. Following this interpretation the thickness of this so called reduced mobility layer (RML) can be estimated from the x value after the plateau where $\Delta\varepsilon/\Delta\varepsilon_{BULK}$ starts increasing. In the present case, the thickness of the RML is estimated to be around 1 nm, and is in good agreement with the literature [2, 12]. From the obtained value of penetration depth φ, we estimate that the influence of the interfacial interaction should be relevant up to thicknesses on the order of 2φ = (14 ± 4) nm. Previously, studies of crystallization of PET confined into thin films showed that this value can be related to the thickness where δ in equation (6.1) starts deviating from zero [2], indicating the upper limit for interfacial interactions. However, this is not the case for PLLA since we observed a non-zero value of δ even at thicknesses as high as 150 nm. This qualitative difference between the two polymers as well as the low value obtained for the RML might be related to the degree of flexibility, which is much higher for PLLA than for PET. This trend can be rationalized considering that chain rigidity increases the correlation between segments and thus the length scale over which confinement effects take place. Moreover, the value of 2φ = (14 ± 4) nm can be seamlessly related to the point in which the HN *bc* parameters starts deviating. This confirms the idea proposed in section A, where changes in *bc* were related to impact of interfacial interactions.

6.2.3. Crystallization behavior of supported thin films

The aim of this section is to emphasize how the morphology of a crystallizing polymer is modified due to the presence of an interface (substrate). The effect becomes more evident for thinner films. Due to the capped structure of the films for BDS, AFM measurements could not be carried out under that geometry. Spin coating allowed preparing PLLA supported thin films with thicknesses (h) of 150 nm, 60 nm, 35 nm, 18 nm and 10 nm. Figure 6.9 shows the AFM height images of the polymer films after melt-quenching, *i.e.* in their amorphous state. A continuous surface is observed for the thicker films (h = 150 nm, 60 nm and 35 nm). Roughness of the films was calculated to be around 1 nm (table 6.2), which coincides well with the expected roughness of an amorphous polymer film. As thickness decreased below 35 nm, dewetting starts taking place. In the case of the 18 nm film, continuity of the film is lost due to the appearance of *valleys* along the surface. These valleys do not reach the bottom of the film yet. Also, surface changes are reflected in the increase of the roughness (table 6.1). Finally, the 10 nm film shows a dewetted structure of polymer *islands* on top of the silicon substrate.

Table 6.2. Roughness values of PLLA supported thin films

Thickness (nm)	Roughness Amorphous (nm)	Roughness Crystalline (nm)
150 ± 10	0.7 ± 0.1	10 ± 1
60 ± 10	0.6 ± 0.1	12 ± 1
35 ± 5	1.0 ± 0.3	3 ± 1
18 ± 5	3.0 ± 0.5	3 ± 1
10 ± 5	5.0 ± 0.5	3 ± 1

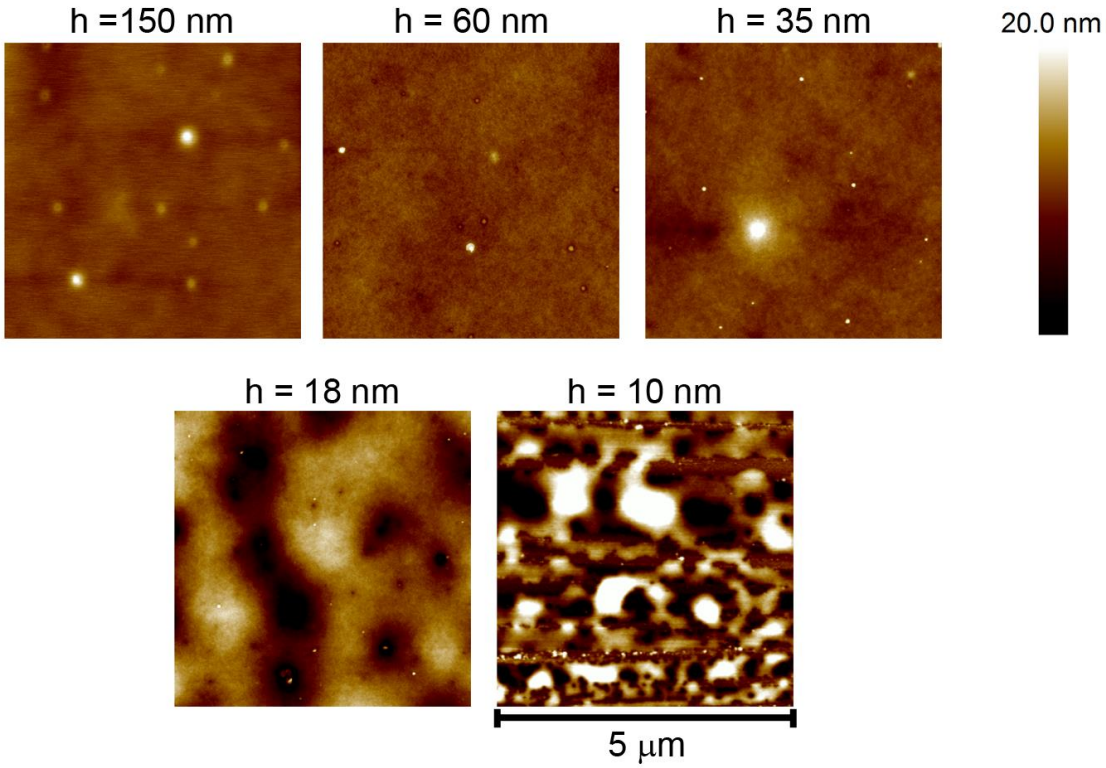

Figure 6.9. AFM topography images of amorphous PLLA supported films. Labels on top of each image indicate the film thickness. Color bar is the same for all AFM images.

Two different crystallization experiments were performed. The amorphous PLLA films were annealed either at 70 ºC or 100 ºC for 20 hours, using a hot plate. Afterwards, changes in topography were quantified by AFM. Results are shown in figure 6.10 for T_c = 70 ºC and figure 6.11 for T_c = 100 ºC. For T_c = 70 ºC, AFM topography images show, for all thicknesses, a change in the surface morphology with respect to the amorphous films. This morphological change is dependent upon thickness. First, the 150 nm and 60 nm films show a spherulitic-like morphoplogy, with a subsequent increase in the roughness values, with respect to the amorphous films. The spherulitic-like morphology is the one reported for bulk crystallization of PLLA[40]. This spherulitic morphology is still observed for the 35 nm film, together with new structures. At this intermediate thickness, the rugosity values do not increase upon crystallization as much as for larger thicknesses. The two thinner films show the formation of new structures. At 18 nm, the spherulites are no

longer seen in the AFM images. Instead, two types of crystalline structures are observed, namely needle-like crystals and dendritic crystals. This is also the case for the 10 nm film, in which the crystalline structures have grown around the dewetted zones. According to the literature, the needle-like crystals can be related to the growth of edge-on lamellae, while the dendritic crystals to flat-on lamellae[41-43].

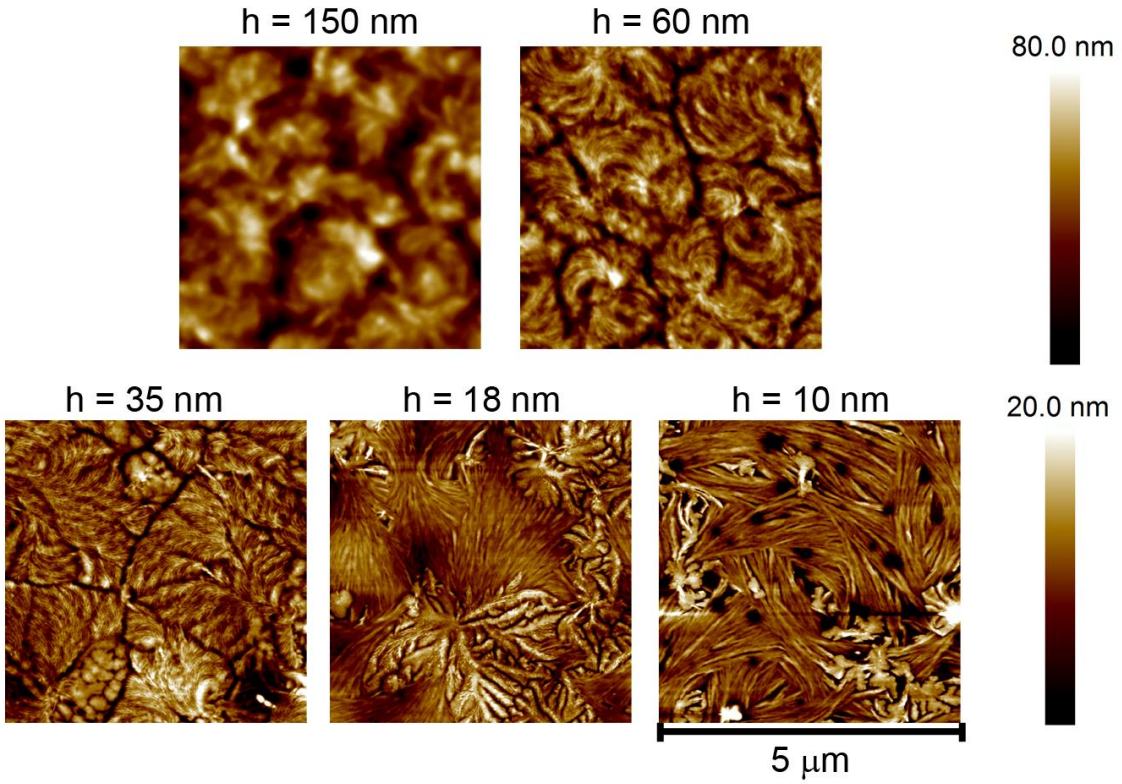

Figure 6.10. AFM topography images of PLLA supported films cold crystallized at 70 ºC for 20 hours. Labels on top of each image indicate the film thickness. Color bar are the same for each raw of AFM images.

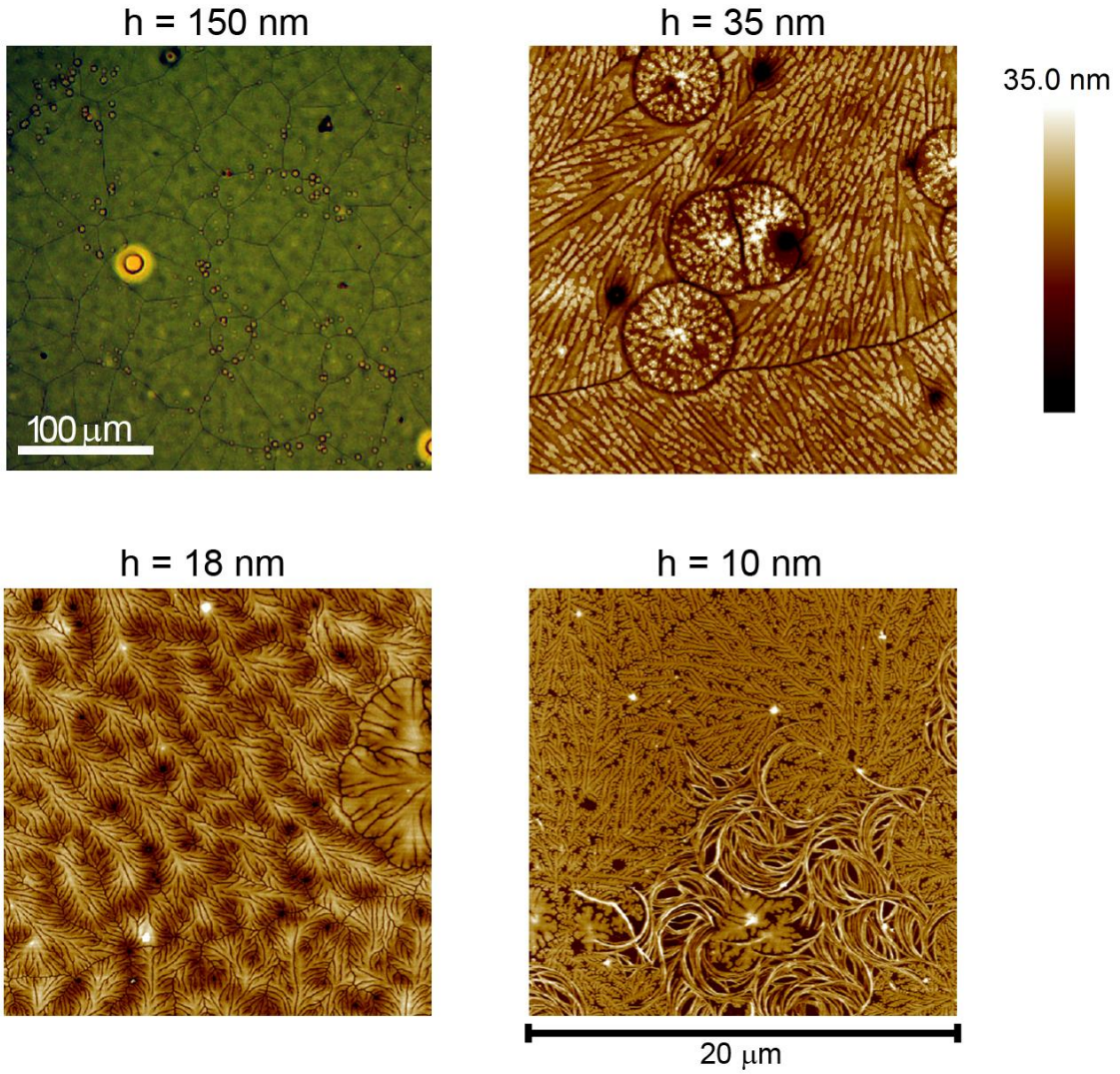

Figure 6.11. Optical microscope image for a 150 PLLA film and AFM topography images of PLLA supported films (35 nm, 18 nm and 10 nm) cold crystallized at 100 ºC for 20 hours. Labels on top of each image indicate the film thickness. Color bar to the right is the same for all AFM images.

In the case of T_c = 100 ºC (figure 6.11), the thicker films (150 nm and 60 nm) show also the development of big spherulites. Actually, at this T_c, spherulites are so big that cannot be observed well by AFM. This is the reason why figure 6.11 shows an optical microscope image of the 150 nm film. This image resembles the results for the 60 nm film. At 35 nm, the spherulitic structure is still preserved, although spherulites are smaller and thus visible by AFM. At this thickness (h = 35 nm) circular structures are also observed. They indicate some sort of frustration in spherulite growth. As for the 70 ºC cold crystallization study, at the smallest thicknesses (18 nm and 10 nm), the crystalline

morphology changed in comparison to the thicker films.

In the 18 nm case, only dendritic crystals are observed in the AFM image. Needle-like structures are no longer present, indicating that the dendritic crystallization might be the most stable layout of the PLLA crystals at this thickness and temperature. This has been previously related to a heterogeneous nucleation rate at the polymer/surface interface becoming predominant and allowing the formation of these flat-on structures[44]. On the other hand, in the 10 nm film, two types of morphologies are seen, namely dendritic crystals and curved needle-like crystals. These curved crystals have been previously reported for PLLA ultrathin films[41]. According to Maillard, at very low film thicknesses (around and below 10 nm) and at temperature well above T_g (90 ºC – 130 ºC), edge-on lamellae act as secondary nuclei to other edge-on lamellae. This leads to U-shape and loop-shape lamellae. The second generation of lamellae tends to grow tangentially to the first generation, in the opposite direction, but with the same curvature behavior.

Collecting all results, so far it is seen that crystallization can occur in supported PLLA films, with thicknesses down to tens of nanometers. Also, there is a change in the crystalline morphology that is dependent with thickness. In the thin film geometry, the arrangement of the polymer chains depends not only in the geometrical confinement[45] but also on the polymer-substrate interaction[2, 19].

6.3. Crystallization of polymer nanoparticles

So far, we have presented results regarding crystallization of poly(L-lactic acid). It has been found that for ultra-thin films (h < 20 nm) the crystallization morphology changed from the spherulitic bulk-like towards dendritic and loop-shaped crystals.

Recently it has been proposed that the crystallization morphology is dependent on the D,L content of the repeating unit of PLA. It has been found that D-rich PLA shows clockwise orientations, while L-rich PLA shows counter clockwise orientations[43, 46]. In order to gain more insight about this fact, in this section, it is presented results of crystallization of the poly(D,L-Lactic Acid) (PDLLA) confined in nanospheres.

6.3.1. Samples and techniques

This part of the work was carried out at the facilites of IEM-CSIC. In this case, the selected polymer was the Poly(D,L-Lactic Acid) (PDLLA). Nanoparticles of this polymer were prepared by the miniemulsion method (chapter 3, section 3.1.2) and by the reprecipitation method (chapter 3, section 3.2.3, sample PLA-R2). Wide angle x-ray scattering experiments were carried out using lyophilized nanoparticles packed between aluminum sheets. To prepare PDLLA nanocrystals, nanoparticles prepared by the miniemulsion protocol were spin coated on silicon wafers, previously treated with a piranha solution. To promote crystallization of the nanoparticles, the deposited wafers were annealed at a fixed temperature of 75 ºC for different times under vacuum. For each annealing time, a new batch of deposited particles was used. After annealing, the resulting morphology of the particles was evaluated by AFM measuremets. Scans were perform in tapping mode, with NCHV probes.

6.3.2. Crystallization of PDLLA nanoparticles

Figure 6.12 shows the the diffraction patterns of the bulk PDLLA, as well as of the nanoparticles, for several temperatures. In general, as the samples were annealed, the development of diffracion peaks is evidenced. This indicates that all samples were able to

crystallize. Specifically,bulk and miniemulsion nanoparticles patterns are quite similar between each other for the whole temperature range. At 30 ºC, these two samples show an amoprhous halo, indicating their amorphous nature. As temperature increased up to 70 ºC, the development of a diffraction peak, around $2\theta = (17.0 \pm 0.3)^{o}$, is seen. This peak has been reported to be associated with the diffraction from the (200) and/or (110) planes of the α form of PDLLA[47]. At higher temperatures, the diffraction patterns show the developement of several other peaks. This behavior indicates that as the samples were annelaed crystallization continues. At 110 ºC diffraction peaks show their highest intensity. Comparing with the literature[47-51], we have indexed the peaks as shown at the 110 ºC temperature in figure 6.12. Results show that the PDLLA has crystallized in the ordered α-phase[48, 49, 52], which is expected when the polymer is crystallized at temperatures below 100 ºC. Indexing results are summarized in table 6.3.

Table 6.3. Crystalline peaks and 2θ position, as observed at 130 ºC (figure 6.12).

Index	BULK	MINIEMULSION	REPRECIPITATION
(010)	$(15.4 \pm 0.3)^{o}$	$(15.3 \pm 0.3)^{o}$	---
(200)/(110)	$(17.0 \pm 0.3)^{o}$	$(17.1 \pm 0.3)^{o}$	$(17.2 \pm 0.3)^{o}$
(203)	(19.5 ± 0.5)	(19.5 ± 0.5)	(19.5 ± 0.5)
(105)	$(22.7 \pm 0.3)^{o}$	$(22.7 \pm 0.3)^{o}$	$(22.8 \pm 0.3)^{o}$

The diffraction patterns of PDLLA reprecipitation nanoparticles are shown in the right column of figure 6.12. In this case, the diffraction patterns are noisier in comparison with to others. This might be related to the amount of material enclosed in the aluminum sheets, which in this case was lesser. As stated previously, as temperatures increases

crystallization evolves; however, comparing with bulk and miniemulsion nanoparticles there are important differences. At 30 ºC, besides the amorphous halo, an increase of the diffraction signal is observed at small values of 2θ (2º-5º). This result can be related to the possible existence of some ordering in the PDLLA chains inside the reprecipitation nanoparticles, which lenghtscale is above of WAXS range. It has been reported that poly(lactic acid) polymers can show a mesophase[53, 54], with distinct chain packing and chain conformation. Mesophases in semicrystalline polymers can be obtained by the melt-quenched method[55]; for example, isotactic polypropylene can be solidified into an intermediate state between crystal and amorphous states when a thin specimen of molten state is rapidily quenched[56]. Also, Stoclet and collaborators have shown that it is posible to induce a mesophase in PDLLA when an external strain was applied[57, 58]. Collecting all these facts, we argue that the preparation procedure used in the reprecipitation method might have lead to the formation of a mesophase in the resulting PDLLA nanoparticles. In this method, a polymer solution is rapidly injected into a non-solvent. In the solution, the polymer chains have maximum mobility, that can be somehow compared to the behavior in the melt state. As the solvent is quickly removed from the nanoparticles while the polymer is being transfered to a non-solvent medium (chains have no mobility), it is possible to assume that the polymer chains are being subjected to a quench-like procedure, that ultimately leads to the formation of the mesophase. It can also be argued that during the fast precipitation, the polymer chains retain residual stresses and thus a sort of strain-induced mesophase takes place. These strains could arise from the physical procedure involved in going from separated chains to nanospheres.

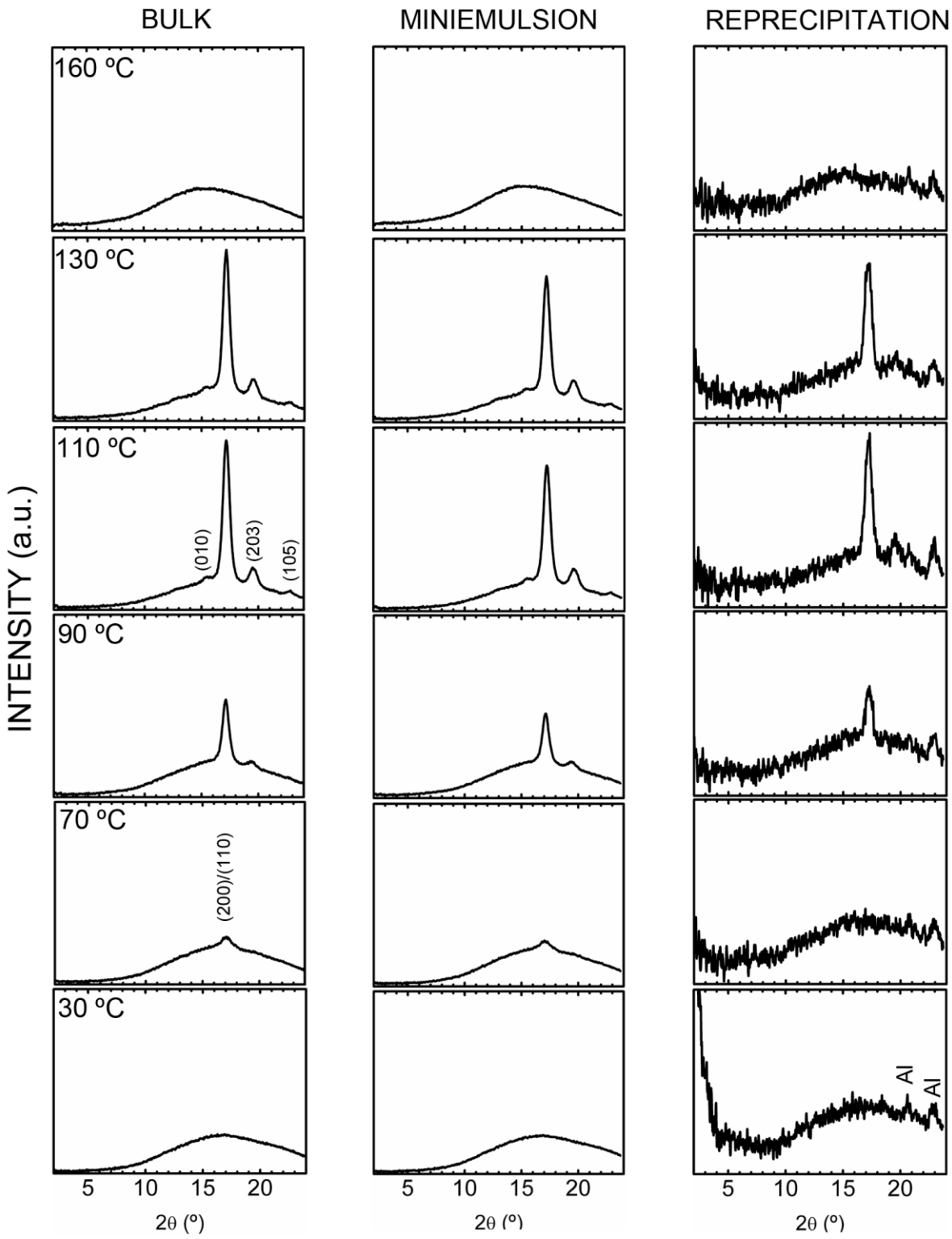

Figure 6.12. WAXS diffraction patterns for bulk PDLLA (left) and PDLLA miniemulsion (center) and reprecipitation (right) nanoparticles.

The preparation method argument just explained can be also justified by comparing the results between reprecipitation and miniemulsion PDLLA nanoparticles. In

the miniemulsion method, nanodroplets of solvent/polymer are formed simultaneously during ultrasonication. After the formation, solvent is slowly evaporated and thus nanoparticles do not suffer a melt-quenche like procedure. Also, the solvent/polymer nanodroplets serve as precursors to the resulting polymer nanoparticles and thus, during solvent evaporation process, polymer chains have enough mobility to lose possible strains. Since the solvent is evaporated at a temperature in which no Bragg peaks are observed, since there is not enough mobility to crystallize, the resulting nanoparticles are amorphous.

The WAXS signature of the *so-called mesophase* in the PDLLA reprecipitation nanoparticles vanishes with temperature, in the range 30 – 60 ºC. At 70 ºC (figure 6.12) the increase a low 2θ is not observed anymore. Figure 6.13 shows the DSC trace of the reprecipitation nanoparticles. Glass transition, crystallization and melting temperatures are highlighted throughout the curve. The glass transition temperature, of the nanoparticles is observed around 60 ºC, indicating no change in comparison to the bulk[59]. Comparing WAXS and DSC results we observe that the mesophase signature in the diffraction pattern dissapears at temperature above T_g. Also, in the DSC curve, just below T_g an endothermic peak can be seen, highlighted with a *. DSC endothermic peaks in semi-crystalline polymers are related to first order transitions, such as the melting of the crystalline structure. Gathering results, it is possible to especulate that this peak is related to the disordering of the polymer chains in the mesophase, that happens just when the polymer start getting mobility due to the incipient glass transition. At temperatures above T_g, the calorimetric curve shows a crystallization peak. The onset of crystallization can be observed around 90 ºC and its maximum at 125 ºC. Finally, the polymer nanoparticles melt at 145 ºC. DSC results of crystallization and melting of the nanoparticles agree with

the WAXS patterns.

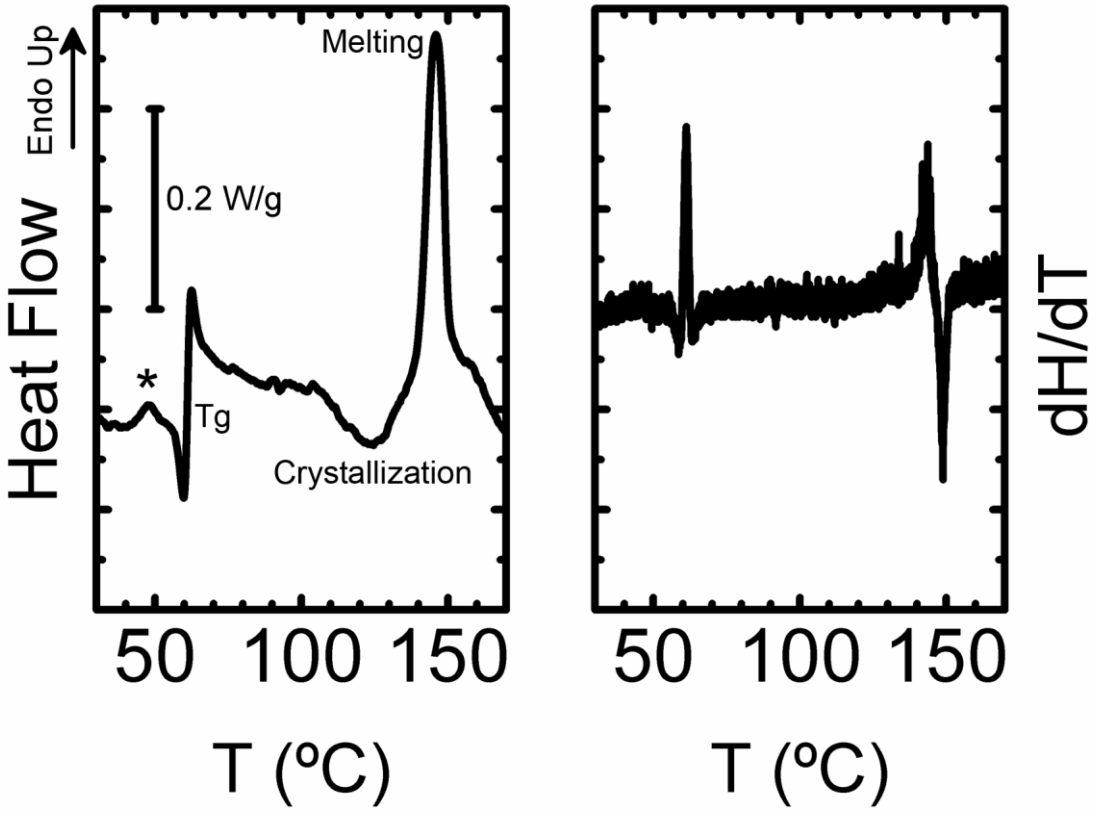

Figure 6.13. DSC trace (left) and heat flow derivative (right) of the reprecipitation PDLLA nanoparticles

6.3.3. Preparation of PDLLA nanocrystals

WAXS results in the previous section showed that polymer nanoparticles of PDLLA were able to crystallize when heated above certain tempreatures, depending on the preparation method. The diffraction patterns also show that nanoparticles prepared via the miniemulsion protocol showed a crystallization behavior quite similar to the bulk polymer. Based on this result we have evaluated the morphological change of PDLLA nanoparticles prepared by the miniemulsion method, when subjected to thermal treatments.

Figure 6.14 show AFM topography images of the PDLLA nanoparticles annelaed at 75 ºC for different times. This temperature is above T_g of the PDLLA and according to

the WAXS patterns, crystallization must take place. Image on top corresponds to the deposited nanoparticles without annelaing. The morphology of the nanoparticles corresponds to nanospheres with diameters around 50 nm (chapter 3, table 3.8). After annealing for 5 minutes, the nanoparticles lose their spherical shape.

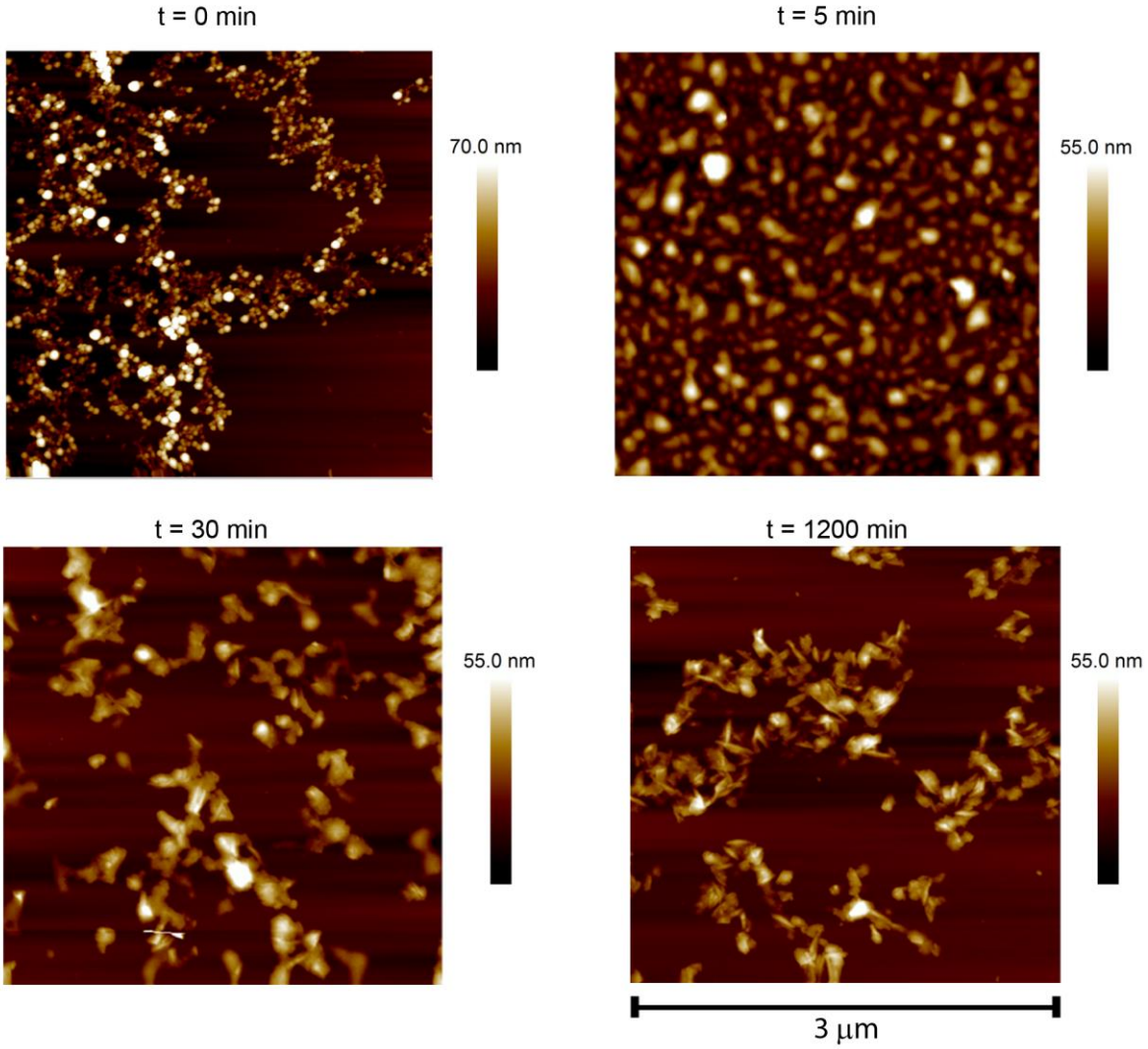

Figure 6.14. AFM images of annelad PDLLA nanoparticles prepared by the miniemulsion protocol

The resulting AFM image relates to the one of a dewetted thin film (see for example, figure 6.9 film @ 10 nm), composed of *islands* of PDLLA with smooth edges. This is the expected behavior of amorphous polymer nanoparticles when annelaed above its T_g, as presented in chapter 5 for PEMA nanoparticles, in which the height:width ratio increase from 1:1 to 1:5. The morphology of the nanoparticles starts changing after 30

minutes at 75 ºC. As time increases, the original smooth edges of the islands observed at 5 minutes start re-shaping into well defined straight contours. Also, in some cases it is possible to see the appearence of needle-like features inside the nanoparticles. This fact is enhanced at the longest annealing time (1200 min).

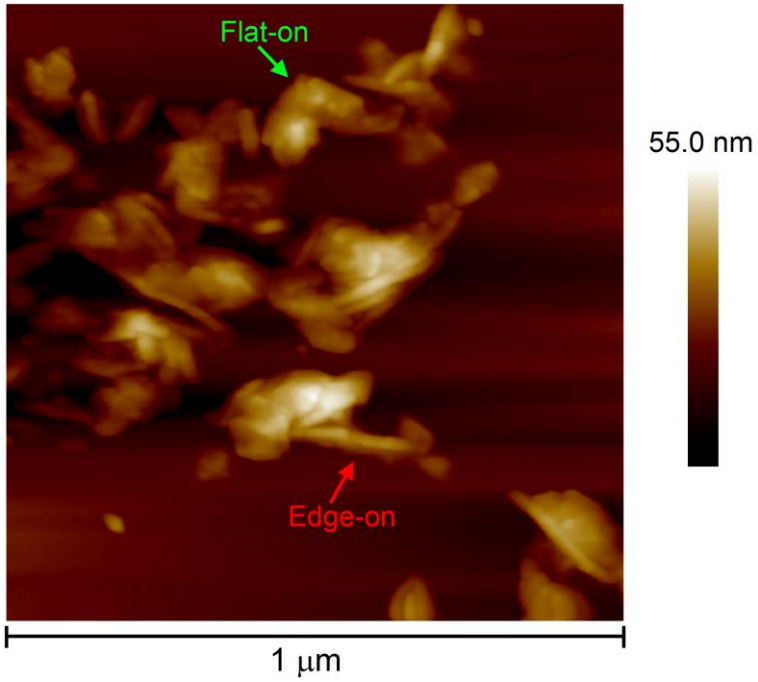

Figure 6.15. AFM topography image of PDLLA nanoparticles annealed at 75 ºC for 1200 minutes.

Figure 6.15 shows an AFM topography image of the PDLLA nanoparticles annelaed at 75 ºC for 1200 min. In this case, a smaller scan was used (in comparison to images in figure 6.14), which allowed getting more insight into the details of the nanocrystals. As stated before, the original spherical nanoparticles present now well defined edges, as expected for crystalline structures. These crystalline structures seem to be formed by the agglomeration of several nanoparticles, since at the annelaing temperature PDLLA is expected to have mobility. Two different structures are observed in the AFM image of figure 6.15, where PDLLA nanoparticles annelaed at 75 ºC for 1200 minutes are shown. First, needle-like crystals (red arrow), resemble the edge-on

crystalline structures in polymer thin films. On the other hand, the green arrow highlights the structures resembling flat-on crystals, compared to thin polymer films[44, 60].

The needle-like crystals prepared from the PDLLA nanoparticles show widths between 15 – 25 nm, heights between 15 – 40 nm and lengths between 100 – 300 nm. On the other hand, flat-on like crystals show sides between 50 – 150 nm and heights in the 15 – 60 nm range. Based on the geometrical sizes of the crystals obtained from the PDLLA nanoparticles it is possible to consider them as *nanocrystals.* In principle these nanocrystals could be recovered from the silicon waffers by washing it in distilled water. Afterwards nanocrystals could be used as additives in composites and/or polymer blends. Also, the heights of these nanostructures are comparable to the ones obtained for ultra-thin films of PLLA. This allows thinking in possible comparissons in the crystallization between the two confined geometries. As shown in section 6.2.3, supported PLLA films annealed at 70 ºC, with h = 18 or 10 nm, shown a morphology characterized by dendritic crystals and needle-like crystals. In the case of the annealed PDLLA nanoparticles, the edge-on elongated structures could be comparable to the needle-like crystals in the supported films. However, no dendritic structures are observed during the crystallization of the nanoparticles. It was previously argued that the flat-on dendritic structures were formed by a heterogenous nucleation at the polymer/substrate interface, and thus, the nature of this dendritic structure is intrinsecally related to the polymer/substrate interactions. These interactions are dependent in the preparation method of the materials. In thin films one starts from a polymer solution, where the polymer chains can freely move, that gets *frozen* and results in a confined structure. In the nanoparticles polymer chains in the nanospheres are already confined when deposited. This difference could be the one responsible for the occurrence of the dendritic crystalline structure in the thin

films.

6.4. Summary

Crystallization of Poly(L-Lactic acid) and Poly(D,L-Lactic acid) in confined geometries was studied. In the thin film geometry, PLLA samples showed that as thickness decreased, the crystallization behaviour changed. First, AFM measurements revealed that crystallization went from a spherulitic geometry to flat-on crystals. PLLA thin films were also studied by dielectric spectroscopy. Besides observing the crystallization behaviour, the adsorption of the polymer in the substrate was also presented and studied. It was found that ultra-thin films did not crystallize but only were adsorbed. Crystallization of the nanoparticles was found to be dependent on the preparation method. Miniemulsion nanoparticles showed crystallization behaviour similar to that of the bulk PDLLA. However, nanoparticles prepared by the reprecipitation method showed a strong low angle scattering in WAXS patterns at room temperature that could be correlated to the existence of a mesophase, probably due to the quench-like procedure that took place during the preparation. This mesophase disappeared at temperatures just below the T_g of PDLLA. Finally, it was shown the possibility of preparing polymer nanocrystals starting from polymer nanoparticles. These nanocrystals consisted in nanometric PDLLA structures that resemble the edge-on and flat-on crystallites usually found in polymer thin films.

6.5. References

1. Grigoriadis, C.; Duran, H.; Steinhart, M.; Kappl, M.; Butt, H.-J.; Floudas, G. *ACS Nano* **2011,** 5, (11), 9208-9215.
2. Vanroy, B.; Wübbenhorst, M.; Napolitano, S. *ACS Macro Letters* **2013,** 2, (2), 168.
3. Liu, Y.-X.; Chen, E.-Q. *Coordination Chemistry Reviews* **2010,** 254, (9–10), 1011-1037.
4. Asada, M.; Jiang, N.; Sendogdular, L.; Gin, P.; Wang, Y.; Endoh, M. K.; Koga, T.; Fukuto, M.; Schultz, D.; Lee, M.; Li, X.; Wang, J.; Kikuchi, M.; Takahara, A. *Macromolecules* **2012,** 45, (17), 7098-7106.
5. Maillard, D.; Prud'homme, R. E. *Macromolecules* **2008,** 41, (5), 1705-1712.

6. Despotopoulou, M. M.; Miller, R. D.; Rabolt, J. F.; Frank, C. W. *Journal of Polymer Science Part B: Polymer Physics* **1996,** 34, (14), 2335-2349.
7. Massa, M. V.; Dalnoki-Veress, K.; Forrest, J. A. *The European Physical Journal E* **2003,** 11, 191-198.
8. Capitán, M. J.; Rueda, D. R.; Ezquerra, T. A. *Macromolecules* **2004,** 37, (15), 5653-5659.
9. Reiter, G.; Sommer, J.-U. *Physical Review Letters* **1998,** 80, (17), 3771.
10. Napolitano, S.; Wübbenhorst, M. *Journal of Physics: Condensed Matter* **2007,** 19, (20), 205121.
11. Bertoldo, M.; Labardi, M.; Rotella, C.; Capaccioli, S. *Polymer* **2010,** 51, (16), 3660-3668.
12. Rotella, C.; Wübbenhorst, M.; Napolitano, S. *Soft Matter* **2011,** 7, (11), 5260.
13. Reiter, G.; de Gennes, P. G. *The European Physical Journal E* **2001,** 6, (1), 25.
14. Forrest, J. A.; Dalnoki-Veress, K.; Dutcher, J. R. *Physical Review E* **1997,** 56, (5 SUPPL. B), 5705.
15. Tsui, O. K. C.; Zhang, H. F. *Macromolecules* **2001,** 34, (26), 9139.
16. Schönhals, A.; Goering, H.; Schick, C. *Journal of Non-Crystalline Solids* **2002,** 305, (1-3), 140.
17. McKenna, G. B. *The European Physical Journal E* **2003,** 12, (1), 191.
18. Wübbenhorst, M.; Lupascu, V. In *Glass transition effects in ultra-thin polymer films studied by dielectric spectroscopy - Chain confinement vs. finite size effects*, 12th International Symposium on Electrets, 2005; 2005; p 87.
19. Napolitano, S.; Capponi, S.; Vanroy, B. *Eur Phys J E Soft Matter* **2013,** 36, (6), 9875.
20. Napolitano, S.; Cangialosi, D. *Macromolecules* **2013,** 46, (19), 8051-8053.
21. Boucher, V. M.; Cangialosi, D.; Yin, H.; Schonhals, A.; Alegria, A.; Colmenero, J. *Soft Matter* **2012,** 8, (19), 5119-5122.
22. Massa, M. V.; Dalnoki-Veress, K. *Physical Review Letters* **2004,** 92, (25), 255509.
23. Li, C. Y. *Journal of Polymer Science, Part B: Polymer Physics* **2009,** 47, (24), 2436-2440.
24. Brás, A. R.; Viciosa, M. T.; Wang, Y.; Dionísio, M.; Mano, J. F. *Macromolecules* **2006,** 39, (19), 6513.
25. Kremer, F.; Schönhals, A., *Broadband Dielectric Spectroscopy*. Springer: 2003.
26. Schönhals, A.; Schlosser, E. *Colloid Polym Sci* **1989,** 267, (2), 125.
27. Schlosser, E.; Schönhals, A. *Colloid Polym Sci* **1989,** 267, (2), 133.
28. Sanz, A.; Nogales, A.; Ezquerra, T. A.; Soccio, M.; Munari, A.; Lotti, N. *Macromolecules* **2009,** 43, (2), 671.
29. Rotella, C.; Napolitano, S.; Vandendriessche, S.; Valev, V. K.; Verbiest, T.; Larkowska, M.; Kucharski, S.; Wübbenhorst, M. *Langmuir* **2011,** 27, (22), 13533.
30. Napolitano, S.; Wübbenhorst, M. *Nature Communications* **2011,** 2, 260.
31. Nogales, A.; Ezquerra, T. A.; Garcia, J. M.; Balta-Calleja, F. J. *Journal of Polymer Science Part B-Polymer Physics* **1999,** 37, (1), 37.
32. Nogales, A.; Ezquerra, T. A.; Denchev, Z.; Sics, I.; Calleja, F. J. B.; Hsiao, B. S. *Journal of Chemical Physics* **2001,** 115, (8), 3804.
33. Sics, I.; Ezquerra, T. A.; Nogales, A.; Denchev, Z.; Alvarez, C.; Funari, S. S. *Polymer* **2003,** 44, (4), 1045.
34. Sanz, A.; Nogales, A.; Ezquerra, T. A.; Lotti, N.; Munari, A.; Funari, S. S. *Polymer* **2006,** 47, (4), 1281.
35. Sanz, A.; Nogales, A.; Ezquerra, T. A.; Soccio, M.; Munari, A.; Lotti, N. *Macromolecules* **2010,** 43, (2), 671.
36. Croll, A. B.; Massa, M. V.; Matsen, M. W.; Dalnoki-Veress, K. *Physical Review Letters* **2006,** 97, (20), 204502.
37. Yin, H.; Napolitano, S.; Schönhals, A. *Macromolecules* **2012,** 45, (3), 1652.
38. Rotella, C.; Napolitano, S.; De Cremer, L.; Koeckelberghs, G.; Wübbenhorst, M. *Macromolecules* **2010,** 43, (20), 8686.
39. Labahn, D.; Mix, R.; Schönhals, A. *Physical Review E* **2009,** 79, (1), 011801.
40. Dionísio, M.; Viciosa, M. T.; Wang, Y.; Mano, J. F. *Macromolecular Rapid Communications* **2005,** 26, (17), 1423.
41. Maillard, D.; Prud'homme, R. E. *Macromolecules* **2008,** 41, (5), 1705-1712.
42. Maillard, D.; Prud'homme, R. E. *Macromolecules* **2010,** 43, (9), 4006-4010.
43. Wang, X.; Prud'homme, R. E. *Macromolecules* **2014,** 47, (2), 668-676.
44. Wang, Y.; Chan, C.-M.; Ng, K.-M.; Li, L. *Macromolecules* **2008,** 41, (7), 2548-2553.
45. Reiter, G. *Chemical Society Reviews* **2014,** 43, (7), 2055-2065.
46. Nurkhamidah, S.; Woo, E. M. *Macromolecular Chemistry and Physics* **2014**, n/a-n/a.
47. Mano, J. F.; Wang, Y.; Viana, J. C.; Denchev, Z.; Oliveira, M. J. *Macromolecular Materials and Engineering* **2004,** 289, (10), 910-915.
48. Wasanasuk, K.; Tashiro, K.; Hanesaka, M.; Ohhara, T.; Kurihara, K.; Kuroki, R.; Tamada, T.; Ozeki, T.; Kanamoto, T. *Macromolecules* **2011,** 44, (16), 6441-6452.
49. Wei, X.-F.; Bao, R.-Y.; Cao, Z.-Q.; Zhang, L.-Q.; Liu, Z.-Y.; Yang, W.; Xie, B.-H.; Yang, M.-B. *Colloid Polym Sci* **2014,** 292, (1), 163-172.
50. Zhang, J.; Tashiro, K.; Tsuji, H.; Domb, A. J. *Macromolecules* **2008,** 41, (4), 1352-1357.
51. Wang, Y.; Li, M.; Wang, K.; Shao, C.; Li, Q.; Shen, C. *Soft Matter* **2014,** 10, (10), 1512-1518.
52. Xiong, Z.; Liu, G.; Zhang, X.; Wen, T.; de Vos, S.; Joziasse, C.; Wang, D. *Polymer* **2013,** 54, (2), 964-971.
53. Zhang, J.; Duan, Y.; Domb, A. J.; Ozaki, Y. *Macromolecules* **2010,** 43, (9), 4240-4246.
54. Wasanasuk, K.; Tashiro, K. *Macromolecules* **2011,** 44, (24), 9650-9660.
55. Strobl, G. *Progress in Polymer Science* **2006,** 31, (4), 398-442.
56. Qiu, J.; Wang, Z.; Yang, L.; Zhao, J.; Niu, Y.; Hsiao, B. S. *Polymer* **2007,** 48, (23), 6934-6947.
57. Stoclet, G.; Seguela, R.; Lefebvre, J. M.; Elkoun, S.; Vanmansart, C. *Macromolecules* **2010,** 43, (3), 1488-1498.
58. Stoclet, G.; Seguela, R.; Lefebvre, J. M.; Rochas, C. *Macromolecules* **2010,** 43, (17), 7228-7237.

59. Bitinis, N.; Verdejo, R.; Cassagnau, P.; Lopez-Manchado, M. A.; Lopez Manchado, M. A. *Materials chemistry and physics* **2011,** 129, (3), 823-831.
60. Xu, J.; Guo, B.-H.; Zhou, J.-J.; Li, L.; Wu, J.; Kowalczuk, M. *Polymer* **2005,** 46, (21), 9176-9185.

CHAPTER 7 – On the ferroelectric behavior under confinement

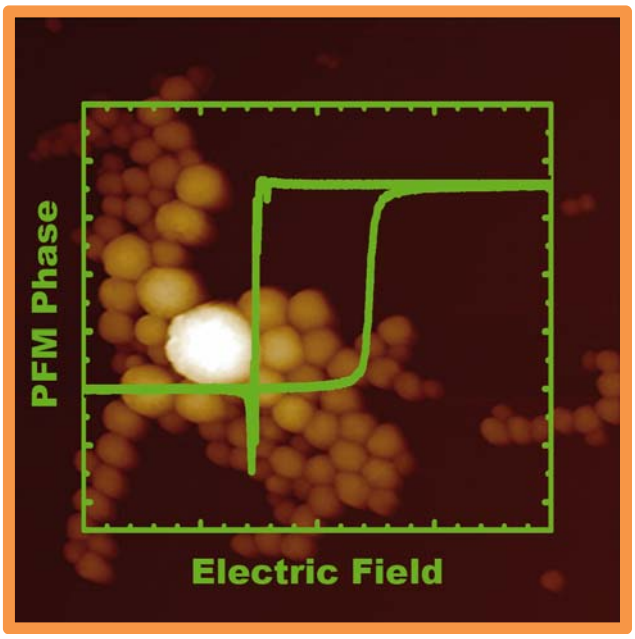

Hysteresis cycle of ferroelectric nanoparticles measured by Piezoresponse Force Microscopy. Back image: AFM topography image of polymer ferroelectric nanoparticles, Image size: (2x2)μm^2.

In this chapter, ferroelectric behavior of polymer nanostructures of P(VDF-TrFE) was studied using several techniques. In a first section, the ferroelectric nature of the nanoparticles has been proven by calorimetry, X-ray diffraction and dielectric spectroscopy. Also, the molecular dynamics is evaluated. In a second section, an AFM based technique is used to evaluate the ferroelectric response of nanoparticles and nanostructured films at the nanoscale.

*Part of the work described in this chapter has been published in *Applied Physics Letters* 2013, **102**(19), 191601.

7. 1. Introduction

Ferroelectricity, which enables the electric switching of electric polarization, has long been an important topic in condensed-matter science, and its application is important as a basic element of devices and memories[1]. For decades, the physical properties of ferroelectric inorganic materials such as polarization, piezoelectricity, and pyroelectricity, have been studied extensively[2-4]. Ferroelectric inorganic materials on the nanoscale, such as zinc oxide (ZnO) nanowires, PZT nanofibers, and AlGaN nanostructures, have been developed and implemented in power generation and biosensors in recent years[5-7]. Different from ceramic materials, ferroelectric polymers represent a unique class of functional insulating materials due to their long-chain rather than ionic-crystal nature. The advantages of easy processing, high flexibility and low-cost, have made polymers attractive for a variety of practical applications. In recent years, the piezoelectricity, ferroelectricity, and pyroelectricity of ferroelectric polymers such as poly(vinylidenefluoride) (PVDF) and its copolymers with trifluoroethylene (TrFE) have been widely investigated[1, 8-12]. Because of its excellent ferroelectric and piezoelectric properties, the P(VDF−TrFE) copolymers are widely used in tactile sensors, solar cells, field-effect transistors, nonvolatile memory devices, IR image sensors, pressure sensors, and acoustic sound transducers[13-15]. Also, with increasing demand for miniaturization in microelectronics, ferroelectric nanostructures have attracted considerable practical and theoretical interest. P(VDF-TrFE) nanostructures are especially interesting towards the development of memory applications, since miniaturization allows the reduction of the coercive field of these polymer systems, and thus allow operation at voltages below 10 V[16].

Ferroelectrics are polar substances of either solid (inorganic or polymeric) or liquid crystal, in which spontaneously generated electric polarization can be reversed by inverting the external electric field[1]. The critical electric field for reversing the polarization is called the coercive field. The electric displacement (*D*) as a function of field strength (*E*) consequently draws a hysteretic curve (*D*–*E* loop) between opposite polarities, and this electric bistability can be used, for example, for non-volatile memory elements[4, 17, 18]. The ferroelectric compounds usually have a Curie temperature T_c for a ferroelectric-to-paraelectric phase transition. As the temperature approaches T_c, the dielectric constant (κ), obeying the Curie–Weiss law, is amplified to large values, which can be exploited for a high-κ condenser and capacitor. Specifically, P(VDF-TrFE) copolymers with TrFE content higher than ≈ 10 % crystallize in a ferroelectric phase[18, 19], monoclinic or orthorhombic, which is similar to the β-crystalline and ferroelectric phase of PVDF[9]. This ferroelectric phase is stable at room temperature and suffers a phase transition to a paraelectric one, hexagonal, as temperature increases[17, 20]. This transition temperature, (Curie temperature), increases with TrFE content[20].

In this chapter, we present results on the physical properties of the ferroelectric copolymer P(VDF-TrFE) when subjected to several types of confinement. In a first section, ferroelectricity of polymer nanoparticles is presented and discussed. This work was carried out at the facilities of IEM-CSIC. Later on, a second section regarding the ferroelectric study at the nanoscale of nanoparticles and nanostructures prepared by Nanoimprint Lithography is presented. The work in this section was carried out at IEM-CSIC and at IMB-CSIC.

7.2. Ferroelectric nanoparticles

7.2.1. Samples and techniques

Surfactant free polymer nanoparticles of P(VDF-TrFE) were prepared following the dialysis nanoprecipitation method, previously detailed in chapter 3 (section 3.2.1.). Two molar concentrations of the ferroelectric copolymer were used, 76:24 and 56:44 (VDF:TrFE). The specific names Ferro76 for the 76:24 molar concentration sample, and Ferro56 for the 56:44 molar concentration sample are used. In order to study their ferroelectric behavior, differential scanning calorimetry (DSC), wide angle x-ray scattering (WAXS) and broadband dielectric spectroscopy (BDS) techniques have been employed. The nanoparticle emulsions were lyophilized in order to obtain a fine powder without water residues. DSC, WAXS and BDS measurements were carried out using the lyophilized samples. Bulk measurements were performed using the sample as received.

DSC measurements were carried out by encapsulating the lyophilized nanoparticle powder in aluminium pans, and heating from -20 ºC up to above the expected melting temperature (T_m) at a rate of 20 ºC·min^{-1}.Typical weight of the samples was about 5 mg. For WAXS experiments lyophilized nanoparticles were packed in aluminum sheets. Bulk sample was measured as received also packed in aluminum sheets. For BDS experiments, bulk films were prepared in a thermoplastics press machine and gold electrodes were sputtered on both sides. Sample was placed inside the cryostat by pressing it with two gold electrodes. Nanoparticles were measured as a lyophilized powder without sputtered gold electrodes. In this case, the sample was placed inside the cryostat pressed between gold electrodes and using adhesive Kapton© spacers to avoid short-circuits.

7. 2. 2. Evidence of ferroelectricity in P(VDF-TrFE) nanoparticles

Throughout this section, the influence of three dimensional confinement on the ferroelectric nature of P(VDF-TrFE) will be presented and discussed. First let's begin by showing the results for a thermal and structural characterization. Afterwards, the results on the dielectric response of the nanoparticles will be presented. Finally, the molecular dynamics of the ferroelectric copolymer is discussed.

Thermal and structural characterization

In the previous chapter we have shown how the glass transition of amorphous polymer nanoparticles can be characterized by DSC. For semi-crystalline polymers confined to the nanoscale, WAXS measurements can also be very useful to deal with structural properties [21, 22]. In this section we present a combined study of WAXS and DSC that allows understanding the ferroelectric properties of nanoparticles and comparing them with those of the bulk. Figure 7.1 shows results of differential scanning calorimetry measurements and X-ray scattering patterns as a function of temperature for both bulk and nanoparticles of P(VDF-TrFE).

Figures 7.1(a) and (c) show that at room temperature the WAXS patterns of bulk P(VDF-TrFE) samples present a sharp maximum around $2\theta \approx 20º$. This indicates the semicrystalline nature of the sample, which maximum is characteristic of the (200)(110) reflection of the orthorhombic ferroelectric crystalline phase of P(VDF-TrFE)[23]. In the case of Ferro76 (76:24 molar concentration bulk sample), this maximum suffers no changes on heating for T< 120 ºC. At T≈ 120 ºC a new peak at lower 2θ values appears. This maximum is characteristic of the hexagonal paraelectric phase of P(VDF-TrFE)[23]. At

T ≈ 130 ºC the two peaks coexist with comparable intensity. At T ≈ 140 ºC only the peak at lower angles is present. Finally, the peak disappears at above 150 ºC and only an amorphous halo is measured, which can be interpreted as result of the melting of the copolymer. On the other hand, Ferro56 (56:44 molar concentration sample) WAXS patterns show that the initial maximum start suffering changes at temperatures above 40 ºC. In fact, between 45 ºC and 70 ºC a sort of transition of the crystalline peak, toward lower 2θ angles, is observed in the WAXS patterns. At 80 ºC the peak is located at around $2\theta \approx 18º$. As in Ferro76, this maximum is characteristic of the hexagonal paraelectric phase of P(VDF-TrFE). This maximum is maintained up to 150 ºC. Above this temperature only an amorphous halo is measured, which can be interpreted as result of the melting of the copolymer.

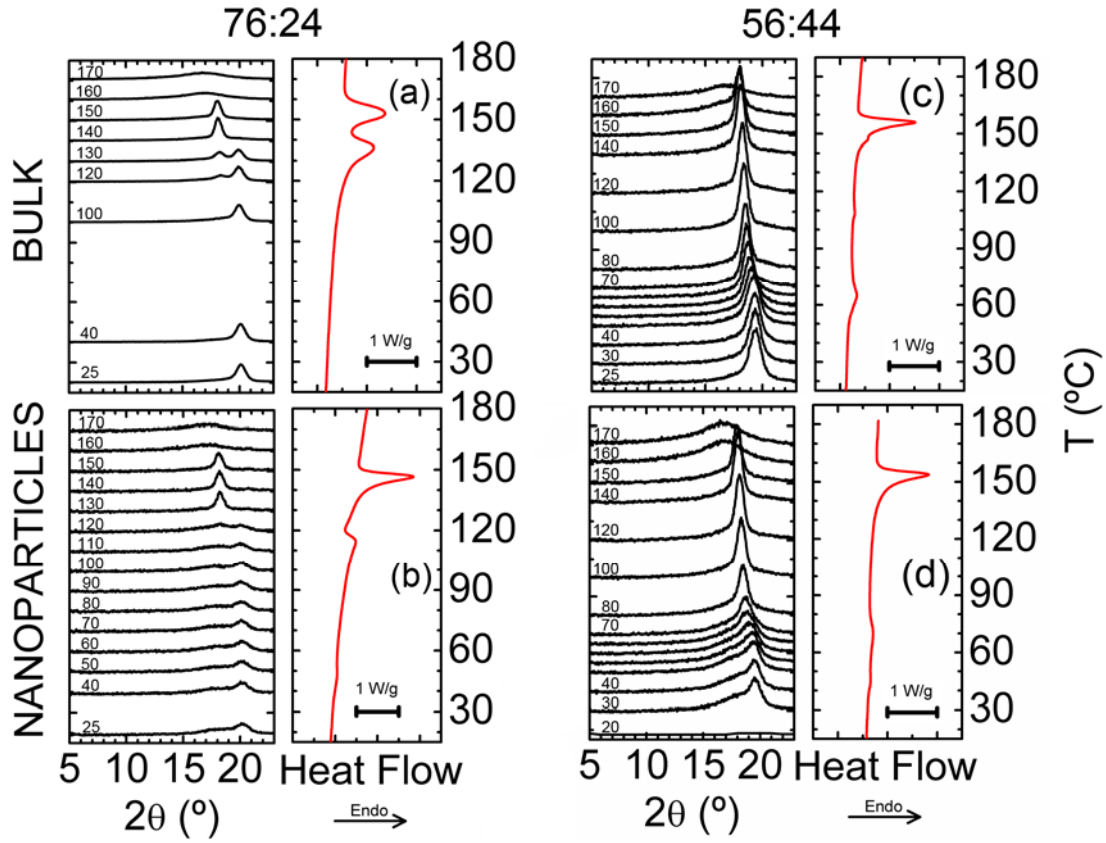

Figure 7.1. Wide Angle X-ray Scattering patterns as a function of temperature and Differential Scanning Calorimetry measurements for (a) bulk and (b) nanoparticles of P(VDF-TrFE) at a molar concentration of 76:24. Right side of the image shows the results for (c) bulk and (d) nanoparticles at a 56:44 molar concentration. Labels on the scattering patterns correspond to the temperature in ºC.

As in the WAXS experiments, the calorimetric trace of the bulk polymers show transitions at temperatures closely related to the evidenced in the scattering experiment. The DSC trace of the bulk polymer Ferro76 shows no transitions below 120 ºC (figure 7.1). Above this temperature two endothermic peaks appeared. Analysis of these peaks show that its maxima are located at 127 ± 1 ºC and 148 ± 1 ºC. The temperature range of the first peak correlates well with the appearance of the second peak at lower angles in the x-ray diffractograms. According to the literature, this peak can be related to the phase transition of the crystalline phase from a ferroelectric to a paraelectric state[18, 24]. Comparison between WAXS and DSC allows concluding that the second endothermic peak is related to the melting of the sample. Subsequent DSC runs showed comparable results. In the case of the bulk polymer Ferro56, two calorimetric transitions are also observed, located at 65 ± 1 ºC and 156 ± 1 ºC. According to the literature[25], the first calorimetric peak can be related to the ferroelectric-to-paraelectric phase transition. Also, comparing with the WAXS results, this is located around the temperature region in which the crystalline peak goes from $2\theta \approx 20º$ down to 18º. Moreover, the comparison with WAXS results allows concluding that the second calorimetric peak can be related to the melting of the sample. As with Ferro76 sample, subsequent DSC runs showed comparable results

Figures 7.1 (b) and (d) show the WAXS and DSC results for the P(VDF-TrFE) nanoparticles of the two molar concentrations. At room temperature, the WAXS patterns exhibit the ferroelectric phase maximum around $2\theta \approx 20º$ analogously to the bulk case in both cases. The presence of this maximum evidences the semicrystalline nature of the nanoparticles. The inherent crystallinity of the nanoparticles provides the necessary mechanical stability to the nanoparticles avoiding coalescence at temperatures above T_g.

In the specific case of the 76:24 molar concentration, as temperature increases the WAXS patterns remain unchanged until T ≈ 110 ºC. At this temperature the Bragg peak characteristic of the hexagonal paraelectric phase of P(VDF-TrFE) appears over the low angle shoulder. As in the bulk sample, this new peak gains intensity with temperature and at T ≈ 130 ºC is the only one present in the pattern. At T > 150 ºC the sample shows and amorphous halo characteristic of the molten state. In the case of the nanoparticles of 56:44 molar concentration, the original Bragg peak remains stable up to 40 ºC where it suffers a transition towards lower 2θ angles, as in the bulk scenario. This transition can be related to the appearance of the paraelectric phase of the copolymer. This phase remains stable up to 160 ºC, where melting takes place. DSC results correlate with the WAXS measurements for both molar concentrations. In both cases, two endothermic peaks are measured, located at 114 ± 1 ºC and 147 ± 1 ºC for the 76:24 molar concentration, and at 70 ± 1 ºC and 154 ± 1 ºC for the 56:44 case. Comparison between WAXS and DSC for the bulk and nanoparticles suggests that the first transition just above orresponds to the ferroelectric-to-paralectric transition of the nanospheres while the second calorimetric peak reveals the melting process. Interestingly enough, it is worth mentioning that in the 76:24 case, the ferroelectric-to-paraelectric transition appears at lower temperatures in comparison to the bulk, while in the 56:44 case appears at slightly higher temperatures. This fact will be discussed in the following lines.

The above presented results indicate that the as prepared nanospheres of P(VDF-TrFE) are semicrystalline and that the crystalline phase is the ferroelectric one at room temperature and below T=110 ºC for the 76:24 case and T = 60 ºC for the 56:44 case. It is also worth noting that for the nanoparticles of both concentrations a weak thermal transition in the DSC measurement appears around 40 ºC which cannot be correlated to

structural changes in the WAXS patterns. A second DSC run, showed that this transition disappeared while the endothermic peaks returned to the bulk values. This evidences that above melting temperature, nanospheres are no longer stable and the system recovers its bulk properties. This result is similar to the obtained for PEMA nanoparticles (chapter 4, section 4.3.3.).

The WAXS patterns were deconvoluted with contributions from the ferroelectric and paraelectric crystalline phases, as well as from the amorphous halo. From the ratio of the integrated intensities of the amorphous halo and of the crystalline peaks to the total intensity[26, 27] the overall contribution degree of the different phases can be obtained. Figures 7.2 and 7.3 show the results obtained. In the Ferro76 case, figure 7.2 (top) shows WAXS patterns at 25 ºC for bulk and nanoparticles along with the fitted peaks. In each case, three Pearson functions were used for fitting the data and to model the ferroelectric (F), paraelectric (P) and the amorphous (A) phases of the polymer. The combination of these three contributions provides a satisfactory description to the WAXS patterns as shown. This same approach was used for the Ferro56 sample which results are shown in figure 7.3 (top). The fitting procedure was performed for the whole investigated temperature range, and results are summarized in figures 7.2 (bottom) and 7.3 (bottom). Specifically, analysis of the area under the curves for the bulk Ferro76 sample, showed that at room temperature, the ferroelectric phase (red squares) represented around 70 % of the total area along with a 10 % paraelectric phase (green stars) and 20 % amorphous phase (blue triangles). Sum of ferroelectric and paraelectric phases gave a total 80 % crystallinity in the copolymer in agreement with previous studies[26, 27]. In the case of the bulk Ferro56 sample, at room temperature the ferroelectric phase represented around

50 % of the total area with a 20 % paraelectric phase and 30 % amorphous phase. This leads to a total 70 % crystallinity in this copolymer.

As temperature increases, no changes are evident until at temperatures below the ferroelectric-to-paraelectric transition previously discussed. For the 76:24 bulk copolymer, no changes are seen in the ferroelectric phase area until T= 120 ºC, where the ferroelectric phase suffers a dramatic drop. This effect is accompanied by an increase of the paraeletric phase. At temperatures above 150 ºC, the sample melts and the only significant contribution is that of the amorphous halo. Previously we showed that the 56:44 bulk sample presented a sort of displacement in its Bragg peak, towards lower values of 2θ, as temperature increased. The decomposition of the x-ray patterns shows that in the region around the ferroelectric-to-paraelectric transition (40 ºC – 70 ºC) the ferroelectric peak suffers a decrease in its area, while the paraelectric phase area increases. Above T = 70 ºC, the paraelectric phase contribution reaches a plateau that is maintained until melting of the copolymer. Finally, for both molar concentrations, bulk WAXS measurements shows that the position of the maxima presents only a slight decrease as temperatures increases related to the expansion of the crystalline unit cells.

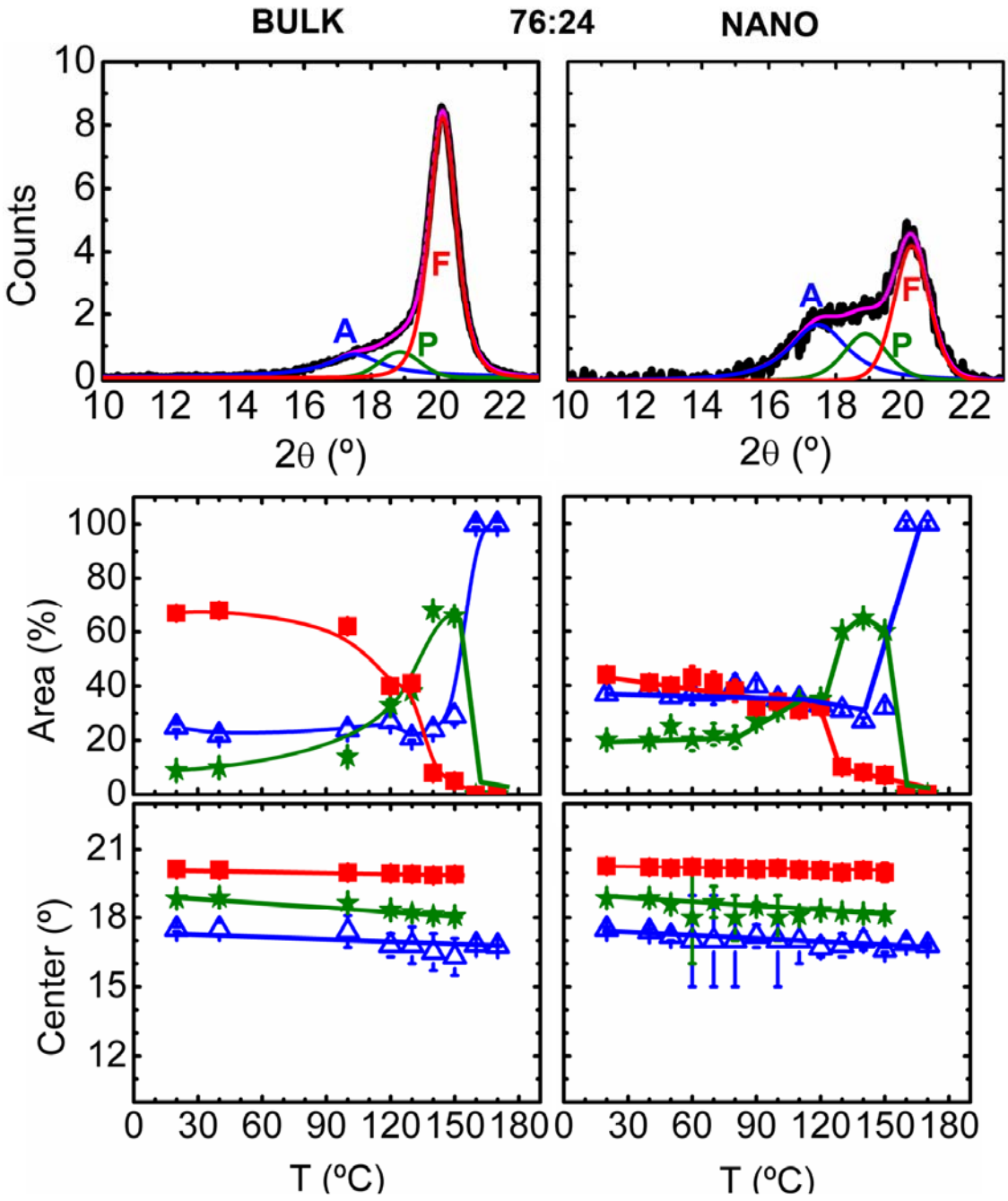

Fig 7.2. (Top) WAXS measurements at 25 ºC for bulk (left) and nanostructured (right) samples of P(VDF-TrFE) at 76:24 molar concentration. F, P and A represent the fitted peaks of the ferroelectric, paraelectric and amorphous phases respectively. (Bottom) Temperature evolution of the area of the fitted peaks and position of its center. Symbols represent the (■) ferroelectric, (★) paraelectric and (△) amorphous phases.

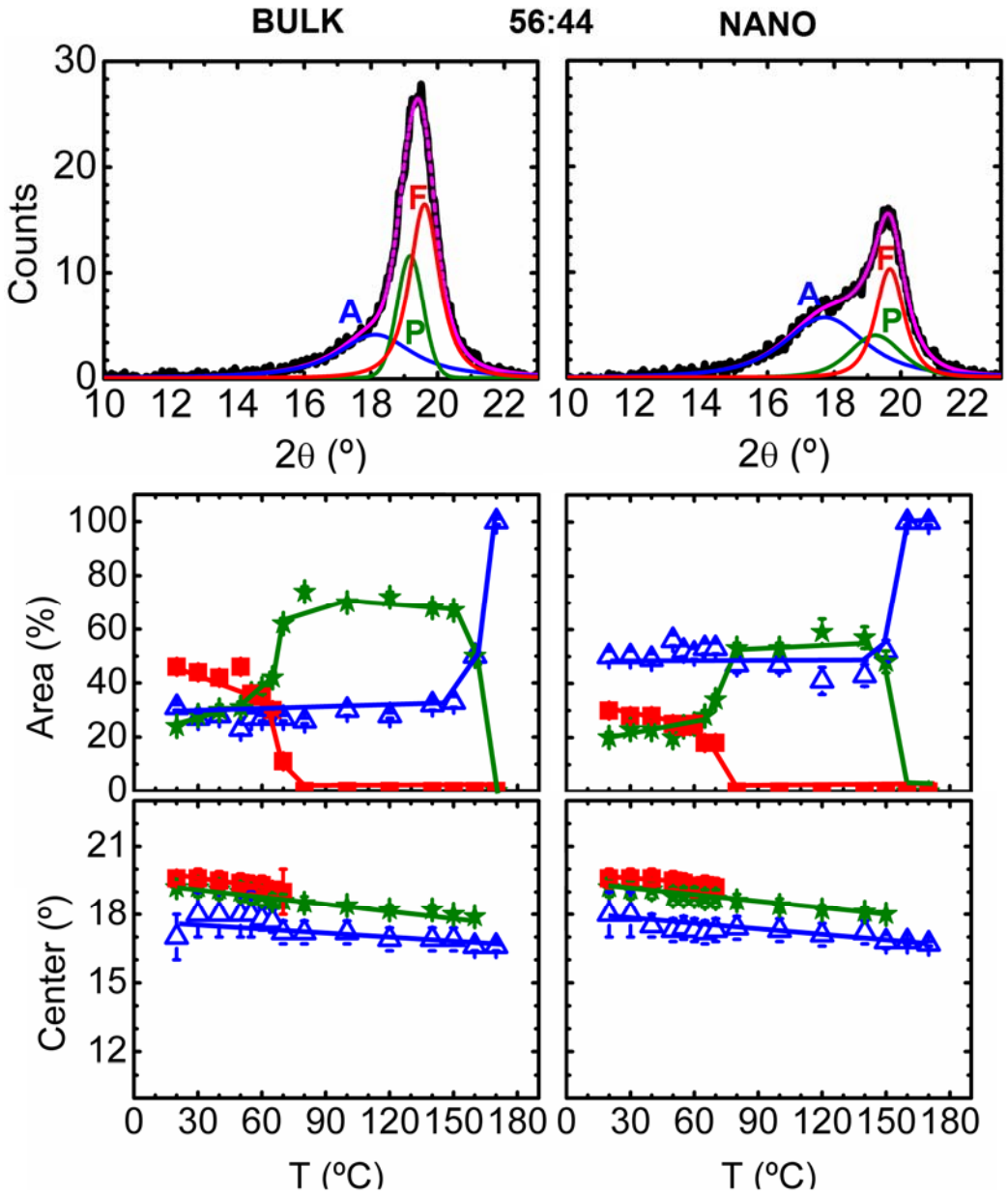

Fig 7.3. (Top) WAXS measurements at 25 ºC for bulk (left) and nanostructured (right) samples of P(VDF-TrFE) at 56:44 molar concentration. F, P and A represent the fitted peaks of the ferroelectric, paraelectric and amorphous phases respectively. (Bottom) Temperature evolution of the area of the fitted peaks and position of its center. Symbols represent the (■) ferroelectric, (★) paraelectric and (△) amorphous phases.

Nanoparticles exhibit different behavior. First, for Ferro76 nanoparticles, the area under fitted curves at room temperature showed a 40 % ferroelectric phase, 20 % paraelectric phase and 40 % amorphous phase. Thus total crystallinity is reduced to 60 %, compared to the 80 % in the bulk. Also, it is remarkable the increase of the paraelectric phase in the nanospheres. The Ferro56 nanoparticles showed a 30 % ferroelectric phase,

20 % paraelectric phase and 50 % amorphous phase. In this case, total crystallinity is also reduced, in comparison to the bulk, to 50 %; however, for this molar concentration no increase in the paraelectric phase is seen. As temperatures raises, almost no changes are evident below the measured ferroelectric-to-paraelectric transition. However Ferro76 nanoparticles, at 110 ºC, suffer a ferroelectric-paraelectric transition, as indicated by the sudden decrease in the ferroelectric peak's area along with the concurrent increase of the paraelectric phase. The quantitative analysis of the WAXS patterns shows that, in agreement with the DSC data, ferroelectric-paraelectric transition occurs at lower temperatures in the nanospheres in comparison with the bulk. This result can be explained by the increment of the paraelectric and amorphous phases in the nanospheres. This effect is expected since constraints imposed by the geometrical confinement prevent crystal growth [28]. However, it is worth emphasizing that the ferroelectric property of the nanospheres persists for temperatures below 100 ºC. In the case of Ferro56 nanoparticles, the ferroelectric-paraelectric transition is observed around 70 ºC, and it is also characterized by the sudden decrease in the area of the ferroelectric peak, as the paraelectric phase is increased. In comparison to the bulk sample, this transition seems to occur at higher temperatures in the nanoparticles. This might be explained in terms of the percentage of crystalline phase in this nanostructured copolymer. In the Ferro76 copolymer, nanostructuring led to an increase of the paraelectric phase in comparison to the bulk (figure 7.2). Thus, in the Ferro76 nanoparticles, the phase transition at Curie temperature (T_c) can occur sooner than in the bulk. However, in the Ferro56 copolymer, nanoparticles show a decrease in their crystalline fraction, comparing with the bulk. In this case, the lower degree of paraelectric phase, in comparison to the bulk, allows an increase of T_c since more chains are required to re-organize.

Dielectric response

The changes in the dielectric permittivity, at the Curie temperature, can be observed by Broadband dielectric spectroscopy (BDS). This technique has been used in the literature to characterize the ferroelectric nature of P(VDF-TrFE) copolymers[19, 29-31]. In this thesis we have used BDS to study the ferroelectric nature of the prepared nanoparticles. Figure 7.4 shows isochronal plots of the real and imaginary parts of the complex dielectric permittivity at10^{-1} Hz for both bulk and nanoparticle P(VDF-TrFE) samples. For the sake of comparison the data have been normalized to the ε'' value measured at -50^{o}C. Left column shows the results for the Ferro76 sample, while right column shows the results for Ferro56. Specifically, in the Ferro76 sample, both bulk and nanoparticles show a sharp transition in ε'(T) and ε''(T) around 110 ºC for nanoparticles and 130 ºC for the bulk sample. In agreement with both WAXS and DSC data, these transitions can be related to the ferroelectric-paraelectric one. On the other hand, the Ferro56 sample shows also a sharp transition in ε'(T) and ε''(T) around 60 ºC for bulk and 70 ºC for the nanoparticles. As before, this transition can be related to the ferroelectric-paraelectric phase change and, as in the other techniques, it appears a lower temperature for bulk than for nanoparticles. In general, these results further corroborate the ferroelectric nature of the nanoparticles.

For all the samples, at lower temperatures a maximum in ε''(T) around -40 ^{o}C is observed. This phenomenon occurs in both bulk and nanoparticles (figures 7.4 (b) and (d)). This can be attributed to the segmental relaxation associated to the glass transition in agreement with previous reports[19, 29, 30]. In this type of polymers the segmental relaxation has been labeled as β-relaxation since dynamical mechanical analysis shows

another relaxation, labeled originally as α, associated to the crystalline phase appearing at higher temperatures[19, 29]. In order to comply with the literature we adopt here a similar criterion. A description of the molecular dynamics as revealed by BDS is provided in the next section.

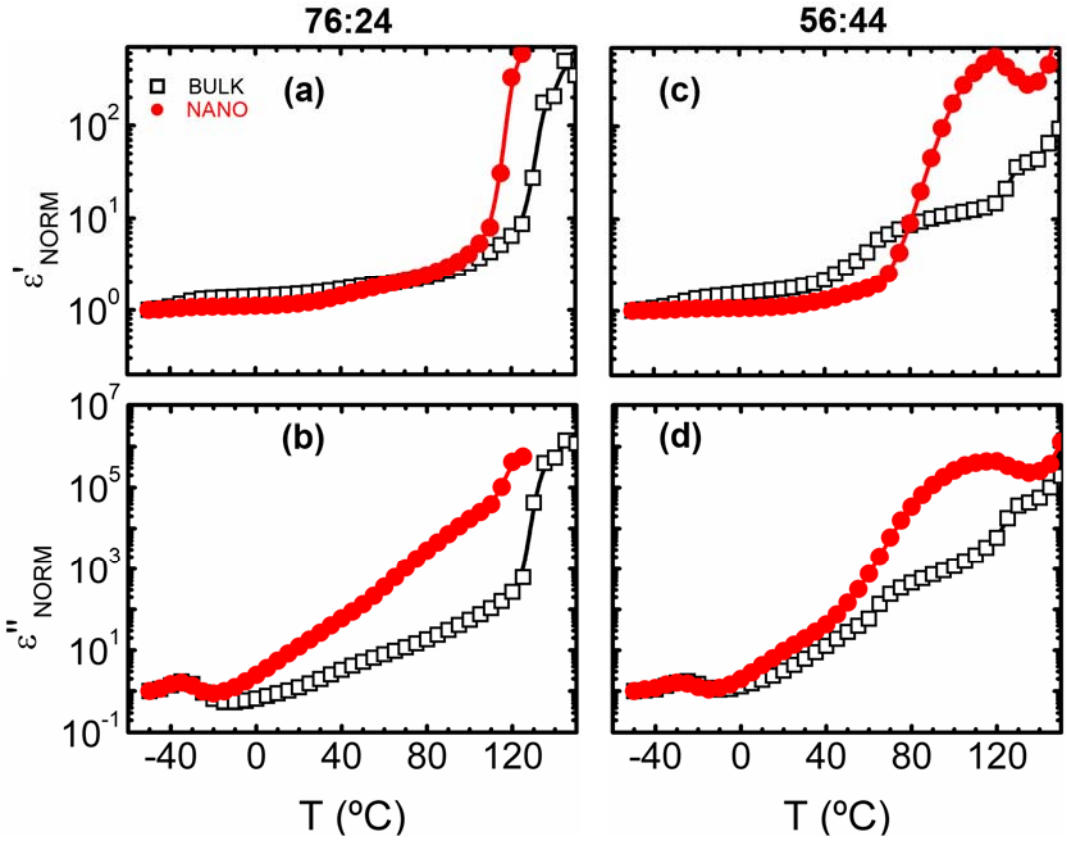

Figure 7.4. Isochronal temperature dependence at 10^{-1} Hz of the real (top) and imaginary (bottom) parts of the complex dielectric permittivity for both bulk (□) and nanometric (●) samples. Each curve is normalized respect the value measured at -50 ºC. (a) and (b) refer to the copolymer of 76:24 molar concentration. (c) and (d) refer to the copolymer of molar concentration 56:44.

7.2.3. Molecular dynamics in ferroelectric nanoparticles

In order to further describe the relaxation processes of the ferroelectric copolymer nanoparticles a dielectric study covering a broad frequency range was performed. Figure 7.5 shows isothermal dielectric loss, ε'', data as a function frequency for bulk and nanoparticles of both molar concentrations. For the sake of comparison the ε'' data have

been normalized to the maximum value at 125 ºC. The β relaxation for bulk and nanoparticles appears as a broad process which is centered around 10^5 Hz at 0^oC. The maximum of this relaxation shifts towards higher values as temperature increases and the relaxation becomes sharper in both cases. A dramatic increase of the intensity of the relaxation is observed as the ferroelectric-paraelectric transition is approached. Notice that this increase seems to happen above 100 ºC in the case of the Ferro76 sample and around 50 ºC for the Ferro56 sample. It has been proposed that for these type of copolymers the intense relaxation observed centered around 10^7-10^8 Hz appears as a consequence of the onset of rotational motion of the molecules within the paraelectric crystalline phase[19, 30]. This process coexists with the segmental relaxation, β, occurring in the amorphous phase. The dielectric loss data can be well described by means of Cole-Cole function (chapter 2, section 2.2.2, equation 2.7). The continuous lines in figure 7.5 are the results of the fits. The obtained fitting parameters for the mean relaxation time $<\tau>$, symmetric broadening *b* and relaxation strength Δε are shown in the following figures for the whole studied temperature range.

Figure 7.6 shows the logarithm of the mean relaxation time as a function of reciprocal temperature for both bulk and nanoparticles. The calorimetric trace has also been included for comparison. For both molar concentrations, the mean relaxation time values for bulk and nanoparticles are quite similar. This indicates that no significant change exists in the amorphous phase segmental dynamics of the nanoparticles in comparison to that the bulk. This can be understood in terms of the nanoparticle size which is still bigger than the threshold expected to start evidencing confinement effects in the segmental dynamics[28]. The continuous line across the data points in figure 7.6 shows

a fit of the Vogel-Fulcher-Tammann (VFT) equation[32] to the mean relaxation time values as:

$$< \tau >= \tau_0 \exp\left[\frac{DT_0}{T - T_0}\right] \qquad \textbf{(7.1)}$$

where τ_0 is the pre-exponential factor, fixed to 10^{-14} s according to the discussion presented by C. A. Angell[33], T_0 is the Vogel temperature and *D* is a dimensionless parameter related to the dynamical fragility[38]. The VFT equation was fitted in the temperature range $3.90 \geq 1000/T\ (K^{-1}) \geq 3.20$. Results are summarized in table 7.1.

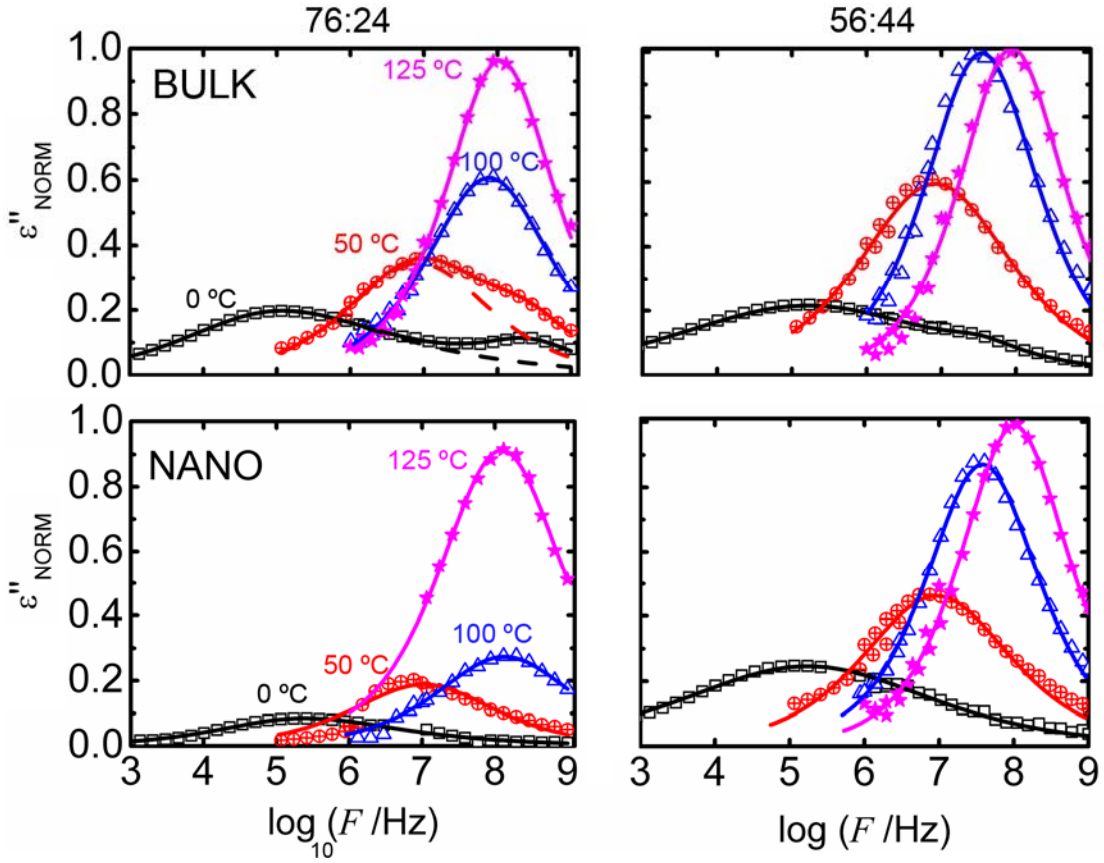

Figure 7.5. Isothermal normalized dielectric loss values, ε'', for bulk and nanoparticles at different temperatures: 0ºC (□), 50 ºC (⊗), 100 ºC (△) and 125 ºC (★).

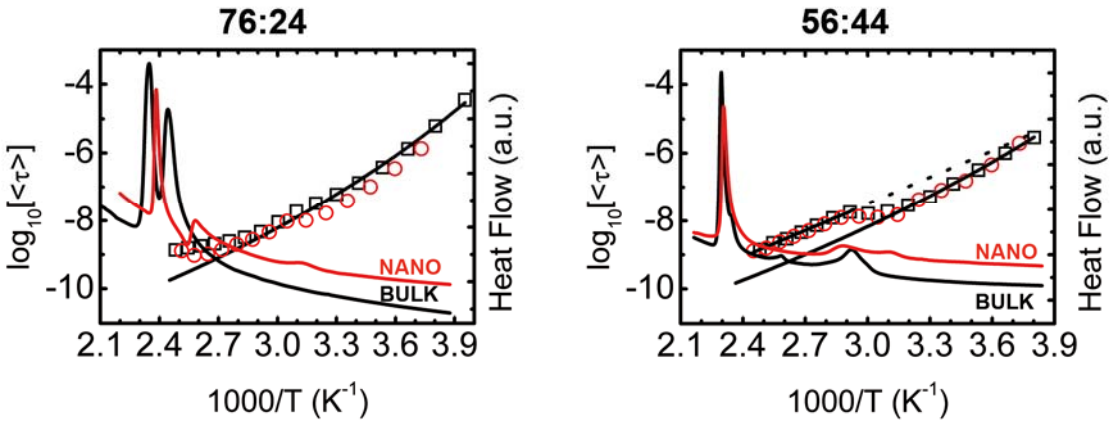

Figure 7.6. Average relaxation time for P(VDF-TrFE) (□) bulk and (○) nanoparticles.

Table 7.1. VFT and Arrhenius fitting parameters for ferroelectric nanoparticles

	Molar Concentration	*D*	τ_0 (s)	T_0 (K)
VFT Fit	76:24	21.6 ± 0.4	10^{-14}	127 ± 3
	56:44	28 ± 1		108 ± 1
Arrhenius Fit		E_A (kJ/mol)	τ_0 (s)	
	56:44	21 ± 1	$10^{-16\pm1}$	

The *D* parameter, sometimes referred to as fragility strength parameter, provides a way to classify glass formers according to the deviation of log<τ> versus T^{-1} from the linear Arrhenius behavior[34] ($D > 10$). In our case, data points show a strong behavior, *i.e.* small deviation from Arrhenius. Below 1000/T = 3.2 K^{-1}, data points in figures 7.6 start deviating from the VFT trend. In the case of the 56:44 molar concentration (figure 7.6 right), a sort of plateau is reached, that coincides with the peak of the ferroelectric-to-paraelectric measured by DSC. This sort of anomaly has been previously described[30] and can be understood as the *signature* of the ferroelectric-paraelectric phase transition. At this molar concentration, for temperatures above 70 ºC ($2.9 \cdot 10^{-3}$ K^{-1}), relaxation time data

shows a linear trend. This is the temperature region in which the relaxation process of the paraelectric phase becomes predominant and superimposes itself over the segmental process. The high temperature linear dependence can be described by an Arrhenius function:

$$< \tau >= \tau_0 \exp\left[\frac{E_A}{k_B T}\right] \qquad \textbf{(7.2)}$$

where E_A is the activation energy, k_B the Boltzmann constant, and τ_0 the relaxation rate in the high temperature limit. Results from the Arrhenius fitting are summarized in table 7.1. In the case of the Ferro76 sample, the deviation from the VFT trend is also evidenced. However, the Arrhenius behavior related to the relaxation of the paraelectric phase is not observed. Comparing with the DSC results, this is understood due to the higher T_c at this concentration.

Relaxation strength ($\Delta\varepsilon$) and symmetric broadening parameter (b) are shown in figure 7.7 for bulk and nanoparticles of both molar concentrations. For every case, the broadening shape parameter of the Cole-Cole relaxation (b) increases with temperature. Specifically, in the Ferro56 sample, a plateau between 70 ºC and 120 ºC is observed. This behavior can be considered as a characteristic feature of the dominance of the relaxation associated to the paraelectric phase[30] in the relaxation spectrum. Regarding the relaxation strength, in the temperature region associated with the relaxation of the paraelectric phase, $\Delta\varepsilon$ starts deviating from the trend observed at lower temperatures characterized by the segmental relaxation. The observed increase can be related to the increasing fraction of paraelectric phase which appears at the ferroelectric-to-paraelectric transition. The

temperature region in which Δε suddenly increases correlates well with the WAXS and DSC results in this work. Moreover, in the 56:44 molar concentration, after the sudden increase, Δε values start decreasing. This Δε decrease relates with the Arrhenius process in the relaxation map and thus can be related to the relaxation of the paraelectric phase inside the crystals. Although being described by an Arrhenius, the decrease of Δε with temperature is usually associated to segmental relaxations. This leads to the idea of interpreting this linear trend as the "final part" of an original VFT process that at lower temperatures is masked by the β-relaxation of the amorphous phase.

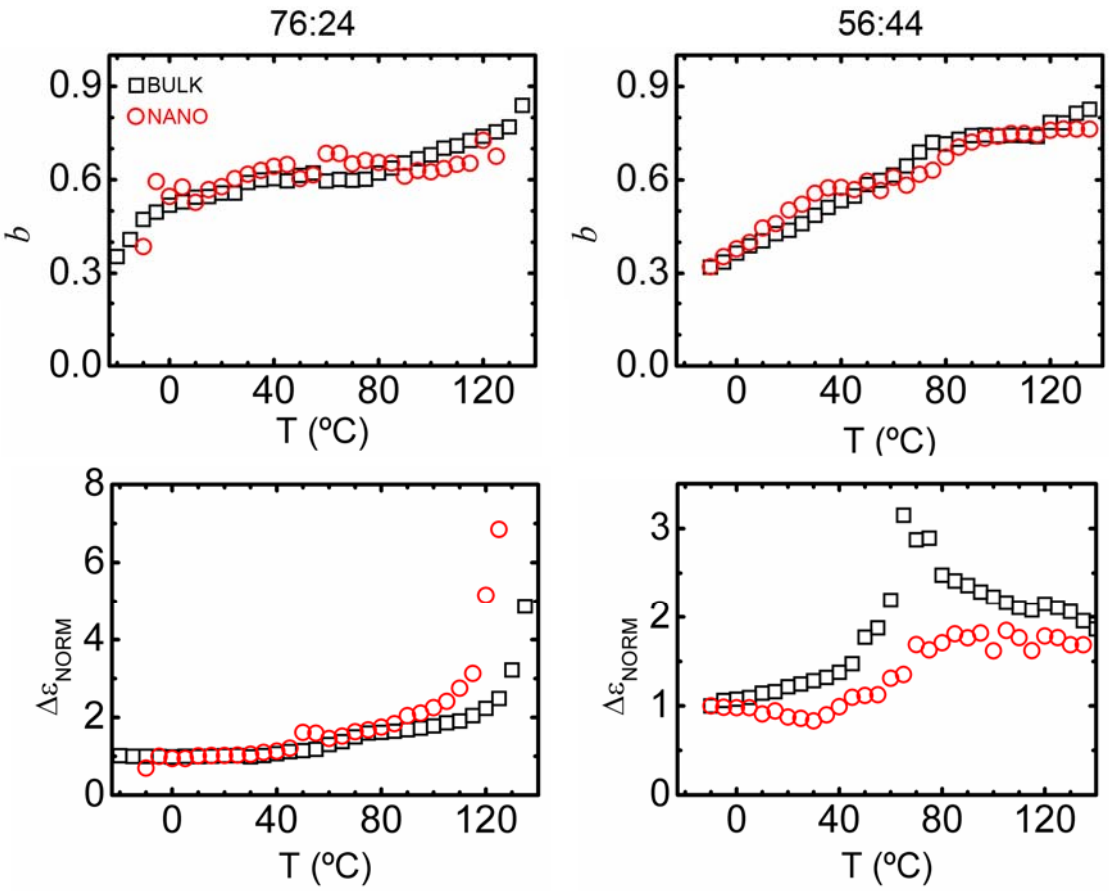

Figure 7.7. Symmetric broadening and relaxation strength parameters of the Cole-Cole functions for bulk (black squares) and nanoparticles (red circles). (Left) 76:24 molar concentration. (Right) 56:44 molar concentration.

7.3. Ferroelectric behavior of polymers at the nanoscale

7.3.1. Samples and techniques

As in the previous sections, surfactant free nanoparticles, prepared via the dyalisis nanoprecipitation method were prepared. In this case, focus was set in the 76:24 molar concentration sample. Also, nanostructured thin films by nanoimprint lithography were prepared. The steps described in chapter 3 (section 3.5), were followed and P(VDF-TrFE) nanogratings of height of about (130 ± 10) nm and pitch (line-to-line distance) of about (210 ± 10) nm, were obtained. The molar concentration of the copolymer used was also 76:24.

For the ferroelectric studies at the nanoscale the Piezo-Response Force Microscopy (PFM) with SCM-PIC probes was used. NIL polymer gratings were investigated by means of Grazing Incidence X-ray Scattering at Wide Angles (GIWAXS).

7.3.2. Probing ferroelectric response at the nanoscale

Polymer Nanoparticles

In the previous sections, WAXS, DSC and BDS results indicated that the P(VDF-TrFE) nanoparticles are semicrystalline in their ferroelectric phase. The aim of this section is to probe the ferroelectric character of the individual nanoparticles. Recently[4, 10, 16, 35], scanning probe techniques have been widely used to prove the ferroelectric response of nanostructured polymer samples. Among them, the piezo-response force microscopy (PFM) is one of the most used. PFM has been introduced previously in chapter 2 (section 2.2.2)

Figure 7.8 shows 5 hysteresis cycles taken at different 76:24 ferroelectric nanoparticles (red lines). For comparison, a measurement of a continuous P(VDF-TrFE) thin film (76:24) is also shown (black line). The voltage loop applied to the samples (-12 V to +12 V) was converted to the modulus of the electric field (**E**) [MV/m], by dividing the voltage per the height of the nanoparticles, or the thickness in the case of the thin film.

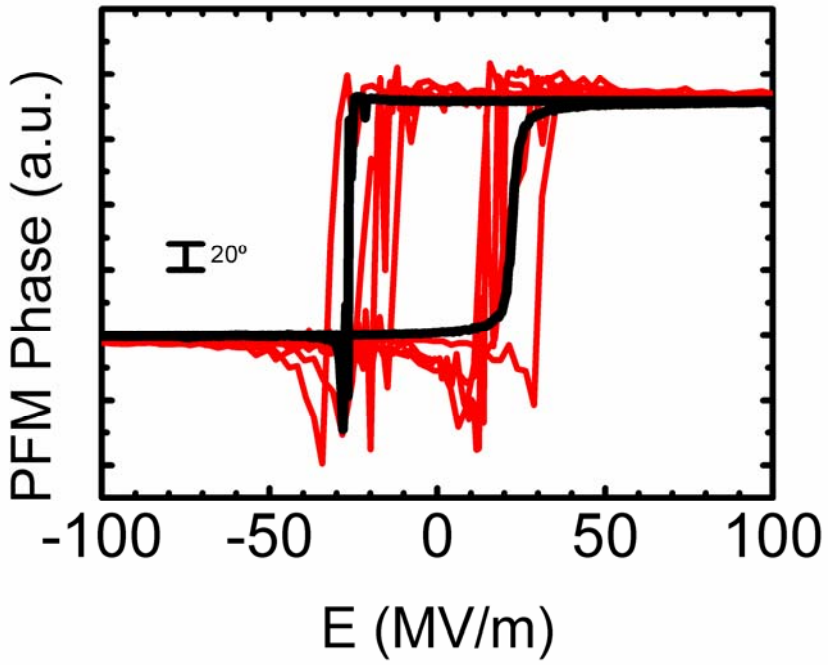

Figure 7.8 Hysteresis cycles for the 76:24 ferroelectric nanospheres (red) and a P(VDF-TrFE) thin film (black). Black bar to the left reflects the scale in the phase.

In ferroelectric samples, PFM hysteresis cycles are characterized by a 180º shift of the PFM phase[10]. These changes are related to the shift of the polymer dipoles in the vertical direction, with respect to the sample surface (out-of-plane polarization). In our study, both nanoparticles and thin film show this shift, demonstrating the evidence of ferroelectricity at nanoscale levels and room temperature. The value of **E** where the shift occurs is called the coercive field of the sample ($\mathbf{E_c}$). For the continuous thin film, the $\mathbf{E_c}$ value is about (25 ± 2) MV/m, while in the nanoparticles slightly reduces to (20 ± 5) MV/m. Although this slight change could be interpreted in terms of rearrangement of the molecules inside the polymer nanoparticles, error values do not allow further discussion.

The shift of the polymer dipoles in the "horizontal" direction (parallel to the sample surface, called in-plane polarization), can also be evaluated via PFM. However, although the continuous film shows a ferroelectric response in this direction (discussed in the next section), in the polymer nanoparticles only noise was measured. This might be related to the spherical shape of the particles that does not allow proper tip-sample contact.

Nanogratings

Polymer nanogratings prepared by NIL were also tested to evaluate their ferroelectric response. As in the previous case, PFM was used as technique. Since PFM works in contact mode, scans were carried out in a direction parallel to the nanogratings to avoid damage of the nanostructures. Figure 7.9 shows the results obtained for vertical (out-of-plane) and horizontal (in-plane) responses of both NIL nanogratings (blue curves) and continuous thin films (black curve). Vertical PFM response shows hysteresis cycles with 180º phase shift at fields different from zero, indicating the presence of ferroelectric domains in this direction. The $\mathbf{E_c}$ of the nanogratings can be calculated to be about (5 ± 2) MV/m, which is much lower in comparison to the continuous thin film. Horizontal PFM response shows also hysteresis cycles characteristics of ferroelectric domains in both thin films and nanogratings. In this case, the $\mathbf{E_c}$ of the thin film is (85 ± 5) MV/m, while in the nanogratings decreases down to (50 ± 10) MV/m, indicating a reduction on the **Ec** values in both out-of-plane and in-plane directions with confinement.

Although results show that NIL nanogratings have a ferroelectric response, two important questions arise. First, why thin films and nanogratings show a hysteresis cycle in both vertical and horizontal directions? And also, why in the nanogratings the values of E_c decrease from those of the bulk?

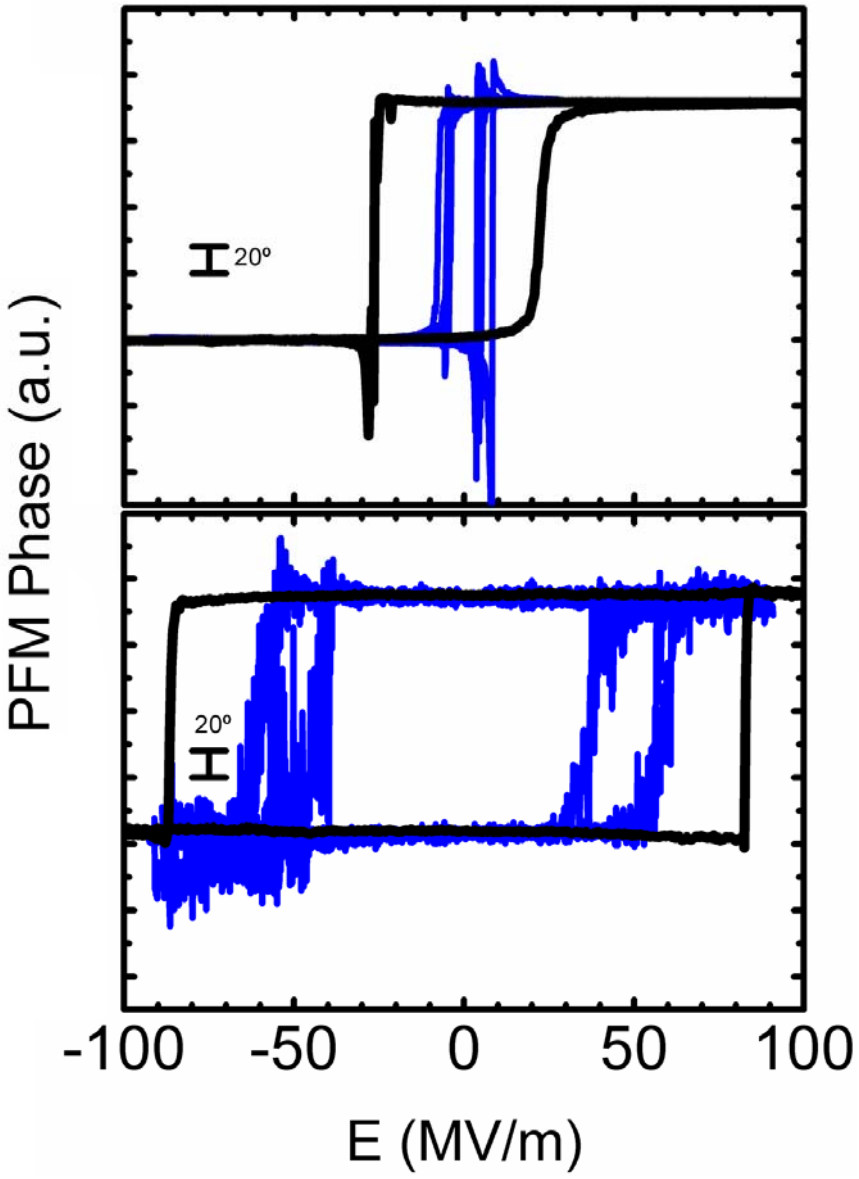

Figure 7.9. PFM hysteresis cycles in vertical (up) and horizontal (down) directions. Black line represents the response of a continuous P(VDF-TrFE) thin film. Blue lines show the response of P(VDF-TrFE) nanogratings. Black bar to the left reflects the scale in the phase.

In order to understand why $\mathbf{E_c}$ values decreases from those of the bulk, one have to consider that organic ferroelectricity depends strongly on the crystalline nature of the polymers. Therefore, the crystalline layout in both thin films and nanogratings has been studied in detail. Figure.7.10 shows an AFM topography image of the P(VDF-TrFE) thin film. This type of spin-coated films typically exhibit roughness values of r.m.s. ≈ ±20 nm, as well as the characteristic morphology of P(VDF-TrFE) copolymers characterized by

random large needlelike crystals (A)[36]. This morphology has been associated to edge-on lamellae, that also coexist with flat-on crystals appearing as irregular flakes on the AFM image (B).

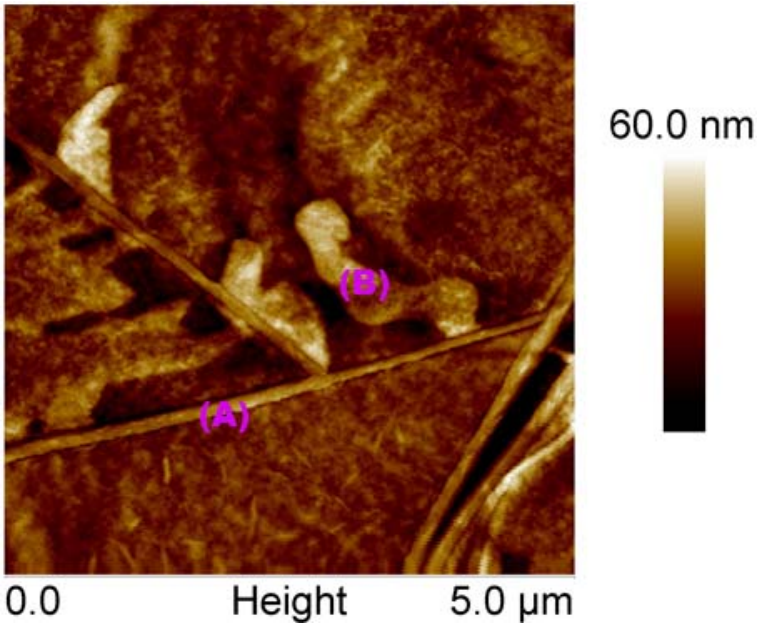

Figure.7.10 AFM topography image of a P(VDF-TrFE) thin film of thickness ≈ 100 ± 2 nm.

The AFM morphology is also supported by GIWAXS experiments which delivers the type of patterns shown in figure 7.11, for both film and nanogratings. The GIWAXS pattern for the thin film (figure 7.11a) shows the strongest reflections (200) and (110), of similar lattice spacing, appearing at a q-value of 13.78±0.34 nm^{-1}. These reflections correspond to the orthorhombic crystal lattice of P(VDF-TrFE) copolymers[36-38]. Also, these two reflections are separated 60^{o} from one another in a hk0 diffraction pattern, indicating that the c-axis, which coincides with the polymer chain direction, is parallel to the X-ray beam[36]. The intensity distribution on the observed semi-ring can be used to characterize both polymer chains and lamellae orientation on these thin films.

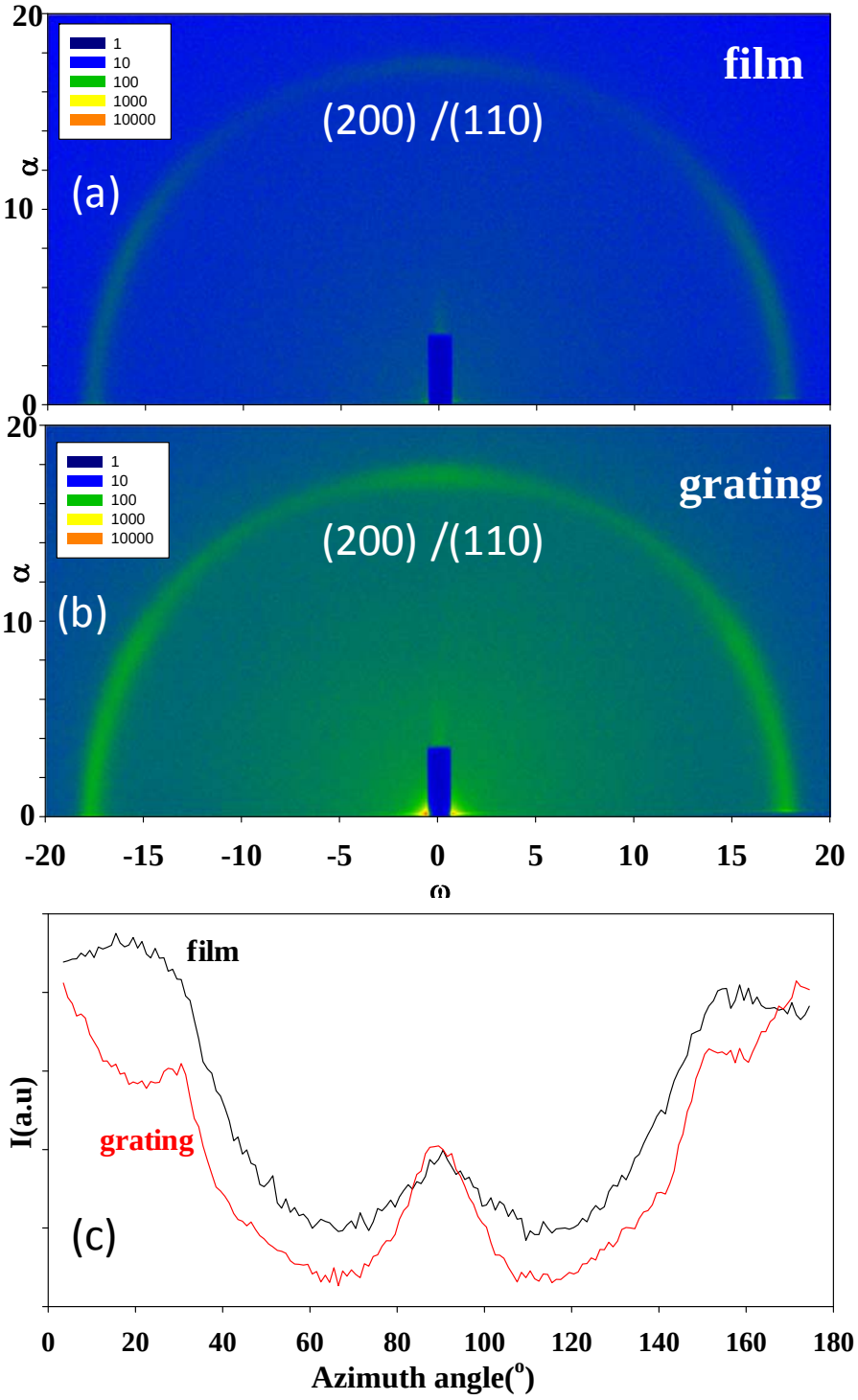

Figure.7.11 GIWAXS patterns of: (a) a P(VDF-TrFE) thin film of thickness ≈ 100 ± 2nm and (b) a P(VDF-TrFE) grating prepared by NIL. (c) Azimuth intensity profiles of the multiple reflection (200)/(110) for both film and grating.

On one hand, the existence of significant intensity on the equatorial region can be attributed to the presence of flat-on lamellae with polymer chains oriented perpendicular

to the surface[36]. On the other hand, a high intensity on the meridian indicate the existence of edge-on lamellae with polymer chains lying on the substrate[39]. Thus, both AFM image and GIWAXS patterns indicate that the P(VDF-TrFE) thin films consist of a mixture of flat-on and edge-on lamellae with some degree of tilting. The presence of both flat-on and edge-on lamellae allows understanding the evidence of ferroelectricity in both vertical and horizontal directions in the thin films. Also, in this case, the differences in coercive fields for vertical and horizontal domains can be qualitatively understood in terms of the molecular motions involved in the flipping process since H-C-F dipole can easily rotate in the edge-on crystals[36] and can be associated to the out-of-plane PFM signal. On the contrary the dipole rotation in flat-on crystals is severely hindered due to steric constrains[36], and thus a higher coercive field is obtained in the in-plane signal.

According to the figures 7.11a and 7.11b GIWAXS patterns of the nanogratings are qualitatively similar to those of the films. However, azimuth intensity profiles of the semi-ring reveal subtle differences between films and gratings (figure 7.11c). In the case of the nanogratings, clear maxima at 30^{o} and 90^{o} are resolved. As mentioned above this feature is characteristic for an edge-on morphology with the polymer chain parallel to the beam. Considering that the X-rays beam impinges the grating along the lines (see scheme in chapter 2, figure 2.1) this indicates that for the nanogratings edge-on lamellae are more abundant than those flat-on. This observation is in agreement with the crystal orientation observed for P(VDF-TrFE) confined within self-assembled organosilicates[39]. As for the films, the hysteresis loops of the nanogratings exhibit a clear anisotropy when comparing vertical and horizontal domain. This can be understood from the GIWAXS results considering the coexistence of edge-on and flat-on crystals on the nanogratings which can explain the evidence of ferroelectric response at vertical and horizontal sampling.

Regarding the decrease of $\mathbf{E_c}$ in the nanostructured sample in comparison to the continuous thin film, Kassa et al[16] suggest that when the sample is imprinted in its paraelectric phase in conditions leading to complete confinement, in cavities of size lower than the natural lamellar length observed in a continuous thin film, the crystallographic a axis aligns preferentially parallel to the substrate, and the crystalline lamellae are of significantly reduced length. These characteristics translate in a strongly decreased coercive field and accelerated ferroelectric switching, which is in part ascribed to the improved coupling between the electric field and the properly oriented dipole moments.

7.3.3. Ferroelectric information management at the nanoscale.

Besides allowing measuring ferroelectric response at the nanoscale, scanning probe techniques have been recently employed for the assesment of writing and reading ferroelectric information at nanometric length scales[2, 10, 35, 40]. In this case, the idea consist of writing information on a ferroelectric surface, by applying a bias with a metallic coated AFM tip. If the applied bias turns into a field of magnitude above of $\mathbf{E_c}$, ferroelectric domains will align along the direction of the field. Due to the hysteresis, when the field is turned off, the dipole moment of the molecules will remain pointing towards the direction imposed. Aftewards, reading can be attained by a PFM scan where biased zones show contrast in the PFM amplitude and phase channels, in comparisson to the unbiased zones[41]. In this work we have tested the posibilities to write and read ferroelectric information in P(VDF-TrFE). As in the previous case, a continuous film and a nanostructured one were evaluated.

Figure 7.12 shows the results obtained for the P(VDF-TrFE) thin film. Top image shows a PFM height topography (AFM contact mode measurement). This image

resembles the one presented in figure 7.10 where needle like structures can be elucidated. Once topography was obtained, the writing protocol was applied. In this specific case, the scanning probe was moved to the center line of the image and a bias of +12 V was applied through the tip during 300 s. Throught this time, the tip was scanning always the same horizontal line, indicated in figure 7.12 by the black arrow.

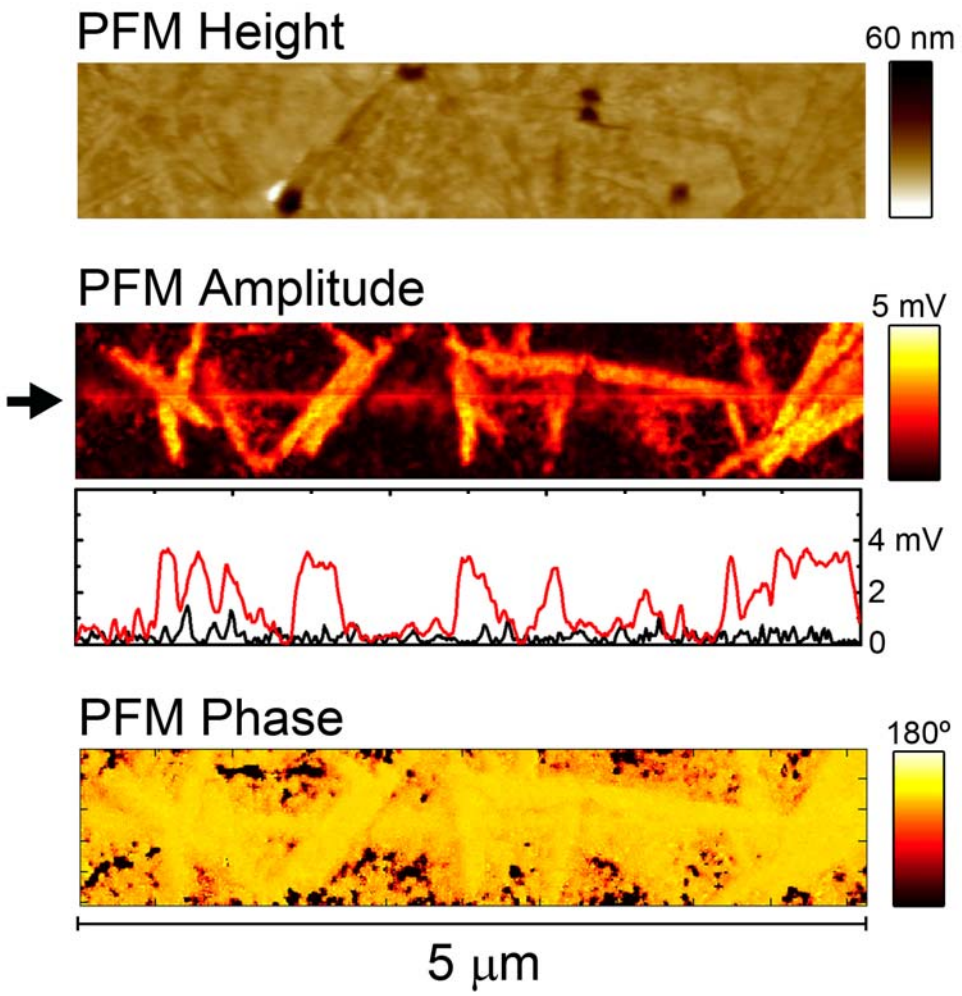

Figure 7.12 PFM height, amplitude and phase of a poled P(VDF-TrFE) thin film.

Before poling, the PFM amplitude images exhibit essentially no contrast. However, after poling over a horizontal line in the sample that can be visualized at the centre of the image. The presence of a non-zero amplitude is a clear manifestation of the ferroelectric response of the polymer. It is obvious that after poling the ferroelectric

response is not restricted to the poling line but it propagates along extended portions of the needlelike crystals as large as several microns. The strong out-of-plane signal further corroborate that the needlelike crystals mainly consist on edge-on lamellae with polymer chains aligned parallel to the substrate[42].

Similarly as for the films, the ferroelectric response of these P(VDF-TrFE) gratings was tested by means of PFM. Figure 7.13 show the topography, PFM amplitude and PFM phase images respectively of a selected region of the grating films. In this case, the PFM image was taken after applying a tip poling voltage of +12 V for 300 s in 5 spots, over the third line visualized in the image. As for the films, before poling, the gratings show no PFM contrast. After poling, the out-of-plane PFM amplitude exhibits the 5 written spots. The average size of the points is ≈ 250 nm^2. It is worth mentioning that the extension of the ferroelectric domains in the gratings is about one order of magnitude smaller than those obtained in the spin-coated films. The decrease of the ferroelectric domains size in the gratings can be attributed to the limitation of the growth of the needlelike polymer crystals imposed by the wall trenches of the grating. The technological interest of this proposed nanostructure for ferroelectric applications lies in the simplicity of fabricating molds based on lines, instead of the squares or dots. Also, this geometry of lines seems to be more versatile since there are no gaps between the written spots, thus there are not geometrical limitations imposed. On the other hand, since the propagation of the ferroelectric signal depends on the poling time [38], it is possible to expect that short times could decrease our spot size almost in a factor 10 [38, 43]. Considering this possibility, one might expect an information density of about 0.5 Terabit/in^2 (0.01 bit/nm^2) by using a line based nanostructured P(VDF-TrFE) film as the one proposed here. This information density compares well with that recently reported[44, 45] for organic-based magnetic

structures incorporating metallic nanoparticles which reached an information density of above 1 Terabit/inch^2.

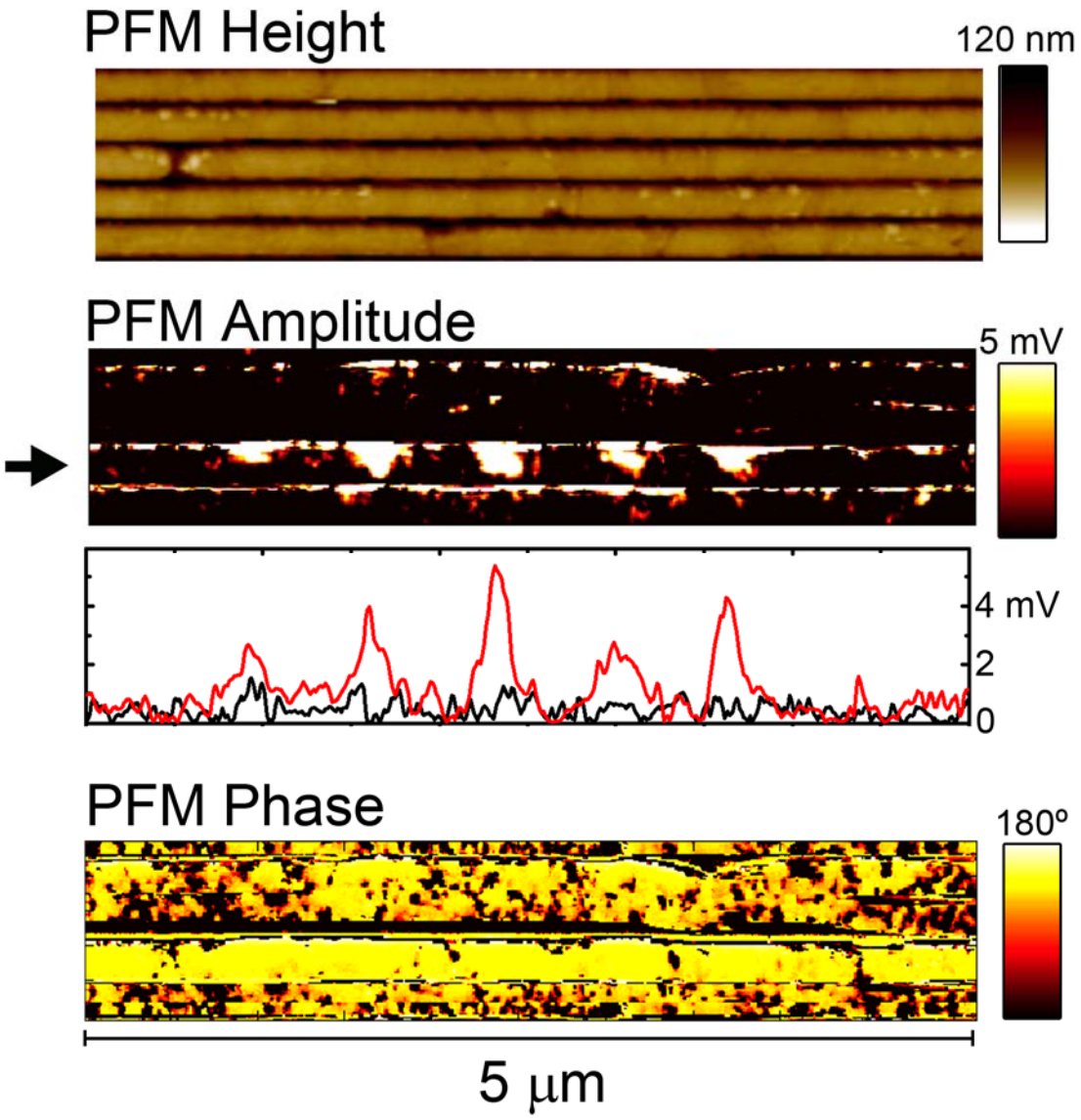

Figure 7.13 PFM height, amplitude and phase of a poled P(VDF-TrFE) nanograting.

7.4. Summary

By combining calorimetry, dielectric and X-ray experiments we have proven that nanoparticles of P(VDF-TrFE) copolymers with VDF:TrFE ratios of 76:24 and 56:44, obtained by the dialysis nanoprecipitation method, are semi-cristalline in nature exhibiting at room temperature the ferroelectric crystalline phase characteristic of the

bulk copolymers. The P(VDF-TrFE) nanoparticles present a ferroelectric-to-paraelectric transition at lower temperature as compared with the bulk. This has been attributed to a lower crystallinity of the nanoparticles in comparison to that of the bulk. In the paraelectric phase the nanoparticles show an intense dielectric relaxation process associated to the rotational motion of the dipoles within the paraelectric crystalline phase. The nature of this dielectric process is similar to that of the bulk. Nanoscale measurements were also performed on 76:24 molar concentration nanoparticles. PFM results showed that particles exhibited hysteresis cycles with **Ec** values similar to the bulk. Nanoimprint Lithography gratings were also tested via PFM. In this case, hysteresis cycles showed a decrease in the **Ec** values in comparison to the bulk. Also, the PFM technique was used to write and read information at nanometric scales. It was shown that the NIL process allowed attaining higher resolution in comparison to the thin film.

7.5. References

1. Horiuchi, S.; Tokura, Y. *Nat Mater* **2008,** 7, (5), 357-366.
2. Ahn, C. H.; Rabe, K. M.; Triscone, J.-M. *Science* **2004,** 303, (5657), 488-491.
3. Garrity, K.; Kolpak, A. M.; Ismail-Beigi, S.; Altman, E. I. *Advanced Materials* **2010,** 22, (26-27), 2969-2973.
4. Youn Jung, P.; In-sung, B.; Seok Ju, K.; Jiyoun, C.; Cheolmin, P. *Dielectrics and Electrical Insulation, IEEE Transactions on* **2010,** 17, (4), 1135-1163.
5. Bowen, C. R.; Kim, H. A.; Weaver, P. M.; Dunn, S. *Energy & Environmental Science* **2014,** 7, (1), 25-44.
6. Chen, X.; Xu, S.; Yao, N.; Shi, Y. *Nano Letters* **2010,** 10, (6), 2133-2137.
7. Xu, S.; Qin, Y.; Xu, C.; Wei, Y.; Yang, R.; Wang, Z. L. *Nat Nano* **2010,** 5, (5), 366-373.
8. Davis, G. T.; Furukawa, T.; Lovinger, A. J.; Broadhurst, M. G. *Macromolecules* **1982,** 15, (2), 329-333.
9. Lovinger, A. J. *Science* **1983,** 220, (4602), 1115-1121.
10. Hu, Z.; Tian, M.; Nysten, B.; Jonas, A. M. *Nat Mater* **2009,** 8, (1), 62-67.
11. Hong, C.-C.; Huang, S.-Y.; Shieh, J.; Chen, S.-H. *Macromolecules* **2012,** 45, (3), 1580-1586.
12. Hahm, S.-W.; Kim, D.; Khang, D.-Y. *Polymer* **2014,** 55, (1), 175-181.
13. Tien, N. T.; Seol, Y. G.; Dao, L. H. A.; Noh, H. Y.; Lee, N.-E. *Advanced Materials* **2009,** 21, (8), 910-915.
14. Zirkl, M.; Sawatdee, A.; Helbig, U.; Krause, M.; Scheipl, G.; Kraker, E.; Ersman, P. A.; Nilsson, D.; Platt, D.; Bodö, P.; Bauer, S.; Domann, G.; Stadlober, B. *Advanced Materials* **2011,** 23, (18), 2069-2074.
15. Yuan, Y.; Reece, T. J.; Sharma, P.; Poddar, S.; Ducharme, S.; Gruverman, A.; Yang, Y.; Huang, J. *Nat Mater* **2011,** 10, (4), 296-302.
16. Kassa, H. G.; Cai, R.; Marrani, A.; Nysten, B.; Hu, Z.; Jonas, A. M. *Macromolecules* **2013,** 46, (21), 8569-8579.
17. Yang, L.; Li, X.; Allahyarov, E.; Taylor, P. L.; Zhang, Q. M.; Zhu, L. *Polymer* **2013,** 54, (7), 1709-1728.
18. Zhu, L.; Wang, Q. *Macromolecules* **2012,** 45, (7), 2937-2954.
19. Yagi, T.; Tatemoto, M.; Sako, J. *Polymer Journal* **1980,** 12, (4), 209-223.
20. Calleja, F. J. B.; Arche, A. G.; Ezquerra, T. A.; Cruz, C. S.; Batallan, F.; Frick, B.; Cabarcos, E. L. *Advances in Polymer Science* **1993,** 108, 1-48.
21. Martín, J.; Nogales, A.; Martín-González, M. *Macromolecules* **2013,** 46, (4), 1477-1483.
22. Martín, J.; Nogales, A.; Mijangos, C. *Macromolecules* **2013,** 46, (18), 7415-7422.
23. Baltá_Calleja, F. J.; Arche, A. G.; Ezquerra, T. A.; Cruz, C. S.; Batallan, F.; Frick, B.; López-Cabarcos, E. *Advances in Polymer Science* **1993,** 108, 1-48.

24. López-Cabarcos, E.; Batallán, F.; Frick, B.; Ezquerra, T. A.; Baltá_Calleja, F. J. *Physical Review B* **1994,** 50, (18), 13214-13224.
25. López Cabarcos, E.; Batallán, F.; Frick, B.; Ezquerra, T. A.; Baltá Calleja, F. J. *Physical Review B* **1994,** 50, (18), 13214-13224.
26. Cabarcos, E. L.; Arche, A. G.; Calleja, F. J. B.; Bösecke, P.; Röber, S.; Bark, M.; Zachmann, H. G. *Polymer* **1991,** 32, (17), 3097-3102.
27. Bourgaux-Leonard, C.; Legrand, J. F.; Renault, A.; Delzenne, P. *Polymer* **1991,** 32, (4), 597-604.
28. Martinez-Tong, D. E.; Soccio, M.; Garcia-Gutierrez, M. C.; Nogales, A.; Rueda, D. R.; Alayo, N.; Perez-Murano, F.; Ezquerra, T. A. *Applied Physics Letters* **2013,** 102, (19), 191601-5.
29. Ngoma, J. B.; Cavaille, J. Y.; Paletto, J.; Perez, J. *Polymer* **1991,** 32, (6), 1044-1048.
30. Ezquerra, T. A.; Kremer, F.; Baltá-Calleja, F. J.; Lopez Cabarcos, E. *Journal of Polymer Science Part B: Polymer Physics* **1994,** 32, (8), 1449-1455.
31. Gregorio, R., Jr.; Ueno, E. M. *Journal of Materials Science* **1999,** 34, (18), 4489-4500.
32. Kremer, F.; Schönhals, A., *Broadband Dielectric Spectroscopy*. Springer: 2003.
33. Angell, C. A. *Polymer* **1997,** 38, (26), 6261-6266.
34. Angell, C. A. *Science* **1995,** 267, (5206), 1924-1935.
35. Kang, S. J.; Bae, I.; Shin, Y. J.; Park, Y. J.; Huh, J.; Park, S.-M.; Kim, H.-C.; Park, C. *Nano Letters* **2011,** 11, (1), 138-144.
36. Jung, H. J.; Chang, J.; Park, Y. J.; Kang, S. J.; Lotz, B.; Huh, J.; Park, C. *Macromolecules* **2009,** 42, 4148-4154.
37. Park, Y. J.; Kang, S. J.; Park, C.; Lotz, B.; Thierry, A.; Kim, K. J.; Huh, J. *Macromolecules* **2008,** 41, (1), 109-119.
38. Lee, J. S.; Prabu, A. A.; Kim, K. J. *Polymer* **2010,** 51, 6319-6333.
39. Kang, S. J.; Bae, I.; Shin, Y. J.; Park, Y. J.; Huh, J.; Park, S.-M.; Kim, H.-C.; Park, C. *Nano letters* **2011,** 11, 138-44.
40. Bonnell, D. A.; Kalinin, S. V.; Kholkin, A. L.; Gruverman, A. *MRS Bulletin* **2011,** 34, 648-657.
41. Hu, Z.; Tian, M.; Nysten, B.; Jonas, A. M. *Nature materials* **2009,** 8, 62-7.
42. Sharma, P.; Reece, T. J.; Ducharme, S.; Gruverman, A. *Nano Letters* **2011,** 11, (5), 1970-1975.
43. Rankin, C.; Chou, C.-H.; Conklin, D.; Bonnell, D. A. *ACS Nano* **2007,** 1, (3), 234-238.
44. Park, S.; Lee, D. H.; Xu, J.; Kim, B.; Hong, S. W.; Jeong, U.; Xu, T.; Russell, T. P. *Science* **2009,** 323, (5917), 1030-1033.
45. Al-Badri, Z. M.; Maddikeri, R. R.; Zha, Y.; Thaker, H. D.; Dobriyal, P.; Shunmugam, R.; Russell, T. P.; Tew, G. N. *Nat Commun* **2011,** 2, 482.

Chapter 8 – General discussion and future outlook

Confinement of polymers in several geometries was studied in this thesis, as presented throughout the previous chapters. Not only the preparation of nanostructures was achieved but also physical properties were studied. First, we showed how different preparation methods of nanoparticles adapt to different polymer/solvent combinations. In general, all protocols allowed preparing nanoparticles with mean diameters below 500 nm, where confinement effects have been shown to occur[1]. Nanostructures of amorphous polymers, such as PBAC, PS and PEMA, generally used for the fundamental studies of confinement[1-3], were prepared. Also, nanostructures of materials with current interest in technologies, such as P(VDF-TrFE)[4], P3HT[5], PCBM[6] and PLA[7], were also developed. Besides the physico-chemical methods of nanoparticles preparations, we have also explored the possibility of nanoparticle formation by laser ablation. It has been shown the possibility of preparing nanostructures, starting from a PBAC polymer target, in several liquid mediums. Different nanostructures were found depending on the nature of the liquid. In a first approach, nanostructure geometry seems to be dependent on the thermal conductivity of the different mediums. Nowadays, we are still working on the chemical characterization of the resulting nanostructures (possible chemical modifications and molecular weight). 1D confined structures, in the thin film geometry, were also prepared for PLA-based polymers and P(VDF-TrFE). Moreover, for this last polymer, thin films were further modified by NIL, and nanogratings were obtained.

Different physical properties of the confined polymer nanostructures were evaluated. First, we have shown the changes in the glass transition of amorphous

polymers, when confined to nanospheres. We have observed an increase in the glass transition temperature in all confined samples (PEMA, PS and PBAC). Invoking an entropy-based model, we have proposed that this increase was related to the number of repeating units in the nanospheres that, below a certain threshold, can arrange more *effectively*, thus allowing a decrease in the entropy of the system. This decrease in entropy (better arrangement of the polymer in the nanospheres) is translated in an increase of the T_g. Our model correlates well not only with our measurements but also with several works in the literature. Also, it was found that the increase in the glass transition temperature was dependent on the bulk T_g of the polymers. Figure 8.1 shows the ΔT_g variation for all the polymers confined to nanospheres here presented, where a T_g was observed by DSC.

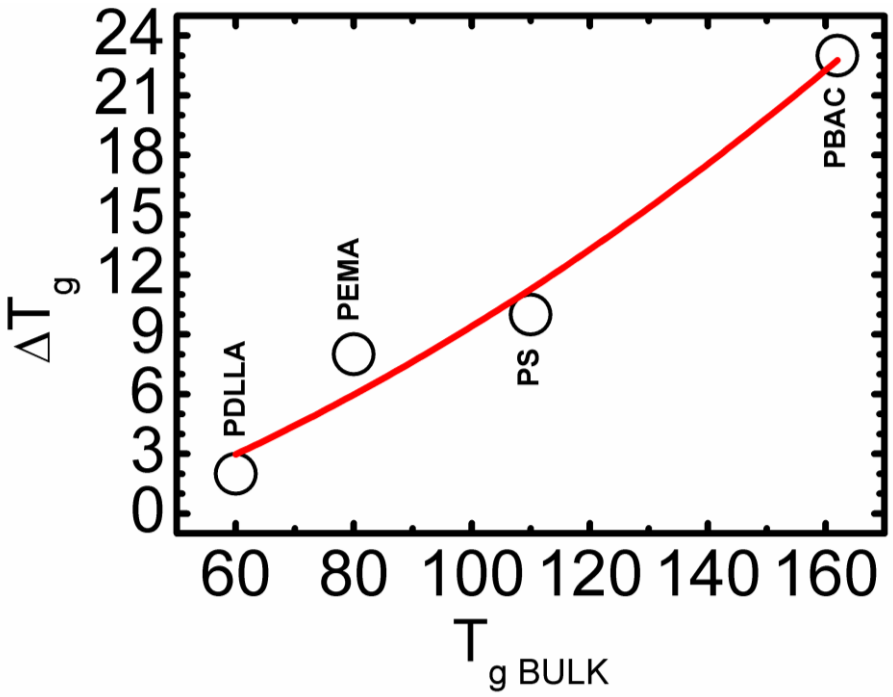

Figure 8.1. Variation in T_g (ΔT_g) as a function of Tg of the bulk polymers (T_{gBULK}). Red line is a guide for the eye.

Figure 8.1 resembles the trend already observed in chapter 5 (figure 5.5). However, now the glass transition temperature of the PDLLA nanoparticles, prepared by the reprecipitation method, (chapter 6) is included in order to provide a broader outlook. As previously, glass transition variations in the confined polymers are dependent on the bulk value, and always positive ($\Delta T_g > 0$). This result follows the entropy-based model of Mi et al[8], where it is stated that the confined glass transition must be always higher or equal to the bulk T_g. Also, one might question whether ΔT_g could reach negative values as the bulk polymer T_g is decreased. Based on equation (5.1) we argue that the trend shown in figure 8.1 will show an asymptotic decrease as T_{gBULK} is further decreased. Thus, ΔT_g values will always remain above zero regardless of the bulk glass transition value. Future work in this area will pursue further understanding of the trend in ΔT_g, by trying to generalize the results using both amorphous and semi-crystalline polymers, and also by analyzing the dependence in other preparation methods.

Crystalline behavior was studied in chapter 6. In this case, focus was set on the PLA-based polymers PLLA and PDLLA. Crystallization in thin films geometries of PLLA was followed by BDS and AFM. The BDS results showed how the reduction of thickness (increase of confinement) affected the crystallization of the polymer. Moreover, it was also presented how it is possible to disentangle the effects from confinement as well as those from adsorption in the polymer/substrate interface. AFM images presented the change in morphology suffered by the polymer as thickness was reduced. We have observed that ultra-thin films of PLLA present interesting loop-shaped and dendritic crystals at these small thicknesses. Previous works in the literature have also reported this result[9, 10]. Following work in this area will be focused in understanding the possible

relation between the changes in the crystallization morphology in relation with the adsorption of the polymer in the substrate and also the preparation of PDLLA thin films in order to further understand the changes imposed by the chirality of the polymer. Regarding the crystallization of nanoparticles of PDLLA, we have found that there are differences in the structural state of the prepared nanoparticles that depend on the preparation method. The as prepared nanoparticles are amorphous, since no diffraction peaks were observed in WAXS patterns. Nanoparticles prepared by the miniemulsion method showed a crystallization behavior similar to that of the bulk. However, the nanoparticles prepared by the reprecipitation method showed the development of a mesophase, evidenced by the increase of intensity at low values of 2θ in the WAXS patterns. One could argue that this mesophase can related to some parts of the polymer chain being *more ordered* than the *regular* amorphous phase, without the arrangement found in the crystalline phase. This assumption relates with the entropy argument proposed for the increase of the glass transition in nanospheres. If the number of possible conformations in the nanospheres is decreased, this might lead to few possible conformations of the polymer chain and thus a better arrangement in comparison with the amorphous bulk phase, *i. e.* development of the mesophase. The fact that the mesophase was only observed in the PDLLA nanoparticles prepared by the reprecipitation method opens a new factor to be taken into consideration when analyzing confinement of polymers: preparation method. However, this result does not imply that the PDLLA nanoparticles prepared by the miniemulsion method are not affected by confinement. Future work will focus interest in the understanding the development of the mesophases in PLA confined polymers and to reach more information on how the preparation method of nanostructures affects the resulting structure.

Ferroelectric response of P(VDF-TrFE), confined in different geometries, was presented in chapter 7. First, it was observed that preparation of nanoparticles, at two different molar concentrations, is possible via the dialysis precipitation method. Also, DSC, WAXS and BDS results show that the as prepared particles were semi-crystalline and ferroelectric. The semi-crystalline nature of the nanoparticles do not allowed observing a T_g in DSC runs, since chains in the crystals do not have enough mobility, while the amorphous phase is also restricted (confined) by the crystals. The absence of a calorimetry T_g in semicrystalline polymers has been well understood. However, this is the reason why these nanoparticles have not been included in the discussion of the glass transition temperature variations. On the other hand, for both molar concentrations, P(VDF-TrFE) nanoparticles showed a similar structural behavior in comparison to their bulk polymers. Extrapolating from our results in chapter 5, bulk-like response is the expected behavior of polymer nanoparticles when sizes are well above 100 nm, as in this case. This result is interesting towards possible applications of the nanostructured polymer in technological aspects, since the ferroelectric nature of the polymer is not highly affected by the geometry. Small deviations from the bulk were found, especially in the 76:44 molar concentration sample, but can be understood in terms of the crystallinity of the system instead of as finite size effects. It is also important to highlight that P(VDF-TrFE) nanoparticles show a hysteresis cycle similar to that of a continuous, bulk-like, thin film, by PFM measurements. This opens the possibility of writing and reading ferroelectric information in each particle, work that remains open to be developed in the near future. In the case of ferroelectric nanogratings prepared by NIL, in this thesis the focus was set into the possible applications of these structures. By PFM, we have observed that the nanogratings had a ferroelectric nature, which differed to that of the bulk-like continuous film. In the NIL structures, the hysteresis cycles were narrower,

indicating that a smaller voltage was necessary in order to flip the direction of the permanent electrical dipoles. This reduction in E_c has been recently reported in the literature[11] and it is proposed as an advantage of nanostructured films, in comparison to continuous films, since it could improve the energy performance of all-organic devices. Future work will focus on the study of ferroelectricity in nanoimprinted P(VDF-TrFE) films, with different geometries. Also, it has been recently proposed in the literature the possibility of preparing functional polymer blends of P(VDF-TrFE)/P3HT[4] and P(VDF-TrFE)/PCBM[6], towards development of improved ferroelectric memory devices. These works have open the possibility of finding a consensus between our P(VDF-TrFE) nanostructures and P3HT and PCBM nanoparticles, towards the development of polymer devices with feasible applications in technological aspects.

References

1. Zhang, C.; Guo, Y.; Priestley, R. D. *Macromolecules* **2011,** 44, (10), 4001-4006.
2. Yin, H.; Napolitano, S.; Schönhals, A. *Macromolecules* **2012,** 45, (3), 1652-1662.
3. Priestley, R. D.; Mundra, M. K.; Barnett, N. J.; Broadbelt, L. J.; Torkelson, J. M. *Australian Journal of Chemistry* **2007,** 60, (10), 765-771.
4. Nougaret, L.; Kassa, H. G.; Cai, R.; Patois, T.; Nysten, B.; van Breemen, A. J. J. M.; Gelinck, G. H.; de Leeuw, D. M.; Marrani, A.; Hu, Z.; Jonas, A. M. *ACS Nano* **2014,** 8, (4), 3498-3505.
5. Pecher, J.; Mecking, S. *Chemical Reviews* **2010,** 110, (10), 6260-6279.
6. Khan, M. A.; Bhansali, U. S.; Cha, D.; Alshareef, H. N. *Advanced Functional Materials* **2013,** 23, (17), 2145-2152.
7. Jiang, Q.; Ward, M. D. *Chemical Society Reviews* **2014,** 43, (7), 2066-2079.
8. Mi, Y.; Xue, G.; Wang, X. *Polymer* **2002,** 43, (25), 6701-6705.
9. Maillard, D.; Prud'homme, R. E. *Macromolecules* **2008,** 41, (5), 1705-1712.
10. Wang, X.; Prud'homme, R. E. *Macromolecules* **2014,** 47, (2), 668-676.
11. Kassa, H. G.; Cai, R.; Marrani, A.; Nysten, B.; Hu, Z.; Jonas, A. M. *Macromolecules* **2013,** 46, (21), 8569-8579.

Conclusions

All the results presented in this thesis allow us concluding:

- It is possible to prepare polymer nanoparticles (diameter < 100 nm) of several amorphous and semi-crystalline polymers, by different methods depending on the polymer nature. Sub-micrometric particles (diameters < 1000 nm) can also be prepared by tuning these methods.

- Pulsed laser ablation of polymers in liquids (PLAL) represents as an alternative to the physico-chemical methods of nanoparticles preparation. Nanostructures, with diameters well below 100 nm were formed with geometries dependent on the surrounding liquid.

- The glass transition temperature of amorphous polymer nanoparticles increases with respect to that of the bulk, as evidenced by DSC. A decrease in the entropy of the nanoparticles is responsible for this change. It has been found that amorphous nanoparticles, that are able to crystallize when annealed, suffer also the effects of confinement.

- Finite size effects affect the crystallization behavior of polymers. Nonetheless, in the case of polymer thin films, care must be taken regarding the influence of both confinement and adsorption of the supporting substrate. These different contributions were evaluated and disentangled by BDS. Also, it is possible to analyze the morphological changes of semi-crystalline polymer thin films by AFM. In the specific case of PLLA, it was found that for thicknesses below 20

nm, a dramatic change in the morphology took place. Finally, it was found that nanocrystals can be prepared starting from amorphous polymer nanospheres of PDLLA.

- Ferroelectric behavior of the P(VDF-TrFE) copolymer, in confined geometries, is preserved. In the case of polymer nanoparticles the ferroelectric response is fairly similar to that of a bulk-like material. In the case of nanogratings, ferroelectricity is affected, as observed by the decrease in the value of the coercive field. This decrease was explained in terms of the changes in the crystalline morphology when the copolymer was crystallized in a confined environment. Also, PFM results showed that the preparation of nanogratings can be of important use towards the miniaturization of all-organic technological devices, such as ferroelectric memories.

The present doctoral thesis gathered several studies regarding the fundamental physical properties of polymer under confinement, as well as possible applications of these systems. The promising results reported herein represent major contributions from the point of view of discussing all the aspects that involve the nanostructuring of polymer systems. As in any other work, there are still possible points to be addressed in the near future that have been already presented in the final summary. We hope to continue expanding these subjects and to contribute as much as possible to the better understanding of the polymer science.

Resumen

El siguiente documento es un amplio Resumen de la Tesis Doctoral titulada **"CONFINAMIENTO EN NANOESTRUCTURAS POLIMÉRICAS: PREPARACIÓN, PROPIEDADES, APLICACIONES E IMPLICACIONES FÍSICAS",** cumpliendo con el art 4.3 de la normativa de desarrollo del régimen relativo a elaboración, tribunal, defensa y evaluación de la tesis doctoral, del Real Decreto 1393/2007 de la Universidad Complutense de Madrid.

Esta Tesis Doctoral ha sido dividida en 8 capítulos. Como introducción al tema, el Capítulo 1 abarca una revisión bibliográfica sobre los polímeros, la física que gobierna a estos sistemas y la problemática del comportamiento físico de estos materiales cuando están confinados. En el capítulo 2, se presentan todos los materiales y técnicas experimentales usadas durante el desarrollo de este trabajo para alcanzar los objetivos planteados.

El confinamiento de polímeros se puede producir mediante la alteración controlada de la geometría de estos materiales. Es posible partir de un material volumétrico o macroscópico, y generar estructuras con tamaños característicos en el orden de los nanómetros, gracias a diversas técnicas físicas y/o químicas. Conocemos a este proceso como *nanoestructuración*. En el capítulo 3 de este trabajo se presenta una batería de técnicas para la nanoestructuración de polímeros en 1, 2 y 3 dimensiones. Además, se muestran los pros y contras de cada una de las técnicas y la familia de polímeros donde es más factible su aplicación. Más aún, el procesamiento de materiales para la preparación de nanoestructuras se profundiza en el capítulo 4, mediante la aplicación de técnicas láser. A continuación, los capítulos 5, 6 y 7 se dedican a explorar cómo pueden verse afectadas las propiedades de los polímeros cuando se encuentran

confinados en nanoestructuras. Primero, en el capítulo 5 se estudian las variaciones de la temperatura de transición vítrea en polímeros confinados en 3 dimensiones. Luego, en el capítulo 6 se estudia cómo se ve afectado el proceso de cristalización en polímeros confinados en películas delgadas, así como en nanopartículas. Finalmente, en el capítulo 7, se estudia la ferroelectricidad en polímeros. En este capítulo, además de presentar las posibles variaciones en el comportamiento ferroeléctrico en nanoestructuras, se propone el uso de nanoestructuras como posibles dispositivos de memorias ferroeléctricas. Todos los resultados obtenidos en la tesis se resumen en el capítulo 8, donde además se enumeran conclusiones generales y se detallan perspectivas futuras.

A lo largo del período de ejecución de esta Tesis Doctoral, y debido al rápido progreso en este campo de investigación, en relación con los conceptos aquí presentados, fue necesario presentar parte de este trabajo para su publicación en revistas científicas internacionales. Las publicaciones son las siguientes:

- Daniel E. Martínez-Tong, M. Soccio, M. C. García-Gutiérrez, A. Nogales, D. R. Rueda, N. Alayo, F. Pérez-Murano, T. A. Ezquerra. ***Improving information density in ferroelectric polymer films by using nanoimprinted gratings***. Applied Physics Letters. Vol 102 (19). 109161. **2013.**

- Daniel E. Martínez-Tong, M. Soccio, A. Sanz, C. García, T. A. Ezquerra, A. Nogales. ***Chain Arrangement and Glass Transition Temperature Variations in Polymer Nanoparticles under 3D-Confinement***. Macromolecules. Vol 47 (2). 4698-4705. **2013.**

- Daniel E. Martínez-Tong, B. Vanroy, M. Wübbenhorst, A. Nogales, S. Napolitano***. Crystallization of poly (L-lactide) confined in ultrathin films: competition between finite size effects and irreversible chain adsorption***. Macromolecules. Vol 47 (11). 2354-2360. **2014.**

1. Introducción

La materia condensada blanda es un término que se usa convenientemente para clasificar materiales que se encuentran en un estado físico diferente a los de un líquido *simple*, pero que tampoco se corresponde a un sólido, tales como se definen en la física del estado sólido. De acuerdo a Gomper y Schick, sistemas tal y como las dispersiones coloidales y los polímeros se pueden clasificar como *materia condensada blanda*[1]. Específicamente, los polímeros, también conocidos como macromoléculas, están constituidos por un gran número de unidades moleculares, vinculadas entre sí a través de enlaces covalentes[2]. De acuerdo con la definición de la IUPAC: Un polímero es una sustancia compuesta de moléculas, caracterizadas por la repetición múltiple de una o varias especies de átomos o grupos de átomos, a los que se le pueden llamar unidades repetitivas constitucionales. Estas unidades repetitivas están enlazadas unas a otras de tal forma que agregar o quitar algunas pocas no causa variaciones en las propiedades físicas generales del polímero[3]. Un polímero puede estar constituido por unidades repetitivas idénticas. Si denominamos por la letra **A** a cada una de estas unidades, la macromolécula formada por la repetición …-A-A-A-A-A-… se conoce como *homopolímero*. En el caso que exista más de una unidad de repetición (**A**, **B**,…) el sistema formado por enlaces covalentes entre estas unidades se conoce como *copolímero*. Es posible encontrar diversas clases de copolímeros, tales como copolímeros en bloque (…-A-A-A-B-B-B-A-A-A-…) o copolímeros aleatorios donde las unidades repetitivas no siguen algún patrón específico. En este último caso, la probabilidad de encontrar a una unidad particular en una posición determinada es independiente de la naturaleza de las unidades que estén a su alrededor[3].

Es útil dividir a los polímeros en dos amplias clases: los completamente amorfos y los semicristalinos. Los polímeros completamente amorfos no muestran picos, característicos de las reflexiones de redes cristalinas, cuando son estudiados mediante

difracción de rayos-X. Estos polímeros no son capaces de cristalizar debido a su estructura molecular. Los polímeros semicristalinos muestran picos en lo difractogramas de rayos-X, provenientes de la ordenación cristalina de segmentos de la cadena molecular. Sin embargo, estos picos suelen estar superpuestos a un fondo amorfo, también conocido como *halo amorfo.* Por tanto, los polímeros semicristalinos consisten de dos componentes, que difieren en su grado de orden: una componente es cristalina y está compuesta por cristales finos, alrededor de 10 nm, con forma de laminilla, mientras que la segunda componente consiste de regiones de polímero amorfas, es decir, sin orden alguno[3]. La estructura final de un polímero, es decir, si está compuesto por cristales + fase amorfa o únicamente por moléculas desordenadas en la fase amorfa, depende tanto de su composición molecular, es decir de cuáles y cuántas son las entidades químicas que componen la unidad de repetición, como de su historia térmica. Si consideramos un polímero a una temperatura en la cual todas sus cadenas moleculares poseen la mayor movilidad posible, al enfriarlo las cadenas podrán reorganizarse en una estructura semicristalina, generando una estructura amorfa. En el primer caso, la temperatura donde ocurre la organización de los cristales se conoce como temperatura de cristalización. A medida que las cadenas poliméricas se organizan en cristales, sus movimientos moleculares se ven restringidos, dando paso a un cambio en el estado físico del material. La temperatura de cristalización depende de lo rápido o lento que se enfríe el material, es decir, de la cinética del proceso. En el segundo escenario, al no organizarse el polímero al ser enfriado, su estructura molecular es similar a la del estado fundido o líquido a alta temperatura; sin embargo, al bajar la temperatura puede llegar un momento en el que las cadenas pierden movilidad. Este punto está caracterizado por aumentos dramáticos en el módulo elástico del material, viscosidad, y otras propiedades mecánicas. A esta

temperatura se le conoce como temperatura de transición vítrea (T_g). La temperatura de transición vítrea no es única, sino depende de la cinética del proceso.

La transición vítrea es uno de los fenómenos más estudiados en la física de polímeros. Debido a su carácter termodinámico y cinético, es sumamente complicado presentar un modelo o teoría capaz de describir este proceso. Sin embargo, a lo largo de muchos años, diferentes teorías han surgido para intentar explicar este fenómeno. Desde el punto de vista más conservador, las teorías de la transición vítrea se suelen clasificar en las siguientes ramas: *volumen libre, cinéticas, y termodinámicas*. Los primeros intentos para realizar una teoría de la transición vítrea se enfocaron en la pregunta de cómo es posible para un material ordinario, que obedece las leyes de la mecánica estadística, llegar a un estado vítreo sin conseguir alcanzar su estado de equilibrio. Una descripción simple a este fenómeno fue dada por Adam y Gibbs[4]. Estos autores, propusieron que el proceso de transición vítrea se podía entender introduciendo un factor denominado *entropía configuracional*. Este parámetro cuantifica el *"exceso"* de entropía que tiene un sistema amorfo en relación a su *contraparte virtual cristalina*, es decir, asumiendo idealmente que el material es capaz de cristalizar. Además proponen que este parámetro es inversamente proporcional al tamaño de *regiones de rearreglos cooperativos*, dentro de las cuales hay suficientes grados de libertad tal que se permite la movilidad del material y por tanto las moléculas se pueden reconformar.

Como se mencionó en los párrafos anteriores, en las temperaturas cercanas a la transición vítrea, los materiales formadores de vidrios sufren cambios pronunciados en sus propiedades mecánicas. Por ejemplo, en el caso de la sílice, el cambio en la viscosidad con la temperatura se puede describir a través de un proceso del tipo Arrhenius:

$$\eta = A\exp\left(\frac{E}{k_B T}\right)$$

donde *A* y *E* son parámetros independientes de la temperatura, *T* es la temperatura del sistema y k_B la constante de Boltzmann. Otros materiales sufren decrecimientos en la viscosidad más pronunciados a temperaturas cercanas a la transición vítrea. En estos casos es posible describir la dependencia de la viscosidad con la temperatura a través de la ecuación Vogel-Fulcher-Tamann (VTF):

$$\eta = A\exp\left(\frac{B}{T - T_0}\right)$$

donde *A* y *B* son factores independientes de la temperatura, *T* es la temperatura y *T0* es un parámetro conocido como *temperatura de Kauzmann.* Siguiendo la teoría propuesta por Adam y Gibbs, la ecuación anterior se puede escribir como:

$$\tau_\alpha = \tau_0\exp\left(\frac{T\ D}{T - T_0}\right)$$

donde τ_α es un tiempo de relajación, *T* la temperatura y *D* es un parámetro ligado al concepto de fragilidad. La *fragilidad* es una manera de clasificar sistemas formadores de vidrios, donde un sistema *frágil* se desvía fuertemente de la ley de Arrhenius, mientras que uno *fuerte* sigue la ley de Arrhenius. El aumento en la viscosidad de los polímeros en la vecindad de la T_g, lo que es igual a un decrecimiento en su movilidad, se suele definir como relajación segmental o relajación α. El adjetivo *segmental* está relacionado al hecho de que en estas regiones de temperatura, el proceso de relajación no ocurre en átomos y/o moléculas aisladas, sino en segmentos de la cadena molecular del polímero.

Previamente se ha postulado que los polímeros, además de formar vidrios al ser enfriados por debajo de la T_g, también pueden formar sistemas semicristalinos. La morfología de los polímeros semicristalinos suele estar constituida por capas de cristales en forma de laminillas, separados por zonas amorfas. Sin embargo, la morfología cristalina de los polímeros depende de la escala en la que se estudie. En el rango de los

milímetros hasta los micrómetros, los polímeros observados mediante microscopía óptica suelen mostrar objetos esféricos llamados *esferulitas*. Estas esferulitas inician con un *núcleo* cristalino que crece hasta chocar con otra esferulita. Este proceso de cristalización se le conoce como nucleación y crecimiento de esferulitas. Asimismo, en escalas entre las unidades de micras y los cientos de nanómetros, la estructura de los polímeros se puede estudiar a través de microscopía por transmisión de electrones o empleando microscopía de fuerza atómica. Por otro lado, la estructura cristalina a nivel molecular se suele estudiar a través de difracción de rayos-X a ángulo alto.

Durante el desarrollo de esta tesis, nos concentraremos en el estudio de polímeros confinados, es decir, estructurados en geometrías con dimensiones características del orden de los 100 nm. Las posibles variaciones en las propiedades y comportamiento físico de los polímeros estructurados al nivel nanométrico, se conocen como efectos de confinamiento. Nuestro estudio está relacionado con el desarrollo rápido que ha tenido la nanociencia y nanotecnología en los últimos años, donde han surgido nuevas preguntas respecto al comportamiento de los materiales poliméricos en estas escalas y donde se han abierto puertas al desarrollo de nuevos sistemas tecnológicos. En el desarrollo de este trabajo nos hemos concentrado, básicamente, en dos geometrías de materiales confinados: películas delgadas y nanopartículas poliméricas.

Las películas delgadas poliméricas consisten en materiales cuasi bidimensionales. En estos sistemas, dos de las dimensiones del material, largo y ancho, tienen longitudes macroscópicas, del orden de los milímetros o decenas de milímetros, mientras que su espesor, o altura, está en la escala nanométrica. Las películas delgadas han despertado la atención de científicos debido a dos grandes aspectos: el tecnológico y el fundamental. En primer lugar, desde un punto de vista tecnológico, las películas delgadas poliméricas son empleadas como recubrimientos en electrónica y biodispositivos. Por otro lado, desde el

punto de vista del estudio fundamental de la física de polímeros, se ha observado que las propiedades de estas películas pueden variar fuertemente con el confinamiento. Estos estudios tuvieron su despertar con los trabajos de Keddie et al[5], a mediado de los años 1990. En estos trabajos, se demostró, a través de medidas de elipsometría, que al disminuir el espesor de las películas delgadas, la temperatura de transición vítrea decrece. Se postuló que el decrecimiento en la T_g en polímeros confinados en películas delgadas estaba relacionado con la existencia de una *capa superficial libre*. Ésta se puede entender como la capa de polímero que está más cerca del aire, y por tanto cuyas moléculas tienen menos interacciones entre sí, lo que le garantiza mayor movilidad. Por otro lado, otros autores han propuesto que los cambios en T_g, sufridos por las películas delgadas, están influenciados por la naturaleza del sustrato. Por tanto, el crecimiento o decrecimiento de la temperatura de transición vítrea con el confinamiento se podría explicar a través de la magnitud de la interacción polímero/sustrato. Incluso, se ha reportado, a través de medidas de espectroscopía dieléctrica de banda ancha, que estos cambios podrían estar relacionados con la formación de una capa polimérica adsorbida irreversiblemente al sustrato, también conocida como capa residual.

En el caso de películas delgadas semicristalinas, el confinamiento es capaz de afectar tanto al crecimiento de los cristales, como a la morfología del polímero. Los cambios en la cristalización de materiales poliméricos toman lugar cuando las películas delgadas tienen espesores del orden, o menores, al tamaño medio de una esferulita. En estas dimensiones, los polímeros suelen formar motivos *aplanados* e incluso con formas *dendríticas.* Al igual que en los estudios de la T_g, la interacción polímero/sustrato puede afectar a la cristalización de polímeros confinados en películas delgadas. Se ha reportado que la formación de capas de polímero adsorbidas de manera irreversible al sustrato afecta la dinámica de cristalización del material.

Las nanopartículas poliméricas se pueden definir como sistemas coloidales, con diámetros mínimos de 5-10 nm con un límite superior de 100 nm, aunque generalmente el rango de diámetros suele estar entre los 100 nm a 500 nm. El término *nanopartículas poliméricas* es una definición colectiva, usada para describir partículas de tamaño nanométrico, donde se incluyen nanoesferas y nanocápsulas. Así como en las películas delgadas, el confinamiento de polímeros en nanopartículas altera las propiedades físicas de los materiales en comparación con su comportamiento macroscópico. Por ejemplo, se ha reportado en la literatura que la T_g de polímeros confinados en nanopartículas puede cambiar, bien sea disminuyendo su valor o aumentándolo. Estos resultados han sido evaluados, por lo general, usando calorimetría diferencial de barrido, aunque otras técnicas como espectroscopía dieléctrica de banda ancha y elipsometría, también han sido empleadas. En el caso del decrecimiento de la Tg de nanopartículas poliméricas, en comparación con los valores medidos en muestras macroscópicas, se ha asumido un modelo similar al de las películas delgadas poliméricas, es decir, la existencia de una superficie libre de mayor movilidad, ubicada en las capas más externas de las nanopartículas. Sin embargo, otros autores han demostrado que la transición vítrea de polímeros confinados en nanopartículas aumenta, en relación al valor macroscópico, argumentando cambios en la organización de las cadenas poliméricas.

2. Objetivos

El objetivo general de esta Tesis Doctoral es la preparación de sistemas poliméricos con diversas geometrías confinadas, y estudiar los cambios físicos consecuencia del confinamiento. Para alcanzar el objetivo general, este trabajo se enfocó en los siguientes objetivos específicos. Primero, preparar diversas nanoestructuras poliméricas, tales como nanopartículas, películas delgadas y superficies modificadas, usando diversos sistemas poliméricos, amorfos y semicristalinos. En segundo lugar, realizar medidas de

propiedades físicas de las nanoestructuras, para obtener información acerca de los posibles cambios generados por el confinamiento, mediante calorimetría diferencial de barrido, espectroscopía dieléctrica de banda ancha y microscopía de fuerza atómica y técnicas derivadas de ésta.

3. Conclusiones

De esta Tesis Doctoral se pueden extraer las siguientes conclusiones:

- Es posible preparar nanopartículas poliméricas, con diámetros < 100 nm, de diferentes polímeros amorfos y semicristalinos, usando diversos métodos de preparación que dependen de la naturaleza del polímero. También es posible preparar partículas con diámetros por debajo de la micra, aplicando variaciones sutiles a estos métodos.
- La ablación con láser pulsado en medios líquidos, PLAL por sus siglas en inglés, se presenta como una alternativa a los métodos físico-químicos de preparación de nanopartículas. A través de PLAL se consiguieron preparar nanoestructuras con diámetros muy por debajo de los 100 nm. Además se encontró que las geometrías de las nanoestructuras eran dependientes de la naturaleza del medio líquido.
- La temperatura de transición vítrea de nanopartículas de polímeros amorfos aumenta respecto al valor medido en muestras macroscópicas, según medidas de calorimetría diferencial de barrido. Se halló que es posible explicar este comportamiento argumentando un decrecimiento en la entropía de los sistemas confinados. También se observó que nanopartículas amorfas, capaces de cristalizar, sufren los efectos del confinamiento.

- La geometría de polímeros confinados en la nanoescala es capaz de afectar al comportamiento cristalino. En el caso específico de películas delgadas, no sólo la geometría nanométrica sino también la adsorción entre polímero y sustrato, altera la cristalización del material. Estas dos contribuciones pueden ser estudiadas, y sus comportamientos pueden ser separados, a través de espectroscopía dieléctrica de banda ancha. Asimismo, es posible estudiar los cambios morfológicos que sufren los cristales poliméricos, cuando son sometidos a confinamiento en películas delgadas, a través de microscopía de fuerza atómica.
- El comportamiento ferroeléctrico prevalece en geometrías confinadas. En el caso de nanopartículas ferroeléctricas, se demostró que la dinámica, estructura y ferroelectricidad es relativamente similar al comportamiento macroscópico. En el caso de nanorejillas, se encontró que el campo coercitivo decrece en relación al caso macroscópico. Este decrecimiento se explicó en base a cambios en la orientación cristalina del material.

4. Aportaciones Fundamentales

A continuación se presenta un breve resumen de los principales hallazgos obtenidos durante esta investigación. En las siguientes secciones se reflejan las aportaciones fundamentales detalladas en cada uno de los capítulos de Resultados y Discusión de la Tesis Doctoral. Por motivos de coherencia con el resto de la Tesis Doctoral, en las siguientes secciones todas las abreviaturas de los materiales, técnicas y métodos se mantienen con sus siglas en inglés.

4.1. Preparación de nanoestructuras poliméricas por métodos físico-químicos

En esta Tesis Doctoral se afrontó el problema de la preparación de nanoestructuras poliméricas. Se presentó la posibilidad de preparar nanopartículas poliméricas de tipo esférico a través de diversos métodos físico-químicos. Primero, con el método de la *miniemulsion*, se prepararon nanopartículas de polímeros amorfos como poli(etil metacrilato) (PEMA), poli(estireno) (PS) y poli(bisfenol A carbonato) (PBAC). En todo caso se consiguieron preparar nanopartículas con diámetro medio por debajo de los 100 nm, cuyas morfologías se estudiaron a través de microscopía de fuerza atómica (AFM). Asimismo, variaciones a este método permitieron la preparación de nanopartículas con diámetros sub-micrométricos. El método de la miniemulsion sirvió también para preparar nanopartículas de polímeros semicristalinos como poli(D,L-ácido láctico) (PDLLA), poli(3-hexiltiofeno) (P3HT), así como del compuesto de bajo peso molecular C_{71}-fenil-butil-metil-éster (PCMB), estos dos últimos de alta importancia hoy en día para el desarrollo de sistemas orgánicos fotosensibles y conductores.

Segundo, se estudiaron técnicas de *desplazamiento de solvente* para la preparación de nanopartículas poliméricas. En primer lugar, se mostró la posibilidad de preparar nanopartículas del copolímero ferroeléctrico poli(fluoruro de vinilideno-trifluoro etileno) P(VDF-TrFE), a través del método de *nanoprecipitación por diálisis*. Análisis de AFM mostraron que se consiguió preparar nanopartículas con tamaño medio alrededor de los 300 nm. La segunda de estas técnicas, llamada *reprecipitación*, permitió la preparación de nanopartículas de PEMA y PDLLA. Variaciones en la concentración polímero/solvente permitieron ajustar los tamaños medios y distribuciones en los diámetros de las nanopartículas. Asimismo, el método de reprecipitación fue modificado para conseguir preparar nanopartículas de P(VDF-TrFE).

También fue posible preparar nanoestructuras de polímeros confinados en 1 y 2 dimensiones. En estos casos, se usó la técnica de *spin coating* para la preparación de películas delgadas, donde el confinamiento está sobre una dimensión, empleando los polímeros PBAC, PDLLA y P(VDF-TrFE). En este último polímero, las películas delgadas fueron modificadas en su superficie a través de la técnica de litografía por nanoimpresión (NIL). Mediante este método se consiguió preparar nanorejillas de P(VDF-TrFE) a través de la alteración de la superficie de una película delgada, usando un sello de silicio.

4.2. Preparación de nanopartículas por ablación de láser pulsado en líquidos

El propósito de esta sección es estudiar la preparación de nanopartículas a través de la ablación por láser pulsado en líquidos. Inicialmente se describe el sistema experimental y la física que gobierna al proceso de ablación. A continuación se muestra la variación en el tamaño de nanopartículas, estudiado por AFM, en función de la fluencia del haz láser. Finalmente se muestran las variaciones geométricas que sufre el material ablacionado en función del medio líquido.

En este estudio, se empleó un blanco de PBAC que se irradió con un láser Nd:YAG. Los estudios en función de la fluencia del haz láser demostraron que cuanto menor es la fluencia del haz, menor es el tamaño de las nanopartículas formadas. Asimismo, para fluencias bajas, 200 $mJcm^{-2}$ y 100 $mJcm^{-2}$, se encontraron diferentes poblaciones de nanopartículas, formadas por nanoesferas, y nanohilos. Se propone que la formación de estas nanoestructuras depende de la interacción haz láser/ líquido.

Posteriormente, se estudió la influencia del medio líquido en la morfología final de las nanopartículas, a fluencia fija de 100 $mJcm^{-2}$. Se observó que la geometría de las nanoestructuras era dependiente de la naturaleza del líquido. Las diferentes variaciones

geométricas abarcaron nanoesferas, nanohilos y nanotoroides. Asimismo, para el caso particular de nanoesferas, se mostró que el diámetro de éstas depende de la conductividad térmica del líquido. Esto es indicativo de cómo la interacción haz-láser / líquido puede jugar un papel fundamental en la preparación de nanoestructuras.

4.3. Estudio de la temperatura de transición vítrea en nanoesferas poliméricas

La presente sección está enfocada en estudiar las posibles variaciones en la temperatura de transición vítrea (T_g) en nanoesferas de polímeros amorfos, preparadas por el método de la miniemulsion. Se empleó la calorimetría diferencial de barrido (DSC) para el estudio de este fenómeno. En esta sección se inicia detallando las curvas calorimétricas para cada material y su relación con la curva obtenida para el caso macroscópico. Luego, se muestra cómo las nanoesferas pierden su geometría confinada al calentarse por encima de T_g. Finalmente se propone un modelo, basado en variaciones entrópicas que permite explicar los resultados obtenidos en este trabajo y su relación con resultados disponibles en la literatura.

El principal resultado de esta sección es el aumento de la T_g en nanopartículas poliméricas de PEMA, PS y PBAC, en relación a su contraparte macroscópica. Asimismo, se encontró que nanopartículas con diámetros mayores mantienen el valor de la T_g macroscópica. Finalmente, se observó que la magnitud del aumento de la T_g es dependiente del valor macroscópico, siendo más pronunciado para el PBAC y menos pronunciado para el PEMA. Para discutir los resultados obtenidos, se invocó un modelo basado en entropía, donde el parámetro fundamental que controla el confinamiento es el número de unidades de repetición del polímero en la nanoesferas.

4.4. Estudio de la cristalización de polímeros en geometrías confinadas.

En esta sección se consiguió estudiar el fenómeno de la cristalización en geometrías confinadas. Se usaron las familias PLLA y PDLLA del poli(ácido láctico), confinados en películas delgadas y nanopartículas, respectivamente. En primer lugar, se estudia la cristalización en películas delgadas de PLLA, mediante espectroscopía dieléctrica de banda ancha (BDS), usando una geometría tipo sándwich. Luego, se presentan las variaciones en morfología en estas películas, estudiadas a través de AFM. Finalmente, se muestran estudios de cristalización en nanopartículas de PDLLA, los cuales se llevaron a cabo usando DSC, AFM y difracción de rayos-X a ángulo alto (WAXS).

Los principales resultados de esta sección se describen a continuación. Primero, los estudios de películas delgadas de PLLA, a través de BDS, permitieron determinar cómo los efectos de confinamiento afectan la cristalización del material. Se encontró que cuanto menor es el espesor de la película, mayor es el tiempo necesario para que el polímero cristalice. Asimismo, a través de los datos experimentales y la aplicación de modelos disponibles en la literatura, fue posible estudiar la influencia de la adsorción del polímero en el sustrato. Los estudios de la morfología cristalina de PLLA en películas delgadas, a través de AFM mostraron una transición entre morfología esferulítica a cristales tipo aplanados, para espesores por debajo de 35 nm. El cambio en morfología coincide con el punto donde el tiempo de cristalización sufre cambios en los resultados observados vía BDS. En el caso de nanopartículas de PDLLA, se observó que diferentes métodos de preparación permiten obtener nanopartículas de geometría esférica, amorfas según los resultados de WAXS. Al calentar las nanopartículas, se ve la aparición de picos de Bragg, indicando la aparición de cristales. En el caso de nanopartículas preparadas por el método de la miniemulsion, los resultados muestran que la cristalización sucede de forma similar al caso macroscópico. Sin embargo, las nanopartículas preparadas por el

método de la reprecipitación se desvían del comportamiento macroscópico, mostrando una mesofase a temperatura ambiente. La aparición de esta mesofase se explica a través de los distintos procesos físicos que engloban cada uno de los métodos de preparación.

4.5. Estudio de la ferroelectricidad de polímeros en geometrías confinadas

En esta última sección se aborda el problema de la ferroelectricidad en polímeros. Esta propiedad física es de gran importancia para el desarrollo de componentes electrónicos orgánicos, tales como memorias no-volátiles. Se usó el P(VDF-TrFE) confinado en nanoesferas, películas delgadas y películas delgadas modificadas en la superficie a través de NIL, impresas en nanorejillas. En la primera parte, se estudia la estructura y dinámica de nanopartículas ferroeléctricas de P(VDF-TrFE). Para ello se emplearon técnicas tales como AFM, DSC, WAXS y BDS. Luego, la ferroelectricidad en la nanoescala se estudió a través de microscopía de piezo-respuesta (PFM). Esta técnica se aplicó para estudiar ambos las películas delgadas y nanorejillas. Asimismo, se mostró la posibilidad de escribir y leer información en la nanoescala usando PFM.

En este estudio, la aportación fundamental consistió en demostrar que el P(VDF-TrFE), confinado en nanoesferas mantiene características ferroeléctricas altamente similares a las del comportamiento macroscópico del material. Este resultado es importante puesto que implica la potencial aplicación de nanoesferas de P(VDF-TrFE) en dispositivos electrónicos sin cambios en los comportamientos físicos del material ampliamente conocidos. Por otro lado, en el caso de películas delgadas y nanorejillas, se mostró que para las últimas el ciclo de histéresis se reduce, indicando que los voltajes necesarios para conseguir la conmutación del momento dipolar disminuyen. Además, en el caso de las nanorejillas, se logró escribir información en forma de puntos, a través de PFM. El uso de nanorejillas permitió que el voltaje aplicado se mantuviera restringido a

un único punto, en vez de propagarse a través de las estructuras cristalinas de las películas delgadas. Todos estos resultados se explicaron en función de la cristalinidad del material evidenciada por medidas de WAXS a incidencia rasante.

5. Referencias

1. Gompper, G.; Schick, M., An Introduction to Soft Matter. In *Soft Matter*, Wiley-VCH Verlag GmbH & Co. KGaA: 2007; pp 1-16.
2. Strobl, G., *The Physics of Polymers*. Springer: Germany, 1996.
3. Gedde, U. W., *Polymer Physics*. Chapman & Hall: England, 1995.
4. Adam, G.; Gibbs, J. H. *The Journal of Chemical Physics* **1965,** 43, (1), 139-146.
5. Keddie, J. L.; Jones, R. A. L.; Cory, R. A. *Faraday Discussions* **1994,** 98, (0), 219-230.

Summary

This document covers a wide summary of the Doctoral Thesis entitled **“CONFINAMIENTO EN NANOESTRUCTURAS POLIMÉRICAS: PREPARACIÓN, PROPIEDADES, APLICACIONES E IMPLICACIONES FÍSICAS”.**

This Doctoral Thesis has been divided in 8 chapters. As introduction to the subject, chapter 1 covers a bibliographic revision about polymers, the physics behind those systems and the problematic of the physical behavior of polymers in confinement. In chapter 2, all materials and techniques used throughout the development of this work are presented.

Confinement of polymers can be generated by the carefully changing the geometry of these materials. It is possible to depart from a macroscopic/bulk polymer material and generate structures with characteristics lengthscales in the order of nanometers, thanks to several physical and chemical techniques. This process is defined as *nanostructuring*. Chapter 3 of this Thesis is dedicated to present the results of a wide range of techniques for the nanostructuring of polymers in 1, 2 and 3 physical dimensions. Also, pros and cons of the techniques are discussed. The material processing for the preparation of polymer nanostructures is further discussed in chapter 4, by the application of laser techniques. Next, chapters 5, 6 and 7 are devoted to explore how confinement can modify the physical properties of polymers. First, in chapter 5, the variation of the glass transition temperature, in polymers confined in 3 dimensions, is studied. In chapter 6, we explore how the crystallization process is altered in polymers confined to thin films and nanoparticles. Finally, chapter 7 is focused on polymer ferroelectricity. In this section, besides showing the possible changes in the ferroelectric

response of confined polymers, also it is presented possible applications of polymer nanostructures for the development of organic memory devices. All the results gathered in this Thesis are summarized in chapter 8, where conclusions are highlighted and future work is presented.

Along the development of this Doctoral Thesis, and due to the quick progress in this research field, in relation to the results here presented, it was necessary to present part of this work for publication in scientific, peer-reviewed, journals. The published articles are:

- Daniel E. Martínez-Tong, M. Soccio, M. C. García-Gutiérrez, A. Nogales, D. R. Rueda, N. Alayo, F. Pérez-Murano, T. A. Ezquerra. ***Improving information density in ferroelectric polymer films by using nanoimprinted gratings***. Applied Physics Letters. Vol 102 (19). 109161. **2013.**

- Daniel E. Martínez-Tong, M. Soccio, A. Sanz, C. García, T. A. Ezquerra, A. Nogales. ***Chain Arrangement and Glass Transition Temperature Variations in Polymer Nanoparticles under 3D-Confinement***. Macromolecules. Vol 47 (2). 4698-4705. **2013.**

- Daniel E. Martínez-Tong, B. Vanroy, M. Wübbenhorst, A. Nogales, S. Napolitano***. Crystallization of poly (L-lactide) confined in ultrathin films: competition between finite size effects and irreversible chain adsorption***. Macromolecules. Vol 47 (11). 2354-2360. **2014.**

1. Introduction

Soft condensed matter is a convenient term for materials in states of matter that are neither simple liquids nor crystalline solids of the type of other branches of solid state physics. According to Gompper and Schick, dispersion colloids, systems of small amphiphiles and polymers can be classified as "classical" soft matter systems[1]. Specifically, polymers (also known as macromolecules), are built up of a large number of molecular units which are linked together by covalent bonds[2]. According to the basic IUPAC definition: A polymer is a substance composed of molecules, characterized by the

multiple repetition of one or more species of atoms or groups of atoms (constitutional repeating units), linked to each other in amounts sufficient to provide a set of properties that do not vary markedly with the addition of one or a few of the constitutional repeating unit[3]. When a polymer consists of only one type of constitutional repeating unit (A) is usually called a homopolymer (…-A-A-A-…). A copolymer, on the other hand, consists of two or more constitutional repeating units (A,B,…). Several classes of copolymers are possible, such as block copolymers (…-A-A-A-B-B-B-A-A-A-…) or alternating copolymers (…-A-B-A-B-A-B-…). Also, it is possible to find random copolymers, where the constitutional repeating units do not follow any strict pattern. In this case, the probability of finding a given constitutional repeating unit at any site is independent of the nature of the adjacent units at that position[3].

It is useful to divide the polymers into two main classes: the fully amorphous and the semi-crystalline. The fully amorphous polymers show no sharp, Bragg reflections in the X-ray diffractograms taken at any temperature. The reason why these polymers are unable to crystallize is commonly their chain structure. The semi-crystalline polymers show Bragg reflections superimposed on an amorphous background (also known as amorphous halo). Thus, they always consist of two components differing in the degree of order: a crystalline component composed of thin (around 10 nm) lamella-shaped crystals and an amorphous matrix[3]. The final structure of a polymer, *i. e*. whether it is composed by crystals + amorphous zones or only by disordered molecules in an amorphous state, depends on its molecular composition as well as in its thermal history. Considering a polymer at a temperature where all its molecular chains have the largest possible mobility, when cooling it down, the chains might reorganize in either a semicrystalline or an amorphous phase. In the first case, the temperature at which the reorganization begins is known a crystallization temperature. As the polymer chain rearrange, their molecular

movements are hindered, leading to a change in the final physical state of the material. The crystallization temperature depends on how fast or slow a material is cooled, which is known as the kinetics of the process. In the second scenario, polymer chains do not organize and its molecular structure is similar to that of a liquid or melt; however, when cooling down the polymer system, one might reach a point where the chains lose their mobility. This point is characterized by a dramatically increase in the elastic modulus, viscosity and other mechanical properties of the material. This temperature is known as glass transition temperature (T_g). The glass transition temperature is not unique but depends on the kinetics of the process.

The glass transition is one of the most studied phenomena in polymer physics. Thermodynamic and kinetic features are present in the glass transition phenomenon, and these processes are interwoven. For this reason, it is very difficult to put forward a theoretical representation of this transition. However, throughout several years, different theories have been proposed to explain this phenomenon. From a conservative point of view, the glass transition theories are classified in the following branches: *free volume, kinectic, and thermodynamic.* First's attempts to develop a theory of the glass transition where focused on the question of how is possible for an ordinary material, obeying the laws of statistical mechanics, to reach a glassy state without conquering an equilibrium state. A simple description of this phenomenon was provided by Adam and Gibbs[4]. These authors proposed that the glass transition process could be understood by introducing a factor called the *configurational entropy*. This parameter quantifies the "*excess*" of entropy in an amorphous system in relation to its crystalline counterpart, namely, assuming that the material is able to crystallize. Moreover, the authors proposed that this parameter is inversely proportional to the size of *cooperative rearranging regions*, in

which there are enough degrees of freedom such that the mobility of the material is allowed and thus molecules can rearrange.

As mentioned in the previous paragraphs, beside glass formers, polymers can also form semicrystalline systems. Morphology of those systems is usually composed by layers of crystals with a lamella shape, separated by amorphous zones. Nevertheless, the crystalline morphology depends on the length-scale at which it is being studied. In the range of the millimeters to micrometers, polymers observed under optical microscopy usually show spherical objects defined as *spherulites*. The formation of the spherulites begins with a crystalline *nucleus* that growth until reaching another spherulite. This crystallization process is known as *nucleation and growth*. Also, in the scale between microns and hundreds of nanometers, the structure of the polymers can be studied by transmission electron microscopy or using atomic force microscopy. On the other hand, crystalline structure in a molecular level is generally investigated by X-ray diffraction at wide angles.

Through the development of this Doctoral Thesis we have focused on the study of confined polymers, namely polymers geometrically structured in dimensions close to 100 nm. The possible variations in the properties and physical behavior of polymers structure at the nanometric level are known as *confinement effects.* Our study is related to the quick development suffered by nanoscience and nanotechnology in the last years, where new questions about the behavior of confined polymers have emerged. In this Doctoral Thesis we have focused our investigation in two confined geometries, namely: polymer thin films and polymer nanoparticles.

Polymer thin films are almost two dimensional materials. In these systems, two of the dimensions of the material, width and length, are macroscopic (millimeters or tens of

millimeters), while its thickness (or height) is in the nanometric scale. Thin films have attracted attention in both fundamental and technological point of view. First, from a technological side, polymer thin films are used as coatings in electronic and bioinspired devices. On the other hand, from the fundamental standpoint, it has been observed that the properties of these films may change with confinement. These works began with the pioneering research of Keddie et al in the mid-1990s[5]. In these works it was proven, by ellipsometry measurements, that as the thickness of the polymer film was decreased, the T_g also decreased. It was proposed that the decreased of the T_g in polymer thin films was related to the existence of *free surface layer,* which can be defined as the polymer layer closer to the air, and thus which molecules has the least interactions among them, leading to higher mobility. Other authors have proposed that changes in T_g, suffered by polymer thin films, are influenced by the nature of the substrate. Thus, the increase or decrease of the glass transition temperature with confinement might be explained by the polymer/substrate interaction. Even more, it has been reported, by broadband dielectric spectroscopy measurements, that the changes in T_g can be related to the development of an irreversible adsorbed polymer layer on the substrate, also known as *residual layer*.

In the case of semicrystalline polymer thin films, confinement is able to affect both the growth of crystals as well as the resulting crystalline morphology. The changes in the crystallization of polymers are reported to appear when the thicknesses of the films are equal or less with respect to the mean size of a spherulite. In these dimensions, polymers tend to form plane features or even ones with dendritic shapes. As with the study of glass transition in confinement, the polymer/substrate interaction might affect the crystallization of polymers confined in thin films. It has been reported that the development of adsorbed polymer layers affects the crystallization of the material.

Polymer nanoparticles can be defined as colloidal systems, with lower diameters around 5-10 nm and with an upper limit about 100 nm, although usually this range is about 100 – 500 nm. The term *polymer nanoparticles* cover a broad definition, used to describe particles of nanometric size. As with the thin films, confinement in polymer nanoparticles alters the physical properties of material, in comparison to their bulk behavior. For example, it has been reported that T_g of confined polymer nanoparticles can change, increasing or decreasing its value. These results have been evaluated, generally, using differential scanning calorimetry, although other techniques as broadband dielectric spectroscopy and ellipsometry have been also applied. The decrease of the glass transition temperature of polymer nanoparticles has been related to the existence of a free surface layer, just as in the polymer thin films. However it has also been reported that Tg in confined polymer nanoparticles might also increase, respect its bulk value. This has been explained arguing changes in the polymer chains organization.

2. Objectives

The main objective of this Doctoral Thesis was the preparation of polymer systems under several confined geometries, and to study the physical changes that resulted from confinement. In order to fulfill this main objective, this research was focused on two specific aspects. First, the preparation of several polymer nanostructures (nanoparticles, thin films and modified surfaces) using several polymer systems (both amorphous and semi-crystalline). Then, measurements of the physical properties of the prepared polymer nanostructures were performed in order to provide further information about the possible changes induced by confinement. In the case of amorphous polymer nanoparticles, the evolution of the glass transition was followed by means of differential scanning calorimetry. For semi-crystalline polymers, the crystallization behavior was studied by atomic force microscopy, X-ray diffraction and broadband dielectric spectroscopy. This

last technique allowed not only observing the physical changes regarding the crystallization kinetics in confinement but also let attaining information about the adsorption mechanisms in polymer/substrate interactions. Finally, the ferroelectric behavior in confined polymer structures was also studied, where possible applications of the polymer nanostructures were evaluated.

3. Conclusions

All the results presented in this thesis allow us concluding:

- It is possible to prepare polymer nanoparticles (diameter < 100 nm) of several amorphous and semi-crystalline polymers, by different methods depending on the polymer nature. Sub-micrometric particles (diameters < 1000 nm) can also be prepared by tuning these methods.
- Pulsed laser ablation of polymers in liquids (PLAL) represents as an alternative to the physico-chemical methods of nanoparticles preparation. Nanostructures, with diameters well below 100 nm were formed with geometries dependent on the surrounding liquid.
- The glass transition temperature of amorphous polymer nanoparticles increases with respect to that of the bulk, as evidenced by DSC. A decrease in the entropy of the nanoparticles is responsible for this change. It has been found that amorphous nanoparticles, that are able to crystallize when annealed, suffer also the effects of confinement.

- Finite size effects affect the crystallization behavior of polymers. Nonetheless, in the case of polymer thin films, care must be taken regarding the influence of both

confinement and adsorption of the supporting substrate. These different contributions were evaluated and disentangled by BDS. Also, it is possible to analyze the morphological changes of semi-crystalline polymer thin films by AFM. In the specific case of PLLA, it was found that for thicknesses below 20 nm, a dramatic change in the morphology took place. Finally, it was found that nanocrystals can be prepared starting from amorphous polymer nanospheres of PDLLA.

- Ferroelectric behavior of the P(VDF-TrFE) copolymer, in confined geometries, is preserved. In the case of polymer nanoparticles the ferroelectric response is fairly similar to that of a bulk-like material. In the case of nanogratings, ferroelectricity is affected, as observed by the decrease in the value of the coercive field. This decrease was explained in terms of the changes in the crystalline morphology when the copolymer was crystallized in a confined environment. Also, PFM results showed that the preparation of nanogratings can be of important use towards the miniaturization of all-organic technological devices, such as ferroelectric memories.

4. Summary of Results

We present a short summary of the most important findings obtained in this Doctoral Thesis. In the following sections the different contributions, widely discussed in the results chapter, are highlighted.

4.1. Preparation of polymer nanostructures by physic-chemical methods

In this Doctoral Thesis we have faced the problem of polymer nanostructures preparation. The possibility of preparing polymer nanoparticles, with spherical shape, through different physic-chemical methods was presented. Fisrt, through the miniemulsion

method amorphous polymer nanoparticles were prepared. For all polymer systems, we obtained nanoparticles with mean diameters below 100 nm. Their morphology was characterized by Atomic Force Microscopy (AFM). Also variations of this method allowed preparing nanoparticles with sub-micrometer diameters. The miniemulsion method was further applied to prepare nanoparticles of semicrystalline polymers.

Second, the so-called solvent-displacement techniques were studied. In a first section it was shown the possibility of preparing polymer nanoparticles of a ferroelectric copolymer, through the dialysis nanoprecipitation method. AFM analysis showed that nanoparticles with mean diameters around 300 nm could be obtained. The second technique, called reprecipitation method, allowed preparing nanoparticles by playing with the polymer solvent concentrations. This enabled the possibility of tuning the mean size and widths of size distributions.

It was also possible to prepared polymer nanostructures in 1 and 2 dimensions. In these cases we used the spin coating technique for preparation of polymer thin films, were confinement takes place in one direction. Furthermore, some of these films were modified by Nanoimprint Lithography, for the preparation of nanogratings.

4.2. Preparation of nanoparticles by pulsed laser ablation in liquids

The purpose of this section is to study the preparation of nanoparticles by pulsed laser ablation in liquids. Initially, the experimental setup and the physics behind the ablation process are described. Then, it is shown the variation in the nanoparticle size, by AFM, as function of the laser beam fluence. Finally, the geometrical variations of the ablated material, as a function of the liquid media, are studied.

4.3. Glass transition temperature variations in polymer nanospheres

This section is focused towards understanding the possible variations in the glass transition temperature (T_g) of polymers confined to nanospheres. Differential Scanning Calorimetry (DSC) was used to study this phenomenon. The most important result of this section is the increase of the nanoparticles' T_g in relation with their bulk signals. We have found that nanoparticles with diameters around and above 100 nm do not show any changes respect to the bulk. To explain the results q model based on the entropy of the system was used. We found that the fundamental parameter controlling the confinement of polymer nanospheres is the number of repeating units enclosed in each system.

4.4. Crystallization of confined polymer systems

In this section the crystallization of polymers in confined geometries was studied. Polymer thin films and nanoparticles were both used. The main results of this study are highlighted in the following lines. First, crystallization of thin films, by Broadband Dielectric Spectroscopy allowed determining how the confinement effects influence the crystallization of the material: the thinner the film the longer the time needed for crystallization. Also through this method the adsorption of the polymer to the substrate was studied. Crystalline morphology was also studied by AFM. Morphology changes were evidenced when film thickness was below 35 nm. In the case of polymer nanoparticles, different preparation methods allowed obtaining amorphous polymer nanoparticles. As the nanoparticles were heated, Bragg peaks appeared in the X-ray diffractograms, as indication of the crystallization phenomenon.

4.5. Ferroelectricity of confined polymer systems

In this last section we explore the problem of ferroelectricity in confined polymers, such as nanoparticles, thin films and imprinted nanogratings. We have found that the ferroelectric copolymer confined in nanospheres retains its ferroelectric characteristics,

quite similar to those of the bulk material. On the other hand, it was also explored the hysteresis behavior in nanogratings and thin films. We observed that the coercive field of the nanogratings decrease in comparison to that of the thin film.

5. References

1. Gompper, G.; Schick, M., An Introduction to Soft Matter. In *Soft Matter*, Wiley-VCH Verlag GmbH & Co. KGaA: 2007; pp 1-16.
2. Strobl, G., *The Physics of Polymers*. Springer: Germany, 1996.
3. Gedde, U. W., *Polymer Physics*. Chapman & Hall: England, 1995.
4. Adam, G.; Gibbs, J. H. *The Journal of Chemical Physics* **1965,** 43, (1), 139-146.
5. Keddie, J. L.; Jones, R. A. L.; Cory, R. A. *Faraday Discussions* **1994,** 98, (0), 219-230.